UNIVERSITY OF
BIRMINGHAM

# PhD Thesis

# Strangeness Enhancement in Singly-strange Hadron Production in p-Pb Collisions with the ALICE Experiment

Oliver Thomas Jevons

A thesis submitted to the University of Birmingham for the degree of Doctor of Philosophy

Nuclear Physics Group
School of Physics and Astronomy
University of Birmingham
November 2021

# Abstract

At conditions of extremely high temperature and energy density, a strongly-interacting state of matter can be formed, known as the Quark Gluon Plasma (QGP). Such QGPs are formed experimentally in heavy-ion collisions, such as those between lead ions (Pb-Pb) carried out at the LHC. Due to the extremely short lifetimes of such states, any produced QGP is not directly observable. Instead, studies are performed on a number of signatures, which indicate the presence of a QGP and its properties. Historically, smaller systems, such as those formed in proton-proton (pp) and proton-lead (p-Pb) collisions, were not thought to be capable of forming a QGP. However, recent ALICE results have shown QGP-like behaviour in pp and p-Pb collisions; as such, these smaller systems are the topic of further study.

One of the observables used to indicate the presence of a QGP is the enhanced production of strange hadrons, relative to their non-strange counterparts. This enhancement is more easily seen in species with a higher strangeness content, such as the multi-strange $\Xi^{\pm}$ and $\Omega^{\pm}$ baryons, however, it is also present for singly strange species such as the $\Lambda$ baryon and $\mathrm{K}^0$ meson. These species can be studied using the high precision tracking and momentum determination available using the ALICE detector, potentially providing further evidence for strangeness enhancement in small systems.

This thesis presents the study of the production of singly strange species (the $K^0_S$ and $\Lambda$, also referred to as V0's) as a function of final state multiplicity in p-Pb collisions at a centre-of-mass energy-per-nucleon of 8.16 TeV. The process by which transverse momentum, $p_{\mathrm{T}}$, spectra are generated and corrected is described, and the spectra, with their errors, are presented. For both species, the spectra display a shift to higher $p_{\mathrm{T}}$ as the multiplicity increases, which suggests the presence of radial flow.

In order to investigate strangeness enhancement in the events studied in this analysis, the $p_{\mathrm{T}}$-integrated yields of both $K^0_S$ and $\Lambda$ are compared with measured yields of charged pions in the same collision system. The hadron-to-pion ratios increase as a function of final state multiplicity, suggesting QGP-like behaviour in small systems. A comparison between the results presented in this thesis and those measured in other collision systems and energies is shown. The hadron-to-pion ratios follow a continuous increase, from the low multiplicities present in pp collisions, to the high multiplicities observed in Pb-Pb collisions, suggesting that strangeness enhancement is an effect which is independent of the initial collision energy or system size.

# Author's Contribution

The work presented in this thesis was carried out whilst I have been a member of the ALICE collaboration, and as such, I cannot claim to be the only person whose work contributed to the results shown. I owe a lot to the teams of engineers and scientists who work on the maintenance and operation of the ALICE experiment, LHC, and CERN computing infrastructure. During my time as part of ALICE, I have been a member of the Light Flavour Physics Working Group (PWGLF), particularly as a member of the Strangeness Physics Analysis Group (PAG). The members of these two groups have given me invaluable advice, which has helped me overcome the problems that I have faced undertaking the analysis presented here.

Given the size of the raw data files generated by ALICE, this analysis was run over more compact Event Summary Data (ESD) files, which hold TTree data structures containing the information needed for this analysis. The ESDs used for the results presented in this thesis were created by Emily Willsher for her analysis on multi-strange baryons in p-Pb collisions at $\sqrt{s_{\mathrm{NN}}} = 8.16$ TeV, using code originally written by David Chinellato for use on Pb-Pb data.

The initial analysis of the candidates held in the ESD files was carried out using post processing macros which I also inherited from Emily Willsher; these being derived from macros written by Livio Bianchi for strangeness analyses on Run 1 data. These macros have been used to apply the candidate selections used for this analysis, as well as extract yields and calculate systematic errors. All of the plots contained within this thesis have, unless otherwise stated, been made by me.

# Acknowledgements

Over the last four years, I have met and interacted with many people who have both helped me to complete my analysis, and keep me sane after long nights of code debugging. First and foremost, I would like to thank my supervisors and strangeness experts at the University of Birmingham: David Evans, Roman Lietava and Orlando Villalobos-Baillie, for helping me through the obstacles that have come to light during my analysis, and for always being willing to offer their advice and support. I also wish to thank the other members of the University of Birmingham ALICE group for helping me to truly feel like part of the team: Peter Jones, Anton Jusko and Marian Krivda.

I also owe many thanks to the whole of the ALICE collaboration, without whom I would not have any data to analyse, let alone a project to complete a PhD on! I also wish to give thanks to the members of the ALICE Strangeness PAG for their advice and ideas during our group meetings. I would particularly like to thank David Chinellato for the amount of time that he has given up helping me to understand some of the more nuanced areas of this analysis, and for being willing to give advice whenever I needed it. I must also mention Meenakshi Sharma, with whom I have completed the work detailed in this thesis; I thank her for her ideas discussed when we met, and I wish her the best of luck in taking this analysis for presentation and publication.

I wish to thank those whom I have shared an office with over the last four years, however briefly the COVID pandemic may have made it: Jack, Nima, Harry, Emily, Kae, Jakub, Stuart, Beckie, Håkan, Yiming, Pedro, Tony, Marianna, Simone, Ross, Angus, Sammy and Luis - our discussions over lunch and board game evenings have given me no end of laughter and joy. In addition to those mentioned previously, I also want to thank those who have put up with me as a flatmate over the years: Jon, Dave, Albert, Sergei and Robbie. I would like to thank the members of the CERN Games Club, particularly the RPG groups, for welcoming me in and making my time living alone more enjoyable. Finally, I would like to thank my family for their continued support during my PhD, and for believing in me, even when I didn't believe in myself.

# Contents

# List of Figures

# List of Tables

# Chapter 1

# The Standard Model

For millennia, human kind has wondered about the building blocks of the world we live in. From the basic ‘elements’ espoused by the ancient Greeks, through the early atomic models of the 19th and 20th centuries, each new theory has refined ideas further and further. The culmination of this process is the modern theory of fundamental particles, known as the Standard Model of particle physics.

Many analyses done within the ALICE collaboration investigate a state of matter known as the Quark Gluon Plasma (QGP), which is a result of extreme conditions on the strong force of the Standard Model. In order to understand the QGP, an understanding of the Standard Model is required. This chapter shall introduce this theory, and shall discuss the aspects of it which lead to the formation of Quark Gluon Plasmas.

## 1.1 The History of Particle Physics

For as long as humans have existed, they have tried to explain the complexity of the world, by considering what all matter is made of. Many Eurasian civilisations used a combination of very similar fundamental “elements” in their explanations; from the earth, air, fire and water (and later aether) of ancient Greece, to the fire, earth, wood, water and metal used in

Chinese philosophy. Ancient Greece was also the birthplace of another important idea: that matter was, at its simplest form, composed of unbreakable, fundamental units; proposed around 450 BC by the philosopher Democritus. This proposal has stuck with physics to this day: the word atom is derived from the Greek word meaning 'indivisible', *atomos*.

Very little of these explanations were changed or expanded upon until the work of the British chemist John Dalton in the early 19th century. Dalton's work on gaseous compounds led to the formulation of his atomic theory, which would set the groundwork for the majority of modern chemistry. This atomic theory (the first use of the word atom in what would become its modern usage) was expanded upon, among others, by Dmitri Mendeleev, who, in the 1860s, formulated elements into some form of ordered list: the periodic table.

It should be noted that, running through all of these previous theories, elements were postulated to be made up of individual, indivisible, units of matter. This was to change in 1897 with the discovery of the first subatomic particle, the electron, by the physicist J. J. Thomson. He observed that cathode rays could travel further through air than a beam of particles of a size comparable to that of an atom. This observation led to the conclusion that cathode rays were composed of very light (three orders of magnitude less massive than the hydrogen atom), negatively charged particles that must come from the atoms of the trace gas inside his cathode ray tubes. This led to the conclusion that atoms were not indivisible; thus the 'plum pudding' model was developed, in which negatively charged electrons lay inside some positively charged volume which comprised the rest of an atom.

Ernest Rutherford would refine this atomic model further in the early 20th century with the now famous 'gold leaf experiment', also known as the Geiger-Marsden experiment. In this, Hans Geiger and Ernest Marsden, under the direction of Rutherford, pointed a beam of alpha particles at a very thin sheet of gold foil, and measured the scattering pattern with a fluorescent screen. The observations that this experiment made would lead to Rutherford's new atomic model, proposed in 1911: that atoms were comprised of electrons surrounding a very small, very dense, positive nucleus, as in figure 1.1. Later in his career, Rutherford

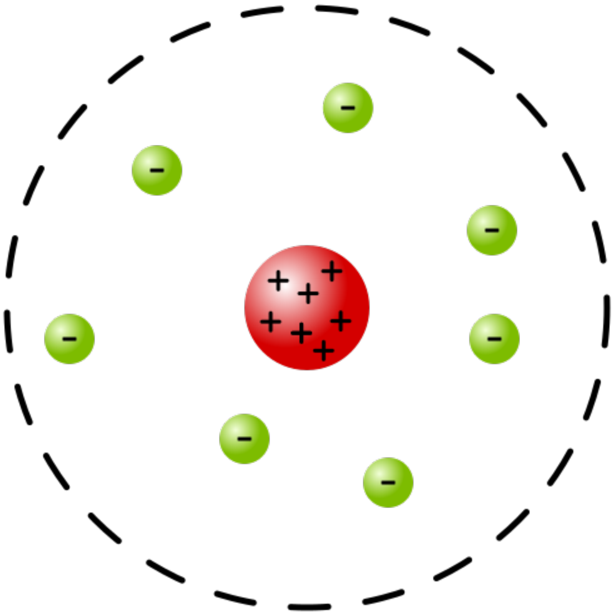

Figure 1.1: The Rutherford atomic model [1]. Note that this differs from the modern interpretation of the atom, with electrons surrounding the nucleus in neat orbitals. This would be proposed by Niels Bohr in 1913.

would also go on to postulate that nuclei were further divisible: into positive protons (already known about as the hydrogen nucleus), and neutral particles that were christened neutrons (these would be experimentally observed in 1932, by one of Rutherford's previous doctoral students, James Chadwick).

In 1947, a collaboration from the University of Bristol discovered the charged pion [2], and from there the field of particle physics exploded. Over the following decades, new particles were being discovered at such a rate that it became abundantly clear that not all of them could be fundamental. New theories were therefore required to explain the similarities and differences between the many entities in this so-called "particle zoo". One such theory, proposed in 1961 by Murray Gell-Mann and Yuval Ne'eman, was the Eightfold Way [3], which grouped the spin-zero mesons and spin-1/2 baryons into octets (hence the name of the theory), and the spin-3/2 baryons into a decuplet.

Gell-Mann would later go on to theorise what gave rise to the structure of the groups described in the Eightfold Way. In 1964, he and George Zweig independently proposed the existence of smaller subatomic particles which Gell-Mann named ‘quarks’ (the name which these particles retain to this day), and that the various baryons and mesons were some combination of quarks and their corresponding antiquarks [4, 5]. In the initial formation of the quark model, only three types, or ‘flavours’ of quarks existed: up, down and strange, however as time went on, more of these were proposed. This updated quark model, along with a description of other fundamental particles such as the electron, and carriers for the known forces of nature, comprise the Standard Model of particle physics.

## 1.2 The Standard Model

As mentioned previously, the Standard Model (SM) of particle physics contains a description of all particles currently considered to be fundamental and the interactions which occur between them, with the exception of gravity. These include the 12 half-integer spin fermions, and the six integer spin bosons. One common way of visualising the particles in the Standard Model is shown in table 1.1, in which the fermions are separated from the bosons. In addition, the SM describes antimatter partners to each particle. These antiparticles have the same physical properties as their matter counterparts (mass, spin, etc.), but opposite charges.

Table 1.1: A representation of the Standard Model of particle physics. The first three columns of particles list the fermions in the SM, and the last two list the bosons.

| | Generation | | | Bosons | |
|---|---|---|---|---|---|
| | I | II | III | | |
| Quarks | u | c | t | g | $H^0$ |
| | d | s | b | $\gamma$ | |
| Leptons | e | $\mu$ | $\tau$ | $W^\pm$ | |
| | $\nu_e$ | $\nu_\mu$ | $\nu_\tau$ | $Z^0$ | |

The fermions in the SM are comprised of two families of particles: the quarks, which interact with the strong force, and the leptons, which do not. The six quarks - with different flavours of up, down, charm, strange, top and bottom - carry fractional electric charge (given in units of the charge of the electron, $|e| = 1.60 \times 10^{-19}$ C), and cannot be observed in isolation, a phenomenon which shall be discussed later in this chapter. The leptons comprise the electrically charged electron, muon and tau (all of which have charge of $-|e|$), and the electrically neutral neutrinos, one corresponding to each charged lepton, which were initially considered to be massless. Direct observations of neutrino flavour oscillations by the Super Kamiokande experiment [6] and Sudbury Neutrino Observatory [7] showed that this was not the case, and provided the first experimental evidence of physics beyond the Standard Model.

A second common subdivision for the fermions is to separate them into three generations, the particles in each generation increasing in mass from those in the generations before (with the exception of the three neutrinos, whose masses are not directly known). The first generation; the up and down quarks, the electron and the electron neutrino, are the particles which comprise all stable matter. The particles in the second and third generations are heavier partners to these first generation fermions, and as such are far more rarely observed.

As mentioned previously, the fermions are not the only particles in the Standard Model: also included are six bosons; five vector bosons, which act as mediators for the fundamental forces, and the scalar Higgs Boson, which is the physical representation of the Higgs field, the source of mass for the particles in the SM. Of the four fundamental forces, only gravity is not described by the SM; this can be seen by the lack of a gravitational term in the Standard Model Lagrangian.

Of the other three fundamental forces, only one has a mediator which can travel across macroscopic scales: the electromagnetic force, whose force carrier is the photon. The quantum field theory description of the electromagnetic force is known as Quantum Electrodynamics (QED), a theory which was developed independently by Richard Feynman, Julian Schwinger and Shinichiro Tomonaga [8–11] in the 1940's. This work would go on to form the basis for the Nobel Prize in Physics in 1965. The strong force, carried by the gluon, governs inter-quark interactions. The field theory describing the strong force is called Quantum

Chromodynamics, and shall be discussed later in this chapter.

The weak force is the phenomenon responsible for, among other things, nuclear beta decay. It utilises multiple force carriers: the $W^{\pm}$ bosons for charged current interactions, those which are capable of changing quark flavour; and the $Z^0$ boson for neutral current interactions. The field theory description of the weak force has it combined with a picture of electromagnetic force, in what is known as electroweak theory. This theory unifies both the weak and electromagnetic interactions as two different parts of the same force. As with QED, the development of electroweak theory led to the awarding of the Nobel Prize in Physics to its authors: Sheldon Glashow, Abdus Salam and Steven Weinberg [12–14].

Spontaneous symmetry breaking in electroweak theory would also lead to the development of what would be come to be known as the Brout-Englert-Higgs mechanism in the 1960's. This theory was developed independently by Peter Higgs [15] and a collaboration between Robert Brout and François Englert [16]; following the discovery of the Higgs Boson by the ATLAS [17] and CMS [18] collaborations, Englert and Higgs were awarded the Nobel Prize in 2013. This discovery has been considered by many to be the confirmation of the final piece of the Standard Model puzzle.

## 1.3 Quantum Chromodynamics

Quantum Chromodynamics (QCD) is the quantum field theory picture of the strong force, and its interactions between quarks. Development of QCD took place over the latter part of the 20th century, building out from the discoveries of numerous hadrons in the 1950's and the Eightfold Way formalism of Gell-Mann and Ne'eman. Much like the electromagnetic force couples to electric charge, the strong force also couples to a property of particles: colour.

### 1.3.1 Colour

Within the models developed by Gell-Mann and Zweig, quarks could be bound in one of two ways: as a quark-antiquark ($q\bar{q}$) pair, known as a meson, or as a quark triplet ($qqq$) state - a baryon. This theory encountered issues with the discoveries of the $\Delta^{++}$, $\Delta^{-}$ and $\Omega^{-}$ baryons; spin-3/2 baryons comprised of three identical quarks (up, down and strange respectively for the $\Delta^{++}$, $\Delta^{-}$, and $\Omega^{-}$). By their composition, these baryons would require the existence of all three quarks to be in the same spin state, which would violate the Pauli Exclusion Principle. Therefore, the existence of these baryons suggests the presence of another quantum number inside the quarks, which can take at least three different values.

Given the analogy between the three possible values of this quantity and the behaviour of light, the quantum number was given the name ‘colour’. For the same reason, the values that this quantity could take were given the names of ‘red’, ‘blue’ and ‘green’. Within the colour picture, all hadrons must be colour neutral; their constituent quarks either taking the same colour and anticolour ($r\bar{r}, b\bar{b}$ or $g\bar{g}$) in the case of mesons, or one of each colour ($rgb$) for baryons. In contrast to QED, the mediator of the strong force carries the quantity that the force couples to. Gluons can carry one of eight combinations of colour and anti-colour, which allows for gluon self-interaction. This allows the strong force to exhibit phenomena such as confinement and asymptotic freedom.

### 1.3.2 Confinement

*Confinement* refers to the phenomenon of quarks not being observed in isolation; only bound within hadrons. To provide context for this, a comparison to the electromagnetic force is useful. The interaction potential within QED is inversely proportional to the distance between charges,

$$V_{QED} \propto -\frac{\alpha_{EM}}{r} \quad ,$$

where $\alpha_{EM} = 1/137$ is the electromagnetic coupling constant. The physical consequence of this is that the strength of the electromagnetic force falls off with distance. For the strong force, this is not the full picture. The potential for the strong force takes the following form,

$$V_{QCD} \propto -\frac{4}{3}\frac{\alpha_s}{r} + kr \quad . \tag{1.1}$$

The first term in 1.1 can be referred to as a 'Coulombic' or 'Coulomb-like' term, as the $1/r$ behaviour mimics that of the QED potential. The second term, that proportional to $r$, is the new term, introduced to reflect the effect of gluon self-interaction. As the distance between two quarks increases, the second term in equation 1.1 comes to dominate, and the energy stored in the QCD potential increases. Eventually, a point is reached where it becomes more energetically favourable to create a quark-antiquark pair from the gluon field between the original quarks. This new quark pair then binds with the old to form a pair of new hadrons, as shown in figure 1.2. As a result of this, quarks are always observed bound into hadron, and never in isolation. This creates the phenomenon of *confinement*.

### 1.3.3 Asymptotic freedom

When referring to the interactions between fundamental particles, it is common to consider forces as being related to a coupling; the strength of that coupling being dictated by a "coupling constant". These 'constants' are poorly named, as they ultimately depend on parameters of the interaction, and the creation of virtual particle-antiparticle pairs allowed by the Heisenberg Uncertainty Principle.

In the case of the electromagnetic interaction, the electric field generated by a charge is screened by the presence of virtual electron-positron pairs. As a test charge is brought closer to the source of this field, the screening effect is reduced, increasing the effective strength of the original charge. This effect is represented mathematically by the electromagnetic coupling constant, $\alpha_{EM}$, increasing as the separation between charges decreases. Another way to

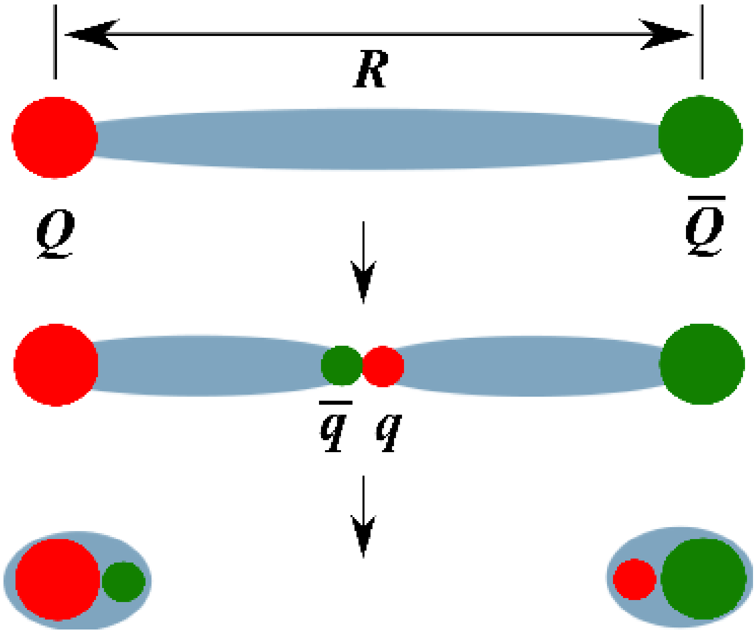

Figure 1.2: Demonstrating the confinement of quarks [19]. Once the distance between the pair of quarks, Q, becomes large enough, a new pair of quarks, q, is created. These bind to the original quarks, forming two new mesons.

consider the changing, or *running* of the coupling constant, is to consider the energy transfer in the interaction. High energy transfers typically refer to small-distance interactions, so $\alpha_{EM}$ can be said to increase with $Q^2$, the 4-momentum transfer in the interaction. This can be seen in figure 1.3.

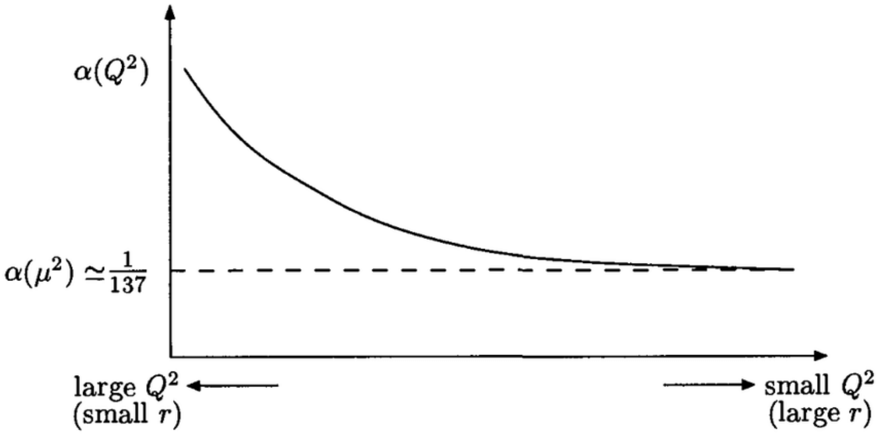

Figure 1.3: Dependence of the electromagnetic coupling constant on 4-momentum transfer, $Q^2$, in an interaction [20]. Also visible are the qualitative relationships between $Q^2$ and the interaction distance, $r$, and the asymptotic value for $\alpha_{EM}$, known as the fine structure constant.

Similarly, when considering a QCD interaction, virtual quark-antiquark pairs screen the source of a colour field. However, this effect is countered by the presence of gluon loops which, due to gluon self-interaction, take on an anti-screening behaviour. Taking into account these effects, the strength of the QCD coupling can be written as follows,

$$\alpha_s(Q^2) = \frac{\alpha_s(\mu^2)}{1 + \alpha_s(\mu^2)(\frac{11N_c - 2N_f}{12\pi})\ln(Q^2/\mu^2)} . \tag{1.2}$$

Equation 1.2 [21] is known as the QCD renormalization group equation. It relates the strength of the QCD coupling at some energy scale, $\alpha_s(Q^2)$, to its measured strength at some other scale, $\alpha_s(\mu^2)$. This equation is related both to the number of available colours, $N_c$ (three), and the number of quark flavours, $N_f$ (six). This parameter-dependent term is positive, and as a result, the denominator of equation 1.2 is greater than 1 for $Q^2 > \mu^2$; $\alpha_s$ therefore decreases as $Q^2$ increases. Figure 1.4 demonstrates the running of the QCD coupling in measurements made using collider experiments.

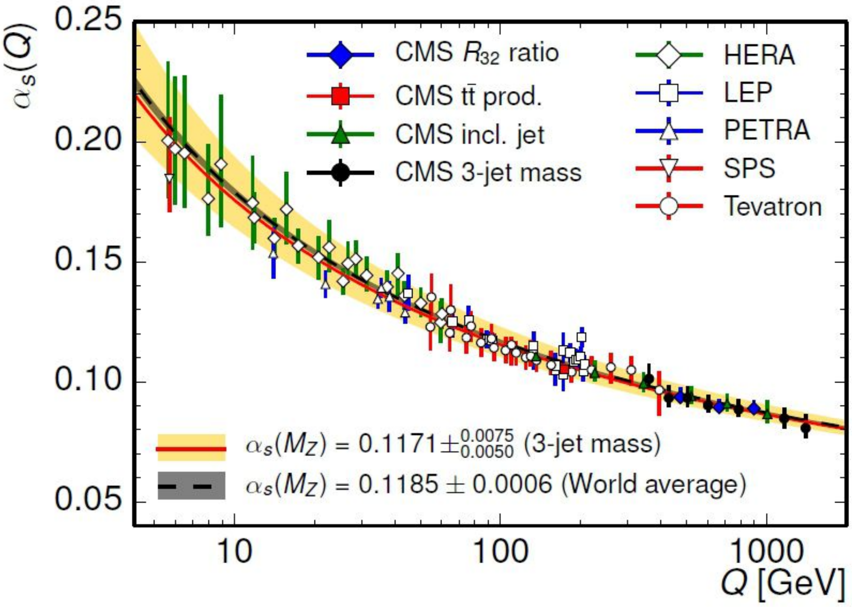

Figure 1.4: The strength of the strong coupling constant as a function of energy scale, as measured by CMS and a number of other collaborations [22].

As the energy scale involved in a QCD interaction increases, or the distance between two colour charges decreases, the coupling involved drops off in a behaviour known as *asymptotic freedom*. This behaviour was initially discovered by David Politzer, David Gross and Frank Wilczek [23–25] in the mid 1970's, for which they received the Nobel Prize in Physics in 2004. A consequence of asymptotic freedom is that, at sufficiently high energy densities, quarks should be able to exist without having to bind into hadrons; a behaviour known as *quark deconfinement*.

The prediction of quark deconfinement at high energy densities led to further proposals that such a state of matter could have existed in the early stages of the universe, or could be replicated in a laboratory environment. Such a state of matter would have quarks and gluons freely moving, unbound into hadrons, analogous to the way that electrons and ions flow freely in a plasma. As a result, this new proposed state of matter was called the Quark Gluon Plasma, or QGP [26].

### 1.3.4 Debye screening

As discussed in section 1.3.2, long range interactions are screened by the presence of free-moving charge carriers which surround the source of a field. Within a sufficiently hot and dense medium, this screening effect is known as *Debye screening*, after the German physicist Peter Debye, who first described it. The screening of a point charge changes the effective length over which it is felt. Thus, for short-range interactions, the QCD potential can be written as follows,

$$V_{QCD} = -\frac{4}{3}\frac{\alpha_s}{r}e^{-r/\lambda_D} \quad ,$$

where $\lambda_D$ is the Debye screening length [27].

The Debye screening length is dependent on the conditions of the matter in which the potential is acting; as the energy density of the medium increases, $\lambda_D$ decreases. When $\lambda_D$ gets comparable to hadronic radii, at around 1 fm, the strong force between quarks becomes smeared to the point that they no longer bind into hadrons.

## 1.4 QCD Models

In order to make any meaningful predictions about the behaviour of strongly-interacting matter, models are required which can replicate the behaviour of a system. These models can take one of two forms: perturbative or non-perturbative. Perturbative QCD (pQCD) is most commonly used to model high-energy inter-parton interactions to extremely high precision. For such models, calculations not only consider the basic interaction taking place (for example, pair production of a quark-antiquark pair), but also higher order virtual corrections. With each increasing order of correction, the calculation more accurately describes the interaction taking place, at the cost of increasing complexity. As a result of this, larger scale medium behaviours are better modelled using less complex, non-perturbative, theories.

### 1.4.1 Lattice QCD

Lattice QCD is a non-perturbative approach to modelling the strong interaction, which can be reliably used to describe the behaviour of strongly interacting matter. To construct lattice QCD calculations, the QCD Lagrangian - which mathematically describes interactions between quarks and gluons - is discretised over a 4 dimensional grid, comprised of three spatial dimensions, and one temporal dimension. This approach relates the volume and temperature to the lattice point separation, $a$,

$$V = (N_s a)^3 \quad , \quad T^{-1} = N_t a,$$

where $N_s$ and $N_t$ are the number of space (three) and time dimensions (one), respectively [28].

Lattice calculations are used to describe the bulk behaviour of strongly-interacting media, and can be used to extract thermodynamic properties, such as pressure, entropy density, or energy density. Figure 1.5 shows the temperature evolution of energy density, $\varepsilon$, over $T^4$ for three different QCD flavour models. A sharp increase in energy density at the critical temperature, $T_c$, for all of the models considered indicates a phase transition from normal hadronic matter to a deconfined state: a QGP. For the three flavour case, this critical temperature is $154 \pm 8$ MeV [29], well within the reasonable range for heavy-ion collisions to replicate.

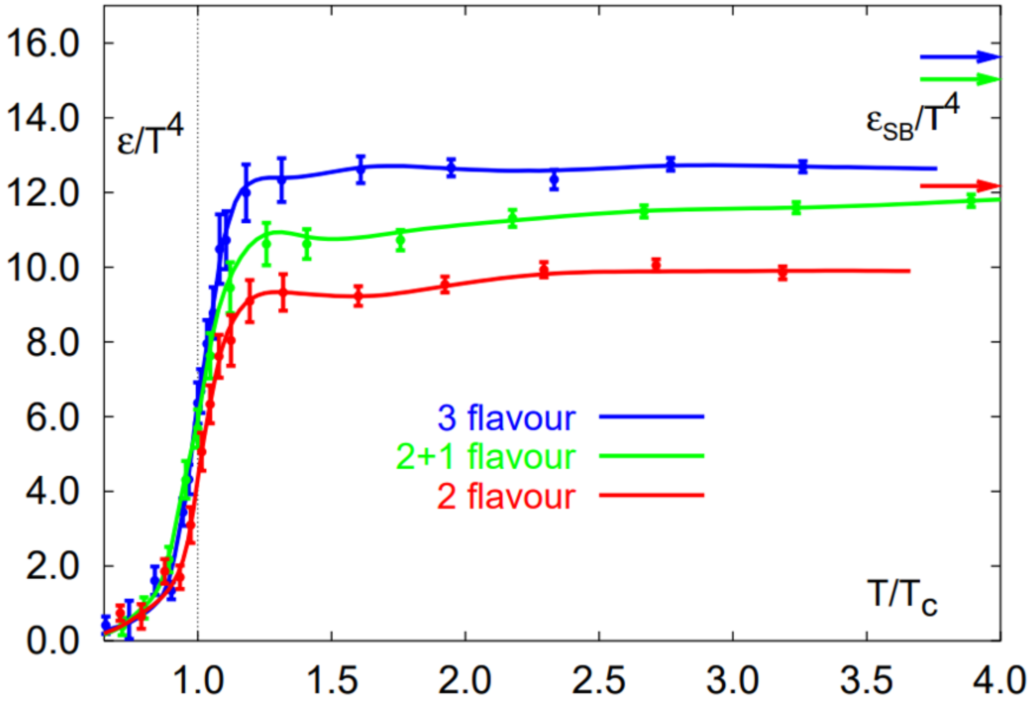

Figure 1.5: QCD energy density as a function of temperature, plotted for different quark flavour models [30]. Temperature, $T$, is expressed as a fraction of the critical temperature, $T_c$. The arrows on the right of the figure show the predicted behaviour for an ideal gas, for each of the different flavour models.

Lattice QCD calculations also predict that, at the high-temperature limit, the QGP would behave like an ideal gas. Figure 1.5 shows the predicted energy densities for an ideal gas, $\varepsilon_{SB}$, using the same flavour models as used for the QCD matter calculations. As can be seen, this value is not reached for temperatures close to $T_c$, which would suggest that quark-gluon interactions are still able to take place within a QGP.

The QCD phase diagram, as shown in figure 1.6, displays the various phases that strongly-interacting matter can take. It relates the possible states of matter both to temperature, $T$, and to baryon chemical potential, $\mu_B$, a quantity which is related to the net baryon density in a system. Current theories suggest that the early universe was in a QGP state shortly after the Big Bang. This corresponds to the region where $\mu_B = 0$, at which the transition from hadron gas to quark gluon plasma occurs at a critical temperature around 150 MeV. This region of phase space, at low $\mu_B$ and high temperature, is where current heavy ion experiments such as ALICE [31] and STAR [32] are probing.

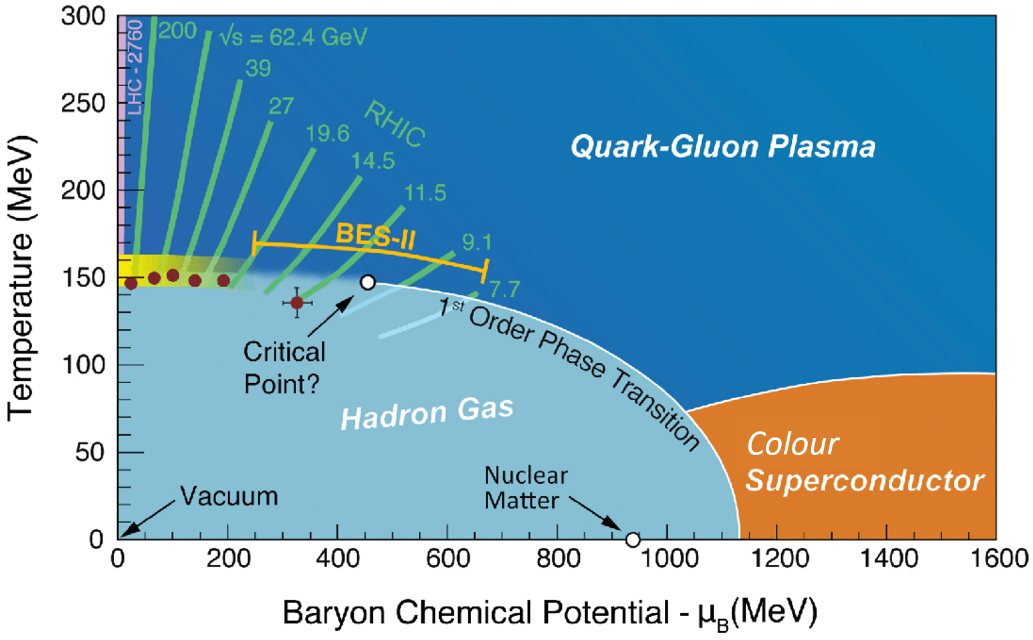

Figure 1.6: QCD phase diagram, labelling the different states of matter present at different values of temperature and baryon chemical potential [33].

# Chapter 2

# The Quark Gluon Plasma

The Quark Gluon Plasma (QGP) is a very hot, very dense state of deconfined matter. The lifetime of a QGP (measured to be of the order of $10^{-23}$ s in Pb-Pb collisions by the ALICE collaboration [34]) is such that a QGP cannot be observed directly. As a result, experimental searches and studies of the QGP utilise a number of secondary observables to both detect the presence of a QGP state and infer its properties.

The following chapter shall outline the history of experimental searches for Quark Gluon Plasmas, and shall discuss a number of the analysis methods that have been used to study them.

## 2.1 Historical QGP Searches

High energy searches for the QGP began in 1986, through fixed-target experiments at CERN's Super Proton Synchrotron (SPS) and the Alternating Gradient Synchrotron (AGS) at the Brookhaven National Laboratory (BNL) in the United States. These searches initially utilised light nuclei, such as oxygen-18 or sulphur-32, but moved towards accelerating heavy ions (mainly gold-197 and lead-208) for colliding beam experiments in the 1990's. At their higher end, these facilities were capable of creating collisions with centre-of-mass energies at the GeV scale; creating collisions with a centre-of-mass energy per nucleon, $\sqrt{s_{\mathrm{NN}}} = 4.6$ GeV in Au-Au collisions (at the AGS), and $\sqrt{s_{\mathrm{NN}}} = 17.2$ GeV in Pb-Pb collisions (with the SPS) [35].

In the year 2000, evidence coming from the SPS was enough for CERN to publish a press release announcing the observation of a new state of matter [36]. The results supporting this announcement came from seven experiments: NA44 [37], NA45 [38], NA49 [39], NA50 [40], NA52 [41], WA97/NA57 [42] and WA98 [43]. As this announcement was being prepared, a new collider was being built at BNL: the Relativistic Heavy Ion Collider (RHIC). RHIC was capable of providing collisions of gold nuclei at up to $\sqrt{s_{\mathrm{NN}}} = 200$ GeV. These higher energy heavy ion collisions were hotter and more dense than the conditions that the SPS could create, allowing RHIC to study the possible creation of the QGP in more depth.

In 2005, complimentary white papers were published by the four experiments located on RHIC: STAR, PHENIX, PHOBOS and BRAHMS [44–47]. These four papers summarised the results that had come from the collaborations, allowing RHIC to confirm the existence of the QGP state within their events. Since 2009, the energy frontier in heavy ion collisions has not been at RHIC, but instead at the LHC. During the LHC Run 1, lead ion collisions took place at $\sqrt{s_{\mathrm{NN}}} = 2.76$ TeV, which was later increased to 5.02 TeV in Run 2. These higher energies allow the experiments on the LHC to investigate the creation and properties of the Quark Gluon Plasma in much higher detail than previous experiments could manage.

## 2.2 Evolution of Heavy Ion Collisions

In order to study the production of the QGP in a laboratory environment, experiments collide heavy nuclei at relativistic energies. Should the conditions at the centre of these collisions exceed the critical temperature and energy density required for QGP formation, estimated to be $T_c \approx 160$ MeV and $\varepsilon_c \approx 0.5$ GeV/fm$^3$ respectively [48], a QGP can be created in the collision. As soon as a QGP is created, it expands and cools, as shown in figure 2.1.

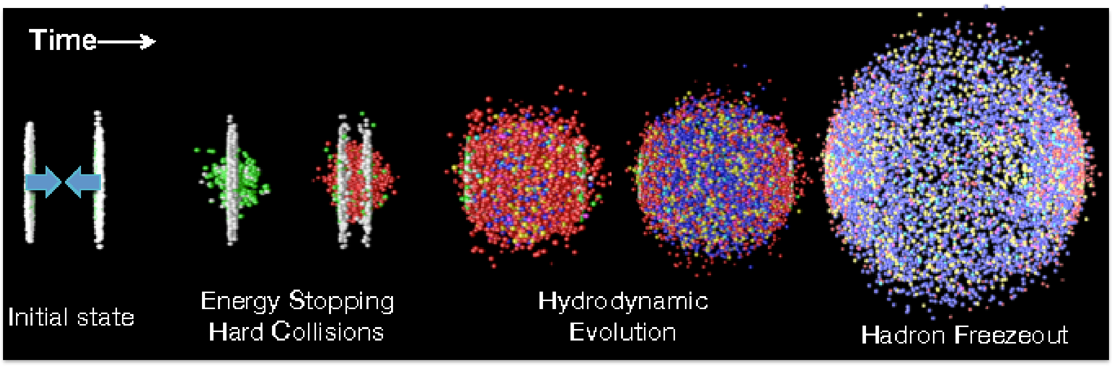

Figure 2.1: Time evolution of a heavy ion collision. The initial state nuclei are shown flat as Lorentz contraction caused by their high speeds lead to this being seen from a lab frame [49].

The very early stages of a heavy ion collision are very similar to those in proton-proton collisions, but at a larger scale. The initial partons undergo inelastic collisions at very high energies, creating many high-momentum particles. It is in these early stages that the majority of heavy flavour quarks (charm, bottom and top) are introduced. Within a heavy ion environment, enough partons are created in the initial collisions that the system is able to undergo *thermalisation*. During this time, the many generated partons undergo both elastic and inelastic collisions, which begins to homogenise the energy density of the system. Once this process is complete, the medium is known as a Quark Gluon Plasma (QGP).

As the QGP expands, it cools, eventually reaching a point where the quarks and gluons within it can come together as hadrons. This occurs via two processes: *coalescence*, where low momentum partons bind as they interact; and *fragmentation*, where a high momentum parton fragments into multiple, lower momentum, hadrons. Eventually, the expanding QGP will undergo a phase transition into a very dense hadron gas, and the system will undergo *chemical freeze-out*; from this point, the flavour composition of the system is fixed.

After chemical freeze-out, the collision system continues to expand and cool. It will continue to do this until the mean distance between hadrons is greater than the range of the strong interaction. At this point, elastic collisions between hadrons will cease, and the system undergoes *thermal freeze-out*, marking the end of the medium's evolution. ALICE has measured the thermal freeze-out time for the QGP produced in its collisions to be around 10 fm/$c$ [34]. The space-time evolution of a QGP is shown in the right-hand side of figure 2.2.

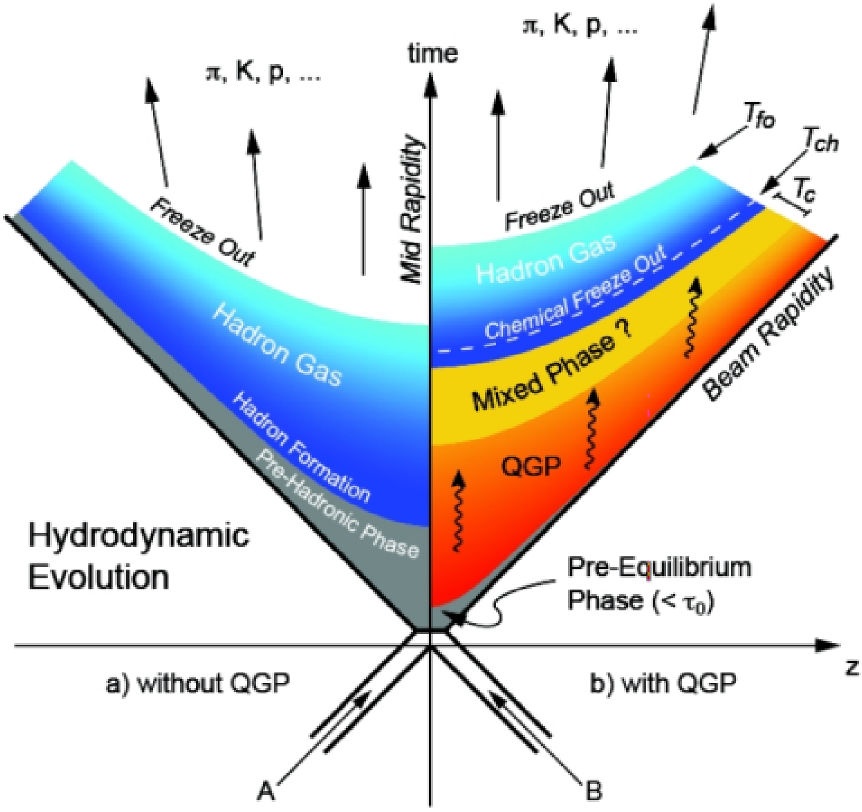

Figure 2.2: Minkowski spacetime evolution of a heavy-ion collision, with and without the creation of a QGP [50]. The chemical freezeout temperature is labelled $T_{ch}$, and the thermal freezeout is $T_{fo}$.

## 2.3 Experimental Observables

The complete evolution of a QGP state occurs in around 10 fm/$c$, which corresponds to around $10^{-23}$ s. As such, direct observation of a QGP is currently impossible; all experiments which study this state must rely on secondary observables in order to judge if a QGP was created in any collisions and to extract properties of the medium. These observables generally fall into one of two categories, depending on the processes that gave rise to them:

- **soft**, low $p_\mathrm{T}$ processes, which constitute the bulk of the QGP system, and allow for the study of general thermodynamic properties.
- **hard** processes, which originate in high $p_\mathrm{T}$ interactions, such as those which produce particle showers known as jets.

### 2.3.1 Jet quenching and high-$p_\mathrm{T}$ particle suppression

A jet is defined as a cone of hadrons, formed by the hadronisation of a high-momentum parton. Such structures are created in the initial hard (high energy) interactions between the colliding beams. If these jets, or the partons which create them, traverse through a medium, the particles in the shower can interact with the medium and lose momentum, either by gluon radiation or inelastic collisions. As a result of this, a jet produced in a QGP will have a lower energy than if it was produced in isolation; ie. it will have been *quenched*.

To test this effect, experiments can investigate back-to-back jets in heavy ion collisions. These jets are produced from the same hard interaction, and should have similar energies. Should the initial collision take place close to the edge of a medium, as in figure 2.3, the two jets will travel different distances through the medium before detection; the jet which has further to travel will lose more energy than its partner. The observation of an energy imbalance can be used as a signature to indicate QGP creation.

Another probe used to investigate jet production in a QGP is the *nuclear modification factor* as a function of $p_\mathrm{T}$. The nuclear modification factor, $R_{AA}$, is defined as the ratio between the $p_\mathrm{T}$ differential particle yield in heavy ion (AA) collisions to the same in proton-proton (pp) collisions:

$$R_{AA}(p_\mathrm{T}) = \frac{1}{\langle N_{coll}\rangle}\frac{1/N_{AA}}{1/N_{pp}}\frac{\mathrm{d}N_{AA}/dp_\mathrm{T}}{\mathrm{d}N_{pp}/dp_\mathrm{T}} \quad , \tag{2.1}$$

where $\langle N_{coll}\rangle$ is the average number of nucleon-nucleon interactions in a heavy-ion collision. The yields in Pb-Pb and pp collisions are normalised to the number of events in the

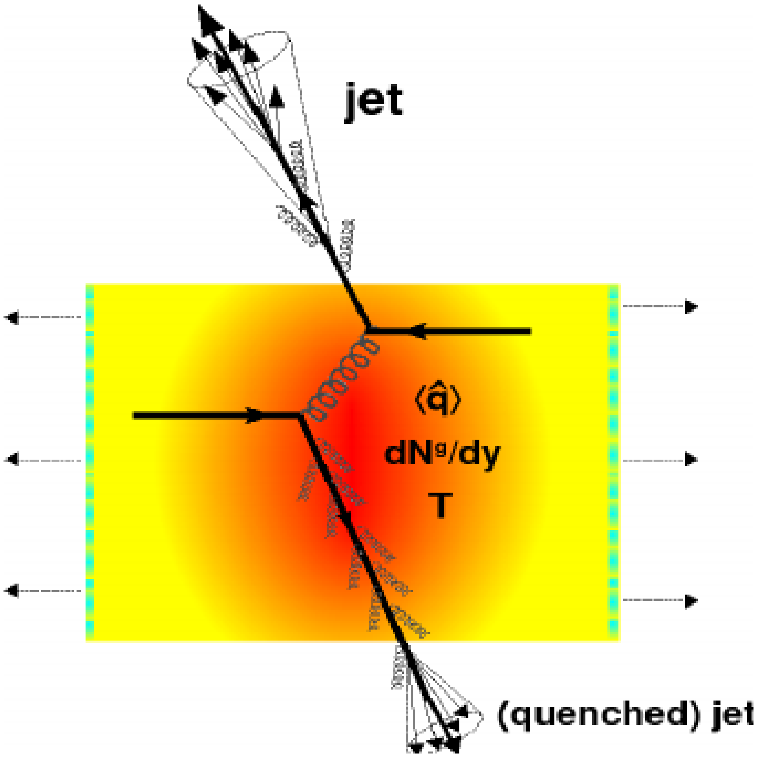

Figure 2.3: Production of two back-to-back jets within a QGP medium [51]. The top jet has less distance to travel through the QGP and so loses less energy than the bottom jet.

corresponding collision system, $N_{AA}$ and $N_{pp}$ respectively. A value of $R_{AA} = 1$ suggests no suppression of events in heavy ion collisions. Jet quenching is indicated by a value of $R_{AA} < 1$.

ALICE measurements of this quantity are shown in figure 2.4, which demonstrate that strong suppression of high $p_{\mathrm{T}}$ charged particles is seen in the most central Pb-Pb events[1]. A note should be made that these values of the nuclear modification factor make the assumption that no QGP is formed in the proton-proton reference events. Recent ALICE results have suggested that this may not be completely true, especially for regions of high multiplicity.

---

[1] Centrality is a measure of how head-on the collision between two nuclei is. The more offset the centres of the colliding nuclei, the less central, or more peripheral, the collision.

[2] The lower the percentile, the higher the centrality; this class contains the 5% most central events.

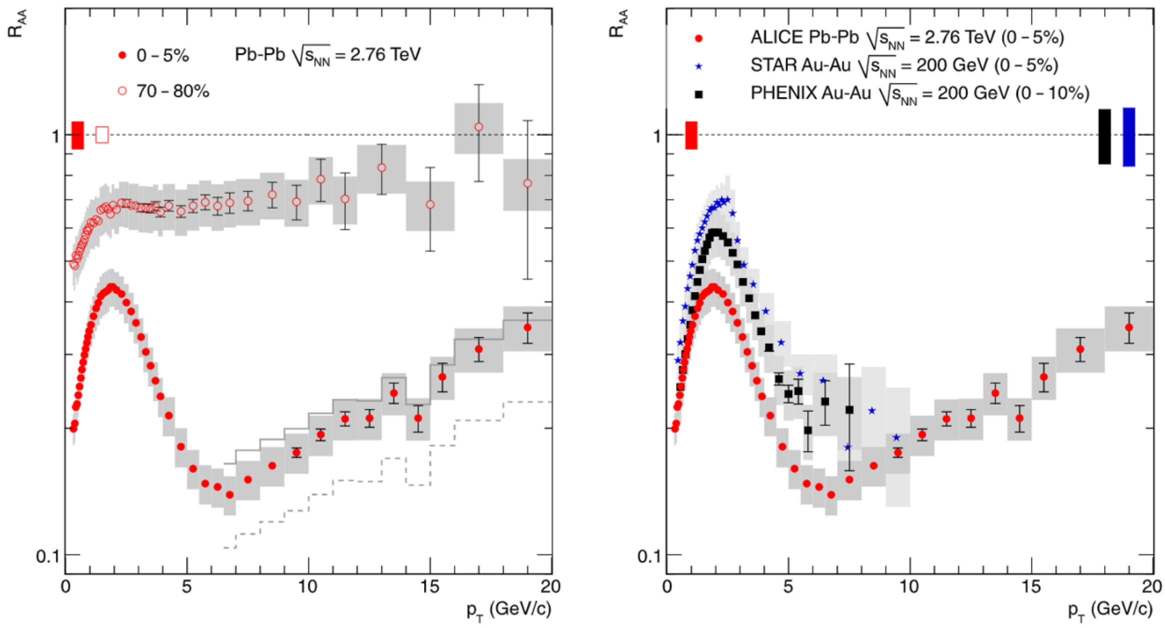

Figure 2.4: $R_{AA}$ of charged particles as measured in Pb-Pb collisions with the ALICE detector [52]. The values for the most central (0-5%)$^2$ Pb-Pb events are compared to peripheral (70-80%) Pb-Pb events (left) and central Au-Au events from PHENIX and STAR (right).

## 2.3.2 Charmonium suppression

A quarkonium state is defined as the bound state of a quark and its corresponding antiquark. In the case of the charm quark, this $c\bar{c}$ pairing is known as charmonium; the lowest energy state of which is the $J/\psi$ meson. Suppression of $J/\psi$ production was posited as a signature of a deconfined state in 1986 [53]. The mass of the charm quark, at 1.3 GeV/$c^2$ [54], is high enough that thermal production of charm quarks in QGP matter is unlikely; any charm in the final state has come from the initial hard scattering, and therefore are present for the full evolution of the QGP system.

The hadronic radius of the $J/\psi$ meson is between 0.2 and 0.3 fm [55], which is less than the Debye radius of a QGP. As discussed in section 1.3.4, if the size of a hadron ($r_H$) is less than the Debye screening radius within a medium ($r_D$), the quarks inside the hadron are unable to bind. Measurements of the suppression of $J/\psi$ production are made using the nuclear modification factor, as in equation 2.1, but using only the yields of the particle of interest. Results from experiments on RHIC demonstrated an observed suppression of $J/\psi$ production in high multiplicity events, as shown in figure 2.5.

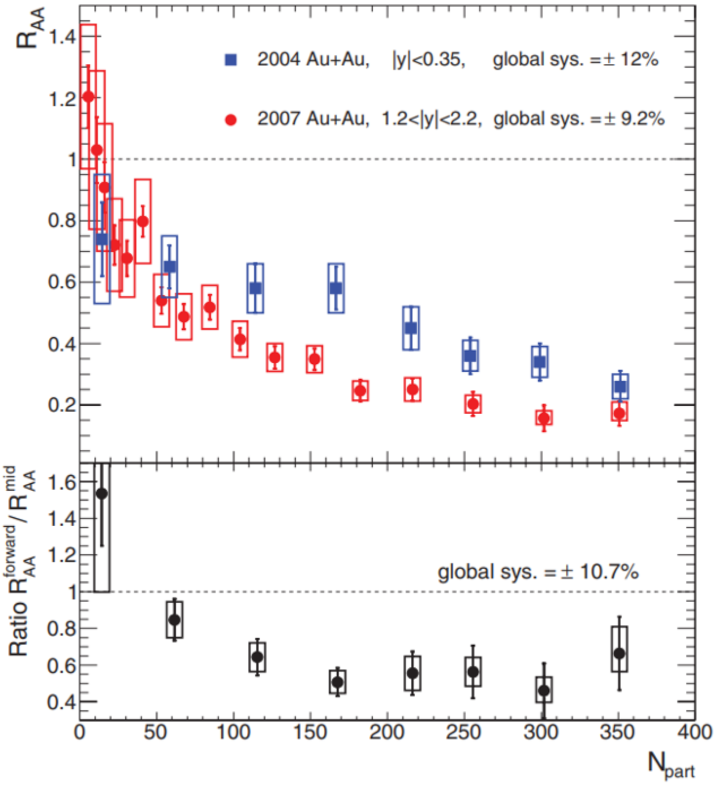

Figure 2.5: Nuclear modification factor of the $J/\psi$ in Au-Au events, as measured by PHENIX [56].

This approach has worked without issues for experiments located at the SPS or RHIC, however the high energy densities within LHC-produced QGPs introduce extra subtlety to the situation. Now, the thermal production of $c\bar{c}$ pairs may no longer be irrelevant, specifically at low $p_{\mathrm{T}}$. In the later stages of QGP evolution, these low momentum quarks and antiquarks can recombine to form charmonia in the final state, if they are close enough in phase space. This effect creates low momentum $J/\psi$, countering the suppression from Debye screening at low $p_{\mathrm{T}}$. Observation of $J/\psi$ regeneration is most easily achieved by comparing measurements of $J/\psi$ $R_{AA}$ in both LHC and non-LHC conditions, as in figure 2.6.

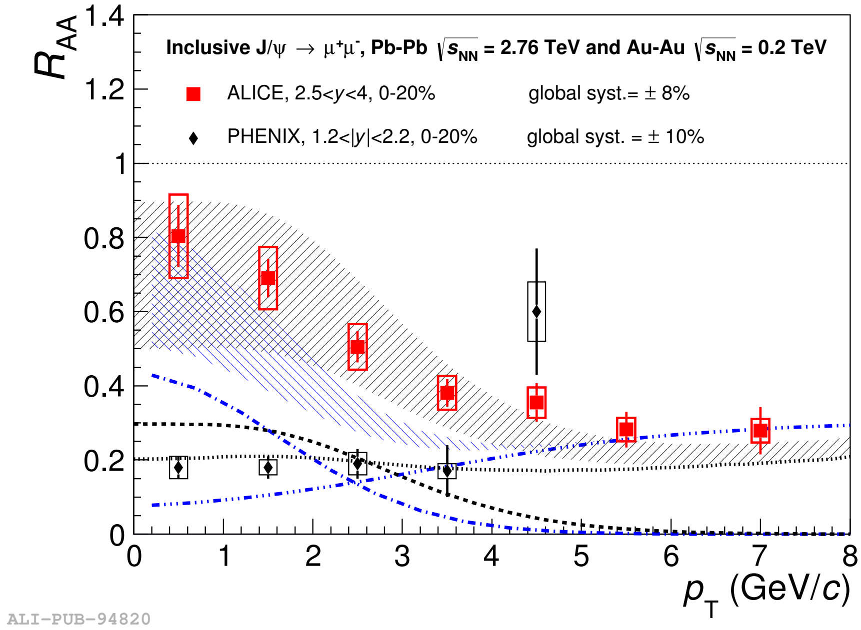

Figure 2.6: $J/\psi$ $R_{AA}$ as a function of $p_{\mathrm{T}}$, as measured in central ALICE and PHENIX events [57]. The increase observed in ALICE results over PHENIX results at $p_{\mathrm{T}} < 4$ GeV/$c$ is due to $J/\psi$ regeneration.

### 2.3.3 Collective flow

When a QGP is formed within a heavy ion collision, the resulting high energy density creates radially outwards pressure against the surrounding vacuum. The effect of this on the particles in the final state is to give all species a common velocity boost away from the initial collision. Thus, particles created in a QGP display a mass-dependent hierarchy in the increase to their mean $p_{\mathrm{T}}$.

If the collision is directly head on, then the resulting velocity boost will be seen the same in all particles. However, this is not the case for all collisions. Heavy ions, as massive composite particles, may collide either head-on, or offset slightly. The transverse distance between the centres of two colliding nuclei is known as the impact parameter, $b$; for a head-on collision, $b = 0$, and for an off-centre collision, $0 < b < r_1 + r_2$, where $r_1$ and $r_2$ are the radii of the colliding particles.

If two heavy ions collide with $b = 0$, and there are no deformations of the initial colliding surfaces, then the observed radial boost will be isotropic. If this is not the case, then the created QGP will not be perfectly spherical and the resulting pressure gradients will build up in different directions, as figure 2.7 shows. These pressure gradients create momentum anisotropies in the final momentum distributions of any particles produced in the QGP; by studying these, experiments are able to investigate the initial state of the collisions.

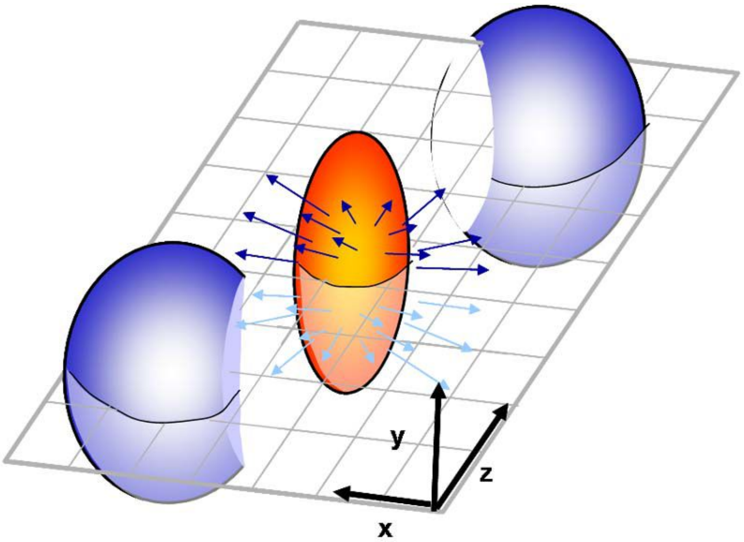

Figure 2.7: Visualisation of the off-centre collision of a pair of heavy ions [58]. The orange region shows where the two nuclei have overlapped, creating a QGP.

In order to quantify the discrepancies in the final momentum spectra, heavy ion experiments decompose them using a Fourier series [59]:

$$E\frac{d^3N}{d^3p} = \frac{1}{2\pi}\frac{\mathrm{d}^2\mathrm{N}}{p_\mathrm{T}\mathrm{d}p_\mathrm{T}\mathrm{d}y}\left(1+\sum_{n=1}^{\infty}2v_n\cos\left[n\left(\phi-\psi_r\right)\right]\right) \quad , \tag{2.2}$$

where $\phi$ is the measured azimuthal angle of a single particle track, and $\psi_r$ is the angle of the reaction plane[3], estimated using the azimuthal distribution of all particles in an event. Any

---

[3] The reaction plane is defined by two lines: the initial beam direction, and the impact parameter between the colliding nuclei.

collective behaviour manifests in the coefficients of the series in equation 2.2,

$$v_n = \langle \cos\left[n\left(\phi - \psi_r\right)\right]\rangle \quad .$$

Often of interest is the second Fourier coefficient, $v_2$, which denotes a behaviour called *elliptic flow*. This can act as a measure of the centrality of a collision, with $v_2$ increasing for more peripheral events, which is shown in figure 2.8.

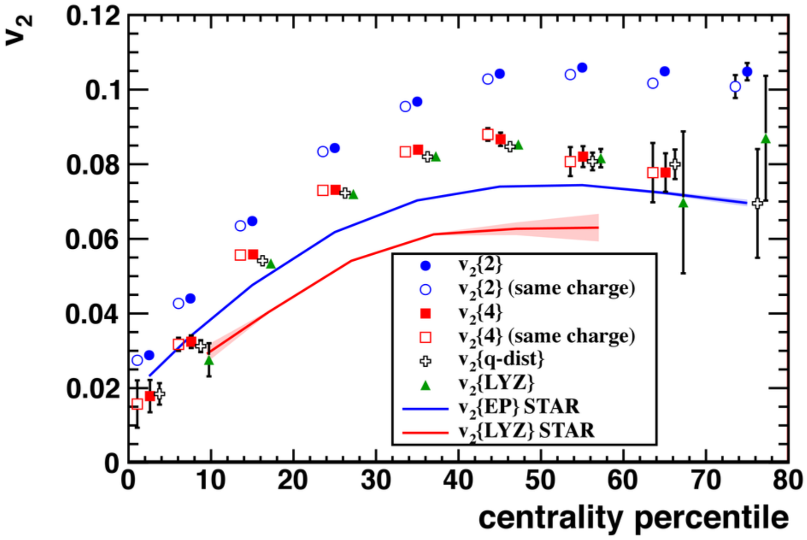

Figure 2.8: Elliptic flow coefficients, $v_2$, of identified hadrons as a function of event centrality in Pb-Pb collisions at $\sqrt{s_{\rm NN}} = 2.76$ TeV [60]. The different data sets denote the same quantity calculated using different methods, and are compared to results from STAR (the solid lines).

### 2.3.4 Direct photons

The final products of a QGP event contain a high number of photons, in addition to the high number of massive particles produced from the various scattering and decay processes. These photons can come from one of three sources: hadronic decays after hadronization of the QGP, production in the initial hard scattering of the colliding beams, or thermal production from the evolving QGP medium.

These latter two classes contain the photons whose source is the medium itself, known as *direct* photons. The yield of these direct photons can be calculated by taking the full, inclusive, yield and subtracting the yield of decay photons. As the direct photons are produced at all stages in a QGP's evolution, they hold important information about the behaviour of the medium, such as temperature or collectivity.

The high $p_\mathrm{T}$ region of the direct photon spectrum is a good place to test theoretical models: this region is dominated by *prompt* photons, those from the initial hard scatterings. The yields of these can be estimated with perturbative QCD calculations, which can then be compared to any measurements made. The spectra of *thermal* photons is expected to show at low $p_\mathrm{T}$, where it will manifest as an excess on top of the prompt photon spectra, as indicated by the lines in figure 2.9.

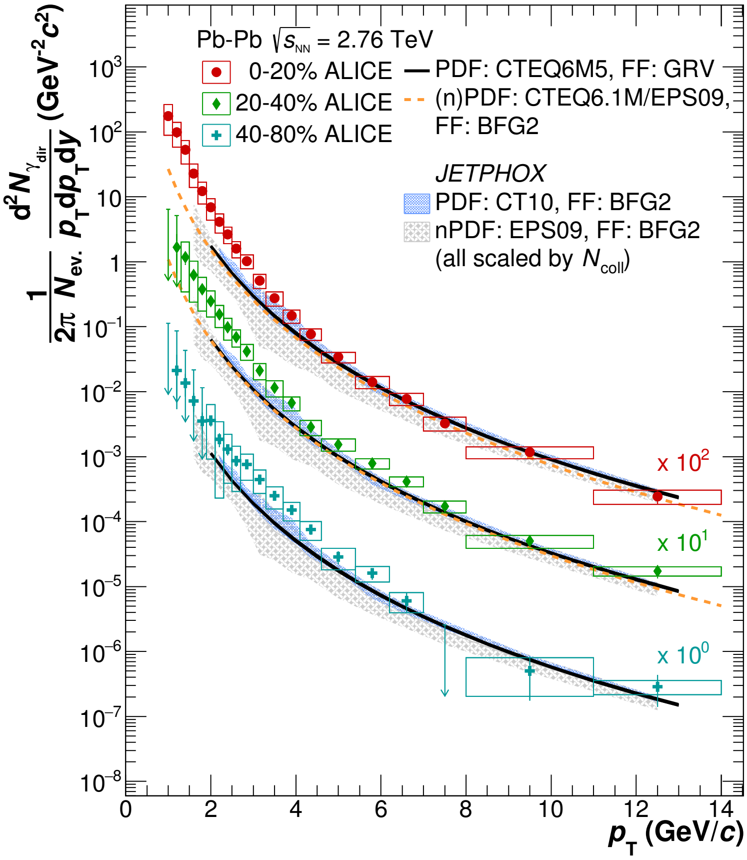

Figure 2.9: Direct photon spectra from Pb-Pb collisions at $\sqrt{s_\mathrm{NN}} = 2.76$ TeV, in three centrality classes [61]. The dashed lines and filled areas show theoretical predictions from NLO pQCD models based on pp collisions, scaled by the number of nucleon-nucleon interactions for each centrality class.

In order to extract and make use of the thermal photon spectra, an exponential decay can be fitted to the direct photon spectrum after subtraction of the estimated yields of prompt photons. The slope of this fit can then be used to estimate the average temperature of the QGP medium. ALICE results in Pb-Pb collisions at $\sqrt{s_{\mathrm{NN}}} = 2.76$ TeV have measured a temperature of 279±12(stat.)±41(syst.) MeV in the most central events [61].

### 2.3.5 Strangeness enhancement

Proposed in 1982 by Rafelski and Müller [62], the idea of strangeness enhancement in deconfined quark media was one of the first observables proposed as a signature for QGP formation. Within the collisions observed at the LHC (either using protons or heavy atomic nuclei), there is no net strangeness in the initial state: any strange quarks observed in the final state must have been produced during the evolution of an event. The prompt production of strange quarks must be done via inelastic collisions of the initial partons in the colliding beams, either via quark-antiquark annihilation ($q\bar{q} \to s\bar{s}$) or gluon-gluon fusion ($gg \to s\bar{s}$) as shown in figure 2.10.

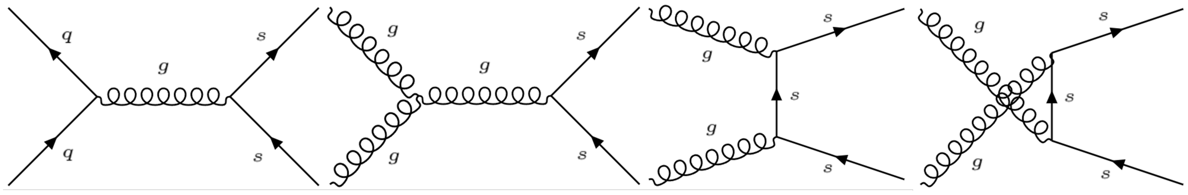

Figure 2.10: Feynman diagrams of $s\bar{s}$ production from partonic interactions. Shown are quark-antiquark scattering, far left, and gluon-gluon fusion.

Within an event in which no QGP is formed, the production of any quark-antiquark pair must also take into account that these quarks must then be bound into hadrons. This requirement gives quarks an *effective* mass; for the strange quark, this is 486 MeV/$c^2$ [63]. Within a QGP, quarks are able to be produced without the need for hadronic binding, so they take a *bare* mass. The bare mass of the strange quark is 95 MeV/$c^2$ [54]. The high temperature conditions within a QGP, and the movement to partonic degrees of freedom rather than hadronic, mean that inelastic interactions between partons are able to form strange quark-antiquark pairs in abundance as the medium evolves, even after the initial collision. In circumstances where a QGP is not created, the higher effective mass of the strange quark drastically reduces the likelihood of thermal production of $s\bar{s}$ pairs. As such, the production of strange hadrons is enhanced greatly if a QGP is created, relative to those where no such medium is formed.

Another property of this strangeness enhancement is that it is predicted to be related to the strangeness content of different hadrons; that the highest enhancement would be present in the yields of the $\Omega$ strange quark triplet, then the $\Xi$ baryon, and finally the singly strange $\Lambda$ and kaon states. Observation of this enhancement in strange quark production can be taken as a signature of QGP formation in the collisions involved. In order to measure any enhancement, yields of strange hadrons are compared to yields of charged pions. These hadron-to-pion ratios are also compared between collision systems; specifically comparing heavy-ion results, where a QGP may be formed, to proton-proton or proton-ion results, systems considered to not be massive enough to sustain QGP evolution. This allows for studies to be made about the onset of QGP formation.

### Historical results

The first measurements of strangeness enhancement in ion-ion collisions were performed at the BNL AGS [64] and CERN SPS [65, 66] in the late 1990's using charged kaons and, in the case of the SPS, strange baryons. These results show not only an enhancement in the production of strange particles relative to nucleon-nucleon collisions, but also that the observed enhancement depended on the strangeness content of the observed species: the more strange quarks were present, the more the production of that species was enhanced [65]. This behaviour, that enhanced production would be strongest for the $\Omega$ species, then the $\Xi$ and $\Lambda$ baryons, has been confirmed repeatedly at multiple energies [67, 68] and colliding ion systems [69].

Strangeness production has also been studied at the energy frontiers of current accelerators, RHIC [70] and the LHC [71], confirming the behaviour seen at earlier experiments. Heavy ion results are commonly given as a function of the average number of participating nucleons in the collision, $\langle N_{part} \rangle$, which can act as a measure of the centrality of a collision. Results from the first Pb-Pb collisions measured by ALICE, in figure 2.11, demonstrate a strong enhancement of strange baryon yields relative to those measured in pp collisions, as expected. Also shown are results from STAR using Au-Au collisions; the Pb-Pb yields are consistent with those shown at STAR, further demonstrating that strangeness enhancement in QGP formation is both a system-independent and energy-independent effect.

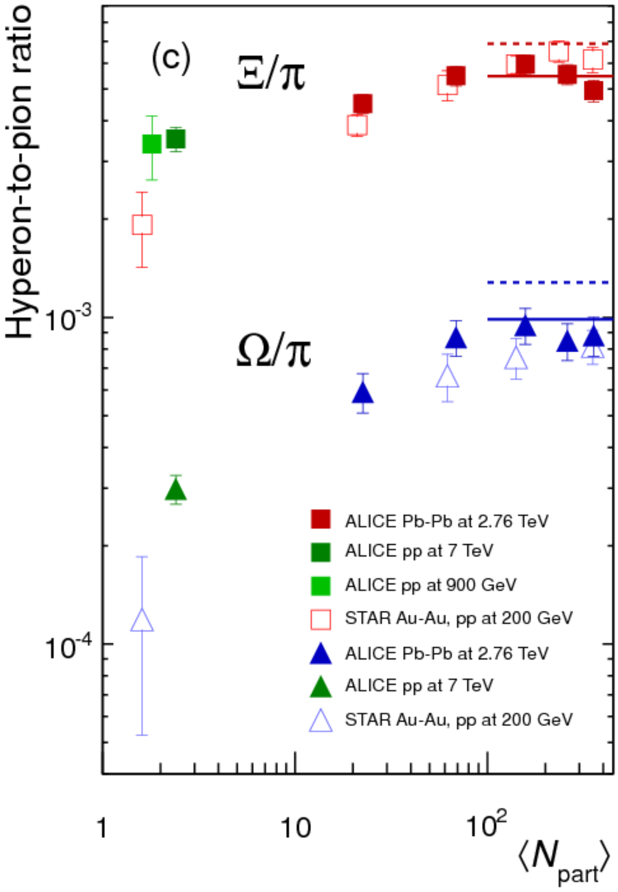

Figure 2.11: $\Xi/\pi$ and $\Omega/\pi$ ratios as a function of $\langle N_{part} \rangle$ for Pb-Pb collisions at $\sqrt{s_{\rm NN}} = 2.76$ TeV with ALICE [71]. These are compared to ALICE results at pp collisions at $\sqrt{s} = 7$ TeV and STAR results at both Au-Au collisions and pp collisions at 200 GeV.

Further studies done by both ALICE and STAR compare yields in heavy ion collisions to those in smaller systems, such as pp [72,73] and p-Pb [74]. To do these comparisons, yields have been plotted as a function of the charged particle density, $\langle dN_{ch}/d\eta \rangle$, created in the collisions. This quantity acts as an indicator of the final state multiplicity, and can be used to directly compare the conditions created in the different collision systems.

Initial results from p-Pb collisions, in figure 2.12, show that the to-pion yields of charged $\Xi$ and $\Omega$ baryons (collectively known as hyperons) increase with final state multiplicity, even in systems where QGP creation is not expected. The p-Pb results also provide a smooth transition as a function of $\langle dN_{ch}/d\eta \rangle$, from the low-multiplicity pp results and almost reaching levels of strangeness saturation observed in Pb-Pb collisions.

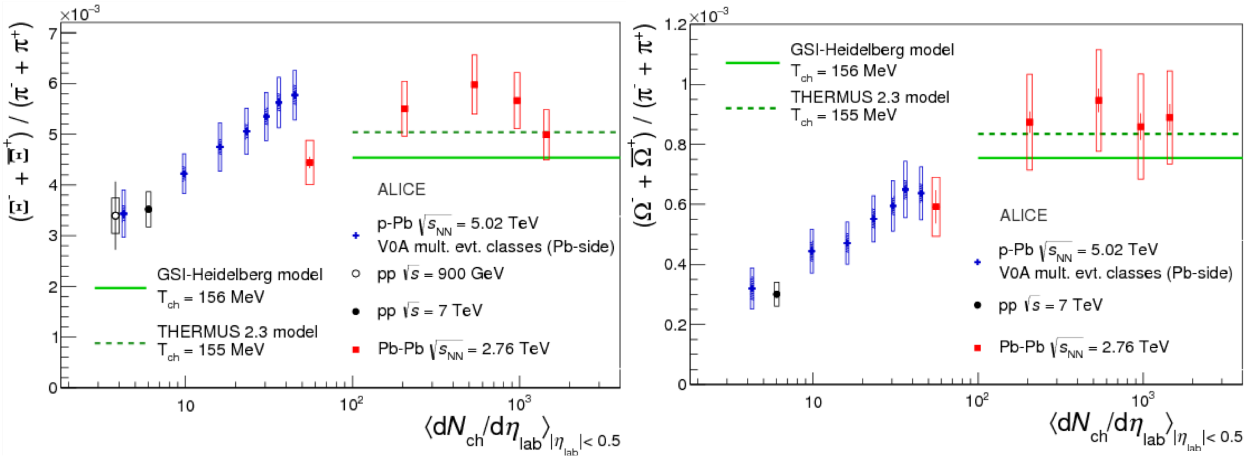

(a) $\Xi$ to $\pi$

(b) $\Omega$ to $\pi$

Figure 2.12: ALICE results of hyperon to pion yields as a function of charged particle multiplicity density in p-Pb (blue), Pb-Pb (red) and pp (black) collisions at the LHC [74].

In addition to within hyperon production, the ALICE collaboration demonstrated that strangeness enhancement was also visible in the yields of singly-strange particles in p-Pb collisions [75], in particular looking at the neutral K meson and the $\Lambda$ baryon. Also investigated were the multiplicity-dependent yields of strange particles in pp collisions, which had not before been seen [76], as shown in figure 2.13. These pp results show the same trend as in p-Pb collisions, suggesting that the strangeness enhancement effect is one that is independent of collision system.

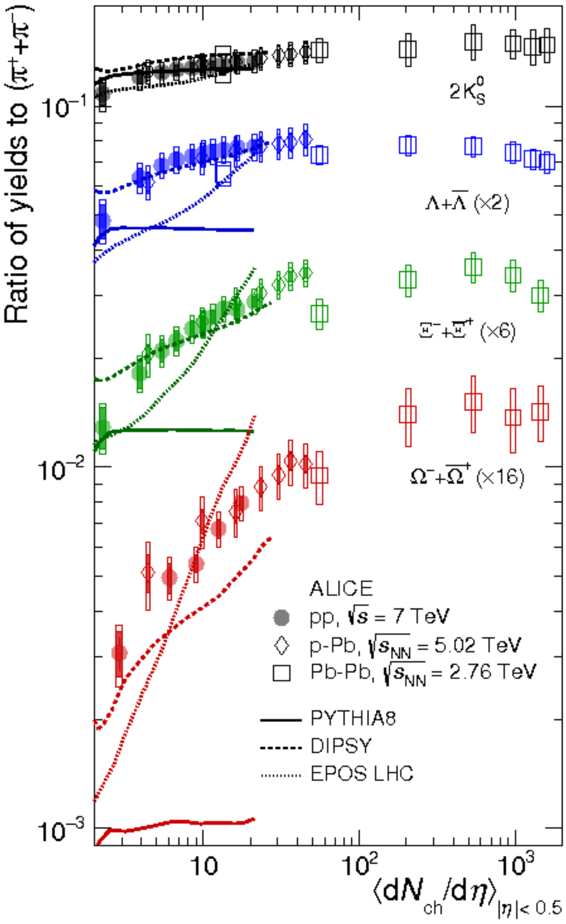

Figure 2.13: Hadron-to-pion ratios in different collision systems, as a function of $\langle dN_{ch}/d\eta \rangle$ [76]. Shown are results for the $K^0_S$ meson, and the $\Lambda$, $\Xi$ and $\Omega$ baryons.

The behaviour observed in proton-proton collisions is not well modelled by Monte Carlo generators commonly used at the LHC: PYTHIA8 [77], EPOS LHC [78] and DIPSY [79]. The best qualitative match for the behaviour seen comes from DIPSY, which describes the interactions between colour charges in a nuclear environment not as a classical string, but as a 'rope', with a higher string tension, which is more likely to hadronise into strange quarks. While this model does provide an increase in the strange yield observed in high-multiplicity collisions, it does not quantitatively reproduce results obtained from multi-strange baryons, suggesting that more theoretical work need to be done in order to understand strangeness enhancement.

# Chapter 3

# ALICE and the LHC

The analysis reported in this thesis was performed using data taken with the ALICE experiment [31]; one of the four main detectors located on the Large Hadron Collider (LHC) at CERN [80]. The following chapter shall describe the CERN accelerator facilities and the ALICE detector, with particular emphasis on the various subdetectors used in this analysis.

## 3.1 The CERN Accelerator Complex

The Large Hadron Collider (LHC) at CERN is a 27 km circumference particle accelerator, located roughly 100 m underground, crossing the French-Swiss border near Geneva. Using a combination of radio frequency accelerating cavities and various large electromagnets, it is able to accelerate two counter-rotating beams of particles, most commonly protons or lead ions, up to 6.5 TeV per proton. The LHC is, however, not the only accelerator utilised by CERN; there are a number of intermediary steps between initial beam source and final collisions, and so a series of machines are used to accelerate and prepare the beams for their final destinations. These intermediary accelerators are not only used as boosters leading to the LHC; they also feed some of CERN's other facilities in their own right, whether an experiment such as NA62 [81], or further acceleration facilities such as the Antiproton

Decelerator [82]. Figure 3.1 shows a schematic diagram of the accelerator complex.

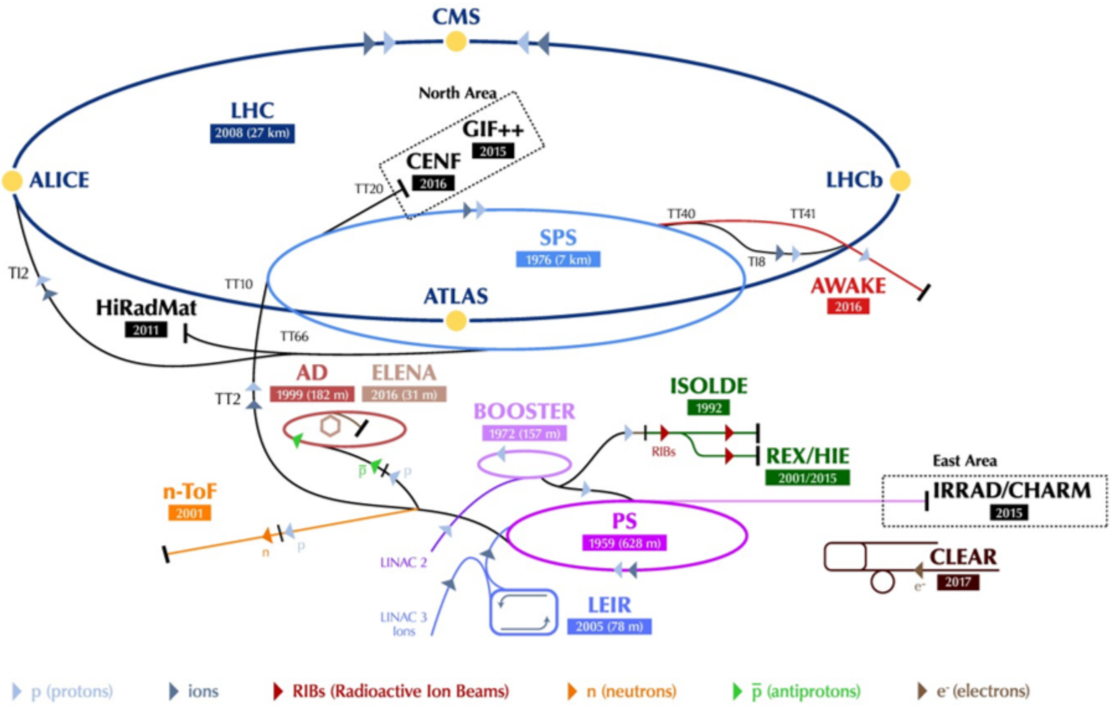

Figure 3.1: The CERN accelerator complex. Modified from [83].

The process of accelerating protons begins with a source of molecular hydrogen, a bottle of hydrogen gas, located at one end of the Linear Accelerator 2 (Linac2). From the gas bottle, these hydrogen molecules are split into atoms, and then ionised. The electrons from these hydrogen atoms are stripped away, leaving behind only the hydrogen nucleus, a proton. Linac2 then uses radiofrequency (RF) cavities to accelerate these protons up to an energy of 50 MeV, before feeding them into the Proton Synchrotron (PS) booster to be further accelerated up to 1.4 GeV. From the beginning of Run 3, Linac2 will be replaced by a new linear accelerator, Linac4, which will accelerate negative hydrogen ions to energies of 160 MeV [84]. The excess electrons will be stripped from these ions as they are injected into the PS booster, leaving only protons in the beam.

The PS booster (labelled as "booster" in figure 3.1) is comprised of four parallel rings, each of which can accelerate protons without input from the others. By controlling which of the four booster rings is filled at any one time, CERN is able to separate the proton stream from Linac2 into discrete bunches, which are then used for the rest of the protons' acceleration process all the way up until final collisions. From the PS booster, the beams of protons are fed into the PS, which takes their energy up to 25 GeV [85]. The PS began life as CERN's flagship accelerator when it launched in 1959. However, when CERN began to build larger accelerators in the 1970's, the PS was moved into a supporting role, acting as a booster for these new machines, a role which it retains today. From the PS, protons are fed into the Super Proton Synchrotron (SPS), where they are accelerated to 450 GeV [86]. Much like the PS before it, the SPS launched as CERN's primary accelerator in 1976, and has since been used in many important analyses, including the discovery of the $W^{\pm}$ and $Z^0$ bosons.

From the SPS, the protons are finally injected into the LHC to be accelerated to their final energies, whether the full collider energy of 6.5 TeV per beam, or a lower energy used for reference studies. As mentioned above, the protons are injected into the LHC in discrete bunches. These bunches contain $1.15 \times 10^{11}$ protons each, and measurements show that each beam contains 2556 of these bunches [87]. The bunches cross at four points around the ring, each corresponding to the location of one of the four large LHC experiments, with a time of 25 ns between bunch crossings.

The acceleration process for lead ions is very similar to that for protons. It begins with an isotopically pure sample of solid lead-208, which is then vaporised and ionized. This sample is then fed through a different linear accelerator than the one used for proton operations, Linac3, where the ion beams are accelerated to 4.2 MeV. From here, the ions are fed into the Low Energy Ion Ring (LEIR), where they are further boosted to 72 MeV and injected into the PS. From the PS, the path taken by the lead ions is identical to that of the proton beams, eventually culminating in the high energy density collisions used by the various LHC experiments to study the Quark Gluon Plasma.

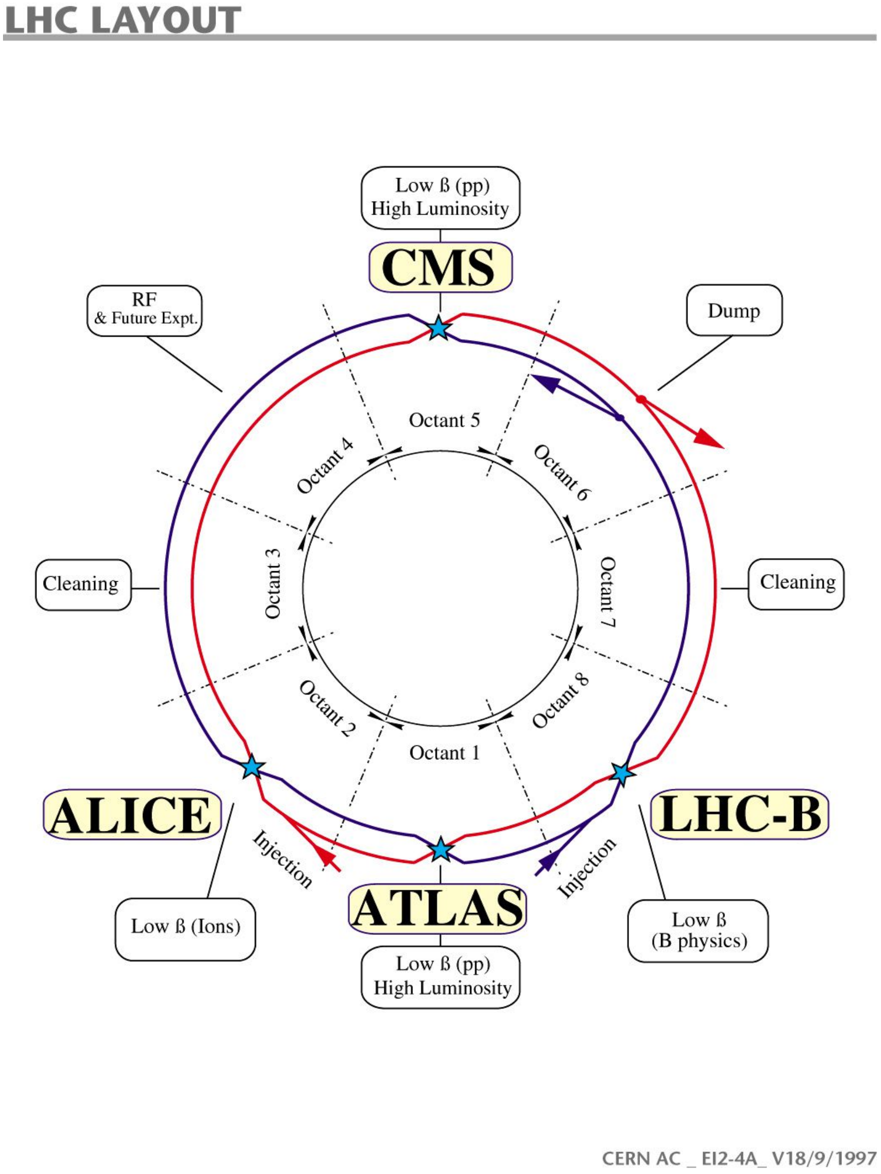

Figure 3.2: Schematic diagram of the LHC, noting its octants, and the location of beam facilities on it [88].

### 3.1.1 The LHC

The LHC is split into eight octants for logistical purposes (as shown in figure 3.2), each comprising a number of straight sections and a pair of transition sections, designed to pass the particle beams between the different octants. The majority of the LHC is comprised of thousands of superconducting magnets, which are kept at a temperature of 1.9 K by the use of liquid helium. 1232 of these magnets are the primary LHC dipoles which are used to bend the beam, and keep it circulating within the LHC beampipe. A further 392 magnets are quadrupoles, used to 'squeeze' the beam, and reduce its spatial dimensions. Once the LHC beams are at their desired energies, they are directed to collide at four interaction points around the ring. These four interaction points are where the primary LHC experiments are housed (as shown in figure 3.2): ATLAS [89] at Point 1, and CMS [90] at Point 5, both general purpose detectors built for studies which included the search for the Higgs boson; LHCb [91] at Point 8, which specialises in the studies of CP violation and other very rare processes; and ALICE [31] at Point 2, optimised for the study of heavy-ion collisions and the Quark Gluon Plasma.

Operation of the LHC began in September 2008, after more than a decade of planning, designing and building. These proton-proton collisions were promptly halted shortly afterwards, after an electrical fault and subsequent helium leak caused major damage to the LHC beampipe and a number of the surrounding magnets. A shutdown of more than 12 months followed, during which time the damaged components were replaced. It was not until November 2009 that the LHC was fully operational again, and at a beam energy of half what it was designed for. This started a three and a half year period of routine operation of the LHC, known as Run 1, lasting until February 2013. During Run 1, the LHC provided proton-proton (pp) collisions at centre-of-mass energies of 0.9, 2.76, 7 and 8 TeV, and three heavy-ion lead-lead (Pb-Pb) runs in 2010 and 2011, with a centre-of-mass-energy-per-nucleon, $\sqrt{s_{\mathrm{NN}}} = 2.76$ TeV. In addition to these, the LHC also ran proton-lead (p-Pb) collisions in 2013, at $\sqrt{s_{\mathrm{NN}}} = 5.02$ TeV.

Following the end of Run 1, the LHC and its experiments went into a year-long period of no beams, Long Shutdown 1 (LS1). During this time, the LHC was upgraded to provide beams at 6.5 TeV, close to the original design energy of 7 TeV per beam. The LHC's restart in April 2015 marked the end of LS1, and the beginning of Run 2. During Run 2, which lasted until December 2018, pp collisions took place at $\sqrt{s} = 13$ TeV, as well as Pb-Pb collisions at $\sqrt{s_{\mathrm{NN}}} = 5.02$ TeV and p-Pb collisions at $\sqrt{s_{\mathrm{NN}}} = 8.16$ TeV. A short run of xenon-xenon collisions at $\sqrt{s_{\mathrm{NN}}} = 5.44$ TeV was also carried out in October 2017.

## 3.2 ALICE

ALICE (A Large Ion Collider Experiment) [31] is one of the main four detectors which utilises the beams accelerated using the LHC. It is located in an experimental cavern roughly 80m underground, on the outskirts of the French village of Saint-Genis-Pouilly near the French-Swiss border. It is designed to investigate the creation and properties of the QGP, and as such is the only one of the primary four LHC experiments optimised for the extreme high-multiplicity environments found in the events resulting from the most central Pb-Pb collisions.

The main detector weighs 10,000 tonnes, and measures 16 m high, by 16 m wide, by 24 m long, with a pair of small subdetectors located along the beampipe 116 m away from the interaction point (IP). The main body of ALICE is comprised of two main sections: a central barrel, located within ALICE's 0.5 T room-temperature solenoid magnet, and a forward muon arm. In total, ALICE is comprised of 18 different sub-detector systems, which can be broadly split into three groups: central detectors, forward detectors and those within the muon arm. Figure 3.3 shows the ALICE detector and all of its subdetector components.

### 3.2.1 ALICE coordinate system

ALICE uses a Cartesian coordinate system, with the origin at the centre of the inner barrel. The $x-y$ plane is defined as being perpendicular to the beamline, with the $x$-axis pointing in towards the centre of the LHC ring, and the $y$-axis pointing vertically upwards. The $z$-axis lies parallel to the beam pipe, and points away from the muon arm. Within ALICE, some components are referred to as being A-side or C-side: A-side corresponds to the side of the detector along the positive $z$-direction; C-side corresponds to the side of the detector along the negative $z$-direction, the side with the muon arm.

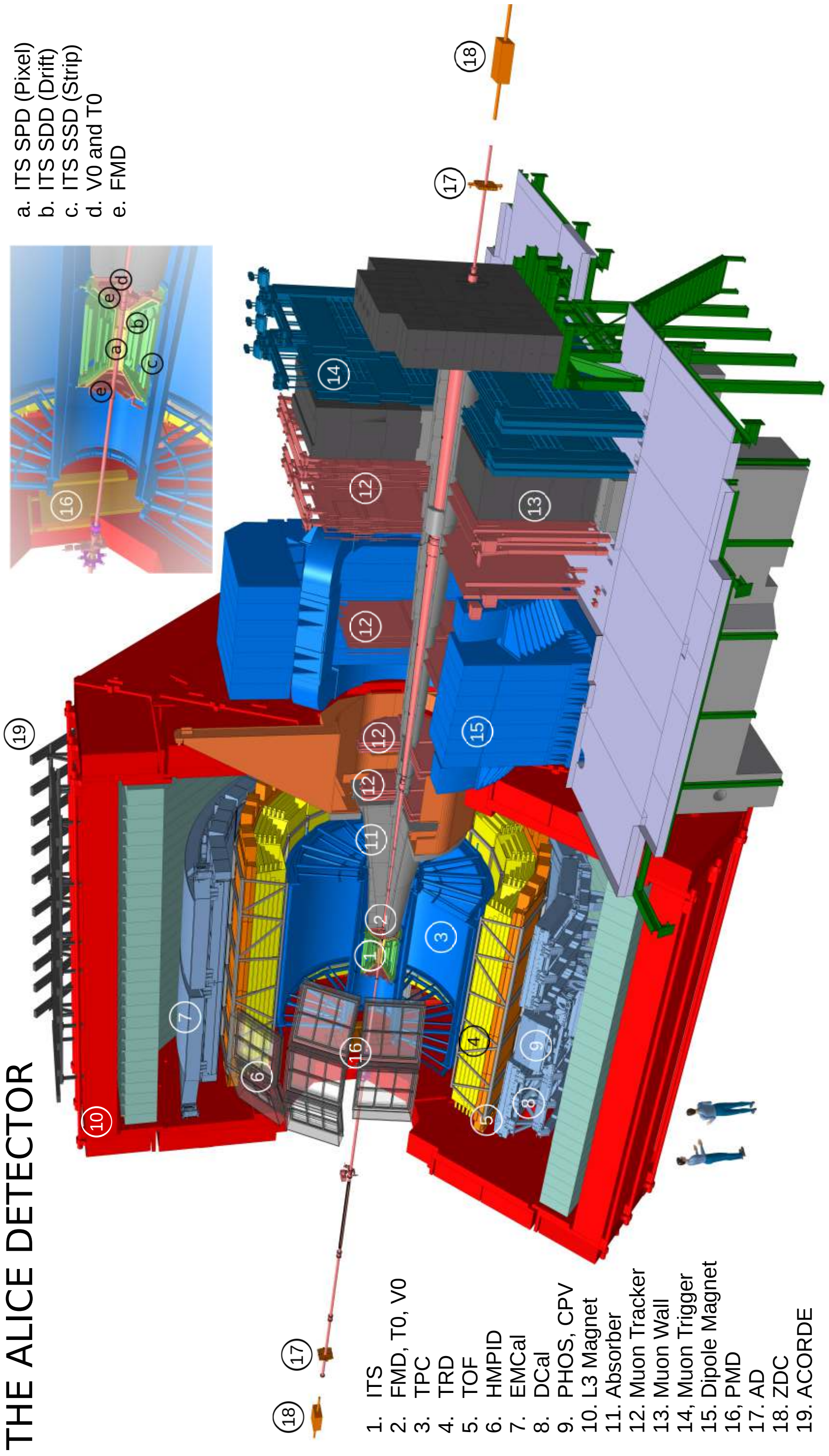

Figure 3.3: Schematic diagram of the ALICE detector, labelling the various subdetectors [92].

Motion within ALICE is often referred to as being either longitudinal or transverse (as this thesis will do). Longitudinal motion is defined as the motion in the $z$-direction, along the beam axis, and transverse motion is defined as that in the plane perpendicular to the beam axis; the $x - y$ plane. Transverse variables in particular are of interest as the colliding nucleons travel along the beam axis and have no transverse components; any motion in the transverse plane is therefore created from the collision.

Within this analysis, a number of constructed variables are of interest. One is the transverse momentum, $p_{\mathrm{T}}$, of particles. This is defined as $p_{\mathrm{T}} = \sqrt{p_x^2 + p_y^2}$, and measures the component of a particle's momentum in the transverse plane. Another variable of use is the longitudinal variable, pseudorapidity, denoted as $\eta$. This is given by

$$\eta = \frac{1}{2} \ln\left(\frac{|\vec{p}| + p_z}{|\vec{p}| - p_z}\right) = -\ln\left[\tan\left(\frac{\theta}{2}\right)\right] \quad ,$$

where $\theta$ is the measured angle between a particle's momentum vector, $\vec{p}$, and the z-axis, and $p_z$ is the component of $\vec{p}$ along the z-axis. By its definition, $\eta = 0$ for particles travelling exactly perpendicular to the beam axis, and approaches infinity as $\theta$ approaches 0. For relativistic particles (those for which their momentum is much greater than their mass), $\eta$ is a very good approximation for the variable rapidity, $y$, defined as

$$y = \frac{1}{2} \ln\left(\frac{E + p_z}{E - p_z}\right) \quad ,$$

where $E$ is a particle's measured energy.

In the majority of the collisions at the LHC, the collision system is symmetric. As such, the centre-of-mass rapidity frame, $y_{CoM}$, and the laboratory rapidity frame, $y_{lab}$, are the same. However, in the asymmetric proton-lead collision system, $y_{CoM}$ is shifted relative to the lab frame by a factor dependant on the atomic mass, $A$, and charge $Z$, of the two colliding particles [93],

$$|\Delta y| \simeq \left| \frac{1}{2} \ln \left( \frac{Z_1 A_2}{Z_2 A_1} \right) \right| \quad . \tag{3.1}$$

For a proton, $A = Z = 1$, and for a lead nucleus, $A = 208$ and $Z = 82$. Applying these to equation 3.1 gives a rapidity shift, $|\Delta y| \simeq 0.465$, for proton-lead collisions. Within ALICE, the notation of asymmetric collision systems first lists the particle travelling from the A-side to the C-side of the detector, and the second from C to A. In the system of interest for this analysis, the p-Pb system, the shift is towards negative rapidity, so for $y_{CoM} = 0$, $y_{lab} = -0.465$.

## 3.3 The ALICE detector

The eighteen subdetectors within ALICE can be separated into three broad categories. The central barrel covers the region $|\eta| < 0.9$, and lies within the magnet used for charged particle momentum determination. Within the central barrel lie detectors used for particle tracking, particle identification and energy determination. The tracking within the central barrel is primarily accomplished by the Inner Tracking System (ITS) and Time Projection Chamber (TPC), and is supplemented by the Transition Radiation Detector (TRD).

All three of these tracking systems are also used for particle identification (PID) of the thousands of particles generated in heavy ion collisions. For the ITS and TPC, this is achieved using measurements of a particle's energy loss as it traverses through the detector, $\mathrm{d}E/\mathrm{d}x$, which shall be discussed in more detail in section 3.5. The PID from these systems is further supplemented using the Time-of-Flight (ToF) and High Multiplicity PID (HMPID) detectors. Also found within the central barrel are detectors used for the measurement of particle energy: the Electromagnetic and Di-Jet calorimeters (EMCAL and DCAL respectively), and the Photon Spectrometer (PHOS). In addition to these, attached to the top of the ALICE magnet yoke is the ACORDE scintillator array, used for the detection of high-energy cosmic rays which reach the experimental cavern.

The forward detectors are located in the high-$\eta$ region, and detect particles travelling close to the beam pipe. These detectors are primarily used for triggering, and for the measurement of global characteristics of each event (final state multiplicity, event centrality, and location of the primary vertex amongst others). Multiplicity measurements are provided by the VZERO (V0) detector, Forward Multiplicity Detector (FMD) and the Photon Multiplicity Detector (PMD). Located next to the V0 is the T0 detector, which has a timing resolution of better than 50 ps, and is used to help locate the primary vertex in an event. Also considered as forward detectors are two the Zero Degree Calorimeters, located 116 m away from the IP along the beam pipe [31]. These are used, in conjunction with measurements of final state multiplicity, to determine the centrality of a collision by measuring the energy of spectator nucleons; those which did not take part in the primary collision.

Also found in the forward region is the muon arm, covering the pseudorapidity range $-4.0 < \eta < -2.5$. The electronic aspects of the muon spectrometer consist of a series of parallel tracking and triggering planes, which detect the flight path of any muons with momentum which take them close to the beam axis in the negative $z$ direction. In combination with a large dipole magnet and front-end absorber, which lies between the interaction point and the first series of detector planes, the muon arm is able to detect the presence of muons, identify their charge, and measure their momenta. The muon arm is primarily utilised for studies of heavy quarkonia, for example the $\Upsilon$; and ultra-peripheral collisions, which investigate the distribution of gluons within the nucleus using the photoproduction of lighter quarkonia, such as the $\rho^0$ and $J/\Psi$.

The rest of this chapter shall discuss, in more detail, the detector subsystems that were utilised in this analysis: the Inner Tracking System; Time Projection Chamber, and VZERO detector.

## 3.4 The Inner Tracking System

The Inner Tracking System [94, 95] lies at the core of the ALICE central barrel, and is the first detector system encountered by any particles which are generated in the mid-rapidity region. The ITS is a cylindrical system surrounding the interaction point, which covers the region $|\eta| < 0.9$ for all layers and $4 < r < 43$ cm. The ITS is primarily a tracking detector, and is able to determine the location of both primary and secondary decay vertices with a very high resolution. This is important for strangeness analyses as the lifetimes of the strange hadrons of interest are such that they typically travel centimetres before decaying. The ITS is comprised of six concentric layers, as shown in figure 3.4; the outer four of which also provide d$E$/d$x$ samples which can be used for the PID of low-momentum particles.

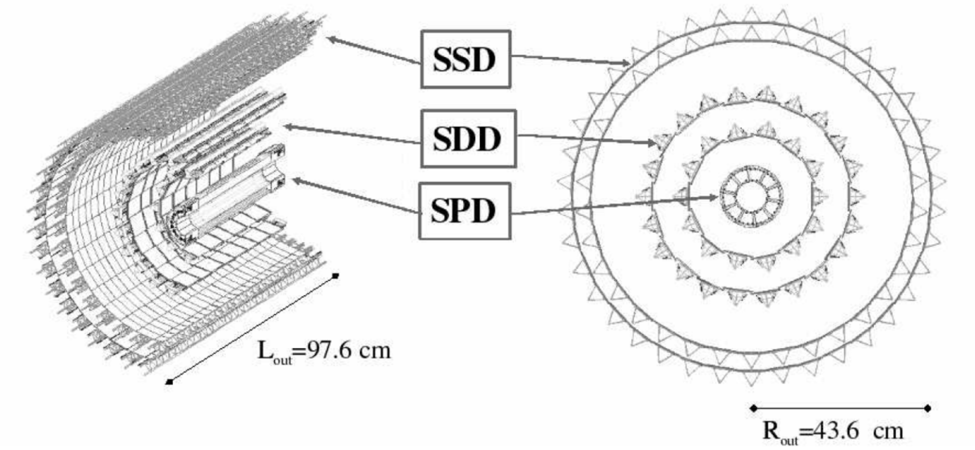

Figure 3.4: Diagram of the ALICE ITS, labelling the three separate sections [95].

### 3.4.1 Silicon Pixel Detector

The innermost two layers of the ITS comprise of the subsystem called the Silicon Pixel Detector (SPD) [96]. The SPD is capable of providing high quality tracking for low-momentum ($p_{\mathrm{T}} < 200$ MeV/$c$) particles, and high-precision vertex location, being able to identify the location of an event's primary vertex with a resolution better than 100 $\mu$m. The SPD is also used to measure final state multiplicity, and as such, has an $\eta$ coverage greater than than the subsequent four layers of the ITS ($|\eta| < 2$ in the inner SPD layer, and $|\eta| < 1.4$ in the outer).

As it is the first of ALICE's detector systems encountered by particles, it must be designed to deal with the extreme track densities present in the most central heavy-ion collisions, which can reach as much as 50 tracks per cm$^2$. The high granularity required in such conditions is provided by the use of $9.8 \times 10^6$ individual pixel cells, each measuring 50 $\mu$m in the $r\phi$ direction and 425 $\mu$m in the $z$ direction.

These cells are bonded to readout chips, which measure 12.8 mm in the $r\phi$ direction and 70.7 mm in the $z$ direction, providing a spatial resolution of 12 (100) $\mu$m in the $r\phi$ ($z$) direction respectively. Each chip holds a matrix of 256 ($r\phi$) x 32 ($z$) silicon cells, which is attached to the base electronics via solder bumps. Twenty chips are arranged linearly to form a stave, which is then placed parallel to the beam pipe. At either end of these staves are Multi-Chip Modules (MCMs) which are responsible for controlling front-end electronics, and are connected to the SPD's readout system via fibre-optic links.

The SPD is comprised of ten sectors, placed cylindrically around the interaction point. Each sector is built upon a carbon-fibre support structure; this holds two staves in the inner layer, 3.9 cm from the beam axis, and four staves in the outer layer, 7.6 cm from the beam axis. In total, the SPD contains 60 staves, which corresponds to 120 read-out channels, and a total detector surface area of 0.21 m$^2$.

Surrounding the SPD, separating it from the next layers of the ITS, is an aluminium-coated carbon-fibre heat shield. This shield prevents the large amount of heat generated by the SPD's electronics from interfering with the operation of the subsequent layers of the ITS. In total, combining both the pixel layers and the heat shield, the material budget of the SPD comes to around 2% of a radiation length [96], which helps minimise scattering from the SPD on the tracks in ALICE's events.

### 3.4.2 Silicon Drift Detector

The Silicon Drift Detector (SDD) subsystem is that which makes up the third and fourth layers of the ITS, offering both high-precision tracking and the capability to provide some of the d$E$/d$x$ samples used for ITS PID [97]. The SDD, with a total surface area of 1.31 m$^2$, is composed of much smaller modules. These modules, each 300 $\mu$m thick, are made of doped silicon with a sensitive area of 70.17 ($r\phi$) x 75.26 ($z$) mm$^2$. A schematic diagram of one such module is shown in figure 3.5. The sensitive area of each SDD module is split in half by a central cathode which lies along the $z$ direction, creating two 'drift regions' per detector. The cathode holds a high bias voltage of $-2.4$ kV, which sets up a drift field between itself and the 256 collection anodes aligned at the other side of each drift region.

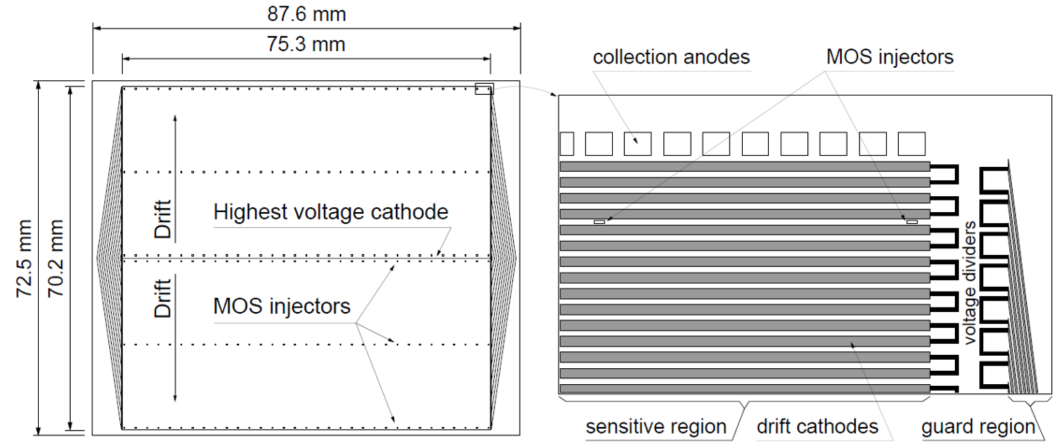

Figure 3.5: Diagram of an ALICE silicon drift detector module. The labelled MOS charge injectors are used to monitor the drift velocity in the SDD [97].

As a charged particle traverses an SDD module, it ionises the surrounding material. The electrons created by such a process then interact with the bias field applied over the SDD, and begin drifting towards the collection anodes at the edge of the silicon. At a bias voltage of $-2.4$ kV, the electrons in the SDD have a drift velocity of 8.1 $\mu$m/ns. When the electrons reach the external anodes, the SDD is able to provide a signal. The signal at each anode is sampled at a rate of around 40 MHz, which then means that each SDD is split into 89.1x10$^3$ sensitive elements, or 'cells', each of which measures 294 x 202 $\mu$m$^2$.

As with the SPD, the SDD layers are arranged in ladders, with multiple detector units per ladder. Between the two layers, the SDD system contains 260 modules (each module comprised of a drift detector and its corresponding readout electronics), each using 512 readout channels. This results in a total of over 133,000 readout channels for the SDD system.

By measuring the drift time for any electrons produced within an SDD module, the location of the original particle can be pinpointed with high precision: the average spatial precision of the SDD is 35(25) $\mu$m in the $r\phi(z)$ direction. In addition to tracking, the SDD system are also capable of measuring the energy loss experienced by a particle as it traverses its volume. This is then able to be used for particle identification, as will be explained in section 3.5.

### 3.4.3 Silicon Strip Detector

At the outer layers of the ITS, the charged particle track density decreases significantly with respect to the centre of the collision ($<$ 1 particle per cm$^2$), and so there is no need for the high granularities present in the more central detectors. To this end, ALICE uses 1698 double-sided silicon micro-strip detectors (known within ALICE by the acronym SSDs) for the fifth and sixth layers of the ITS [98]. These are able to provide both energy loss measurements (as with the SDDs, used for the identification of low-momentum particles), and good position information which is used to match tracks between the ITS and the TPC which surrounds it.

The individual SSD modules are 300 $\mu$m thick, double-sided sensors, which measure 75 x 42 mm$^2$ in area, and which hold 768 sensitive strips on each side. The strips on either side of each sensor are tilted by 17.5 mrad with respect to the short edge of the module, and 35 mrad with respect to each other, as shown in figure 3.6. By identifying which pair of strips register a signal in coincidence, the position of a particle interacting with an SSD module can be located. The spatial precision of the SSD modules is 20 $\mu$m in the $r\phi$ direction, and

830 $\mu$m in the $z$ direction [31].

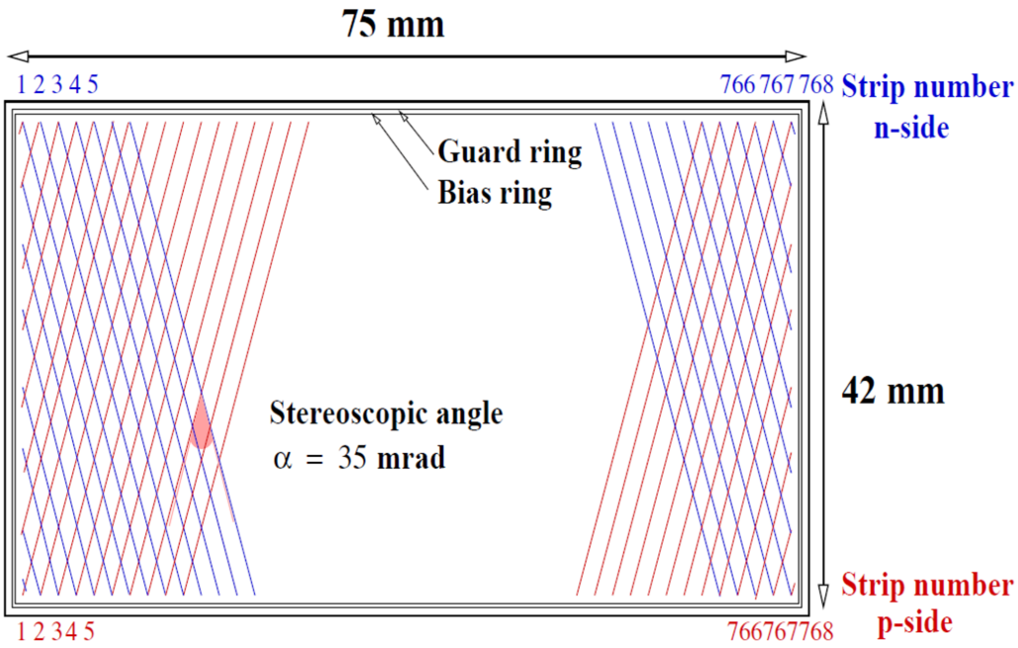

Figure 3.6: Schematic diagram of a silicon strip sensor [94].

## 3.5 The Time Projection Chamber

Surrounding the ITS is a large Time Projection Chamber (TPC), a diagram of which is shown in figure 3.7. The TPC within ALICE fulfils two roles: it provides complete tracking for particles over a very wide range of momenta (from around 0.1 GeV/$c$ to 100 GeV/$c$), and high accuracy particle identification for low momentum ($p_{\mathrm{T}} < 1$ GeV/$c$) particles.

The main body of the ALICE TPC is a cylindrical field cage with an inner radius of 0.8 m, an outer radius of 2.5 m, and a length of 5 m, covering the region $|\eta| < 0.9$. The 88 m$^3$ volume of the TPC is split in half by the large high voltage electrode at 100 kV, which sets up a uniform electric field of 400 V/cm aligned along the $z$-axis. The operation of the TPC is much like that of the SDD, except the charged particles do not traverse through solid silicon; the TPC is filled with a gas mixture of neon, carbon dioxide and nitrogen in ratios of 90:10:5. This gas mixture has been optimised for drift speed, reducing the chances

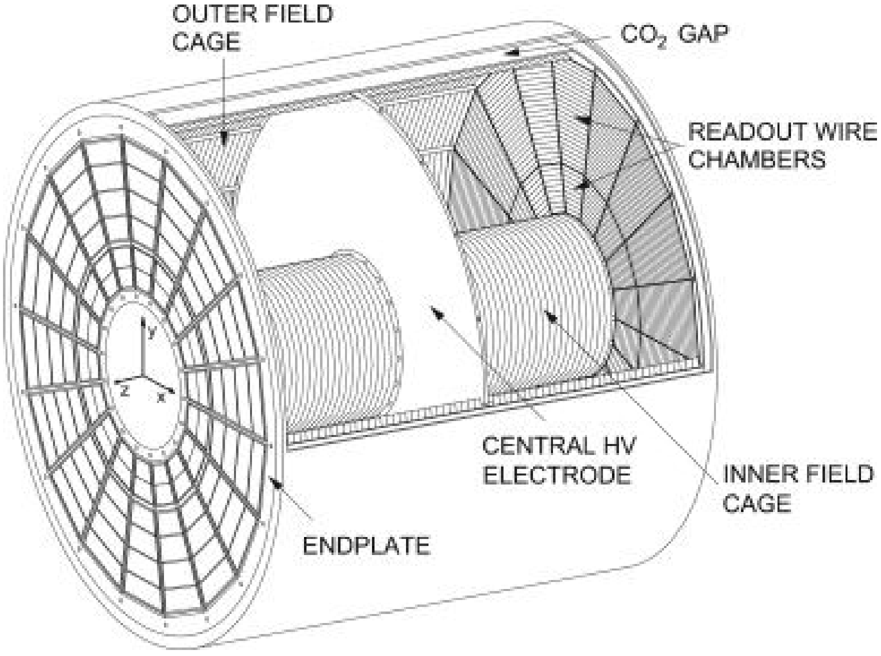

Figure 3.7: Three-dimensional schematic of the ALICE Time Projection Chamber [99].

of multiple scattering, and stability over time. Despite these attempts at stability, the drift velocity within the TPC is still highly temperature dependent. Due to this, the TPC requires a thermal stability of greater than 0.1 K, which is achieved via the use of heat screens and cooling circuits.

The read-out of the TPC is provided by use of 72 multi-wire proportional chambers (MWPCs) located at the endplates. As the ionisation electrons approach the MWPCs, they are accelerated by a strong electric field, which causes a charge avalanche. This is then picked up by the cathode pads which act as readout for the MWPCs. By identifying which of the readout pads has fired, the $r\phi$ position of a track can be identified; its location along the $z$-axis can be determined by measuring the time that the ionisation took to drift across the detector. The position resolution of the TPC is dependent on the radial position of a track in question. As such, the resolution is 1100(800) $\mu$m in the $r\phi$ direction and 1250(1100) $\mu$m in the $z$ direction at the inner(outer) radius of the TPC.

In addition to tracking, the TPC is used for particle identification for many of the particles created within ALICE. For this, two measurements are needed for each particle:

its momentum and energy loss as it traverses the TPC. The energy loss measurements are provided directly by the TPC; the momentum measurements come after offline event reconstruction, by measuring the curvature of a track within the central barrel magnetic field.

PID within the TPC, ITS and TRD is all done using measurements of energy loss as a particle passes through a material. The equation describing this energy loss is known as the Bethe-Bloch formula:

$$-\frac{\mathrm{d}E}{\mathrm{d}x} \propto \frac{Z}{A\beta^2}\left(\frac{1}{2}\ln\left(\frac{2m_e c^2\gamma^2\beta^2}{I}\right) - \beta^2\right) \quad , \tag{3.2}$$

where $Z$, $A$ and $I$ are properties of the material being traversed (its atomic number, atomic mass and mean excitation potential, respectively), $\beta = v/c$ is the speed of the particle being detected and $\gamma = 1/\sqrt{1-\beta^2}$ [100]. Equation 3.2 can also be written in such a form that its right-hand side is dependent only on the mass and momentum of the particle being measured. Since both momentum and energy loss are able to be measured by the TPC, the only free parameter is a particle's mass. If the energy loss of various particles are plotted against their momenta, patterns form which can be used to separate species of different masses, as shown in figure 3.8.

## 3.6 The V0 detector

Within the forward region near to the interaction point lie two arrays of plastic scintillator detectors; these comprise the VZERO (or V0) system. The two arrays are labelled V0A and V0C, and are placed as shown in figure 3.9: the V0A lies 340 cm away from the IP, on the A-side of the central barrel, and covers the pseudorapidity region $2.8 < \eta < 5.1$; the V0C is fixed to the front of the muon absorber, at $z = -90$ cm, and covers $-3.7 < \eta < -1.7$. Both V0 detectors consist of 32 scintillator tiles arranged in four concentric rings in the $r\phi$ plane.

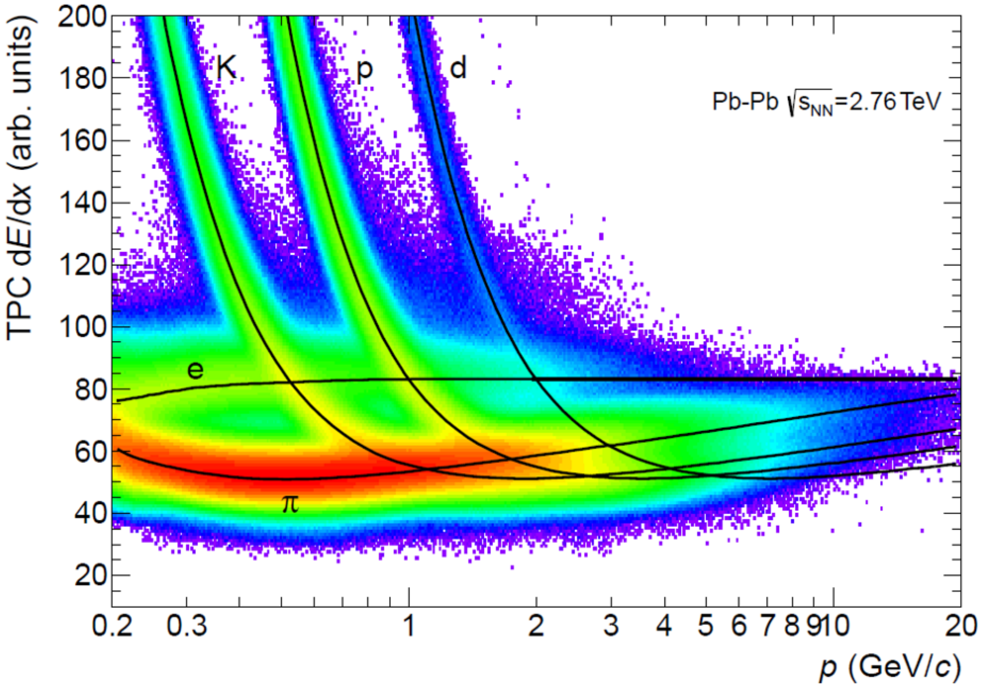

Figure 3.8: Energy loss for various particles versus their momenta, as measured by the TPC in Pb-Pb collisions. The drawn lines show parameterizations of the expected behaviour for various species [101].

The interaction of charged particles with the scintillator material causes excitations within the detector material. As the scintillator de-excites, it releases photons, which are picked up by a series of wavelength-shifting fibres which run along the side of the detectors. These fibres take the light to a series of photomultiplier tubes (PMTs), where the signal is amplified and read out. The scintillators do not discriminate between species or momenta; any particle hitting the V0s will create the same signal. Therefore, the total energy deposited in the scintillators is proportional to the number of particles passing through the V0 system, which allows the V0s to be used as an estimator of final state multiplicity.

For symmetric collision systems, such as pp and Pb-Pb, the event multiplicity estimator is taken as the combined amplitude of the signals from the V0A and V0C arrays; this estimator is notated as V0M. For the asymmetric p-Pb collisions, the taken multiplicity estimator is the amplitude of the signal from the V0 array in the Pb-going direction. For this analysis, that corresponds to the V0A detector. The distributions of these signals are

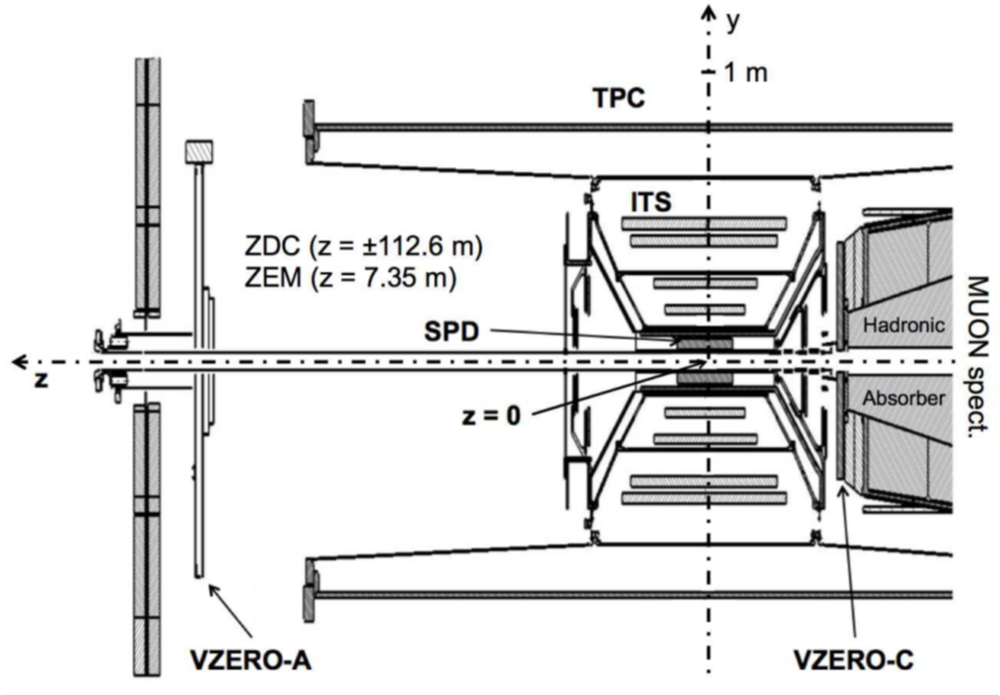

Figure 3.9: Cut-away schematic of the ALICE central barrel, showing the location of the two VZERO arrays [102].

then divided into percentiles to define multiplicity classes.

The V0 system is also used to provide triggering for ALICE; due to the very fast read-out speed that the scintillators are able to provide, hits in the V0 can be used as early indicators of the presence of a collision. These trigger signals are also used for event classification: a Minimum Bias event is one in which both V0 arrays record at least one hit, and is the least strict classification used for a trigger.

Further to the above, the V0 detectors are also used to discriminate between real events and background from beam-gas interactions. To do this, the time-of-flight is measured for each array. From these, a beam-gas interaction can be identified by looking at correlations between the measure times, as shown in figure 3.10.

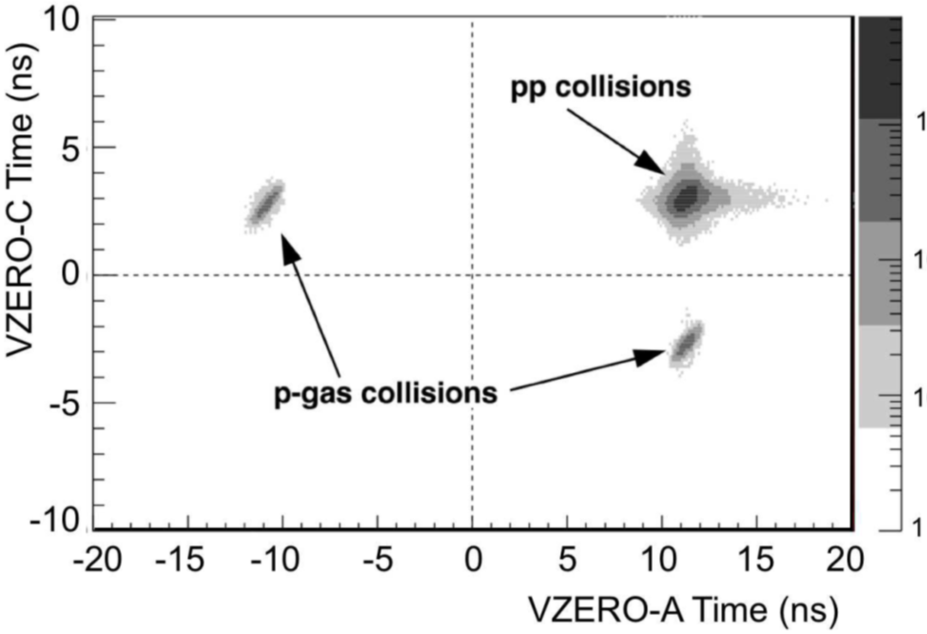

Figure 3.10: Weighted average time-of-flight of particles detected in the V0A versus those in the V0C in pp collisions. The concentration of points in the upper right corner of the plot describe real pp collisions, whereas the other two concentrations result from interactions with residual protons in the beam pipe. [102]

# Chapter 4

# Event Selection and Data Analysis

The analysis detailed in this thesis looks at two hadrons: the $\mathrm{K}^0_\mathrm{S}$ meson and the $\Lambda$ baryon, both of which contain a single strange quark. As both of these particles are neutrally charged, they are not detected by the ALICE tracking systems; they are instead reconstructed from their weak decay products, which can be measured. The following chapter shall discuss the criteria used for the selection of individual candidates, as well as any corrections which needed to be applied.

## 4.1 Multiplicity Estimation

The results from this analysis are to be put in terms of the final state charged particle pseudorapidity density, $\langle dN_{ch}/d\eta \rangle$, so that they can be compared to similar results from other energies and system sizes. In order to do this, a method must be used to determine an event's multiplicity. Within ALICE, a number of these exist, including counting the number of tracklets measured in the SPD, and the energy incident on the Zero Degree Calorimeters, located more than 100 m from the interaction point along the LHC beamline. Within this analysis, the V0A subdetector was used to provide an estimation for multiplicity, as described in section 3.6.

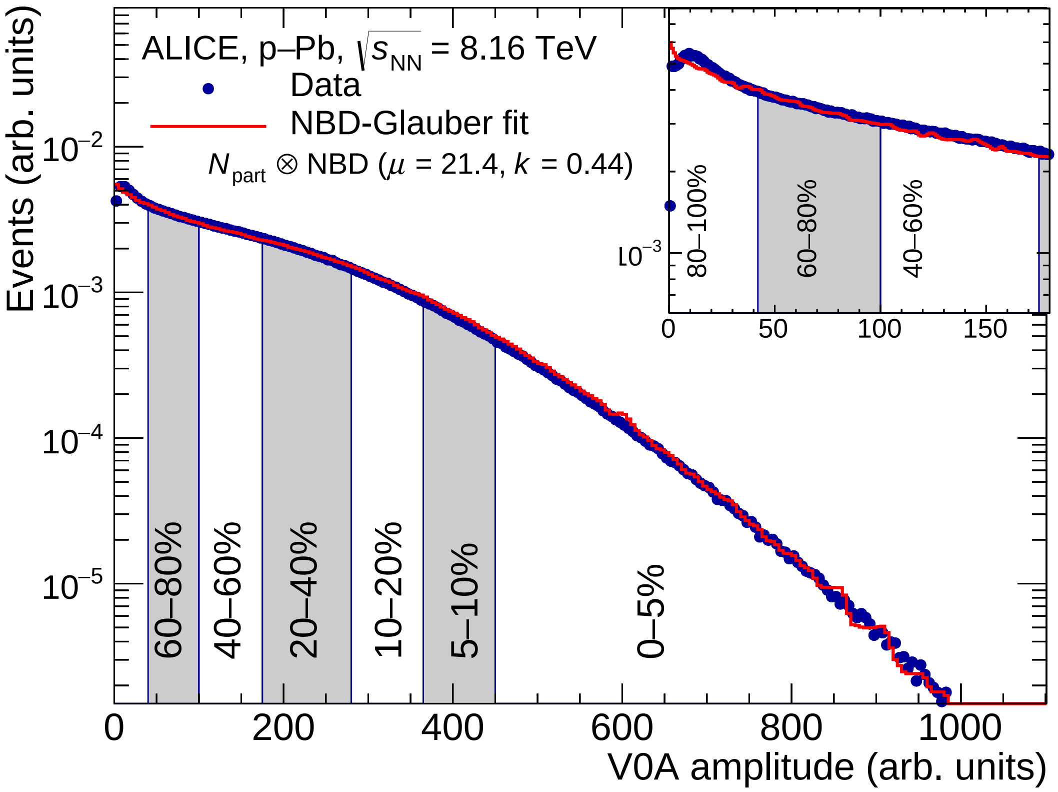

Figure 4.1: Distribution of the signal amplitude from the V0A detector in p-Pb collisions at $\sqrt{s_{\mathrm{NN}}} = 8.16$ TeV [103]. Also marked are multiplicity classes, split into percentiles, and separated by the vertical lines.

The amplitude of the signal from the V0A detector is used to separate events into classes, each class containing a set percentage of the total data set, as shown in figure 4.1. In order to calculate the mean charged particle density for each of these classes, the data are fitted using a Glauber model [104], shown as a red line in figure 4.1. Millions of collisions of composite particles, such as heavy nuclei, are simulated; the model is then used to calculate the number of participant nucleons, $N_{\mathrm{part}}$, and the number of nucleon-nucleon collisions, $N_{\mathrm{coll}}$, for each event. The generated distribution of $N_{\mathrm{coll}}$ can then be matched to the measured track multiplicity from ALICE data, and used to calculate the average number of nucleon-nucleon interactions for each multiplicity class.

For this analysis, the same multiplicity classes were used for both the $\mathrm{K}^0_\mathrm{S}$ and $\Lambda$ candidates. The chosen classes, and their corresponding charged particle multiplicity densities, are shown in table 4.1. The highest multiplicity classes in this p-Pb analysis overlap with the lowest multiplicity classes in Pb-Pb analyses, and the lowest p-Pb multiplicity classes overlap the highest multiplicity classes from pp collisions. This allows proton-lead analyses to investigate the transition in behaviour from the smallest to the largest systems.

Table 4.1: Multiplicity classes used for both $\mathrm{K}^0_\mathrm{S}$ and $\Lambda$ analyses, plus the midrapidity charged particle multiplicity density for each class [105].

| V0A class | $\langle dN_{ch}/d\eta\rangle_{\lvert\eta\rvert<0.5}$ |
|---|---|
| 0-1% | 64.00 ± 1.66 |
| 1-5% | 50.50 ± 1.31 |
| 5-10% | 42.40 ± 1.10 |
| 10-15% | 37.30 ± 0.97 |
| 15-20% | 33.64 ± 0.87 |
| 20-30% | 29.30 ± 0.76 |
| 30-40% | 24.49 ± 0.66 |
| 40-50% | 20.34 ± 0.53 |
| 50-60% | 16.46 ± 0.43 |
| 60-70% | 12.77 ± 0.34 |
| 70-80% | 9.21 ± 0.24 |
| 80-100% | 4.47 ± 0.14 |

## 4.2 Event Reconstruction

As discussed, the particle species of interest to the analyses in this thesis are neutrally charged, and as such need to be reconstructed from their weak decay products. The most common decay for the $\mathrm{K}^0_\mathrm{S}$ is to a $\pi^+\pi^-$ pair, with a branching fraction of 69% [106]. For the $\Lambda(\bar{\Lambda})$, the most likely decay is to a $p\pi^-$ $(\bar{p}\pi^+)$ final state, with a branching fraction of 64% [107]. The average distance a particle travels before decaying, $L$, is given by

$$L = \frac{p\tau}{m} \quad ,$$

where $\tau$ is the proper lifetime of the particle, $p$ its momentum, and $m$ the mass. For both species considered in this analysis, this distance is of the order of centimetres. Table 4.2

gives details of the decays detailed in this thesis.

Table 4.2: Properties of the $\mathrm{K^0_S}$ and $\Lambda$ species [106, 107]. The mass, lifetime and branching fraction of the $\bar{\Lambda}$ are expected to be identical to its matter counterpart.

| Species | Mass (MeV/$c^2$) | Lifetime, $c\tau$ (cm) | Decay channel | Branching fraction (%) |
|---|---|---|---|---|
| $\mathrm{K^0_S}$ | 493.677 ± 0.016 | 2.686 ± 0.001 | $\pi^+\pi^-$ | 69.20 ± 0.05 |
| $\Lambda(\bar{\Lambda})$ | 1115.683 ± 0.006 | 7.89 ± 0.06 | $p\pi^-(\bar{p}\pi^+)$ | 63.9 ± 0.5 |

Given the lack of charge of the $\mathrm{K^0_S}$ and $\Lambda$, and the distinctive V shape of their decays, these species are referred to as $\mathrm{V^0}$s. The reconstruction of a $\mathrm{V^0}$ candidate begins with the tracks of the decay products, known as a candidate's *daughters*. Each of these tracks is reconstructed from the outside in, starting from signals in the TPC, matching to hits in the various layers of the ITS. Combinations of these tracks which reconstruct to a common vertex, away from the primary vertex, are then identified with a $\mathrm{V^0}$ candidate.

The algorithm which reconstructs the $\mathrm{V^0}$ candidates used in this analysis initially reconstructs all pairs of oppositely-charged reconstructed tracks in an unbiased way. Following this, all possible combinations of two tracks are evaluated, to see if they could possibly be from the decay of a $\mathrm{V^0}$. As figure 4.2 shows, the expected decay topologies are very simple, containing only two final state particles. As such, it is very easy for unconnected combinations of tracks to look like a real $\mathrm{V^0}$, and further selections are required.

These extra selections are performed based on the topology of a real $\mathrm{V^0}$ decay, and remove candidates whose behaviour differs from what is expected. A detailed diagram of a $\mathrm{V^0}$ decay, including the quantities used for candidate selection, is shown in figure 4.3. The geometric properties considered in the acceptance or rejection are listed below:

- **Distance of closest approach (DCA) of the $\mathrm{V^0}$ daughters**: Given the known topology of a $\mathrm{V^0}$ decay, it is required that both reconstructed daughter tracks are consistent with originating from the same vertex, within the resolution of the detector. To assist with applying this restriction, a cut was placed on the DCA between the tracks of the two daughters, removing candidates whose daughters were likely to not

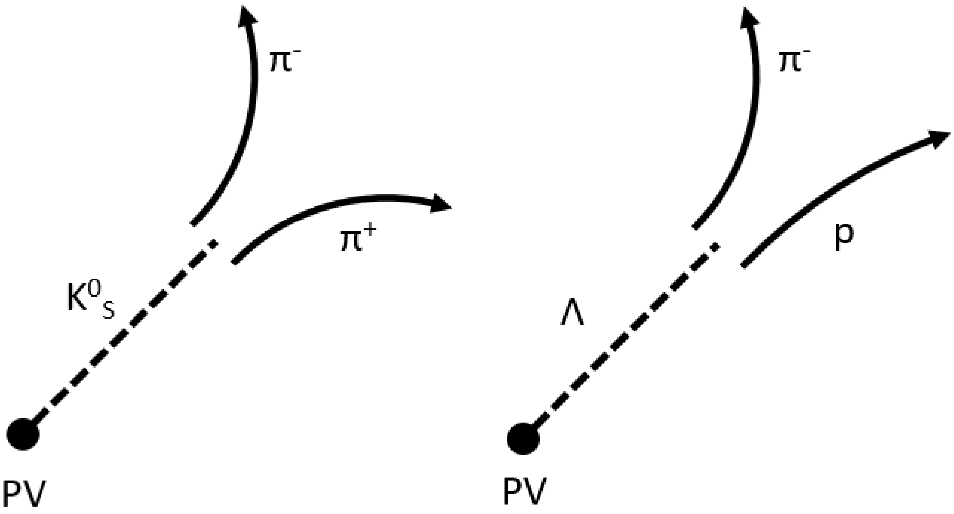

(a) $\mathrm{K^0_S}$ (b) $\Lambda$

Figure 4.2: Expected topologies for V0 decays. The expected shape of a $\bar{\Lambda}$ decay is a charge-swapped version of that for the $\Lambda$.

have come from the same vertex. Unlike other distance cuts, this value was measured in $\sigma$, a constructed variable which is a result of the track reconstruction algorithm matching signals from the ITS to those from the TPC.

- **DCA between daughter tracks and the primary collision vertex (PV)**: A candidate was rejected if either of the two daughter tracks came too close to the PV when reconstructed. This was to ensure that the daughters were both more likely to have originated from a weak decay, and not the initial collision.

- **$\mathbf{V^0}$ decay radius**: Each $V^0$ candidate was assigned a *decay vertex*, a point on the line joining the two daughter tracks at their points of closest approach, weighted by the uncertainties on the tracks. A minimum cut was placed on the distance between this and the primary vertex, referred to as the $V^0$'s *decay radius*, to ensure sufficient separation between the reconstructed decay vertex and the point of collision.

- **Cosine of the $\mathbf{V^0}$ pointing angle**: The *pointing angle* of a candidate was defined as the angle between two lines; the momentum vector of the reconstructed $V^0$, and the line connecting the $\mathrm{V}^0$ decay vertex to the PV. A cut was placed to keep this value close to one, ensuring that the momentum of the $\mathrm{V}^0$ pointed back to the primary vertex.

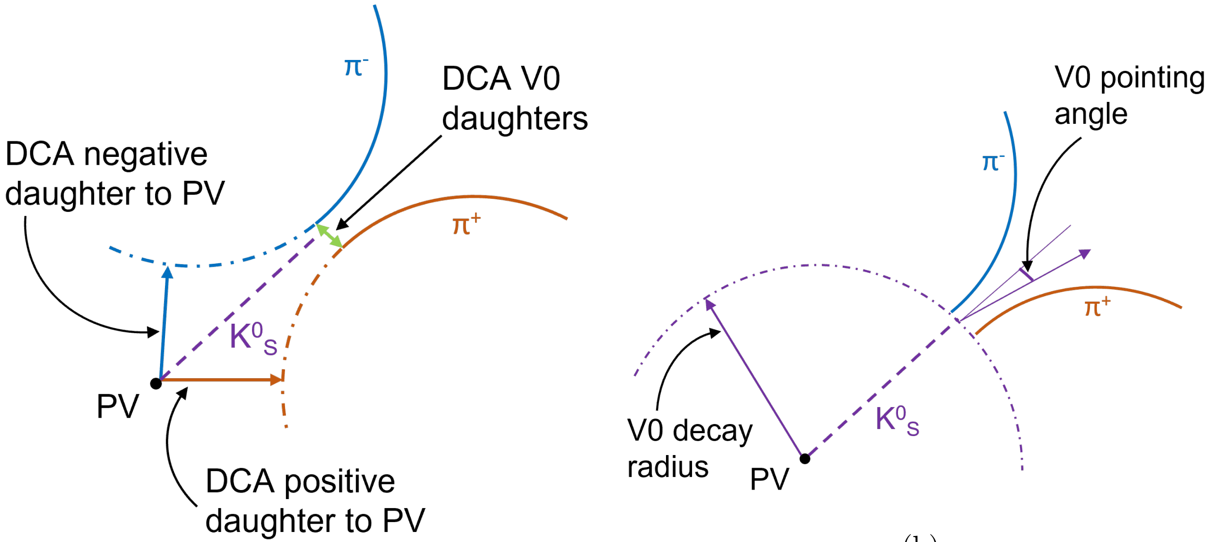

(a)

(b)

Figure 4.3: Topological selections as applied to an example $\mathrm{V}^0$ decay, in this case for a $\mathrm{K}^0_{\mathrm{S}}$. On the left are shown the various distances of closest approach used, and on the right are the $\mathrm{V}^0$ decay radius and pointing angle.

In addition to these topological variables, cuts were also placed on quantities describing the quality of the tracks used in the reconstructions process. In order to remove background from tracks of the wrong species, a cut was placed on the TPC PID information: a candidate was rejected if either of its daughter tracks were further than $4\sigma$ from the expected behaviour. In addition, a minimum was placed on the number of hit TPC clusters by a track, identifying good quality tracks. Out of a possible 159 clusters, accepted tracks are required to have hit at least 70.

A further cut was also placed on the *invariant mass* of each candidate. This quantity is calculated from the energies and momenta of the daughters coming from a particle decay, and is indicative of the mass of the mother; in the case of the $\mathrm{V}^0$ species investigated here, this becomes

$$M^2_{\mathrm{V}^0} = \left(\sqrt{m_+^2 + p_+^2} + \sqrt{m_-^2 + p_-^2}\right)^2 - \left(\underline{p}_+ + \underline{p}_-\right)^2 \quad , \tag{4.1}$$

where $m_{\pm}$ and $\underline{p}_{\pm}$ are the PDG mass and vector momentum respectively of the positive or negative $\mathrm{V}^0$ daughter[4]. This $M^2$ quantity is, as the name suggests, Lorentz invariant, and as such avoids the problem of the relative motion of decay and laboratory frames.

As previously stated, the $\mathrm{V}^0$ reconstruction algorithm, known as the *finder*, combined all identified tracks with all other reconstructed tracks of the opposite electric charge. Should a combination of tracks come from a real candidate, equation 4.1 will return a value close to the mass of the expected $\mathrm{V}^0$ species. However, as figure 4.2 shows, the decay topology for the $\mathrm{K}^0_\mathrm{S}$ is almost identical to that of the $\Lambda$. As such, it is possible for some kaon candidates to be reconstructed as a $\Lambda$ or vice versa. In order to remove the contribution from such mis-identifications, $\mathrm{K}^0_\mathrm{S}$ candidates were reconstructed as if they are a $\Lambda$ (using the proton mass instead of the $\pi^{\pm}$ mass for one of the daughters), and vice versa. A $\mathrm{K}^0_\mathrm{S}$ candidate is rejected if this 'misidentified mass' is within 5 MeV/$c^2$ of the PDG value for the $\Lambda$ mass, and a $\Lambda$ candidate is rejected if the misidentified mass is within 10 MeV/$c^2$ of the $\mathrm{K}^0_\mathrm{S}$ mass.

The rapidity range used for this analysis is $-0.5 < y_{lab} < 0$, which is chosen to reflect the acceptance of the ALICE central barrel, and the nature of decays coming from the asymmetric p-Pb collision system. As discussed in section 3.2.1, the value of rapidity in the lab frame is shifted by a value of $-0.465$ relative to the centre-of-mass frame. As such, the rapidity interval chosen for this analysis roughly corresponds to $0 < y_{CoM} < 0.5$, which is comparable to other analyses performed within ALICE. A cut is also placed on the pseudorapidity of the daughter tracks. The acceptance of the ALICE inner barrel is $|\eta| < 0.9$, so a cut is placed at $|\eta| < 0.8$ in order to avoid edge effects in the detectors.

### 4.2.1 Data Sample

The data set used for this analysis was taken from proton-lead collisions at a centre-of-mass energy-per-nucleon of 8.16 TeV, which took place at the end of 2016. In particular, this analysis used the data from six low interaction rate runs, within the larger *LHC16r_CENT*

---

[4] This equation is written using natural units, where $c = \hbar = 1$.

dataset, where *CENT* refers to the *CENT* detector cluster, which includes the TPC and the full ITS. There is also a *FAST* cluster, which excludes the SDD, ALICE's slowest detector, when it is busy. This low interaction rate sample consists of around 40% of the total *LHC16r_CENT* dataset.

The probability of $n$ interactions taking place within a single bunch crossing is described by a Poisson distribution,

$$\Pr(n, \mu) = \frac{e^{-\mu}\mu^{n}}{n!} \quad ,$$

where $\mu$ is the average number of interactions per bunch crossing. The probability of more than one interaction per bunch crossing can be calculated,

$$\Pr(n \geq 2, \mu) = 1 - \Pr(n \leq 1, \mu) = 1 - [\Pr(n = 0, \mu) + \Pr(n = 1, \mu)] = 1 - (1 + \mu)e^{-\mu} \quad .$$

For the low interaction rate data used for this analysis, the value of $\mu$ is 0.02 or less, which corresponds to a probability of more than one interaction per bunch crossing of less than 0.02%. This subsample was chosen for the analysis as it minimises the risk of having to deal with *pileup*, where multiple interactions in the same bunch crossing can increase the complexity of analysis.

### 4.2.2 Initial event selection

Prior to the application of tight geometric and track quality cuts, the data underwent a process of basic event selection. The parameters used for this are those used within ALICE for other p-Pb analyses. The data were collected using a minimum bias trigger, which requires at least one hit to be registered in both the V0A and V0C subdetectors. In addition, a cut was placed accepting events in which the primary vertex had a $z$-coordinate between -10 cm and +10 cm, within the middle of the central barrel.

A cut was also placed in order to remove any in-bunch pileup events. An event was rejected if a second interaction vertex was found more than 0.8 cm from the first along the $z$ axis, with

- at least 5 associated tracklets, if the total number of reconstructed tracklets for the event, $N_{tracklets}$, is greater than 50
- at least 4 associated tracklets, if $20 < N_{tracklets} \leq 50$, or
- at least 3 associated tracklets, if $N_{tracklets} \leq 20$

After the application of these selections, the files containing the V$^0$ candidates were still too large for fast offline analysis. In order to create more compact files, a very loose set of cuts was applied to the remaining V$^0$ candidates; loose enough to not bias the final data, but tight enough to remove a large amount of background. Table 4.3 contains the set of these preliminary cuts.

Table 4.3: Loose topological cuts used to create the real data files used in this analysis

| Cut type | Cut value |
|---|---|
| V$^0$ decay radius (cm) | $>$ 1.0 |
| Cosine of V$^0$ pointing angle | $>$ 0.95 |
| DCA of V$^0$ daughters ($\sigma$) | $<$ 2.0 |
| DCA of positive daughter to PV (cm) | $>$ 0.02 |
| DCA of negative daughter to PV (cm) | $>$ 0.02 |
| $c\tau$ (cm) | $<$ 100 |

## 4.3 Signal Extraction

So that a signal could be extracted, and compared to previous analyses, the invariant mass was plotted for all candidates which passed the candidate selection criteria, the particular details of which shall be described in section 4.4. The resulting distributions, as shown in figures 4.4 and 4.5, were subsequently fitted with a composite function: a gaussian, to describe the peak, and a second degree polynomial, to describe the underlying background.

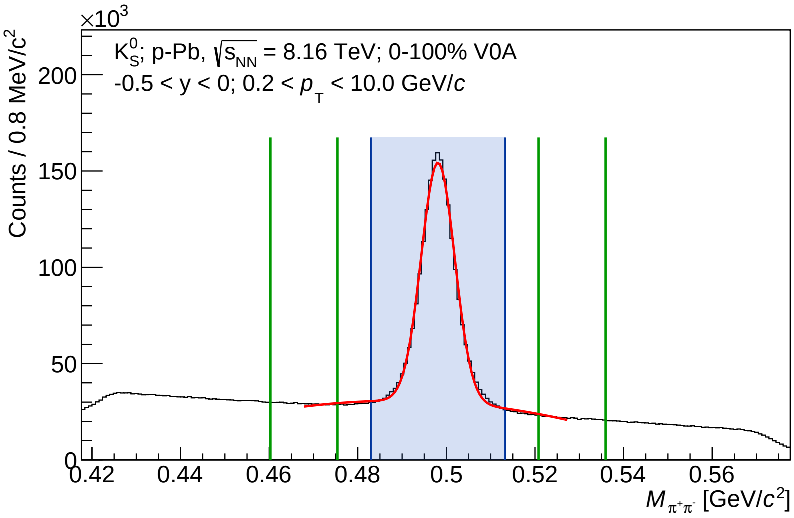

(a) Pre-cuts

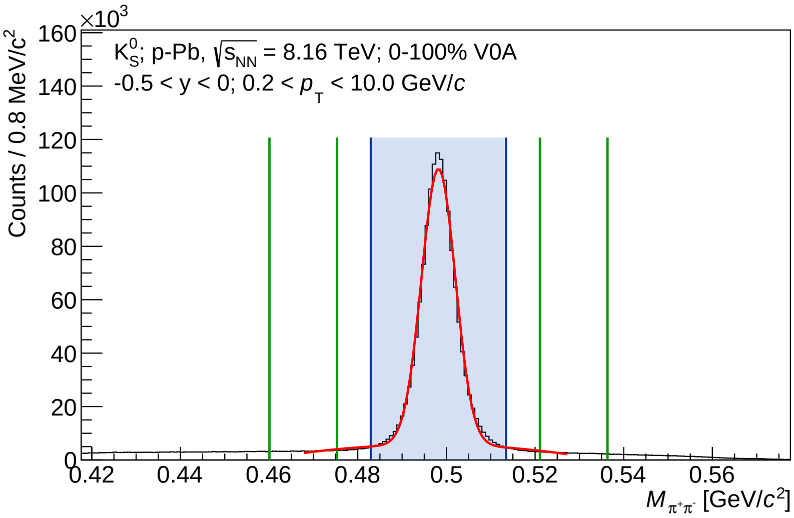

(b) Post-cuts

Figure 4.4: Invariant mass distribution of all $K^0_S$ candidates, before and after the application of topological cuts. Also shown are the function used to fit the peak, in red, and the peak and background side bands, denoted by the blue and green lines respectively.

Following this fitting procedure, signal and background regions were chosen based on the mean, $\mu$, and width, $\sigma$, of the gaussian fit to the peak. A signal region was defined as $\mu \pm 4\sigma$, and the lower and upper background regions were defined as $[\mu - 10\sigma, \mu - 6\sigma]$ and

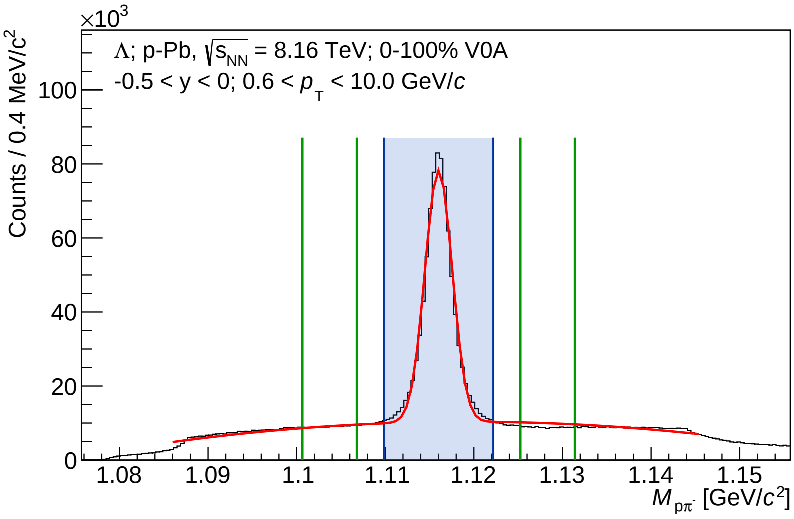

(a) Pre-cuts

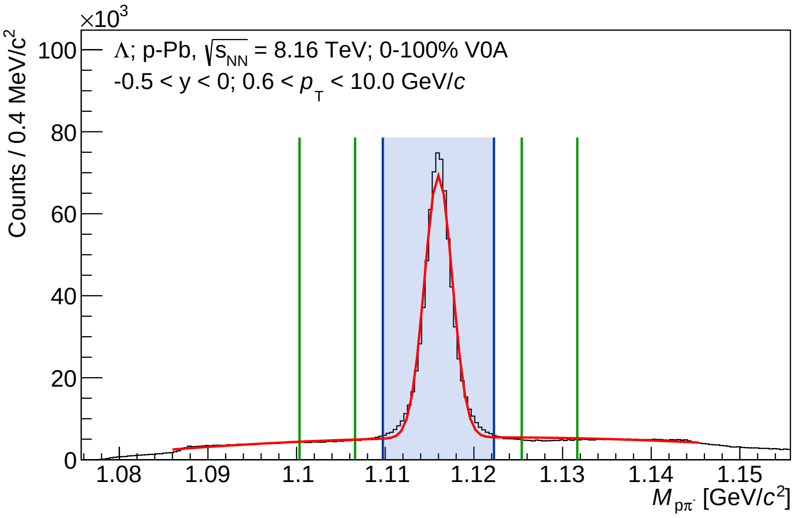

(b) Post cuts

Figure 4.5: Invariant mass distribution of all $\Lambda$ candidates, before and after the application of topological cuts. Also shown are the function used to fit the peak, in red, and the peak and background side bands, denoted by the blue and green lines respectively.

$[\mu + 6\sigma, \mu + 10\sigma]$, respectively.

The events within the signal region are composed of both true $V^0$s, and background events which happened to pass event selection. The background as a function of invariant mass was taken to be linear; as such, the number of candidates in both side bands were summed in order to give an estimation of the background under the peak. This was then subtracted from the number of counts in the peak region to calculate the final signal.

The data used were separated into transverse momentum bins in order to provide a $p_{\mathrm{T}}$ spectrum. The bins used were as follows

- $\mathrm{K}^0_{\mathrm{S}}$: {0.2, 0.3, 0.4, 0.5, 0.6, 0.7, 0.8, 0.9, 1.0, 1.1, 1.2, 1.4, 1.6, 1.8, 2.0, 2.2, 2.4, 2.6, 2.8, 3.2, 3.7, 4.2, 5.0, 6.0, 10.0} GeV/$c$
- $\Lambda(\bar{\Lambda})$: {0.6, 0.7, 0.8, 0.9, 1.0, 1.1, 1.2, 1.4, 1.6, 1.8, 2.0, 2.2, 2.4, 2.6, 2.8, 3.2, 3.7, 4.2, 5.0, 6.0, 10.0} GeV/$c$

The bins start above zero as very low momentum candidates cannot be detected by the ALICE inner barrel; the daughter tracks of any such candidates do not traverse the detectors due to their small radii of curvature. As such, in order to extract full yields, the $p_{\mathrm{T}}$ spectra for the different $\mathrm{V}^0$ species were plotted and fitted, a procedure which shall be discussed further in section 5.1.1.

## 4.4 Cut Study

The values used for the topological cuts were chosen in a method very similar to other high-energy physics analyses. The eventual aim of the cuts chosen was to maximise the available signal counts, whilst minimising the number of background events, thereby increasing the signal-to-noise ratio. For this, the signal significance, $\sigma$, was calculated,

$$\sigma = \frac{S}{\sqrt{S+B}} \quad ,$$

where $S+B$ is the combined signal plus background counts in the signal region, and $S$ is the background-subtracted signal counts. This quantity was used as it allowed for the desired reduction in noise, whilst also not running into the issue of dividing by zero, should there be no background counts.

The data were first analysed applying no topological cuts other than the very loose cuts used to create the data files used for this analysis, as detailed in table 4.3. Then, one of the topological cuts was tightened slightly, and the data re-analysed. This process was repeated a number of times, and $\sigma$ was calculated for all possible values of the cut in question. This process was then repeated for all of the topological selection criteria.

Also used for cut selection was the fraction of signal remaining as each cut was tightened, relative to the signal from the loosest possible cut value. This value,

$$Signal\ fraction = \frac{Raw\ signal(chosen\ cut)}{Raw\ signal(fully\ loose)} \quad ,$$

reflected the fraction of signal lost by each successive tightening of each cut. This was calculated using both real data, and data from Monte Carlo simulations of $\mathrm{V}^0$ candidates, in order to compare the behaviour of real events with simulated ones. This comparison was performed in order to minimise any biases that may have been introduced in the corrections required by the raw spectra. Figure 4.6 shows two of the plots used for topological cut selection. For a full set of the plots used, see appendix A.

The final values chosen for each cut were those that maximised the significance, whilst also:

– retaining a signal fraction of at least 95%, and

– showing no more than a 3% discrepancy between real data and Monte Carlo signal loss.

For the $\mathrm{K}^0_\mathrm{S}$ analysis, this process was completed in a single pass. However, for the $\Lambda$ cut determination, multiple passes were required, each time replacing the cuts not being investigated with the values chosen from the previous pass. This was because of a visible discrepancy between real data candidates, and those from Monte Carlo simulations. After three passes, the optimal cut values did not vary wildly between passes, and so were set as

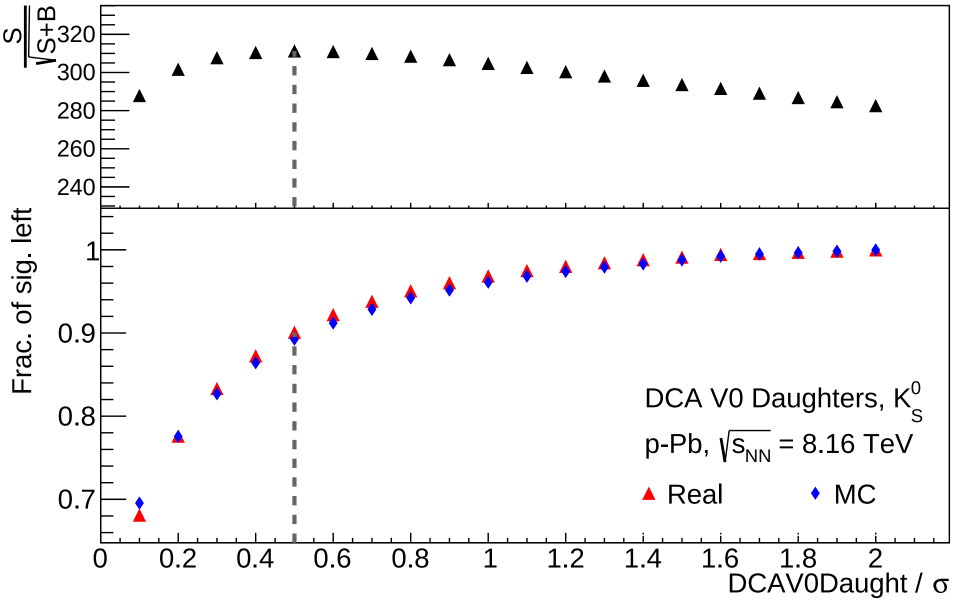

(a) $K^0_S$

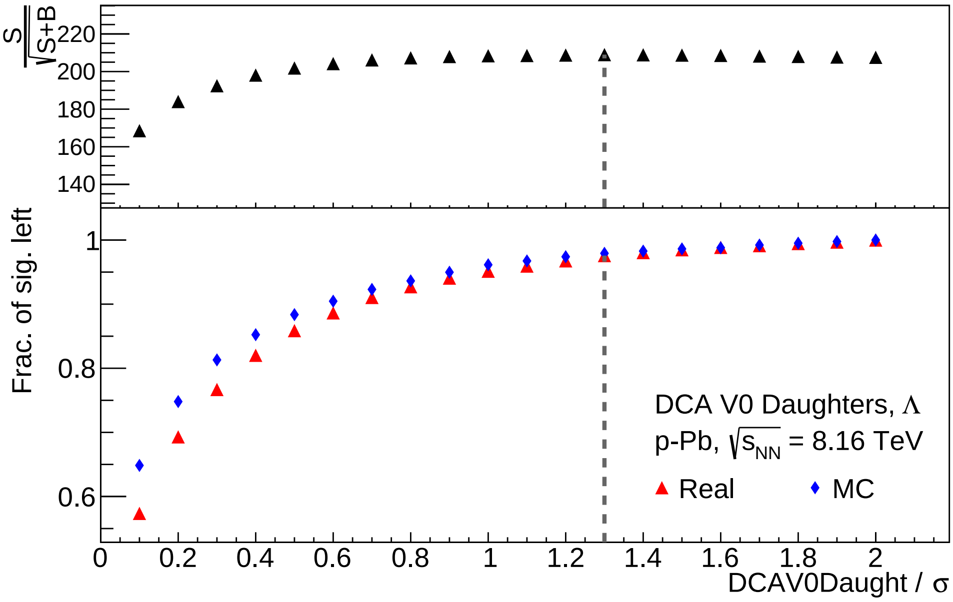

(b) Λ

Figure 4.6: Cut study plots as a function of cut value for the DCA $V^0$ daughters cut. The top of each plot shows the signal significance for each cut, and the lower pad shows the fraction of signal remaining (relative to a fully-loose cut). Also indicated, by the grey line, are the cut values at which the significance is maximised. Note that, for the $K^0_S$ analysis, this does not match the cut used due to the greater than 5% signal loss caused.

the chosen cuts.

Table 4.4 lists the default values used for the topological and track quality cuts used for the analyses detailed in this thesis. Note that the $\bar{\Lambda}$ cuts are identical to those used for the $\Lambda$ analysis, with the DCA cuts for the positive and negative daughters swapped.

Table 4.4: Default topological and track quality cuts used for the $K^0_S$, $\Lambda$ and $\bar{\Lambda}$ analyses.

| Cut type | $K^0_S$ | $\Lambda(\bar{\Lambda})$ |
|---|---|---|
| $V^0$ decay radius (cm) | $> 1.0$ | $> 1.0$ |
| Cosine of $V^0$ pointing angle | $> 0.995$ | $> 0.985$ |
| DCA of $V^0$ daughters ($\sigma$) | $< 0.8$ | $< 1.3$ |
| DCA of positive daughter to PV (cm) | $> 0.06$ | $> 0.02(0.05)$ |
| DCA of negative daughter to PV (cm) | $> 0.06$ | $> 0.05(0.02)$ |
| $c\tau$ (cm) | $< 15$ | $< 40$ |
| | | |
| Number of TPC clusters hit | $\geq 70$ | $\geq 70$ |
| TPC PID (number of $\sigma$ from Bethe-Bloch curve) | $\pm 4$ | $\pm 4$ |
| Signal extraction window ($\sigma$ from peak) | $\pm 4$ | $\pm 4$ |
| Competing species rejection window (MeV/$c$) | $\pm 5$ | $\pm 10$ |

## 4.5 Spectral Corrections

The spectra generated by the process outlined previously required corrections before the final fitting and yield extraction process could be carried out. These corrections are required in order to take into account the efficiencies of the detectors and reconstruction algorithms, as well as the detector acceptances and contributions to the final yields from decay channels not considered for analysis. For these corrections, general purpose Monte Carlo (MC) simulations of the real data were used. The MC data were made by two different event generators, EPOS-LHC [78] and DPMJET [108]. These were then propagated through a simulation of the ALICE detector, made using GEANT4 [109].

The efficiencies were extracted by running the MC data through a near-identical analysis to the real data, and comparing the results to the truth level, generated $V^0$ candidates.

The main way in which the two candidate selections differed is that the MC analysis checks that a $\mathrm{V}^0$ candidate is associated with a generated $\mathrm{V}^0$ at the truth level. The efficiency is calculated separately for each $p_{\mathrm{T}}$ bin, as

$$\varepsilon(p_{\mathrm{T}}) = \frac{N_{recon}(p_{\mathrm{T}})}{N_{gen}(p_{\mathrm{T}})} \quad , \tag{4.2}$$

where $N_{recon}(p_{\mathrm{T}})$ and $N_{gen}(p_{\mathrm{T}})$ are the number of reconstructed and generated $\mathrm{V}^0$ candidates in a specific $p_{\mathrm{T}}$ bin. The reanalysis performed on MC data provided $N_{recon}$, and the values for $N_{gen}$ were extracted directly from the generated $\mathrm{V}^0$ candidate distributions.

It is important to check if there is a multiplicity dependence in the efficiencies. For this, the Monte Carlo data, both reconstructed and generated, were separated into the same multiplicity bins as the data, and the efficiency calculated again for each bin. These were then compared to the multiplicity-integrated MC sample, as shown in figure 4.7. As can be seen, within errors, the efficiency values for each multiplicity bin agree with those from the full Monte Carlo sample, suggesting no significant multiplicity dependence. As such, the multiplicity-integrated efficiency values were used for the correction of spectra.

### 4.5.1 Feeddown Removal

For many ALICE strange particle analyses, the species of interest can all be assumed to have been created in the initial collisions and subsequent QGP evolution. However, for $\Lambda$ and $\bar{\Lambda}$ analyses, this is not the case. This is because a non-negligible fraction of the $\Lambda$ detected in the final state actually come from the weak decays of heavier, multistrange species. As such, this contribution, known as *feeddown*, must be calculated and removed from the final $p_{\mathrm{T}}$ spectra in order to isolate the prompt $\Lambda$ spectra.

Figure 4.8 shows the invariant mass of all $\Lambda$ and $\bar{\Lambda}$ candidates in the Monte Carlo data which pass their respective event selections. These candidates also have associated information, identifying whether they are primary, from the initial collisions of the LHC

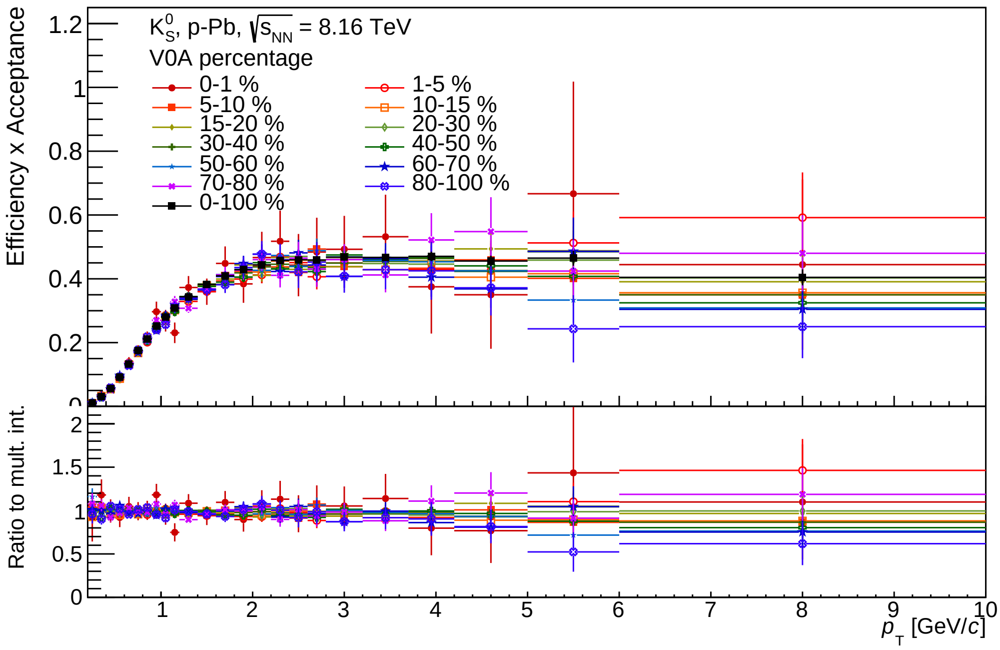

(a) $K^0_S$

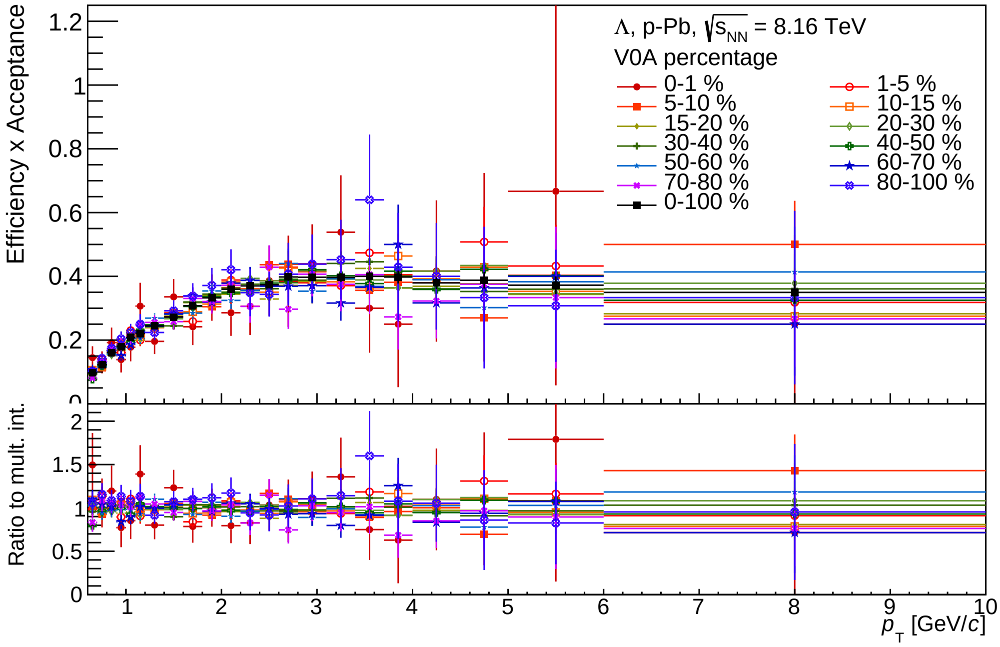

(b) $\Lambda$

Figure 4.7: Multiplicity dependence of efficiencies, for all multiplicity bins. The upper panel shows a direct comparison of efficiency values, and the lower panel shows the ratio of efficiency values to those from multiplicity-integrated MC data.

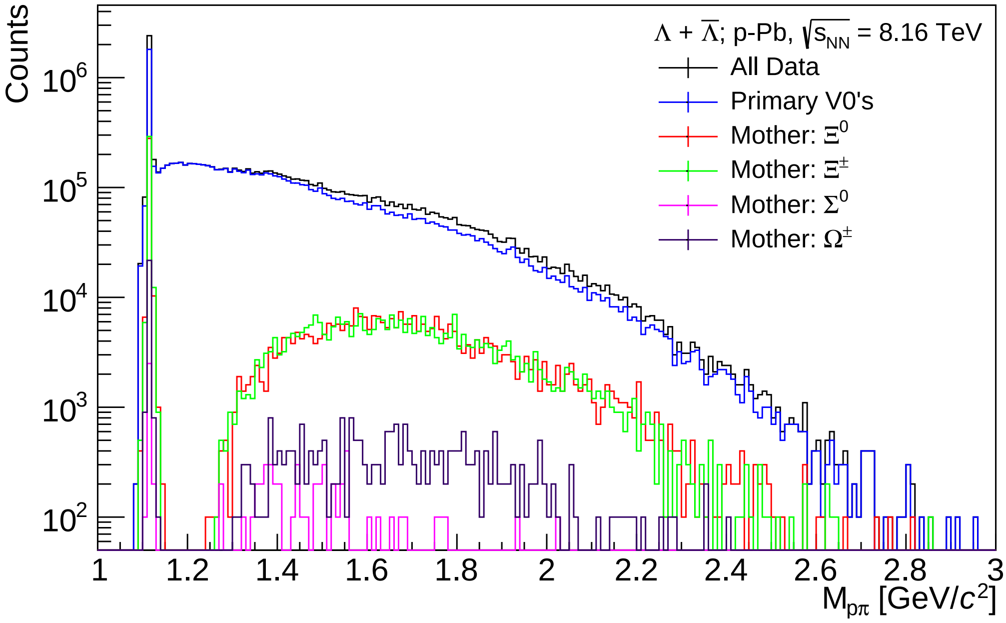

(a) Wide mass range.

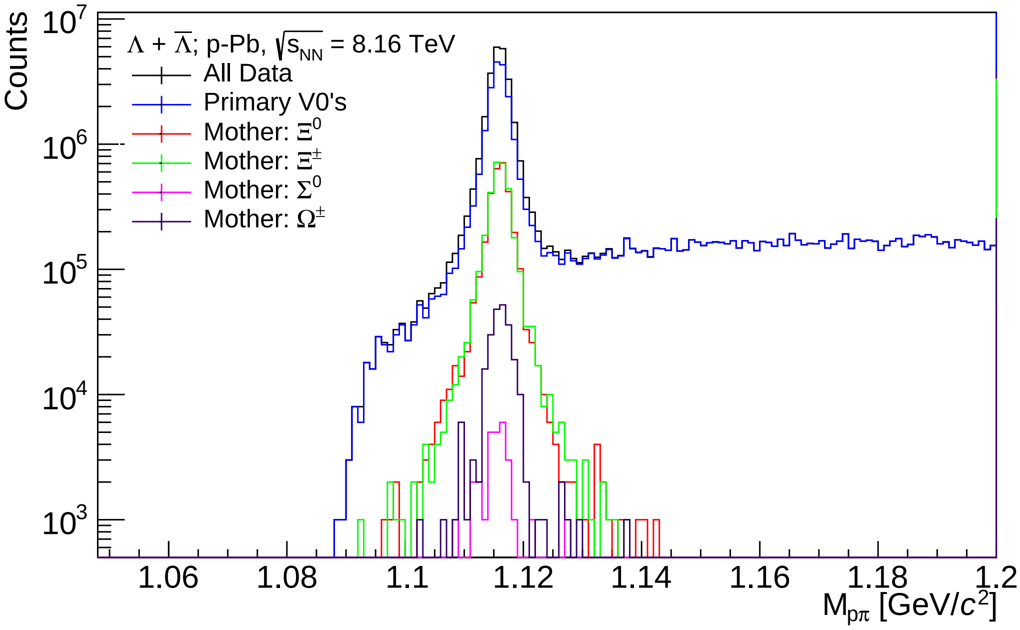

(b) Focus on $\Lambda$ mass peak.

Figure 4.8: Invariant mass distribution of $\Lambda$ and $\bar{\Lambda}$ candidates, from the Monte Carlo data set. The uppermost black line denotes the full data set, and the blue line denotes all candidates which are identified as primary. All other lines denote candidates identified as resulting from weak decays of heavier particles, separated by the identity of the mother.

beams; secondary, from the weak decays of some heavier particle; or from the interactions of other particles with the detector material. Those candidates identified as being secondary also have associated flags identifying the mothers which created them.

Counting the identified candidates in the MC data suggests that around 25% of all $\Lambda$ and $\bar{\Lambda}$ candidates are from feeddown procedures, and that, of those, around 96% come from the decays of charged or neutral $\Xi$'s. As such, the procedure detailed here shall only take into consideration the feeddown contribution as a result of the decays of $\Xi^{\pm}$ or $\Xi^{0}$.

From simulated data, it was shown that there was no meaningful difference in the distributions of topological variables between primary and secondary $\Lambda$ candidates. This demonstrated that there was no method by which secondary $\Lambda$'s could be identified at the candidate selection level. As such, the feeddown contribution was calculated after the creation of the initial spectra, by using Monte Carlo data to estimate the fraction of secondary candidates in the whole data set.

The feeddown contribution to the final $\Lambda$ spectra could not be taken from Monte Carlo data alone, as the $\Xi$-to-$\Lambda$ ratio and $p_{\mathrm{T}}$ spectra differed to those seen in the real data. Therefore, simulated data was used in order to find the probability that a generated $\Xi$ of a given $p_{\mathrm{T}}$ created a reconstructed $\Lambda$ of a particular $p_{\mathrm{T}}$. These probabilities were then scaled using measured $\Xi$ spectra, in order to calculate the expected feeddown contribution to be removed.

The particular method used for this analysis utilised a *feeddown matrix* (FDM), as shown in figure 4.9, separated into bins identifying the $p_{\mathrm{T}}$ of the $\Lambda$ candidate and of its mother. The content for each bin in the FDM was calculated from MC data, by

$$FDM_{ij} = \frac{N_{recon}(\Lambda_{2^o,i} \mid \Xi_j)}{N_{gen}(\Xi_j)} \quad . \tag{4.3}$$

Equation 4.3 expresses the content of the $[i,\, j]$th bin of the feeddown matrix. The numerator, $N_{recon}(\Lambda_{2^o,i}|\Xi_j)$, is the number of reconstructed secondary $\Lambda$ candidates in the $i$th $\Lambda$ $p_{\mathrm{T}}$ bin, who have identified $\Xi$ mothers with a reconstructed $p_{\rm T}$ in the $j$th $\Xi$ $p_{\rm T}$ bin. This is divided by $N_{gen}(\Xi_j)$, which is the number of truth level $\Xi$ candidates with a generated transverse momentum in $\Xi$ $p_{\rm T}$ bin $j$.

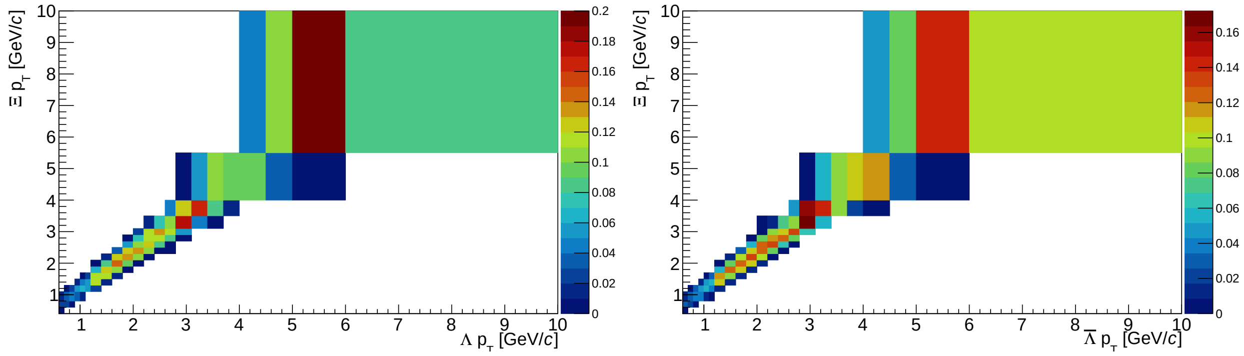

(a) $\Lambda$ (b) $\bar{\Lambda}$

Figure 4.9: Feeddown matrices calculated for the $\Lambda$, left, and $\bar{\Lambda}$, right, analysis.

The feeddown matrices created by this process are effectively probability distributions, detailing the likelihood that a $\Xi$ in $p_{\rm T}$ bin $j$ will decay into a $\Lambda$ in $p_{\rm T}$ bin $i$, and that the decay $\Lambda$ will be detected and reconstructed by the ALICE detector. The FDM can then be used to estimate the feeddown contribution to the real spectra. In an ideal regime, one where the probability of $\Xi$ to $\Lambda$ conversion, $P(\Xi \rightarrow \Lambda)$, is measured continuously, the feeddown $\Lambda$ spectra would be expressed as

$$N(\Lambda_{FD}) = \int \mathrm{Pr}(\Xi \rightarrow \Lambda)(\Xi p_{\rm T}) \times N(\Xi)(\Xi p_{\rm T})\, d\Xi p_{\rm T} \quad , \tag{4.4}$$

where $\mathrm{Pr}(\Xi \rightarrow \Lambda)$ is the probability of a $\Xi$ decaying into a reconstructed $\Lambda$, and the integral is performed over all $\Xi$ $p_{\rm T}$. However, as the conversion probability, contained within the feeddown matrix, and measured spectra are discrete, this turns equation 4.4 into

$$\frac{dN(\Lambda_{i,FD})}{dy} = \sum_j FDM_{ij} \frac{dN(\Xi_{j,meas})}{dy} \quad . \tag{4.5}$$

The values for $dN(\Xi_{j,meas})/dy$ were taken from fully corrected measured $\Xi^{\pm}$ spectra, presented at the Strangeness in Quark Matter [110] and International Nuclear Physics Conferences [111] in 2019. For those bins which overlapped directly with the measured $\Xi$ spectra, the spectral content was used - multiplied by the width of the respective $p_{\mathrm{T}}$ bin, as the spectra contain values for $d^2N/dydp_T$. For those feeddown matrix bins which extend past the contents of the measured spectra, a fit was used to calculate what the content should be at that point. These fits were Lévy-Tsallis functions, which shall be discussed in more detail in section 5.1.1.

Once all rows in the feeddown matrices had been multiplied by their respective real $\Xi$ measurements, all columns were summed in order to create the final feeddown spectra. These spectra were created separately for each multiplicity bin used in the analysis; all using the same feeddown matrix, made using multiplicity-integrated Monte Carlo data. This choice was made in order to maximise the number of candidates used in the creation of the matrix, and minimise the likelihood that low statistics would result in an empty bin that would otherwise have been filled. The final feeddown spectra were then subtracted from the raw real $\Lambda$ spectra, prior to the application of efficiency corrections, in order to create the dedicated prompt spectra.

It should be noted that the feeddown $\Lambda$ contribution comes, not only from the decays of charged $\Xi$'s, for which there are measured results, but also from $\Xi^0$ decays. The $\Xi^0$, which decays to $\Lambda\pi^0$ with a branching fraction of 99.9% [112], has no measured yields in the ALICE detector. As such, an assumption has to be made about the production of $\Xi^0$ relative to charged $\Xi$'s: that the yields of $\Xi^0$ and $\Xi^{\pm}$ are equal.

In order to take the contribution from neutral $\Xi$'s into account, two methods can be used. One method creates the feedown matrices using only reconstructed candidates whose mother is a charged $\Xi$, then doubling the final feeddown spectra. This method, for the purposes of this thesis, shall be referred to as the *double charged* method. The other method, used by default in the analyses reported here, fills the feeddown matrix with $\Lambda$ candidates whose mother is *either* a charged or neutral $\Xi$, before multiplication by the measured $\Xi^{\pm}$ spectra. This method, which makes the assumption that the $p_{\mathrm{T}}$ spectra of $\Xi^0$ matches that of $\Xi^{\pm}$, is referred to here as the *inclusive mother* method.

The final feeddown spectra are shown in figure 4.10, and the ratio of each spectrum to the raw spectrum calculated from real data is shown in figure 4.11. The results presented in figure 4.11 shall henceforth be referred to as the calculated *feeddown fraction*.

As can be seen from figure 4.11, the feeddown fractions calculated for $\Lambda$ candidates and those calculated for $\bar{\Lambda}$ candidates do not differ significantly, both species displaying a feeddown fraction of the order of 20 %. It is also evident that the fraction of the final spectra which is covered by feeddown increases as a function of final state multiplicity, particularly at low $p_{\mathrm{T}}$ (below 1.5 GeV/$c$).

Another proposed source of $\Lambda$ feeddown is the electromagnetic decays of $\Sigma^0$ baryons, with the process $\Sigma^0 \rightarrow \Lambda\gamma$ having a branching fraction of almost 100% [113]. Measurements made by the STAR collaboration [114] support theoretical predictions that the $\Sigma^0/\Lambda$ ratio is around 1/3. Within ALICE, the combination of detector restrictions and extremely low lifetime of the $\Sigma^0$, $(7.4 \pm 0.7) \times 10^{-20}$ s [113], results in any $\Lambda$ candidates produced in this way being indistinguishable from primary $\Lambda$s. As such, and because the quark content of the $\Sigma^0$ and $\Lambda$ are identical, this potential source of feeddown is not taken into account.

## 4.6 Self-consistency Test

Prior to the calculation of final systematic uncertainties, a self-consistency test was performed in order to justify the results that this analysis provided. For this test, the MC sample was divided into two separate files, denoted in this report as A and B; one was then used in place of the real data, and the other was used to calculate the efficiency corrections. The self-consistency test was first performed on $\mathrm{K}^0_{\mathrm{S}}$ candidates, in order to avoid the complication that would arise from the feeddown removal process.

Spectra were calculated from the ‘real data’ file, in a lesser range than covered by the

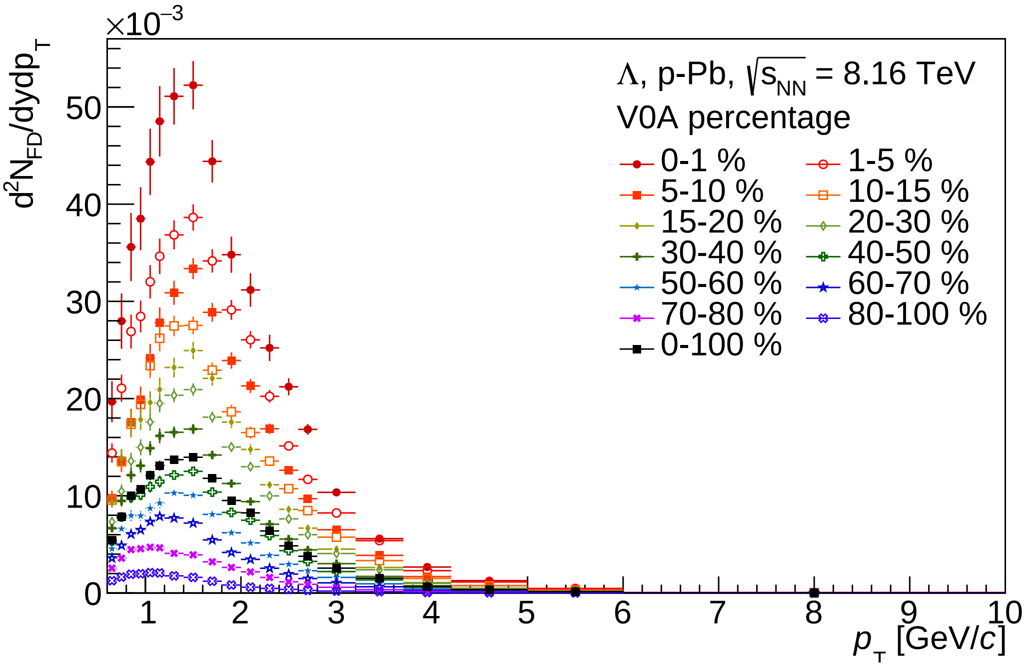

(a) $\Lambda$

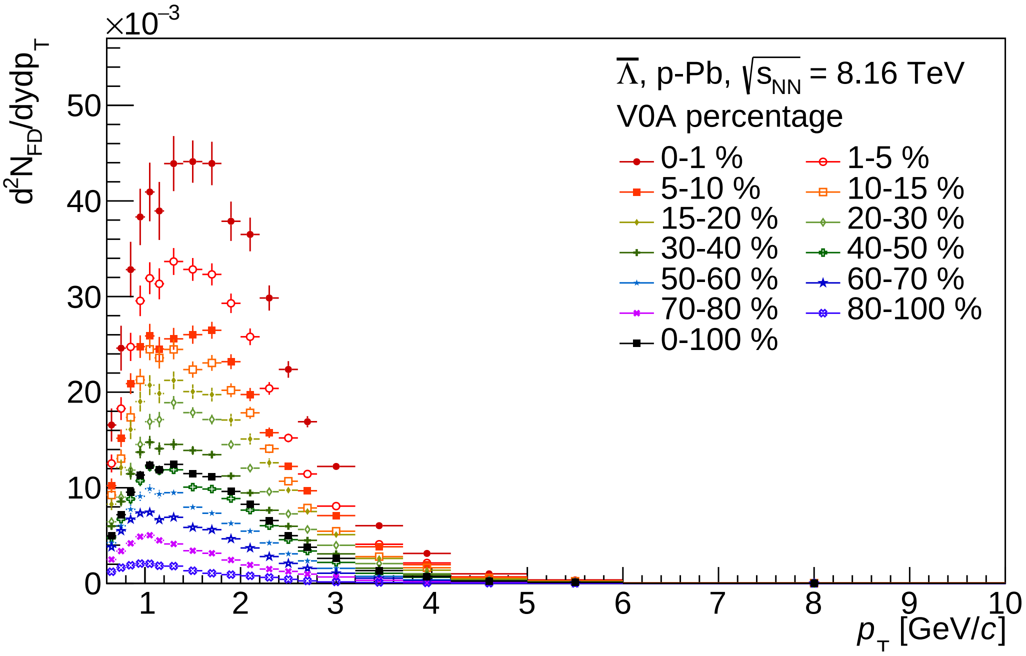

(b) $\bar{\Lambda}$

Figure 4.10: Feeddown spectra for all multiplicity bins, shown with the multiplicity-integrated feeddown spectrum.

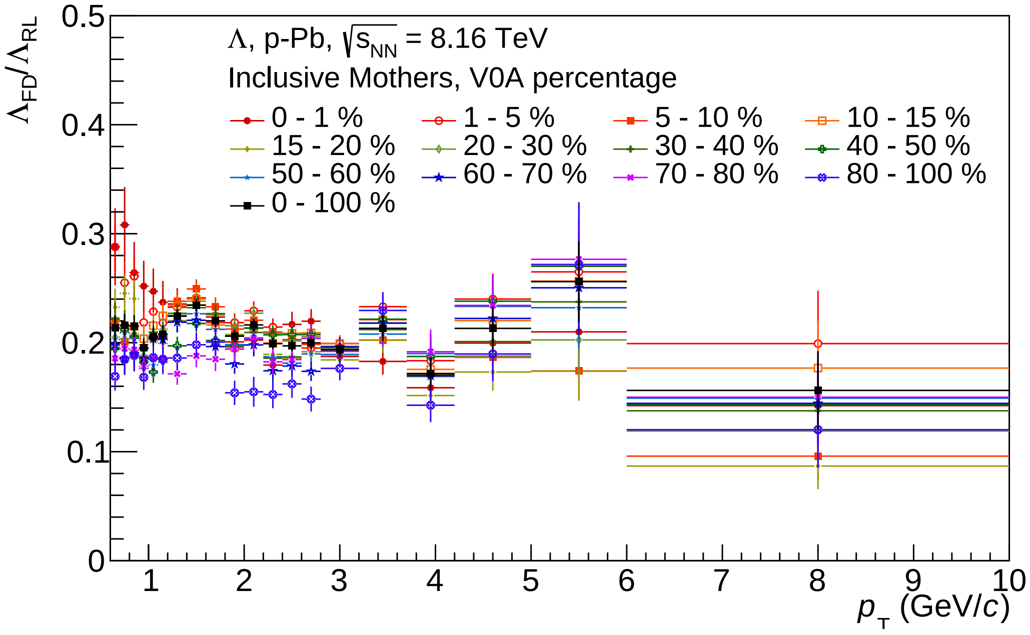

(a) $\Lambda$

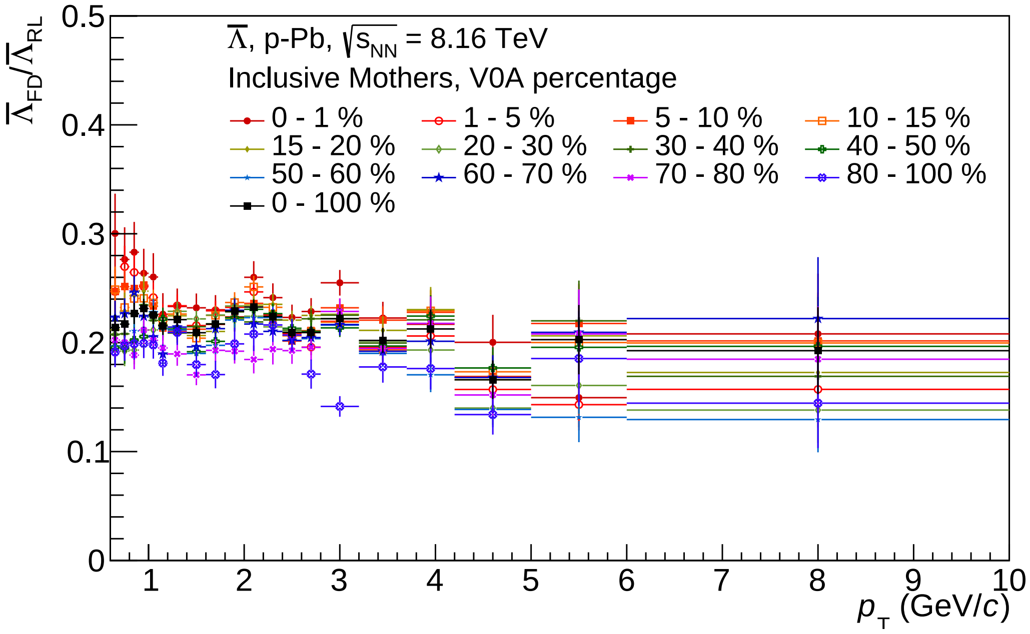

(b) $\bar{\Lambda}$

Figure 4.11: Ratio of feeddown spectra to raw real spectra, shown for all multiplicity bins, including multiplicity-integrated data.

real data used in the primary analysis. This was carried out due to the low statistics present at high $p_{\mathrm{T}}$ in the individual files, an issue that the full combined Monte Carlo data do not encounter. These spectra were then fitted, and the yields extracted, as performed for the primary analysis.

In order to judge the reliability of these reconstructed yields, references are required from the generated candidates. To create these reference yields, the distributions of generated candidates were separated into the same multiplicity bins as used for the analysis, and the number of entries in each bin were summed from 0 GeV/$c$ up to the maximum $p_{\mathrm{T}}$ used for the reconstructed spectra. The ratios of reconstructed yields to those from generated $\mathrm{K}^0_{\mathrm{S}}$ candidates are shown in figure 4.12.

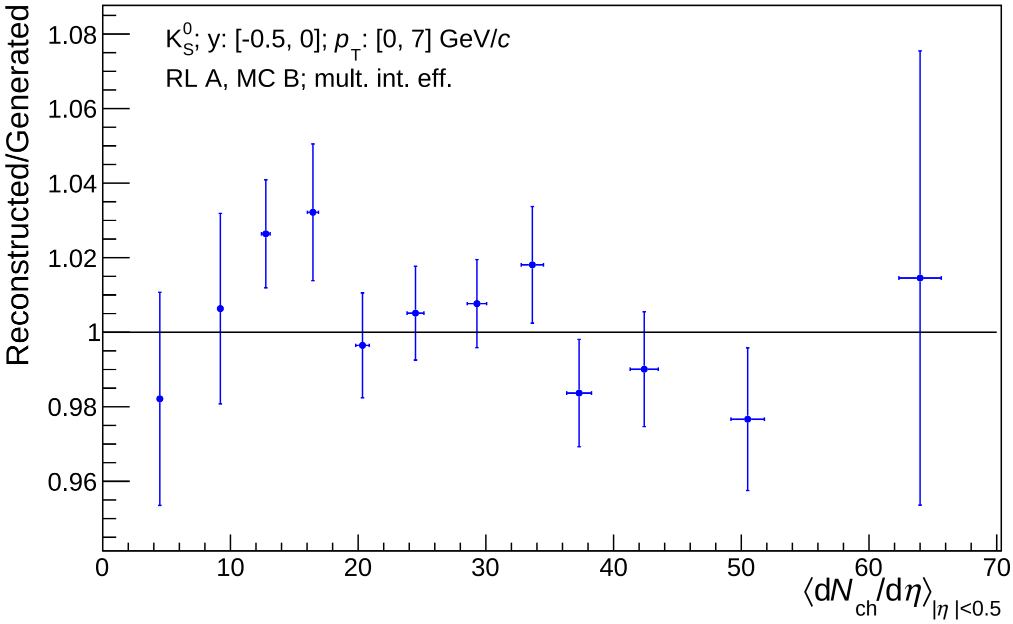

Figure 4.12: Ratio between file A generated yields, and file A reconstructed yields, using file B for efficiency correction.

As can be seen from figure 4.12, the reconstructed and generated yields can be considered to be consistent once statistical errors are taken into account. Despite this, the yields do not agree as well as would initially be expected, and so this deviation was investigated. Two sources of systematic error were considered as potential candidates for the discrepancy in yields: the fitting and extrapolation procedure used to extract yields from the $p_\mathrm{T}$ spectra, and the choice to use multiplicity-integrated efficiencies across all multiplicity bins.

The uncertainty due to the use of the fitting procedure was calculated by rebinning the generated $p_\mathrm{T}$ spectra to match the reconstructed spectra, and fitting them to extract yields. Figure 4.13 shows the ratios between the yields calculated from fitting the generated spectra, and those taken from bin counting applied to the same spectra. These ratios demonstrate that the fitted yields are lower than the raw counted yields at mid- to high-multiplicity, due to the fitting function underestimating the yield in the extrapolated region. As such, an error of 1 % was applied in order to account for the use of the fitting procedure.

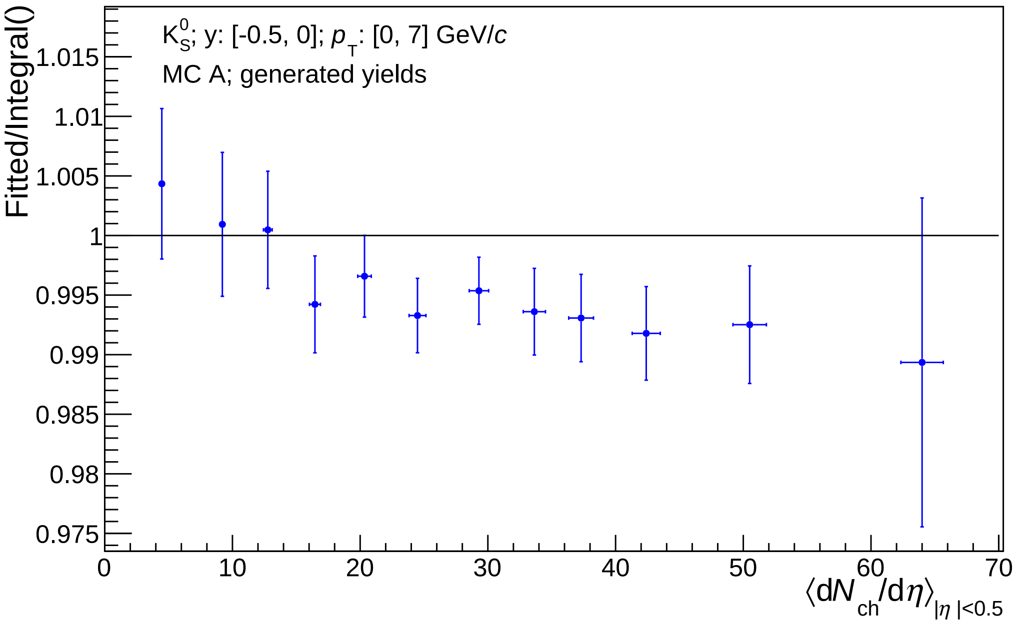

Figure 4.13: Ratio between file A generated yields, calculated via bin counting and the fitting procedure.

In order to evaluate the error due to the use of multiplicity-integrated efficiencies, the self-consistency test was run twice, using the same file for both efficiencies and candidate selection. One run was performed with the same procedure as for the primary analysis; using multiplicity-integrated efficiencies. The second used efficiencies calculated separately for each multiplicity bin. Figure 4.14 shows the ratio between reconstructed and generated

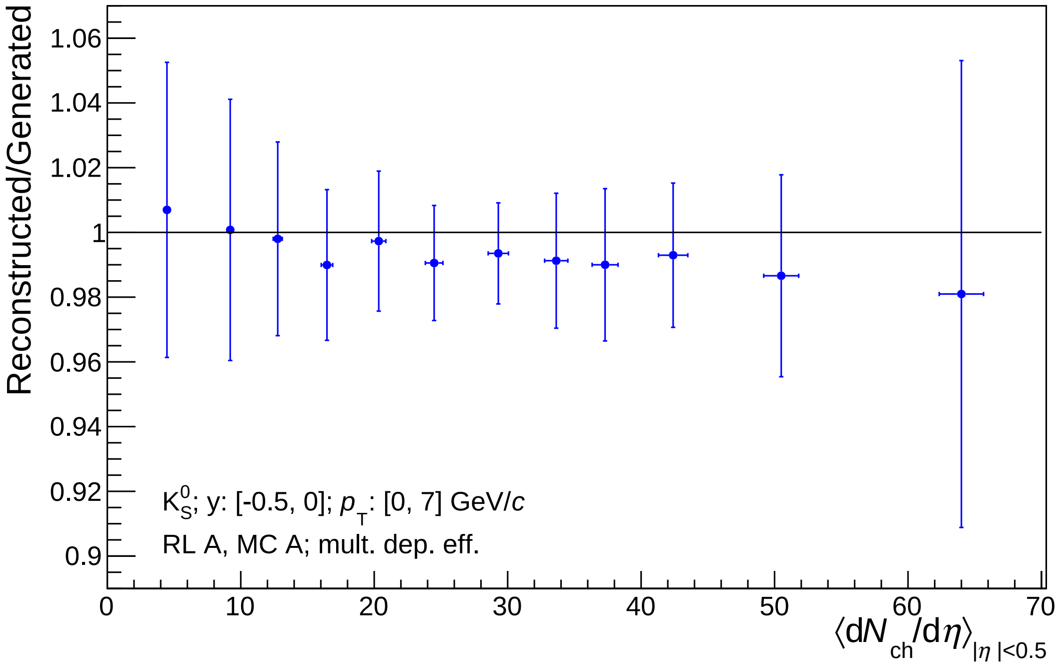

(a) Multiplicity-dependent efficiencies

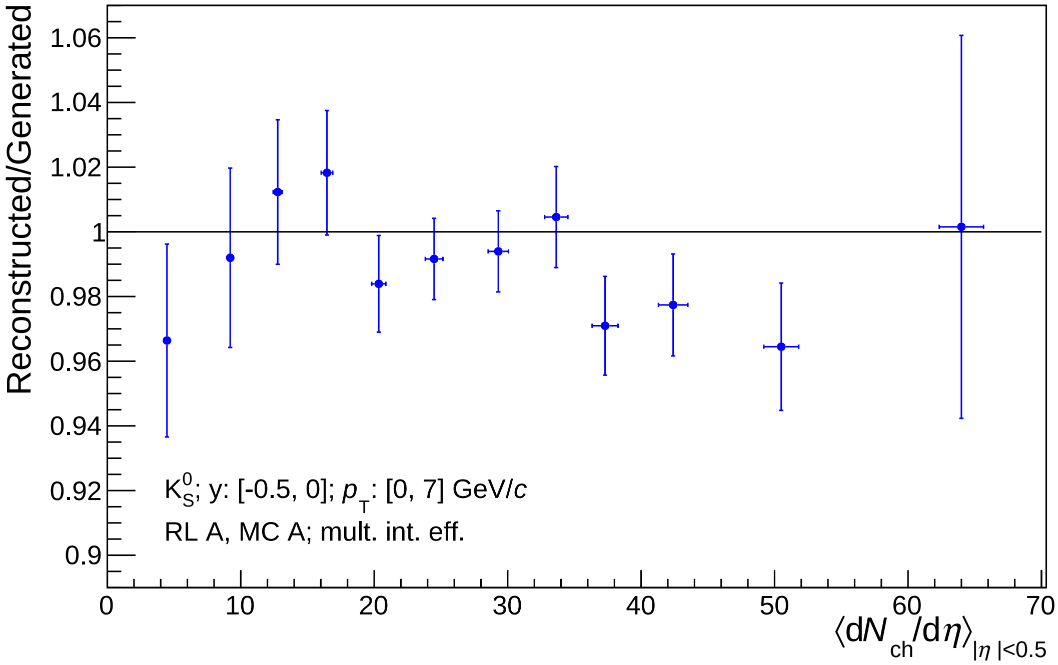

(b) Multiplicity-integrated efficiencies

Figure 4.14: Ratio of reconstructed $\mathrm{K^0_S}$ candidates to the truth level yield, using the same file for both candidate selection and efficiency correction.

yields for both cases discussed. Another test that may be of interest is to perform the same comparison, but using different files for the efficiencies and candidate selection. The plots from this are shown in appendix B; they suggest that if the different candidates are used to create and correct the $p_T$ spectra, using the multiplicity-integrated efficiencies provides more accurate results.

Once the 1 % error due to the fitting procedure is taken into account, the reconstructed yields calculated using multiplicity-differentiated efficiencies can be considered to be consistent. Therefore, the observed discrepancy between reconstructed and generated yields that can be seen in figure 4.14b is due to the use of multiplicity-integrated efficiencies. To account for this, a 2 % error was applied, which was then added in quadrature with the uncertainty due to the use of the fitting procedure. Figure 4.15 shows these uncertainties applied to figure 4.12. As can be seen, the ratios of reconstructed-to-generated yields now lie within errors of unity, and so can be considered to be consistent.

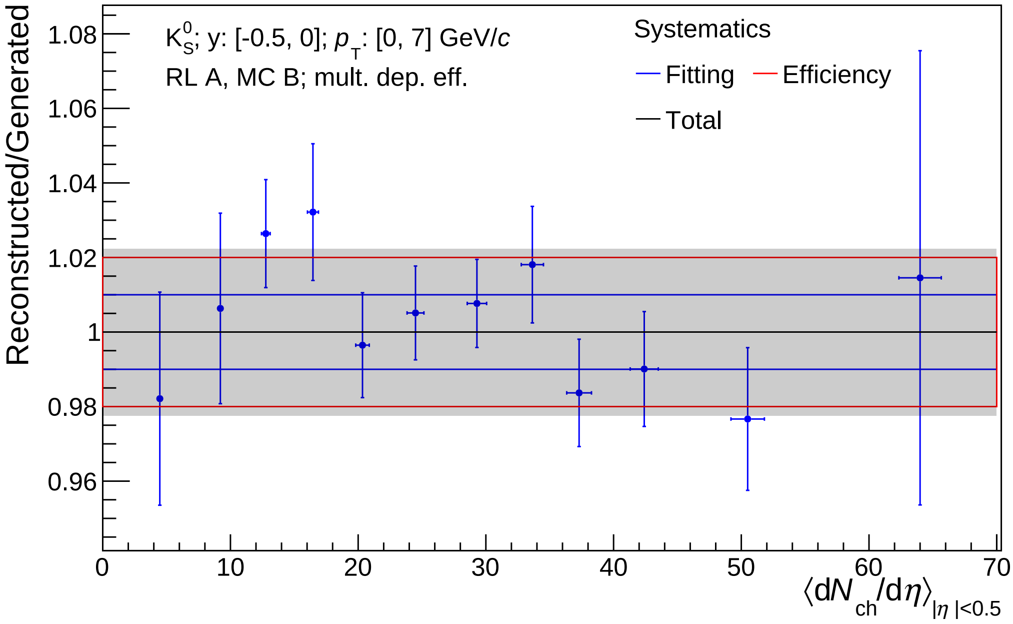

Figure 4.15: Ratio between self-consistency test yields of reconstructed and raw generated $K^0_S$ candidates, with systematic errors shown.

Following the completion of this, the self-consistency test was performed again, looking at $\Lambda$ candidates. Again, to avoid the complication of feeddown removal, only known prompt candidates were initially used. Due to the $\Lambda$ spectra starting at a higher $p_{\mathrm{T}}$ than the $\mathrm{K}^0_{\mathrm{S}}$ spectra, the uncertainty due to the fitting procedure has a greater impact on the reconstructed yields. As such, a larger error, 3 %, was assigned to account for the fitting process. The uncertainty due to the use of multiplicity-integrated efficiencies was also larger, at 4.5 %. When the total error is taken into account, the reconstructed $\Lambda$ yields from only known primary candidates can be considered to be consistent with the generated yields, as shown by figure 4.16.

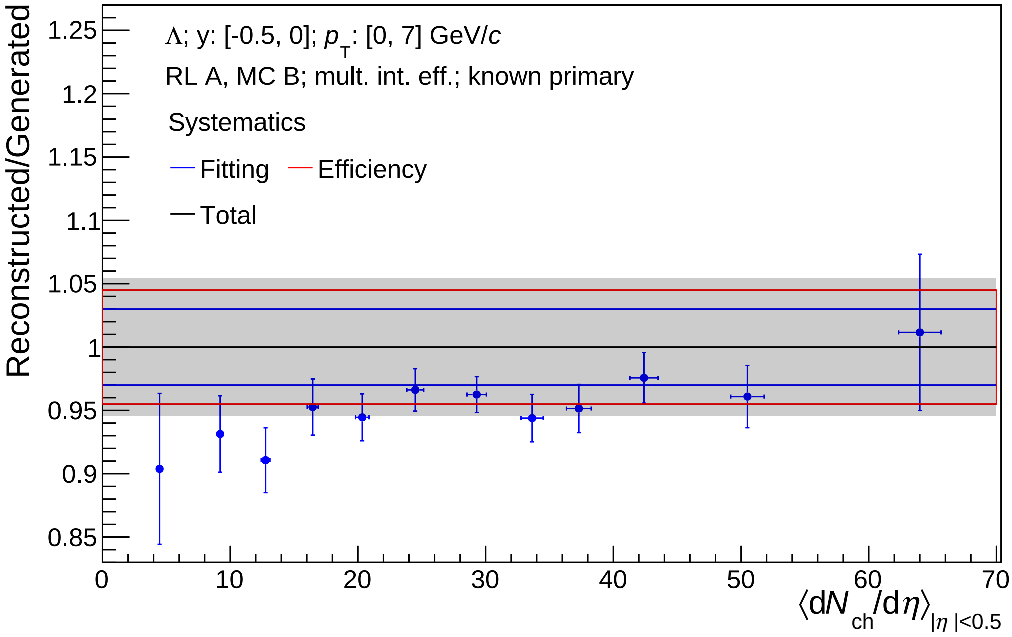

Figure 4.16: Ratio between self-consistency test yields of known primary reconstructed $\Lambda$ candidates and raw generated candidates.

After the completion of the self-consistency test using only known primaries, it was repeated, using all reconstructed $\Lambda$ candidates. As such, a feeddown removal procedure needed to be applied, as described in section 4.5.1. As the self-consistency test uses only Monte Carlo data, the $\Xi^-$ spectra used to generate the feed down spectra were extracted from the distributions of generated $\Xi$ candidates. Figure 4.17 shows the ratio between generated and feeddown corrected reconstructed $\Lambda$ yields. With the application of the systematic errors calculated using the known primary candidates, the feeddown corrected yields can be considered to be in agreement with the generated yields.

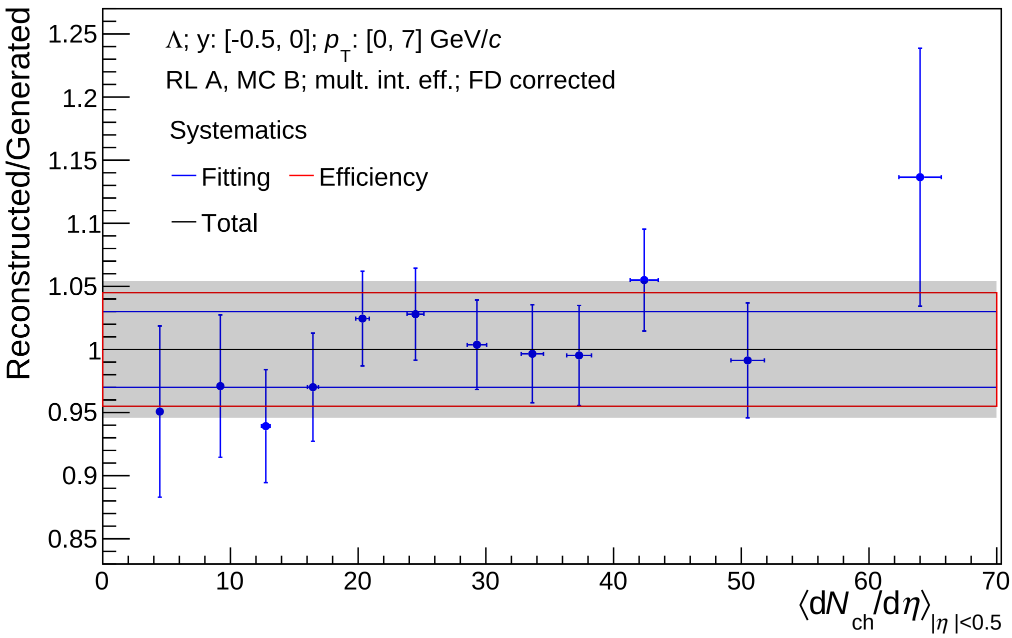

Figure 4.17: Ratio between self-consistency test yields of all reconstructed $\Lambda$ candidates, corrected for the feeddown contribution, and raw generated candidates.

## 4.7 Systematic Errors

Should the analysis be repeated independently, the chosen topological cuts will differ from those used here depending on the criteria applied to select them. As the Monte Carlo does not perfectly describe the real data, these alternate cuts will cause the corrected spectra to differ slightly from the ones calculated here. This constitutes a source of systematic error on these results. As such, it is useful to investigate the effects of varying the candidate selection criteria, and evaluate the systematic error that this imposes upon the spectra.

In order to study the effects of varying the cuts, different values for each needed to be chosen. These extra values are referred to by one of four labels, as described below:

- **very loose** cuts were placed according to the selections used to filter the AODs, as detailed in table 4.3.

- **loose** cuts were placed to at the point of half the signal loss of the default cut, for variables for which this was possible. These should reflect the loosest reasonable cuts that could be used.

- **tight** cuts were placed at the point of 5% signal loss. These should reflect the tightest reasonable cuts that could be used.

- **very tight** cuts were placed at the point of 10% signal loss. These reflect very extreme circumstances in which the analysis could be performed.

After the choice of these systematic cut values, any for which the real data and Monte Carlo signal losses disagreed by more that 3% were either adjusted or removed. The justification for this is that the systematic cuts should theoretically be ones which could have been used for the main analyses. If a cut showed large real data to MC discrepancy, it was not used for the default analysis, so the same approach was taken here.

The final values used for the study of systematic uncertainties are reported in tables 4.5, for the $\mathrm{K^0_S}$ analysis, and 4.6, for the $\Lambda$ and $\bar{\Lambda}$ analysis. Figure 4.18 shows significance and fraction of signal remaining against cut value, as in figure 4.6, but with marks denoting the final default and systematic cut choices. Figure 4.18 shows the relevant plots for only one of the cuts investigated; the full set are located in appendix C.

Following the selection of these systematic cuts, the analysis was repeated multiple times. For each of these repetitions, one of the default cut values was replaced with a systematic cut. Following this process, the multiplicity-integrated spectra created for a single variable were compared, as shown in figure 4.19. The final systematic uncertainty from a single source, for a given $p_{\mathrm{T}}$ bin was then compared to the corresponding Roger Barlow sigma [115].

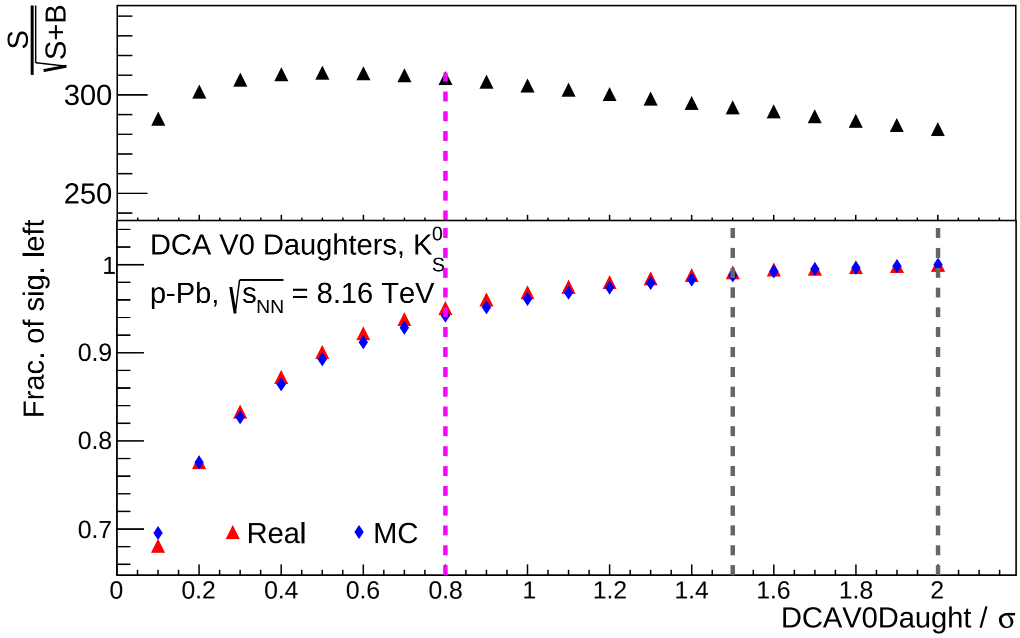

(a) $K^0_S$

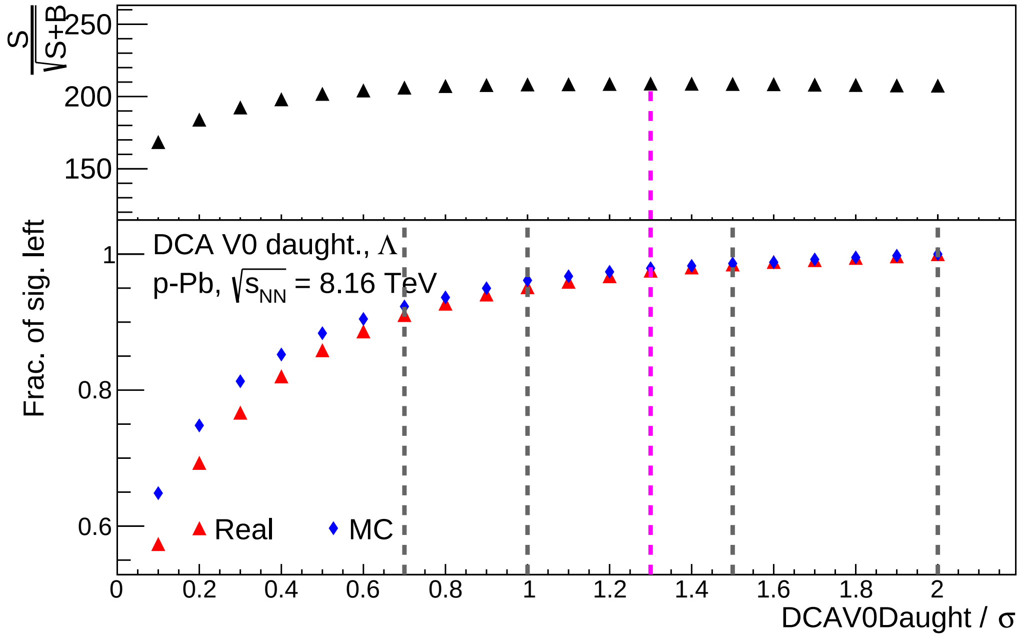

(b) Λ

Figure 4.18: Significance and fraction of signal remaining for the DCA $V^0$ daughters cut. The vertical lines denote cut choices: magenta, default; and grey, used for systematics determination.

Table 4.5: Values of the cuts used for the systematic cut study of the $\mathrm{K^0_S}$ analysis. The labels for the cut types are shorthand equivalents of the names in table 4.4.

| Cut type | Very Loose | Loose | Tight | Very Tight |
|---|---|---|---|---|
| $R_{\mathrm{V}^0}$ (cm) | | | $> 1.4$ | $> 2.7$ |
| $\cos\theta_{PA}$ | $> 0.95$ | $> 0.975$ | $> 0.998$ | $> 0.999$ |
| DCA $\mathrm{V}^0$ daught. ($\sigma$) | $< 2.0$ | $< 1.5$ | | |
| DCA pos. to PV (cm) | $> 0.02$ | $> 0.04$ | $> 0.12$ | $> 0.22$ |
| DCA neg. to PV (cm) | $> 0.02$ | $> 0.04$ | $> 0.12$ | $> 0.22$ |
| $c\tau$ (cm) | | $< 20$ | $< 10$ | $< 8$ |
| | | | | |
| Least TPC clusters | | | $\geq 80$ | $\geq 90$ |
| TPC PID ($\sigma$) | | ± 5 | ± 3 | |
| Sig. ext. ($\sigma$) | ± 6 | ± 5 | ± 3 | |
| Comp. spec. rej. (MeV/$c^2$) | No cut | | | |

Table 4.6: Values of the cuts used for the systematic cut study of the $\Lambda$ ($\bar{\Lambda}$) analysis. The labels for the cut types are shorthand equivalents of the names in table 4.4.

| Cut type | Very Loose | Loose | Tight | Very Tight |
|---|---|---|---|---|
| $R_{\mathrm{V}^0}$ (cm) | | | $> 1.9$ | $> 2.8$ |
| $\cos\theta_{PA}$ | $> 0.95$ | $> 0.97$ | | |
| DCA $\mathrm{V}^0$ daught. ($\sigma$) | $< 2.0$ | $< 1.5$ | $< 1.0$ | $< 0.7$ |
| DCA pos. to PV (cm) | $> 0.02$ | | $> 0.05(0.17)$ | $> 0.08(0.25)$ |
| DCA neg. to PV (cm) | $> 0.02$ | | $> 0.17(0.05)$ | $> 0.25(0.08)$ |
| $c\tau$ (cm) | $< 100$ | $< 60$ | | |
| | | | | |
| Least TPC clusters | | | $\geq 80$ | $\geq 90$ |
| TPC PID ($\sigma$) | | ± 5 | ± 3 | |
| Sig. ext. ($\sigma$) | ± 6 | ± 5 | ± 3 | |
| Comp. spec. rej. (MeV/$c^2$) | No cut | | ± 5 | |

Roger Barlow's sigma is defined by

$$\sigma_\Delta = \sqrt{\sigma_1^2 + \sigma_2^2} \quad ,$$

where $\Delta = a_1 - a_2$ is the difference between two independent measurements, $a_1$ and $a_2$, and $\sigma_1$ and $\sigma_2$ are the uncertainties on those measurements. Physically, $\sigma_\Delta$ represents the

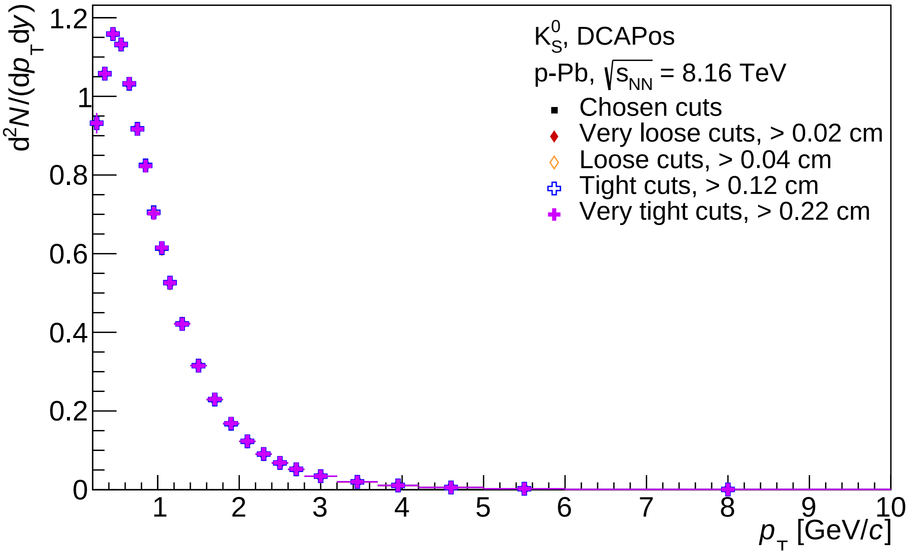

(a) Raw spectra, overlaid.

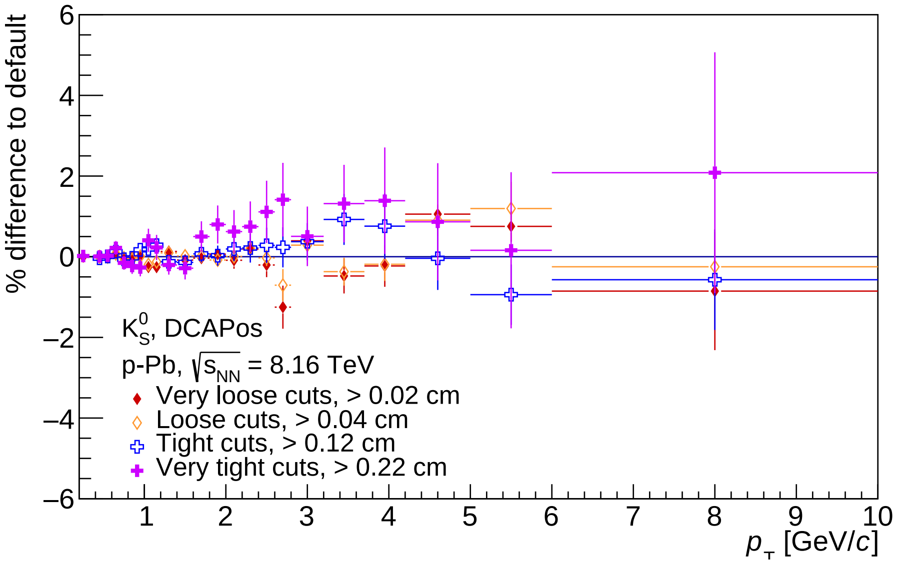

(b) Percentage difference to default cuts.

Figure 4.19: Systematic uncertainty determination, considering only the DCA of the positive daughter to the PV, for the $K^0_S$ analysis. Errors shown are Roger Barlow's sigma [115].

acceptable deviation in $\Delta$ due to statistical fluctuations on $a_1$ and $a_2$; here $a_1$ is the spectral content measured using the default cuts and $a_2$ is the spectral content measured with the systematic cuts. If the systematic difference, as shown in figure 4.19b, was within one $\sigma_\Delta$ of unity, then that difference can be reliably disregarded and considered to be due to statistical fluctuations.

The final bin-by-bin systematic was taken to be half the maximum spectral deviation, if that deviation was at least one $\sigma_{\Delta}$ from unity. This process was repeated for all selection criteria considered for the systematic study. For most, the final error was the $p_{\mathrm{T}}$-dependent uncertainty generated by the comparisons of spectra. The exception to this is for the signal extraction window in the $\Lambda$ and $\bar{\Lambda}$ analyses. For this variable, a constant uncertainty of 1.5% was applied across all $p_{\mathrm{T}}$ bins, as the bin-by-bin fluctuations were not considered to be indicative of a $p_{\mathrm{T}}$-dependent error.

In addition to the sources of error discussed above, a further systematic was required to account for uncertainties in the material budget considered in the Monte Carlo data. This extra uncertainty was evaluated using Monte Carlo simulations with varying material budgets; five runs were used, using ±4.5%, ±10% and 0%, relative to the default used for the corrections in this analysis [116]. The spectra from the four varied budget runs were then compared to the 'no-change' run; the final material budget error was taken to be half the maximum deviation from one of the different ratios calculated. The histograms used for this process were fitted with an exponential decay; these functions, as shown in figure 4.20, were then taken as the material budget uncertainty for this analysis.

For the $\Lambda$ and $\bar{\Lambda}$ analysis, a further source of error was considered: that caused by the choice of feeddown removal method. In order to estimate this, the final multiplicity-integrated spectrum was calculated twice, once with each of the two different procedures outlined in section 4.5.1. The ratio of one to the other was then calculated in order to determine whether a $p_{\mathrm{T}}$-dependent cut was required or not. It was decided that the bin-by-bin fluctuations did not suggest the need for a $p_{\mathrm{T}}$-dependent cut, and so an uncertainty of 1% was applied across all $p_{\mathrm{T}}$ bins.

The cut-based uncertainties were then combined in quadrature, creating final errors from topological sources. These were then combined with the uncertainties calculated from

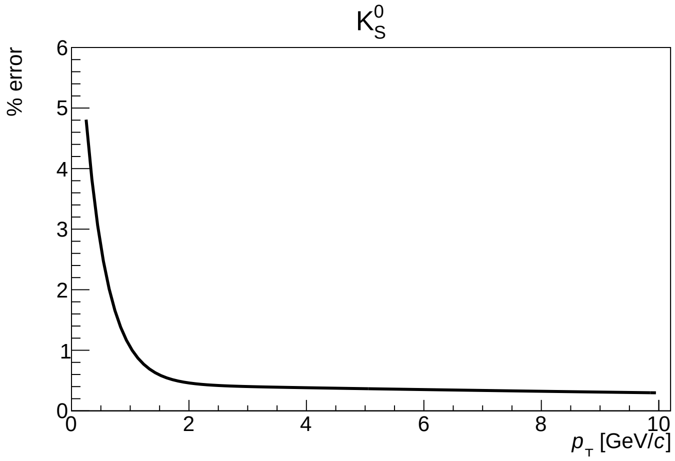

(a) $K^0_S$

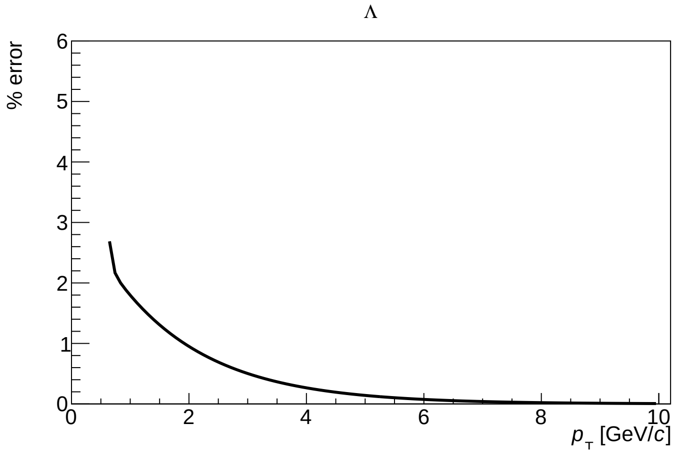

(b) $\Lambda$

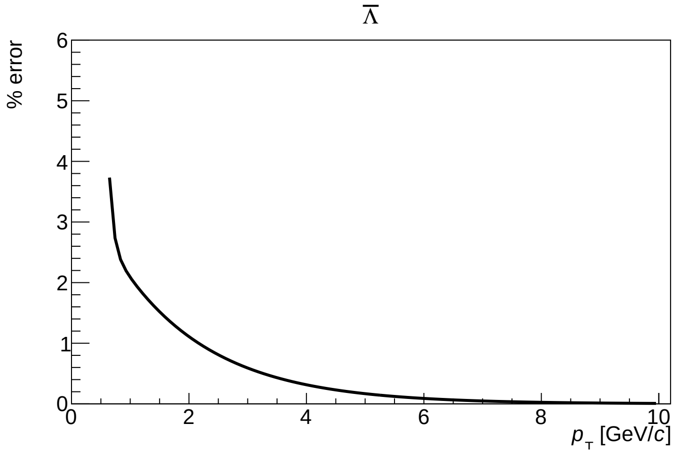

(c) $\bar{\Lambda}$

Figure 4.20: Material budget uncertainties, as a function of $p_T$, for the $K^0_S$, $\Lambda$ and $\bar{\Lambda}$ analysis [116].

the track quality cuts. Figures 4.21, 4.22 and 4.23 show the topological and total systematic uncertainties for the $K^0_S$, $\Lambda$ and $\bar{\Lambda}$ analyses, respectively. For all of the species considered, two sources of error are reliably important: the uncertainty stemming from the choices of topological cuts, and, particularly at low $p_T$, the material budget used in the simulated data.

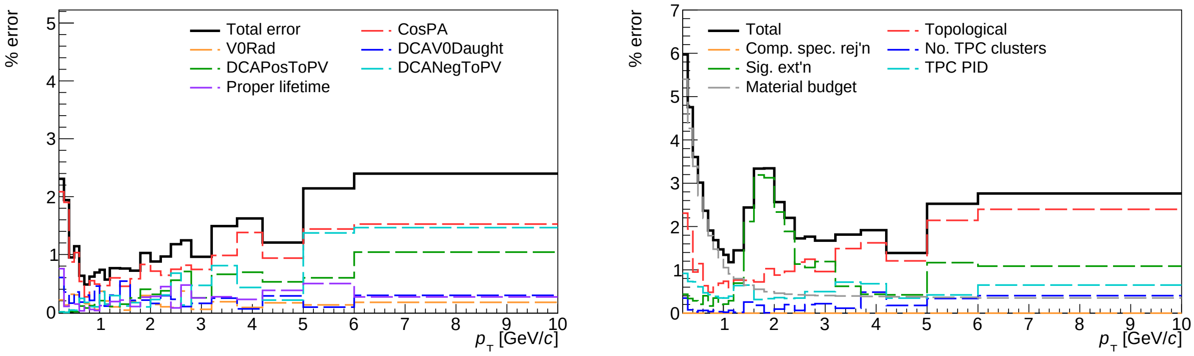

(a) Topological uncertainties.

(b) Total systematic.

Figure 4.21: Topological and total systematic uncertainties as a function of $p_T$, for the $K^0_S$ analysis.

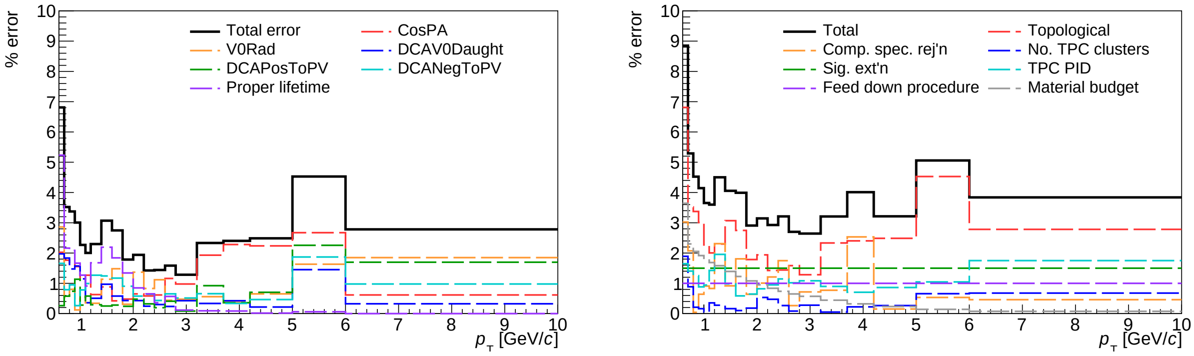

(a) Topological uncertainties.

(b) Total systematic.

Figure 4.22: Topological and total systematic uncertainties as a function of $p_T$, for the $\Lambda$ analysis.

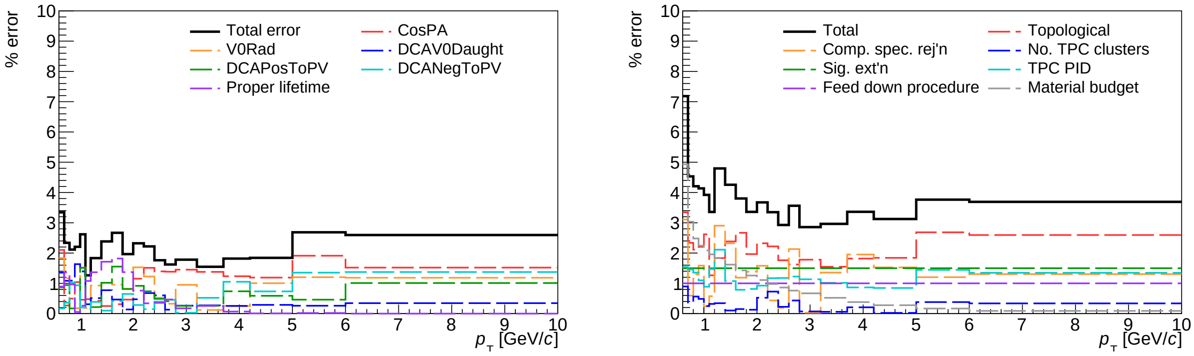

(a) Topological uncertainties.

(b) Total systematic.

Figure 4.23: Topological and total systematic uncertainties as a function of $p_{\rm T}$, for the $\bar{\Lambda}$ analysis.

# Chapter 5

# Results

The following chapter shall present the final corrected spectra calculated for $V^0$ species in p-Pb data at $\sqrt{s_{\mathrm{NN}}} = 8.16$ TeV, and then shall describe the process used to extract $p_{\mathrm{T}}$-integrated yields from them. These yields, along with a systematic uncertainty from the yield extraction procedure, shall then be shown. Finally, these results shall be given context using analyses of light non-strange hadrons, and comparing the values observed here to those from similar analyses in other collision systems and energies.

## 5.1 Transverse Momentum Spectra

Figure 5.1 shows the final, corrected transverse momentum spectra for the $\mathrm{K}^0_{\mathrm{S}}$ and combined $\Lambda$ and $\bar{\Lambda}$ analyses. A trend that is visible here is that the peaks of the spectra move towards higher values of $p_{\mathrm{T}}$ as the final state multiplicity increases. This hardening of the spectra is consistent with the existence of collective behaviour, as described by hydrodynamic models of the media created after the initial collisions [117].

The ratio between the $\Lambda$ and $\bar{\Lambda}$ corrected spectra are shown for three multiplicity bins in figure 5.2, which demonstrates that the $\Lambda$ and $\bar{\Lambda}$ spectra are consistent with each other, within statistical errors. As such, the results for these two particles are combined for the

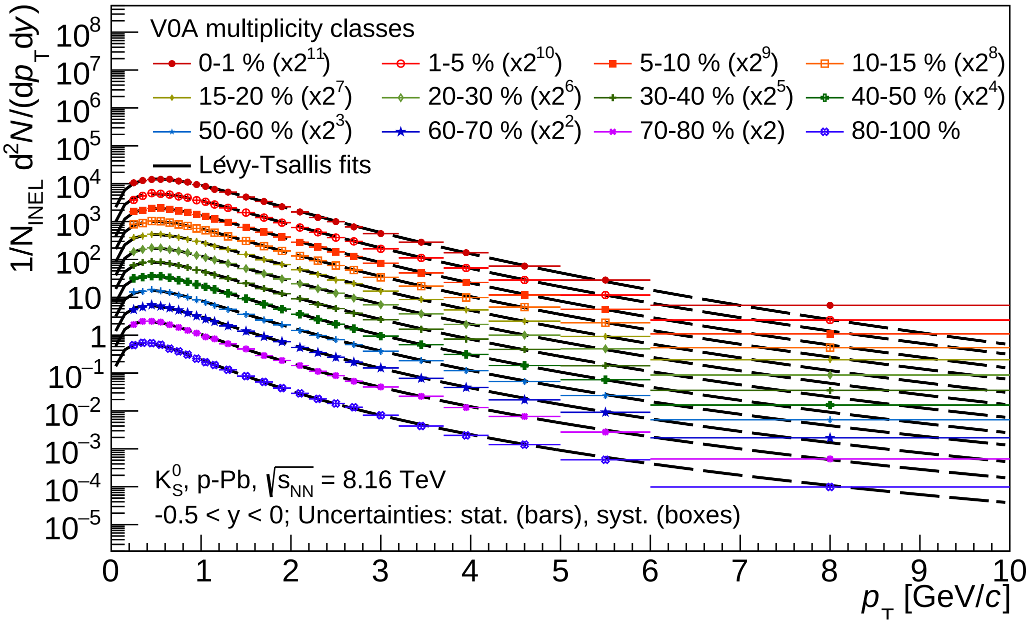

(a)

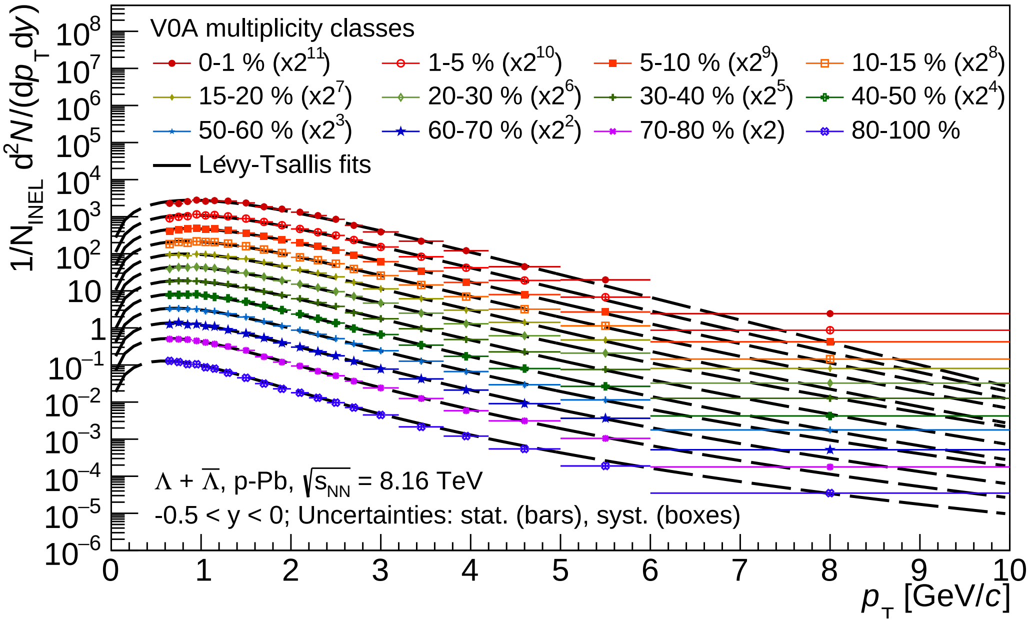

(b)

Figure 5.1: Full $p_{\mathrm{T}}$ spectra for the $\mathrm{K}^0_{\mathrm{S}}$ analysis, top, and $\Lambda + \bar{\Lambda}$ analysis, bottom. Shown with the dashed lines are the Lévy-Tsallis functions [118] fitted to the spectra.

purposes of presentation. Due to this, from this point on unless otherwise specified, the term '$\Lambda$ analysis' will refer to the combined results from both $\Lambda$ and $\bar{\Lambda}$.

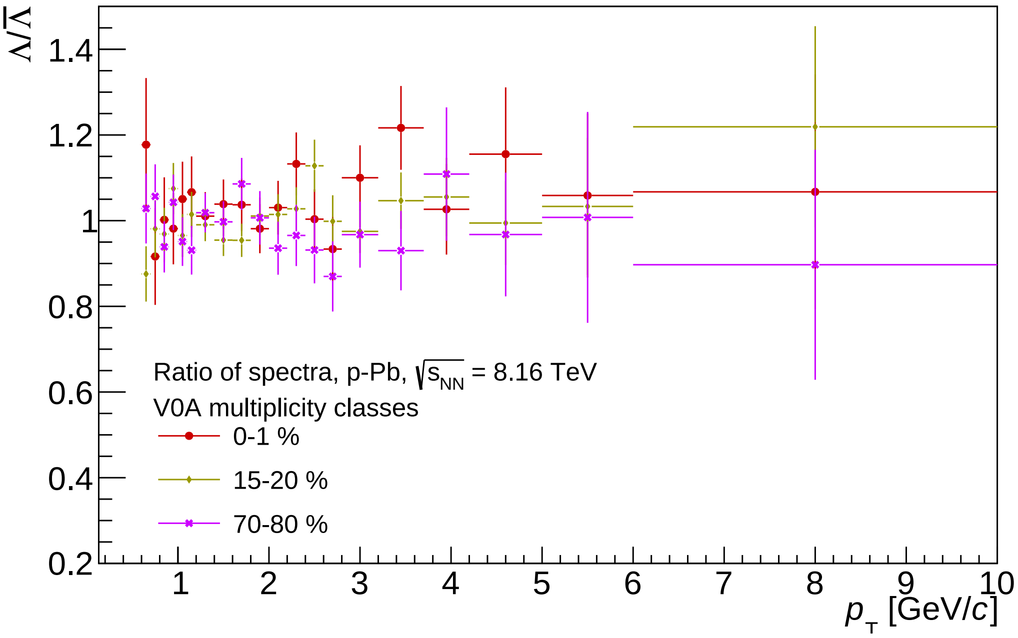

Figure 5.2: Ratio of $\Lambda$ to $\bar{\Lambda}$ corrected spectra, as a function of $p_T$, for low- mid- and high multiplicities. Only the propagation of statistical errors are shown.

As was described in section 4.3, and as is clearly visible in figure 5.1b, the measured $p_T$ spectra do not go down to 0 GeV/$c$. As such, in order to extract $p_T$-integrated yields, the spectra must be fitted, and used to calculate the 'unseen' contribution to the final yield.

### 5.1.1 Spectral fitting

For this analysis, the default fitting function used was the Lévy-Tsallis function [118]. At low momentum, the thermal physics which dominate the distribution of particles is described with exponential behaviour, with a power law tail used to model the hard processes which dominate at high momentum. The form of the Lévy-Tsallis function used for the fits in this analysis is thus

$$\frac{\mathrm{d}^2\mathrm{N}}{\mathrm{d}y\mathrm{d}p_\mathrm{T}} = \frac{(n-1)(n-2)}{nT_k[nT_k + m(n-2)]}\frac{\mathrm{dN}}{\mathrm{d}y}p_\mathrm{T}\left(1 + \frac{\sqrt{p_\mathrm{T}^2 + m^2} - m}{nT_k}\right)^{-n} , \qquad (5.1)$$

where $T_k$ is the kinetic freeze-out temperature, $n$ is a free parameter, and $\sqrt{p_\mathrm{T}^2 + m^2} \equiv m_\mathrm{T}$ is known as the *transverse mass*.

After the spectra are fitted with the function given in equation 5.1, the full $p_\mathrm{T}$-integrated yields can be calculated. For this, the fits are extrapolated from the region in which candidates are measured, down to 0 GeV/$c$. The final yield is given by the sum of all measured candidates in the $p_\mathrm{T}$ bins defined by the analysis, plus the integral of the fitting function, within the extrapolated region.

## 5.2 Multiplicity Dependence of Yields

The total calculated yields for the $\mathrm{K}^0_\mathrm{S}$ and $\Lambda$ analyses are displayed in tables 5.1 and 5.2. Also given are the mean charged particle density, $\mathrm{dN}_{ch}/\mathrm{d}\eta$ and the percentage of the final yield extracted from the fitting and extrapolation procedure. This extrapolation fraction ranges from 6 % to 10 % for the $\mathrm{K}^0_\mathrm{S}$ analysis, and from 17 % to over 30 % for the $\Lambda$ analysis. This demonstrates just how much of the predicted yields lie in the unobservable low momentum region, especially in analyses of heavier species.

Figure 5.3 shows the final calculated yields for all species considered, as a function of $\langle \mathrm{dN}_{ch}/\mathrm{d}\eta \rangle$. Both tables 5.1 and 5.2 and figure 5.3 demonstrate an increase in particle yields, as a function of final state multiplicity, as would be expected.

### 5.2.1 Uncertainties

The statistical uncertainties on the final yields are calculated within the fitting procedure. In order to evaluate these, the corrected spectra were varied 1000 times with bin contents

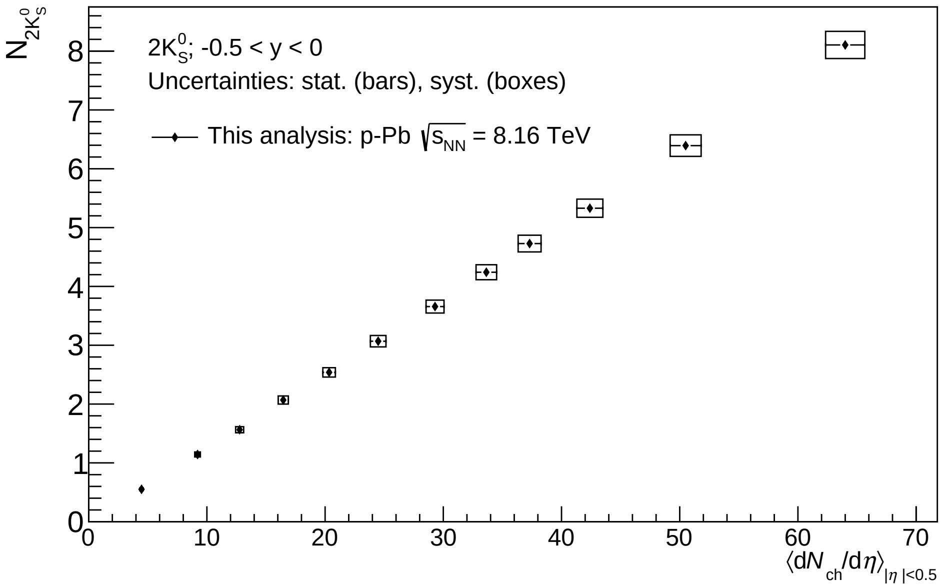

(a) $2K^0_S$

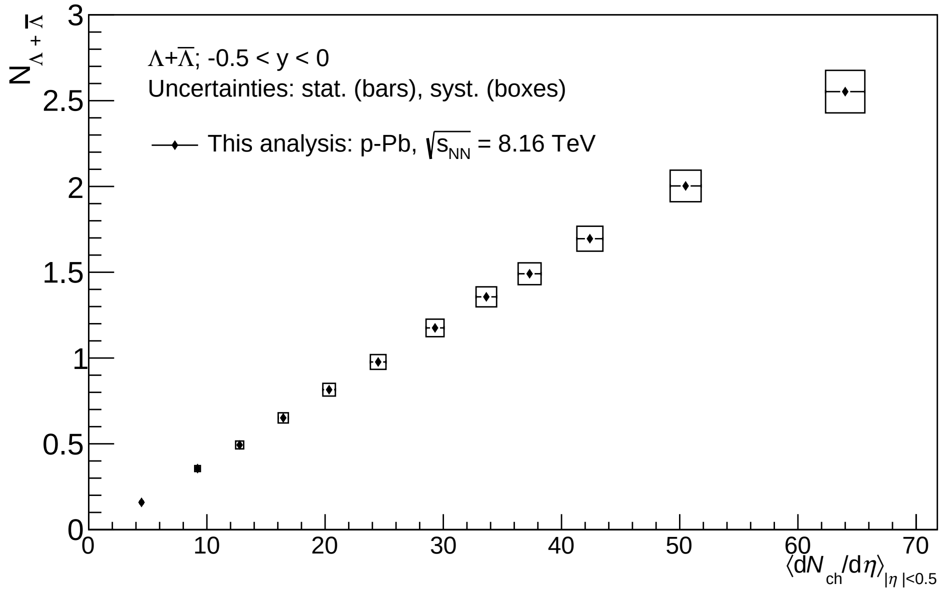

(b) $\Lambda + \bar{\Lambda}$

Figure 5.3: Final calculated yields as a function of final state multiplicity for the analyses described in this thesis. Statistical errors are indicated as bars, and systematic errors as boxes.

Table 5.1: Two times the $K^0_S$ yield for all V0A multiplicity bins, presented with both statistical and systematic errors. Also given is the percentage of each yield which comes from the extrapolation of the fitting function.

| V0A mult. bin | $\langle dN_{ch}/d\eta \rangle$ | $dN/dy$ ($2K^0_S$) | Extrap. (%) |
|---|---|---|---|
| 0-1 % | 64.00 ± 1.66 | 8.105 ± 0.047 (stat.) ± 0.227 (syst.) | 5.7 |
| 1-5 % | 50.50 ± 1.31 | 6.394 ± 0.022 (stat.) ± 0.181 (syst.) | 5.9 |
| 5-10 % | 42.40 ± 1.10 | 5.330 ± 0.019 (stat.) ± 0.152 (syst.) | 5.9 |
| 10-15 % | 37.30 ± 0.97 | 4.729 ± 0.019 (stat.) ± 0.140 (syst.) | 6.0 |
| 15-20 % | 33.64 ± 0.87 | 4.241 ± 0.017 (stat.) ± 0.125 (syst.) | 6.2 |
| 20-30 % | 29.30 ± 0.76 | 3.657 ± 0.012 (stat.) ± 0.108 (syst.) | 6.3 |
| 30-40 % | 24.49 ± 0.66 | 3.069 ± 0.011 (stat.) ± 0.095 (syst.) | 6.6 |
| 40-50 % | 20.34 ± 0.53 | 2.539 ± 0.010 (stat.) ± 0.078 (syst.) | 6.9 |
| 50-60 % | 16.46 ± 0.43 | 2.069 ± 0.009 (stat.) ± 0.066 (syst.) | 7.3 |
| 60-70 % | 12.77 ± 0.34 | 1.564 ± 0.007 (stat.) ± 0.048 (syst.) | 7.8 |
| 70-80 % | 9.21 ± 0.24 | 1.143 ± 0.007 (stat.) ± 0.039 (syst.) | 8.6 |
| 80-100 % | 4.47 ± 0.14 | 0.551 ± 0.003 (stat.) ± 0.020 (syst.) | 10.2 |

Table 5.2: $(\Lambda+\bar{\Lambda})$ yield for all V0A multiplicity bins, presented with both statistical and systematic errors. Also given is the percentage of each yield which comes from the extrapolation of the fitting function.

| V0A mult. bin | $\langle dN_{ch}/d\eta \rangle$ | $dN/dy$ ($\Lambda + \bar{\Lambda}$) | Extrap. (%) |
|---|---|---|---|
| 0-1 % | 64.00 ± 1.66 | 2.553 ± 0.020 (stat.) ± 0.142 (syst.) | 16.7 |
| 1-5 % | 50.50 ± 1.31 | 2.003 ± 0.012 (stat.) ± 0.113 (syst.) | 17.4 |
| 5-10 % | 42.40 ± 1.10 | 1.695 ± 0.009 (stat.) ± 0.093 (syst.) | 18.0 |
| 10-15 % | 37.30 ± 0.97 | 1.491 ± 0.009 (stat.) ± 0.082 (syst.) | 18.6 |
| 15-20 % | 33.64 ± 0.87 | 1.357 ± 0.009 (stat.) ± 0.076 (syst.) | 18.9 |
| 20-30 % | 29.30 ± 0.76 | 1.176 ± 0.006 (stat.) ± 0.064 (syst.) | 20.0 |
| 30-40 % | 24.49 ± 0.66 | 0.977 ± 0.005 (stat.) ± 0.054 (syst.) | 20.9 |
| 40-50 % | 20.34 ± 0.53 | 0.815 ± 0.005 (stat.) ± 0.046 (syst.) | 22.3 |
| 50-60 % | 16.46 ± 0.43 | 0.651 ± 0.004 (stat.) ± 0.038 (syst.) | 23.6 |
| 60-70 % | 12.77 ± 0.34 | 0.493 ± 0.004 (stat.) ± 0.030 (syst.) | 25.2 |
| 70-80 % | 9.21 ± 0.24 | 0.356 ± 0.003 (stat.) ± 0.025 (syst.) | 28.2 |
| 80-100 % | 4.47 ± 0.14 | 0.159 ± 0.002 (stat.) ± 0.014 (syst.) | 31.8 |

which fluctuated within the statistical errors on the default spectra. The reproduced spectra were then fitted as with the default spectra, and the distribution of yields was calculated. The statistical error on the yield was taken as the standard deviation of this distribution.

The systematic error on the yields was comprised of two contributions: that coming from the systematic errors on the spectra, as described in section 4.7, and the uncertainty derived from the fitting and extrapolation procedure. In order to calculate the contribution derived from the spectra, the fitting procedure was repeated two more times, once with the systematic uncertainties subtracted from the default data points, and once with the systematic uncertainties added. The final uncertainty contribution from the spectra was taken as the mean of the differences between the two ‘systematic’ yields and that calculated as default.

For the uncertainty from the fitting and extrapolation procedure, the spectra were fitted with other functions which could have been used to describe them. The functions considered were as follows, where $A$ denotes a normalisation constant:

1. A $p_{\mathrm{T}}$ *exponential*, where the spectra are assumed to decrease exponentially with $p_{\mathrm{T}}$:

$$\frac{\mathrm{d}^2\mathrm{N}}{\mathrm{d}y\mathrm{d}p_{\mathrm{T}}} = A\, p_{\mathrm{T}}\, e^{-p_{\mathrm{T}}/T} \quad .$$

2. An $m_{\mathrm{T}}$ *exponential* function, similar to the $p_{\mathrm{T}}$ exponential above, but with the spectrum decreasing as a function of $m_{\mathrm{T}}$, as defined alongside equation 5.1:

$$\frac{\mathrm{d}^2\mathrm{N}}{\mathrm{d}y\mathrm{d}p_{\mathrm{T}}} = A\, p_{\mathrm{T}}\, e^{-m_{\mathrm{T}}/T} \quad .$$

3. A *Boltzmann* distribution:

$$\frac{\mathrm{d}^2\mathrm{N}}{\mathrm{d}y\mathrm{d}p_{\mathrm{T}}} = A\, p_{\mathrm{T}}\, m_{\mathrm{T}}\, e^{-m_{\mathrm{T}}/T} \quad .$$

4. A *Fermi-Dirac* function:

$$\frac{\mathrm{d}^2\mathrm{N}}{\mathrm{d}y\mathrm{d}p_{\mathrm{T}}} = A\, \frac{p_{\mathrm{T}}}{e^{mT/T}\, +\, 1} \quad .$$

5. A *Bose-Einstein* function:

$$\frac{\mathrm{d}^2\mathrm{N}}{\mathrm{d}y\mathrm{d}p_{\mathrm{T}}} = A\,\frac{p_{\mathrm{T}}}{e^{mT/T}\ -\ 1} \quad .$$

6. A *Boltzmann-Gibbs Blast Wave* function [119], which assumes a particle source in thermal equilibrium, which is undergoing isotropic radial expansion. The functional form of the BG blast-wave includes an integral over the radii of the source, from zero to $R$, its final radius:

$$\frac{\mathrm{dN}}{p_{\mathrm{T}}\mathrm{d}p_{\mathrm{T}}} \propto \int_0^R rdr\; m_{\mathrm{T}}\; I_0\left(\frac{p_{\mathrm{T}}\sinh\rho}{T_K}\right)\; K_1\left(\frac{m_{\mathrm{T}}\cosh\rho}{T_K}\right) \quad ,$$

   where $I_0$ and $K_1$ are modified Bessel functions and

$$\rho = \tanh^{-1}(\beta_T) \quad .$$

   The kinetic freeze-out temperature, $T_k$ and transverse flow velocity, $\beta_T$ are commonly referred to as the main parameters of the Blast-Wave function.

The default fit range covered the full $p_{\mathrm{T}}$ range of corrected spectra, up to 10 GeV/$c$, and extending down to 0 GeV/$c$. However, in order to optimise the quality of the different fits, the upper limit used for the fitting procedure was reduced as necessary. The final systematic uncertainty from the fitting procedure was decided on a bin-by-bin basis, by fitting all default spectra with all possible functions, and extracting both the yield information and $\chi^2$ per degree of freedom in each case. The spectra and fits for the two most extreme multiplicity bins are shown in figures 5.4 and 5.5 for the $\mathrm{K}^0_{\mathrm{S}}$ analysis, and 5.6 and 5.7 for the $\Lambda$ analysis. Appendix D contains plots covering all multiplicity bins, for both analyses described in this chapter.

After the fitting procedure was completed, the ratios were calculated between the yields from the default Lévy-Tsallis function, and those from the alternate fitting functions. The final percentage uncertainty was calculated from the ratios of yields from the functions which gave a good fit to the $p_T$ spectra (with a $\chi^2$ per d.o.f of 4 or lower), and which satisfied this fit quality restriction for all multiplicity bins. For the $K^0_S$ data, this meant the mean of the ratios of yields from the Blast-Wave, $m_T$ exponential, Fermi-Dirac, and

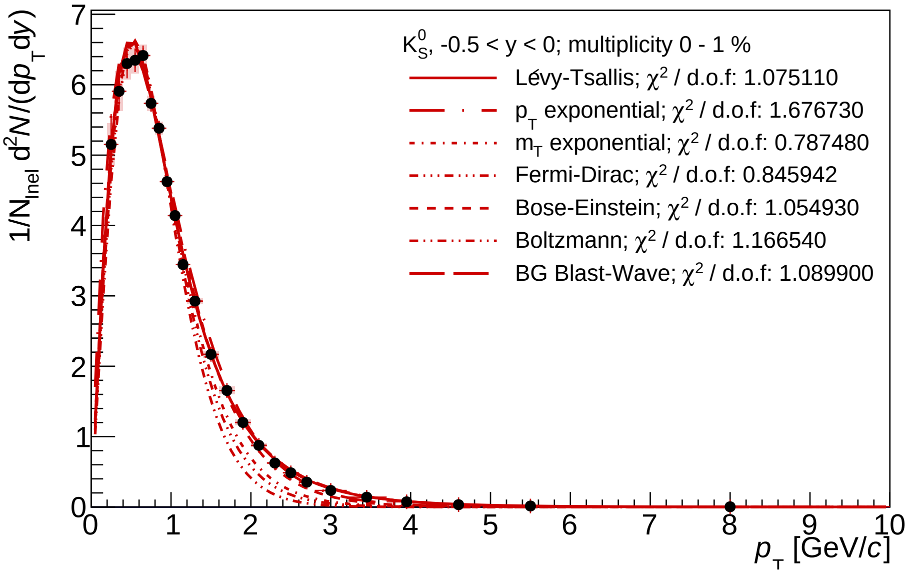

(a) Corrected spectra and fits.

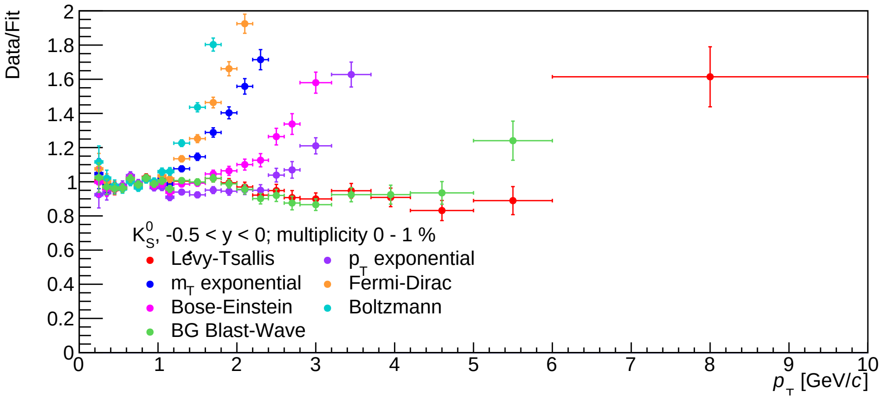

(b) Ratio between fits and real data.

Figure 5.4: Spectra and fits for the 0-1 % multiplicity $K^0_S$ analysis. The lower plot shows the ratio between all fits and data. All fits, as detailed in section 5.2.1 are shown, including those not ultimately used in the determination of the systematic error.

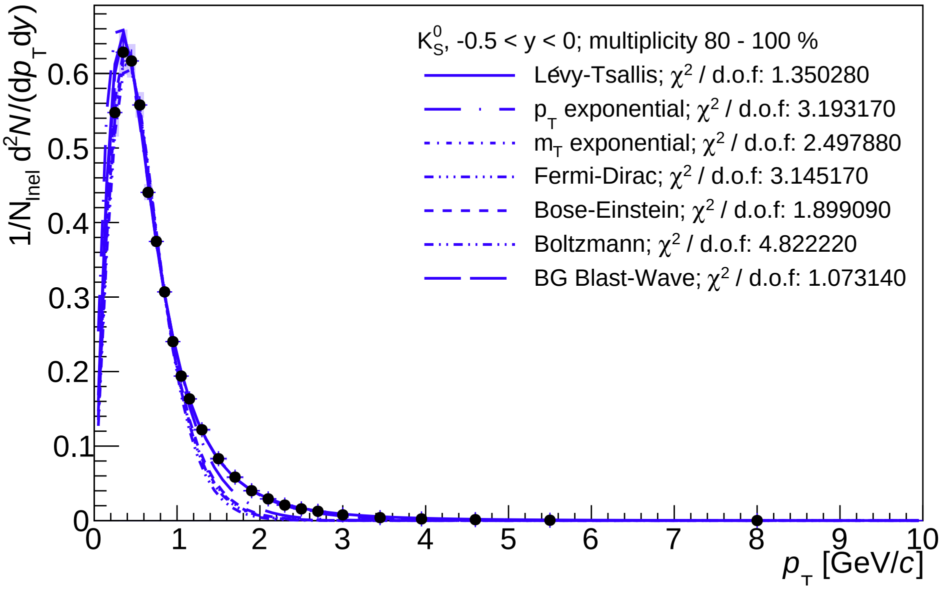

(a) Corrected spectra and fits.

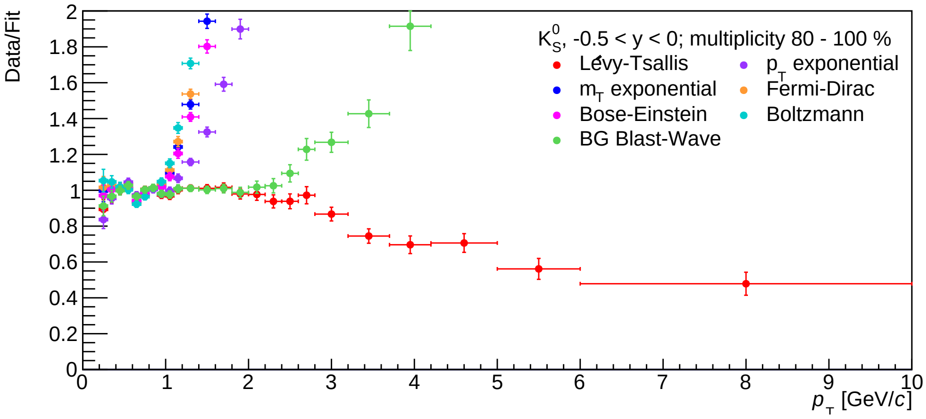

(b) Ratio between fits and real data.

Figure 5.5: Spectra and fits for the 80-100 % multiplicity $K^0_S$ analysis. The lower plot shows the ratio between all fits and data.

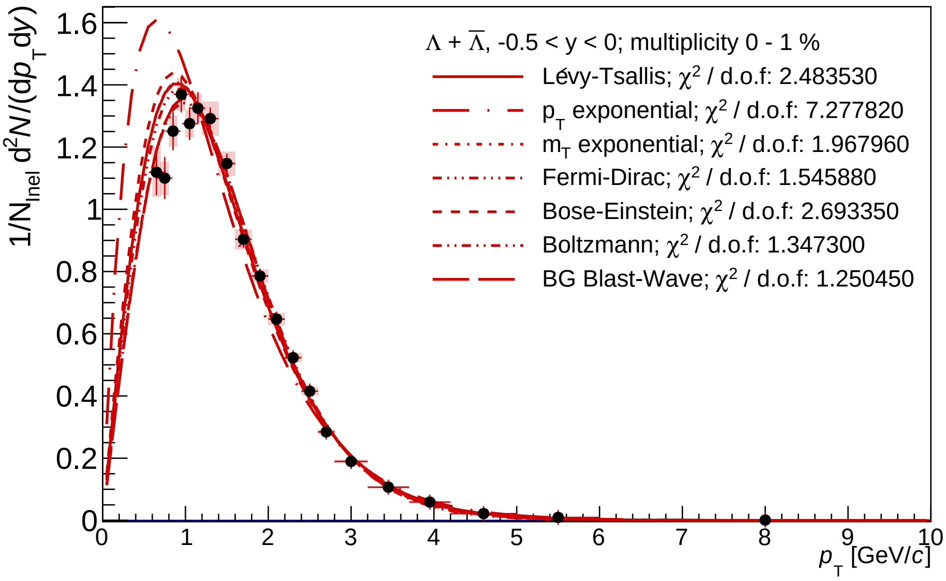

(a) Corrected spectra and fits.

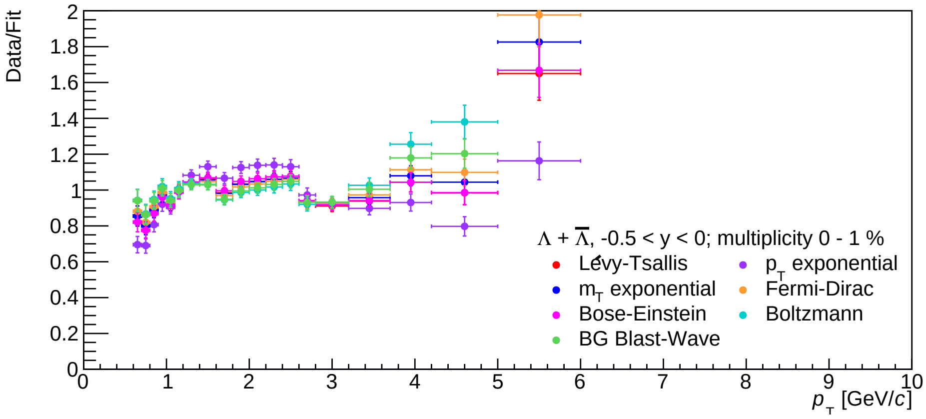

(b) Ratio between fits and real data.

Figure 5.6: Spectra and fits for the 0-1 % multiplicity $\Lambda + \bar{\Lambda}$ analysis. The lower plot shows the ratio between all fits and data. All fits, as detailed in section 5.2.1 are shown, including those not ultimately used in the determination of the systematic error.

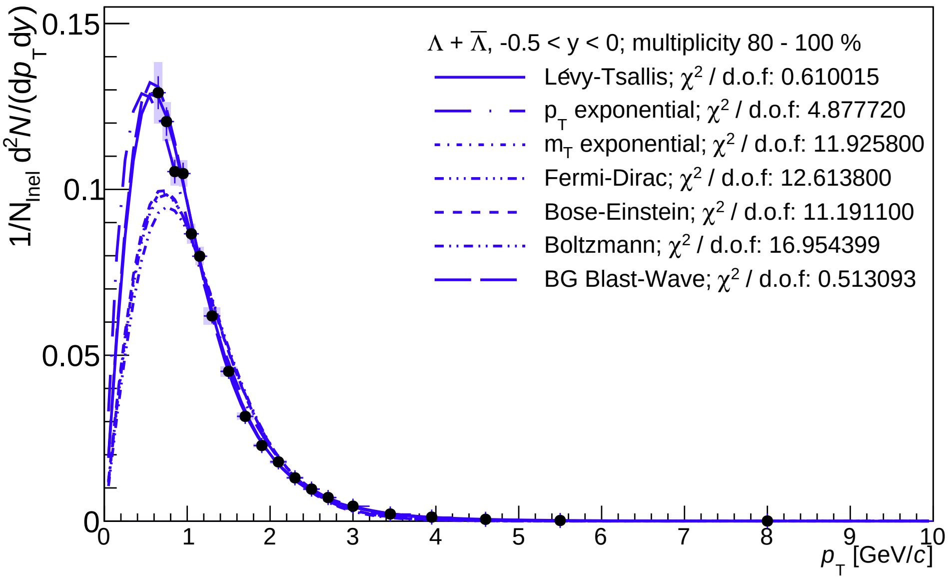

(a) Corrected spectra and fits.

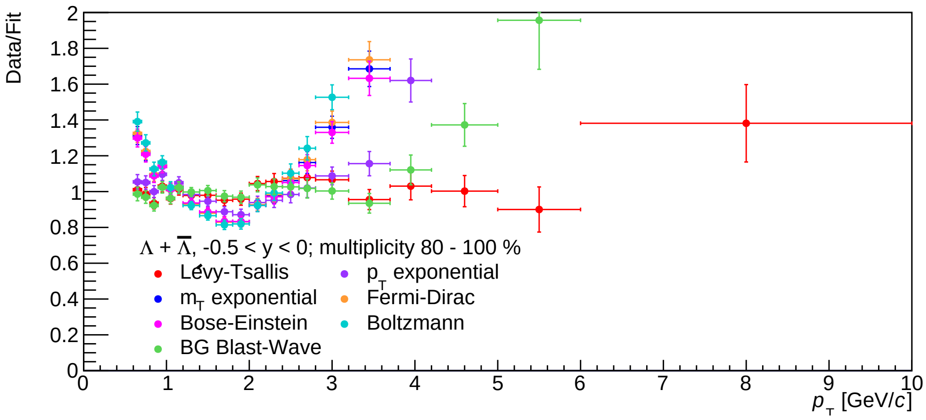

(b) Ratio between fits and real data.

Figure 5.7: Spectra and fits for the 80-100 % multiplicity $\Lambda + \bar{\Lambda}$ analysis. The lower plot shows the ratio between all fits and data.

Bose-Einstein functions. For the $\Lambda$ analysis, the values were solely the yield ratios from the Boltzmann-Gibbs Blast Wave fits.

It should be noted that the systematic error derived from the fitting function comes only from the low $p_{\mathrm{T}}$ region, where the functions are extrapolated to find the integrated yield. As can be seen in figures 5.4 to 5.7, the functions fit well in the region where the majority of the spectra lie; any effect on the fits from the poor agreement at high $p_{\mathrm{T}}$ is considered negligible. The average systematic error due to the extrapolation procedure is of the order of 1 % for all species considered in this analysis.

## 5.3 Baryon-to-Meson Ratios

Previous $\mathrm{V}^0$ analyses, in Pb-Pb, p-Pb and pp collisions, have investigated the $p_{\mathrm{T}}$ dependence of the $\Lambda$ to $\mathrm{K}^0_{\mathrm{S}}$ ratio [75,120]. Figures 5.8 and 5.9 show this ratio as measured in pp collisions at $\sqrt{s}$ = 0.9 and 7 TeV, p-Pb collisions at $\sqrt{s_{\mathrm{NN}}}$ = 5.02 TeV, and Pb-Pb collisions at $\sqrt{s_{\mathrm{NN}}}$ = 2.76 TeV. As can be seen, the $\Lambda/\mathrm{K}^0_{\mathrm{S}}$ ratio is enhanced significantly as a function of final state multiplicity at mid $p_{\mathrm{T}}$. This observation is generally explained by recombination and collective flow; a description which is justified by similar behaviour from the $\mathrm{p}/\pi$ ratio [75].

Investigating this effect will thus provide a useful crosscheck for this analysis: the observed enhancement seems to suggest an effect only dependent on $\mathrm{dN}_{ch}/\mathrm{d}\eta$, and as such should be visible in the data used here. Figure 5.10 shows the ratio between the combined $\Lambda$ and $\bar{\Lambda}$ spectra and the $\mathrm{K}^0_{\mathrm{S}}$ spectrum, multiplied by two, for both the lowest (80-100 %) and highest (0-1 %) multiplicity bins in this analysis.

As can be seen, the same trend is observed; that the ratio peaks at between 2 GeV/$c$ and 3 GeV/$c$, and that the peak is more pronounced for more central events. Plots covering the full multiplicity range used in this analysis can be found in appendix E. In addition, the peaks in figure 5.10 have similar amplitudes to the peaks in the left plot of figure 5.8,

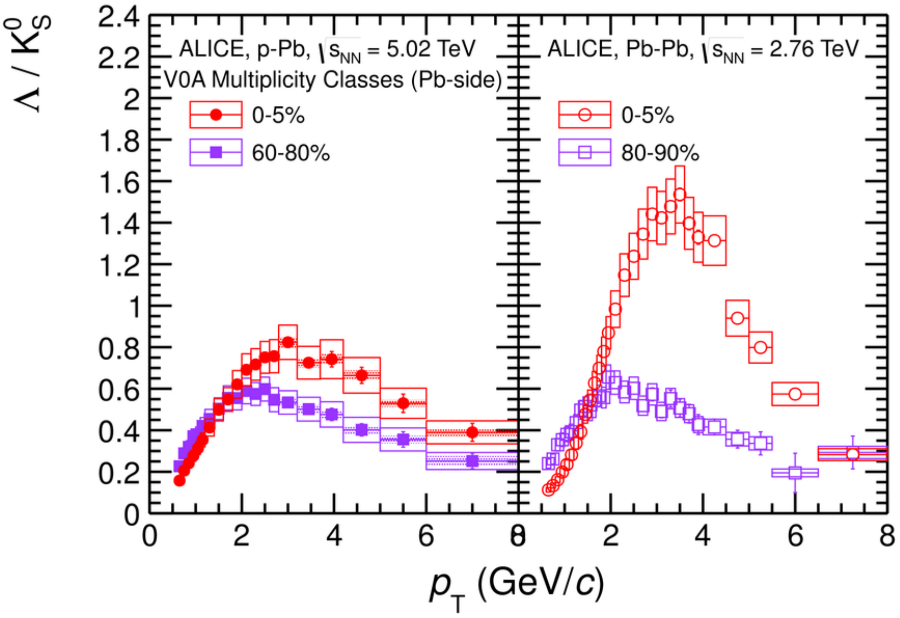

Figure 5.8: $\Lambda/K^0_S$ ratio as a function of $p_T$, as measured in p-Pb collisions at $\sqrt{s_{NN}}$ = 5.02 TeV, left, and Pb-Pb collisions at $\sqrt{s_{NN}}$ = 2.76 TeV, right [75]. Shown are the results in both high, red, and low, purple, multiplicity bins.

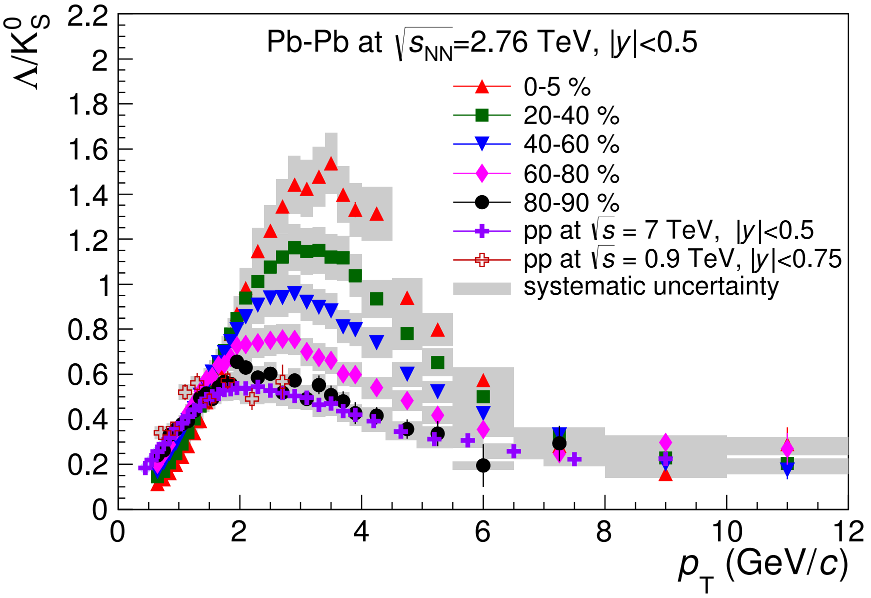

Figure 5.9: $\Lambda/K^0_S$ ratio as a function of $p_T$, as measured in Pb-Pb collisions at $\sqrt{s_{NN}}$ = 2.76 TeV and pp collisions at $\sqrt{s}$ = 0.9 and 7 TeV [120].

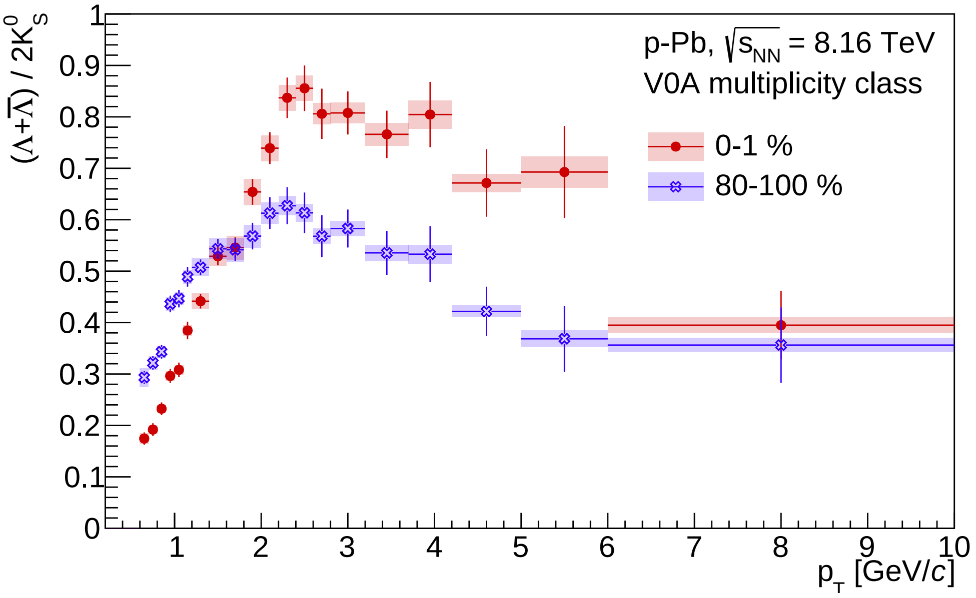

Figure 5.10: $\Lambda/K^0_S$ ratio as a function of $p_T$, as measured in this analysis, from both the highest and lowest multiplicity bins.

suggesting that the $\Lambda$-to-$K^0_S$ ratio is an effect dependent on the final state multiplicity, rather than the system size or collision energy.

## 5.4 Ratio To Pion Yields

The previous sections in this chapter have presented the yields of $K^0_S$ and $\Lambda$, and demonstrated that they increase as a function of final state multiplicity. However, the question which this analysis aims to investigate is whether or not the yields of singly-strange species increase faster that the yields of non-strange hadrons. To this end, the multiplicity-dependent yields of $K^0_S$ and $\Lambda$ were compared to the measured yields of charges pions in the same collision system, at the same energy.

Figure 5.11 shows the hadron-to-pion ratios for both species considered in this analysis. A detail to note regarding figure 5.11 is that fewer points are displayed than in figure 5.3. This is because the measured pion yields used fewer multiplicity bins than were used for the $V^0$ analyses. Table 5.3 displays the bins, and corresponding final state multiplicities, used in both this and the charged pion analyses. As can be seen, the $V^0$ analysis uses finer binning than the $\pi^{\pm}$ analysis; where necessary, the $V^0$ multiplicity bins were combined in order to match those used for the $\pi^{\pm}$ yields.

Table 5.3: V0A multiplicity bins, as used in both the $V^0$ analysis presented in this thesis, and in the analysis of charged pions, used for the investigation of strangeness enhancement.

| $V^0$ ($K^0_S$, $\Lambda(\bar{\Lambda})$) | | $\pi^{\pm}$ | |
|---|---|---|---|
| V0A mult. bin (%) | $\langle dN_{ch}/d\eta \rangle$ | V0A mult. bin (%) | $\langle dN_{ch}/d\eta \rangle$ |
| 0-1 | 64.00 ± 1.66 | 0-5 | 53.22 ± 1.38 |
| 1-5 | 50.50 ± 1.31 | 5-10 | 42.40 ± 1.10 |
| 5-10 | 42.40 ± 1.10 | 10-20 | 35.49 ± 0.92 |
| 10-15 | 37.30 ± 0.97 | 20-40 | 26.89 ± 0.70 |
| 15-20 | 33.64 ± 0.87 | 40-60 | 18.39 ± 0.48 |
| 20-30 | 29.30 ± 0.76 | 60-80 | 10.97 ± 0.29 |
| 30-40 | 24.49 ± 0.66 | 80-100 | 4.47 ±0.14 |
| 40-50 | 20.34 ± 0.53 | | |
| 50-60 | 16.46 ± 0.43 | | |
| 60-70 | 12.77 ± 0.34 | | |
| 70-80 | 9.21 ± 0.24 | | |
| 80-100 | 4.47 ± 0.14 | | |

As can be seen in figure 5.11, the yields of strange neutral hadrons increase more than the yields of pions as the final state multiplicity increases. This demonstrates that strangeness enhancement does indeed exist within p-Pb collisions at $\sqrt{s_{\mathrm{NN}}} = 8.16$ TeV, as would be expected from previous results [76].

## 5.5 Energy and System Dependence of Results

Previous sections have shown that the yields of both $V^0$ species investigated increase with final state multiplicity, and that these yields increase faster than the yields of non-strange, light hadrons, suggesting strangeness enhancement is present. Previous ALICE results have demonstrated that strangeness enhancement exists in other systems, and so it is useful to put the results presented here into context.

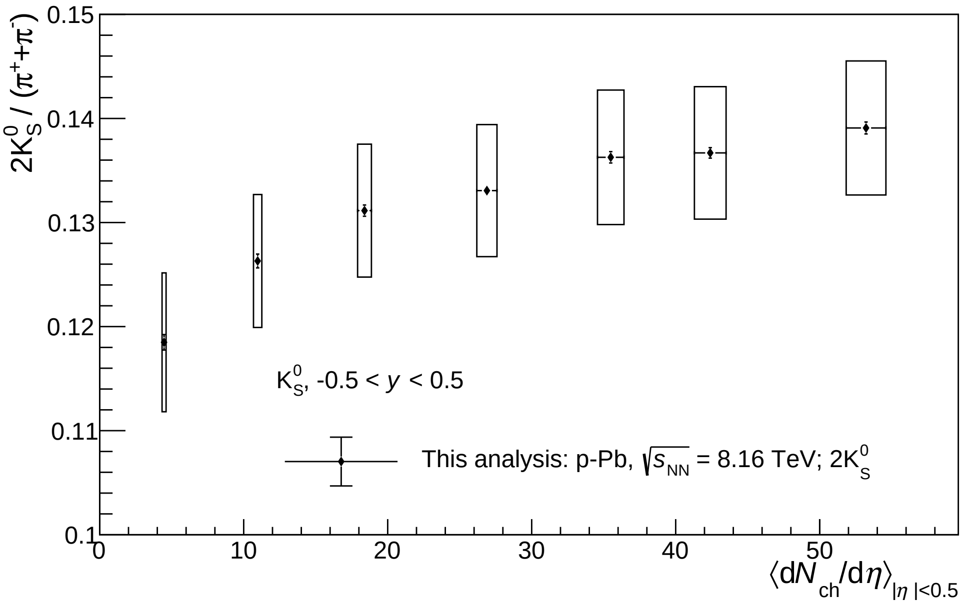

(a) $K^0_S$ to pion.

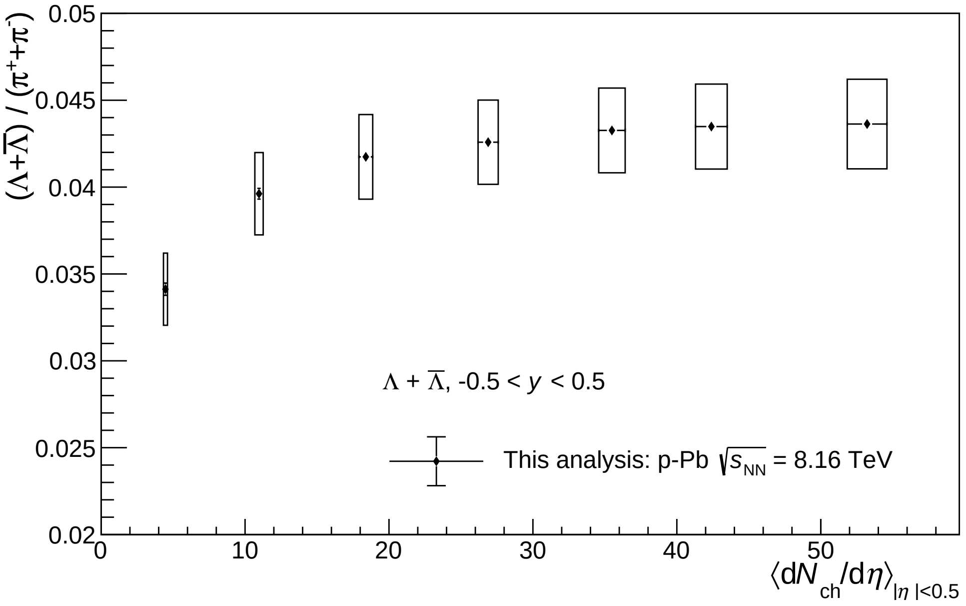

(b) $\Lambda$ to pion.

Figure 5.11: Ratios to combined $\pi^+ + \pi^-$ yields for the $K^0_S$, top, and $\Lambda + \bar{\Lambda}$, bottom. Statistical errors are shown as bars, systematic as boxes.

To this end, the following section shall compare the yields and to-pion ratios calculated here, firstly to published results from p-Pb collisions at $\sqrt{s_{\mathrm{NN}}} = 5.02$ TeV, to investigate any energy dependence present, and then to published results from other systems [76], in order to investigate any system size dependence.

### 5.5.1 Energy dependence

Figure 5.12 shows the measured yields of $\mathrm{K}^0_\mathrm{S}$, and combined $\Lambda$, for both this analysis, and that performed in p-Pb collisions at $\sqrt{s_{\mathrm{NN}}} = 5.02$ TeV [75]. As can be seen, the yields of $\mathrm{K}^0_\mathrm{S}$ agree well as a function of multiplicity, between the analysis performed here, and that already published. The combined $\Lambda$ and $\bar{\Lambda}$ yields do not agree as closely, however they are consistent within errors. These behaviours demonstrate that the production of $\mathrm{V}^0$'s as a function of multiplicity can be considered not strongly dependent on the initial collision energy.

Figure 5.13 shows the hadron-to-pion ratios for both species considered, both as calculated in this analysis, and in that from p-Pb collisions at $\sqrt{s_{\mathrm{NN}}} = 5.02$ TeV. As is shown, the ratios from the two energies agree within errors, demonstrating that strangeness enhancement of singly-strange neutral hadrons is not strongly dependent on the collision energy.

### 5.5.2 Collision system dependence

Previous analyses of $\mathrm{V}^0$ species have been carried out in different collision systems and energies to the analysis described in this thesis. Observations made from these analyses suggest that the yields and levels of strangeness enhancement are independent of the collision system used, and dependent only on the final state multiplicity. As such, it is important to compare the results yielded from this analysis to those from previous analyses. Figure 5.14 shows the yields of both $\mathrm{K}^0_\mathrm{S}$ and $\Lambda$ from pp collisions at $\sqrt{s} = 7$ [76] and 13 TeV [121], p-Pb

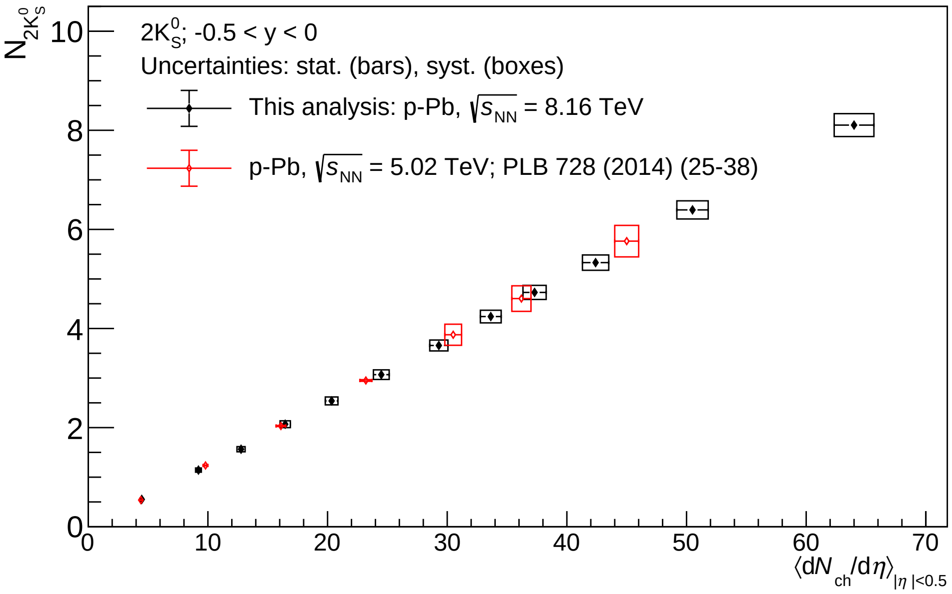

(a) $2K^0_S$.

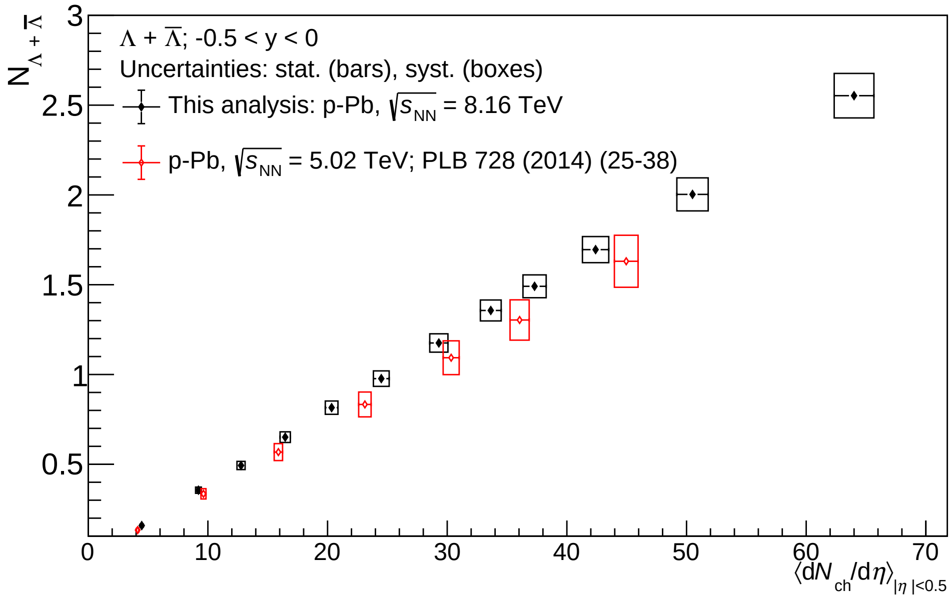

(b) $\Lambda + \bar{\Lambda}$.

Figure 5.12: Calculated $V^0$ yields, as measured both in this analysis, and from previously published p-Pb ALICE data [75].

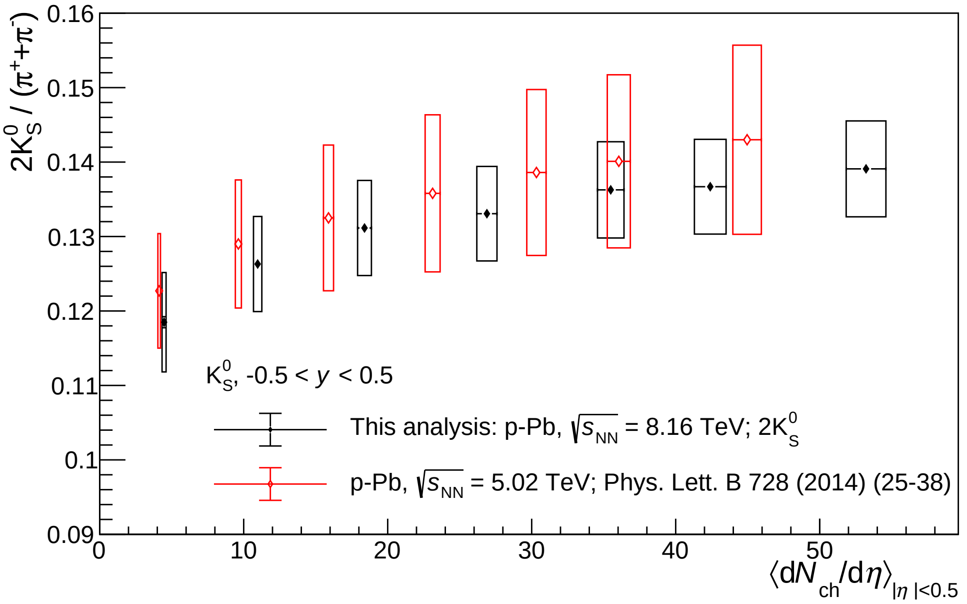

(a) $2K^0_S$.

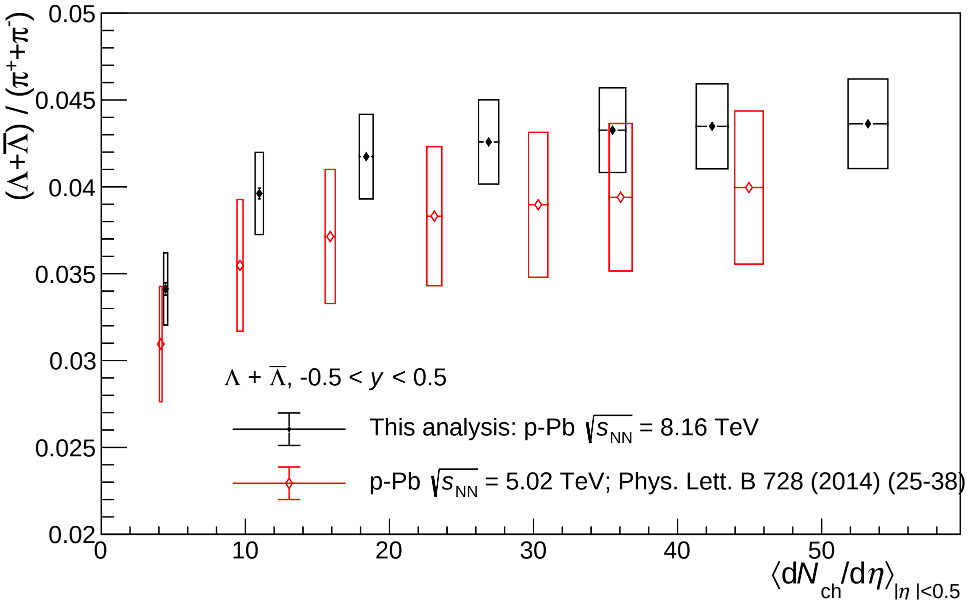

(b) $\Lambda + \bar{\Lambda}$.

Figure 5.13: Ratios of $V^0$ yields to combined yields of $\pi^+ + \pi^-$ for both this analysis, and that published using Run 1 p-Pb data [75]. Statistical errors are shown as bars, systematic as boxes.

collisions at $\sqrt{s_{\rm NN}} = 5.02$ [75] and 8.16 TeV, and Pb-Pb collisions at $\sqrt{s_{\rm NN}} = 2.76$ TeV [76]. As can be seen, both the combined $\Lambda + \bar{\Lambda}$ and $\rm K^0_S$ yields show a smooth increase with multiplicity across all systems. In figure 5.14, only the two most peripheral Pb-Pb points are shown; those which overlap with the multiplicity range covered by the pp and p-Pb analyses.

Figure 5.15 shows the hadron-to-pion ratios for this analysis, compared to published results in pp, p-Pb and Pb-Pb collisions, as well as preliminary results from Pb-Pb collisions at $\sqrt{s_{\rm NN}} = 5.02$ TeV [122]. Similarly to the comparison made to previous p-Pb results, figure 5.15 demonstrates that the hadron-to-pion ratios measured in this analysis show consistency with the ratios measured in other collision systems and energies with ALICE.

## 5.6 Future Analyses

The analysis presented in this thesis uses data from only the six low interaction rate runs in the 2016 p-Pb ALICE data set. As such, a first follow-up analysis to this one can use the full minimum bias data set, instead of just 40 % of the full set. This increase in statistics should slightly improve the errors calculated for the analyses presented here, and will allow for finer binning at low-to-mid multiplicities, should it be desired.

Further strangeness analyses of ALICE 2016 p-Pb data can also use a high-multiplicity data set; collected with the application of a designated high multiplicity trigger, which saved events which had simultaneous signals in both V0 detectors above a certain threshold. This gives the high multiplicity data much higher statistics for the 0-5% highest multiplicity events, allowing this range of multiplicity to be more finely binned. This increase in granularity will allow higher values of $\mathrm{dN}_{ch}/\mathrm{d}\eta$ to be studied, providing more crossover between the results from p-Pb and Pb-Pb collisions. Any results thus generated will allow for the validation of the suggestion that strangeness enhancement truly is a system-independent effect. In addition, the higher $\mathrm{dN}_{ch}/\mathrm{d}\eta$ values will give ALICE an opportunity to investigate if a quark-gluon plasma can be created in small systems, or if other physics is at play.

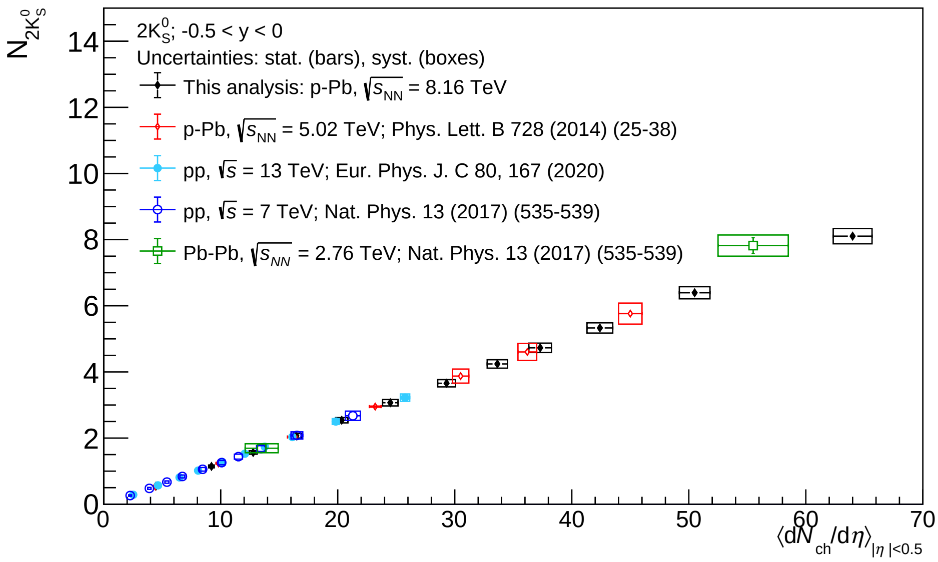

(a) $2K^0_S$.

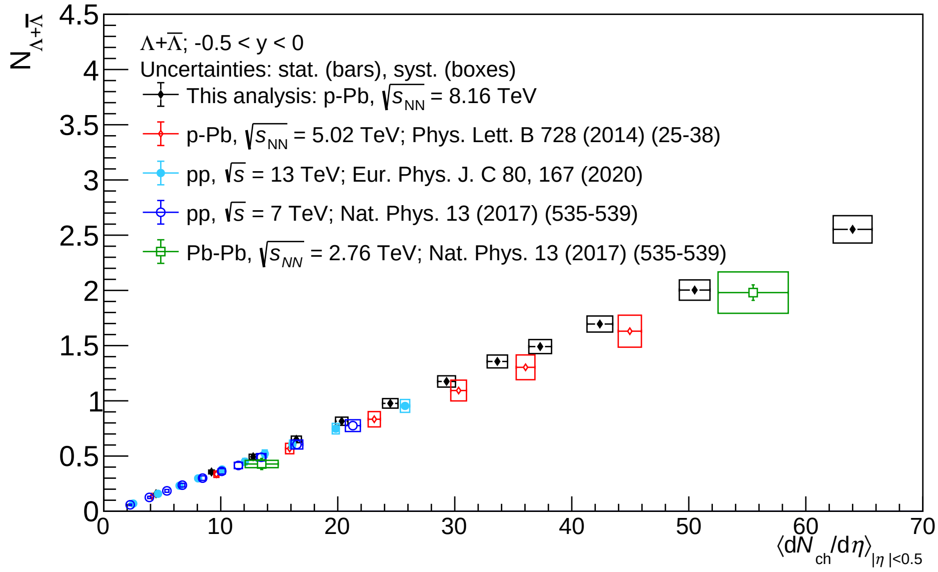

(b) $\Lambda + \bar{\Lambda}$.

Figure 5.14: Calculated $V^0$ yields, for ALICE analyses in pp, p-Pb and Pb-Pb collision systems [75, 76, 121]. The focus here is on the multiplicity range which is covered by this analysis; the Pb-Pb data reaches multiplicity densities two orders of magnitude higher than shown.

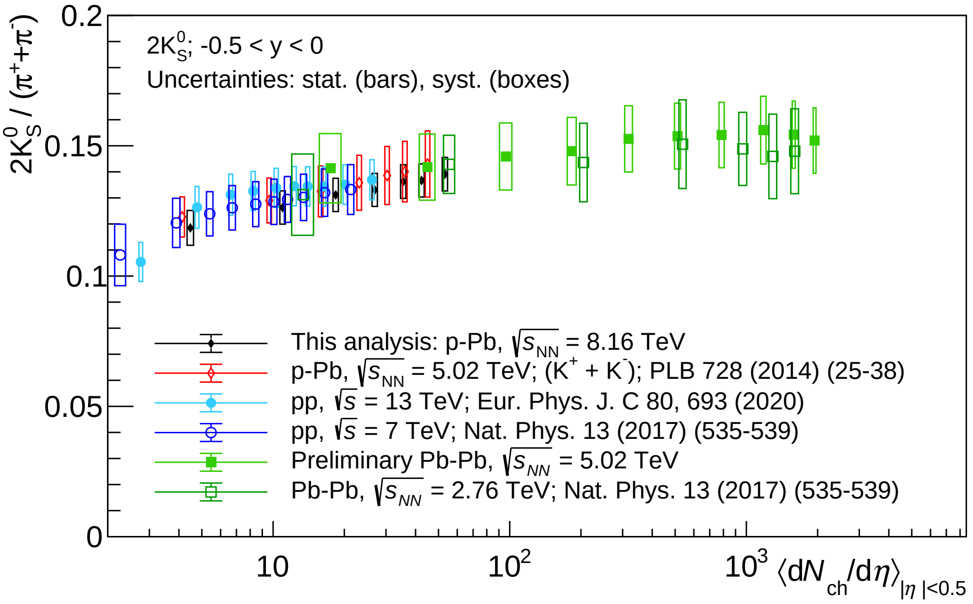

(a) $2K^0_S$.

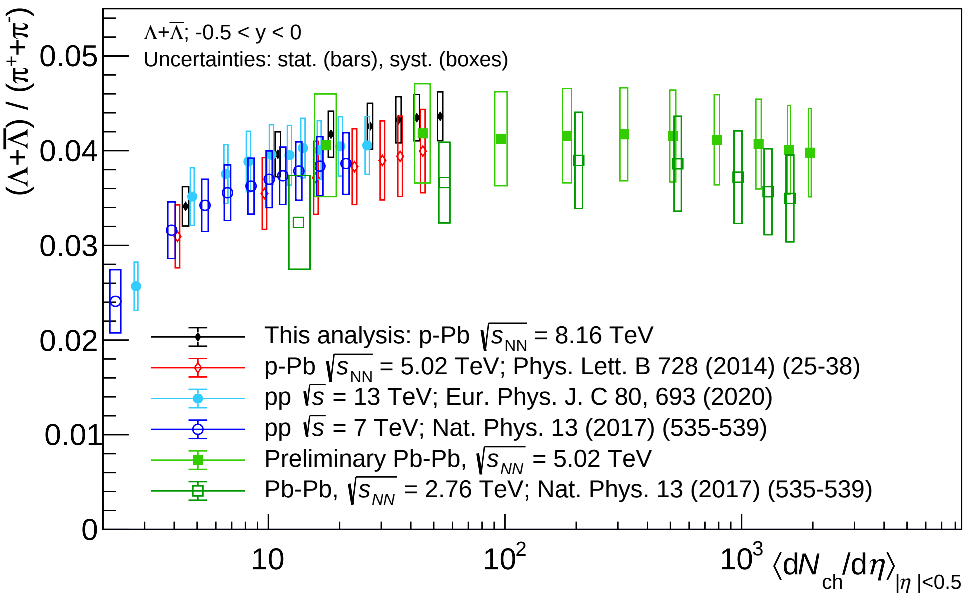

(b) $\Lambda + \bar{\Lambda}$.

Figure 5.15: Hadron-to-pion ratios, as measured in pp, p-Pb and Pb-Pb collision systems, with ALICE.

## 5.7 Conclusions

This thesis presents the measurements of the yields of singly-strange neutral hadrons, $K^0_S$ and $\Lambda(\bar{\Lambda})$, in p-Pb collisions at $\sqrt{s_{NN}} = 8.16$ TeV as recorded by the ALICE experiment at CERN. The process by which candidates were selected through identification of their decay topologies was described, a method only available due to the high precision given by the tracking, momentum measurement and particle identification systems within the ALICE detector.

The process by which the final transverse momentum spectra were generated and corrected was also described. This included an explanation of the removal of the feeddown contribution to the $\Lambda$ spectra, which originated not from the initial collisions, but from the decays of $\Xi^{\pm}$ and $\Xi^0$.

The transverse momentum spectra for both species investigated were shown. Both species demonstrate spectral hardening, where the peak of the spectra shifts to higher $p_T$ as the final state multiplicity increases. This is consistent with the presence of collective behaviour in the material created by p-Pb collisions, as described by hydrodynamic models of the medium created by heavy-ion collisions.

The process by which the $p_T$ spectra were fitted was described, and the extrapolated yields of both species were shown as a function of $dN_{ch}/d\eta$. These yields were compared to those measured in other collision systems and energies with ALICE, and it was observed that the yields reported here are consistent with those already published by ALICE. Ratios between the contents of the $K^0_S$ and $\Lambda$ spectra were shown as a function of $p_T$. These ratios are compared to those reported by ALICE from p-Pb collisions at $\sqrt{s_{NN}} = 5.02$ TeV, pp collisions at $\sqrt{s} = 0.9$ and 7 TeV, and Pb-Pb collisions at $\sqrt{s_{NN}} = 2.76$ TeV, and are seen to support the conclusion that the hardening of $p_T$ spectra is an effect which is independent of system size or collision energy.

Finally, the possibility of strangeness enhancement for these species was investigated by comparing the yields reported here to those of charged pions from the same collision system. The ratio of hadron-to-pion yields was observed to increase as a function of final state multiplicity, confirming the enhanced production of singly-strange hadrons in p-Pb collisions. The calculated ratios were also compared to the those obtained by ALICE from other collision systems. It was observed that the hadron-to-pion ratios calculated here are consistent with the observation that strangeness enhancement evolves smoothly as a function of $\mathrm{dN}_{ch}/\mathrm{d}\eta$ from pp to Pb-Pb collisions.

The results presented here provide an extension to the $\mathrm{dN}_{ch}/\mathrm{d}\eta$ range covered by p-Pb collisions at $\sqrt{s_{\mathrm{NN}}} = 5.02$ TeV, and hence provide more overlap with measurements made in Pb-Pb collisions. This allows ALICE to investigate if the observed enhancement of strange yields is a smooth effect as a function of final state multiplicity. Further analyses of the data set used here can help with increasing statistics, and can improve on the measurements reported in this thesis. In addition, this analysis has helped provide a baseline for potential analyses of a dedicated high-multiplicity data set, which can investigate whether or not the observed strangeness enhancement continues to rise or if it reaches saturation, as observed in Pb-Pb collisions.

# Bibliography

[1] Bensteele1995, "Rutherford atomic planetary model." `https://commons.wikimedia.org/w/index.php?curid=21332267`. Own work, CC BY-SA 3.0; accessed 08/04/21.

[2] C. M. G. Lattes, H. Muirhead, G. P. S. Occhialini, and C. F. Powell, "Processes Involving Charged Mesons," *Nature*, vol. 159, pp. 694–697, 1947.

[3] M. Gell-Mann, "The Eightfold Way: A Theory of strong interaction symmetry," 1961. Technical Report, https://www.osti.gov/biblio/4008239.

[4] M. Gell-Mann, "A Schematic Model of Baryons and Mesons," *Phys. Lett.*, vol. 8, pp. 214–215, 1964.

[5] G. Zweig, "An $\mathrm{SU}_3$ model for strong interaction symmetry and its breaking; Version 2," p. 80 p, Feb 1964. Version 1 is CERN preprint 8182/TH.401, Jan. 17, 1964.

[6] Y. Fukuda, T. Hayakawa, E. Ichihara, *et al.*, "Evidence for oscillation of atmospheric neutrinos," *Phys. Rev. Lett.*, vol. 81, pp. 1562–1567, Aug 1998.

[7] Q. R. Ahmad *et al.*, "Measurement of the rate of $\nu_e + d \to p + p + e^-$ interactions produced by $^8B$ solar neutrinos at the Sudbury Neutrino Observatory," *Physical Review Letters*, vol. 87, Jul 2001.

[8] The Editors of Encyclopaedia Britannica, "Encyclopaedia Brittanica; Quantum Electrodynamics." `https://www.britannica.com/science/quantum-electrodynamics-physics`. Accessed: 15-04-2021.

[9] R. P. Feynman, “Space-Time Approach to Quantum Electrodynamics,” *Phys. Rev.*, vol. 76, pp. 769–789, Sep 1949.

[10] J. Schwinger, “Quantum Electrodynamics. I. A Covariant Formulation,” *Phys. Rev.*, vol. 74, pp. 1439–1461, Nov 1948.

[11] S. Tomonaga, “On a relativistically invariant formulation of the quantum theory of wave fields,” *Prog. Theor. Phys.*, vol. 1, pp. 27–42, 1946.

[12] S. L. Glashow, “The renormalizability of vector meson interactions,” *Nuclear Physics*, vol. 10, pp. 107 – 117, 1959.

[13] A. Salam, “Weak and Electromagnetic Interactions,” *Conf. Proc.*, vol. C680519, pp. 367–377, 1968.

[14] S. Weinberg, “A Model of Leptons,” *Phys. Rev. Lett.*, vol. 19, pp. 1264–1266, Nov 1967.

[15] P. W. Higgs, “Broken Symmetries and the Masses of Gauge Bosons,” *Phys. Rev. Lett.*, vol. 13, pp. 508–509, Oct 1964.

[16] F. Englert and R. Brout, “Broken Symmetry and the Mass of Gauge Vector Mesons,” *Phys. Rev. Lett.*, vol. 13, pp. 321–323, Aug 1964.

[17] G. Aad *et al.*, “Observation of a new particle in the search for the Standard Model Higgs boson with the ATLAS detector at the LHC,” *Physics Letters B*, vol. 716, p. 1–29, Sep 2012.

[18] S. Chatrchyan *et al.*, “Observation of a new boson at a mass of 125 GeV with the CMS experiment at the LHC,” *Physics Letters B*, vol. 716, p. 30–61, Sep 2012.

[19] M. N. Chernodub, “QCD string breaking in strong magnetic field,” *Mod. Phys. Lett. A*, vol. 29, p. 1450162, 2014.

[20] L. C. S. Morii T and M. S. N, *The physics of the Standard Model and beyond.* Physics textbook, Singapore: World Scientific, 2004.

[21] U. Aglietti, “Introduction to perturbative QCD,” in *1st School on Field Theory and Gravitation*, 4 1997.

[22] V. Khachatryan *et al.*, “Measurement of the inclusive 3-jet production differential cross section in proton-proton collisions at 7 TeV and determination of the strong coupling constant in the TeV range,” *Eur. Phys. J.*, vol. C75, no. 5, p. 186, 2015.

[23] H. D. Politzer, “Reliable perturbative results for strong interactions?,” *Phys. Rev. Lett.*, vol. 30, pp. 1346–1349, Jun 1973.

[24] D. J. Gross and F. Wilczek, “Asymptotically free gauge theories. i,” *Phys. Rev. D*, vol. 8, pp. 3633–3652, Nov 1973.

[25] D. J. Gross and F. Wilczek, “Asymptotically free gauge theories. ii,” *Phys. Rev. D*, vol. 9, pp. 980–993, Feb 1974.

[26] E. Shuryak, “Quark-gluon plasma and hadronic production of leptons, photons and psions,” *Physics Letters B*, vol. 78, no. 1, pp. 150–153, 1978.

[27] H. Satz, “Colour deconfinement and quarkonium binding,” *Journal of Physics G: Nuclear and Particle Physics*, vol. 32, p. R25–R69, Feb 2006.

[28] F. Karsch and E. Laermann, “Thermodynamics and in-medium hadron properties from lattice QCD,” 5 2003.

[29] F. Karsch, E. Laermann, and A. Peikert, “Quark mass and flavor dependence of the QCD phase transition,” *Nucl. Phys. B*, vol. 605, pp. 579–599, 2001.

[30] F. Karsch, “Lattice QCD at high temperature and density,” *Lect. Notes Phys.*, vol. 583, pp. 209–249, 2002.

[31] K. Aamodt *et al.*, "The ALICE experiment at the CERN LHC. A Large Ion Collider Experiment," *JINST*, vol. 3, p. S08002. 259 p, 2008. Also published by CERN Geneva in 2010.

[32] J. N. Marx, *The STAR Experiment at RHIC*, pp. 233–237. Boston, MA: Springer US, 1996.

[33] "Quark-matter fireballs hashed out in Protvino." `https://cerncourier.com/a/quark-matter-fireballs-hashed-out-in-protvino/`. Accessed: 04-05-2021.

[34] F. Panagiota *et al.*, "Overview of results from ALICE at the CERN LHC," *Journal of Physics: Conference Series*, vol. 455, p. 012004, Aug 2013.

[35] P. Braun-Munzinger and J. Stachel, "Overview of results from ALICE at the CERN LHC," *Nature*, vol. 448, pp. 302–309, Jul 2007.

[36] CERN, "New State of Matter created at CERN." `http://press.cern/press-releases/2000/02/new-state-matter-created-cern`. Accessed: 14-08-2018.

[37] NA44 Collaboration, H. Atherton, J. Bondorf, H. Bøggild, and K. H. et al, *Results from CERN experiment NA44*. 1991.

[38] U. Faschingbauer, M. G. Trauth, and J. P. Wurm, "Study of electron pair production in hadron and nuclear collisions at the CERN SPS," tech. rep., CERN, Geneva, 1988.

[39] S. Afanasiev *et al.*, "The NA49 large acceptance hadron detector," *Nucl. Instrum. Meth. A*, vol. 430, pp. 210–244, 1999.

[40] M. Abreu *et al.*, "J/$\psi$ and Drell-Yan cross-sections in Pb-Pb interactions at 158 GeV/c per nucleon," *Physics Letters B*, vol. 410, no. 2, pp. 327–336, 1997.

[41] K. P. Pretzl *et al.*, “Search for strange quark matter in relativistic heavy ion collisions at CERN (NA52),” p. 15 p, Mar 1995.

[42] V. Manzari, F. the NA57 Collaboration (Antinori, and others), “Experiment NA57 at the CERN SPS,” *Journal of Physics G: Nuclear and Particle Physics*, vol. 25, no. 2, p. 473, 1999.

[43] M. M. Aggarwal *et al.*, “Recent results on Pb + Pb collisions at 158-A-GeV from the WA98 experiment at CERN,” *Nucl. Phys.*, vol. A638, pp. 147–158, 1998.

[44] J. Adams *et al.*, “Experimental and theoretical challenges in the search for the quark gluon plasma: The STAR Collaboration’s critical assessment of the evidence from RHIC collisions,” *Nucl. Phys.*, vol. A757, pp. 102–183, 2005.

[45] K. Adcox *et al.*, “Formation of dense partonic matter in relativistic nucleus-nucleus collisions at RHIC: Experimental evaluation by the PHENIX collaboration,” *Nucl. Phys.*, vol. A757, pp. 184–283, 2005.

[46] B. B. Back *et al.*, “The PHOBOS perspective on discoveries at RHIC,” *Nucl. Phys.*, vol. A757, pp. 28–101, 2005.

[47] I. Arsene *et al.*, “Quark gluon plasma and color glass condensate at RHIC; The Perspective from the BRAHMS experiment,” *Nucl. Phys.*, vol. A757, pp. 1–27, 2005.

[48] B. Müller, J. Schukraft, and B. Wysłouch, “First results from Pb+Pb collisions at the LHC,” *Annual Review of Nuclear and Particle Science*, vol. 62, p. 361–386, Nov 2012.

[49] T. K. Nayak, “Heavy Ions: Results from the Large Hadron Collider,” *Pramana*, vol. 79, pp. 719–735, 2012.

[50] “Evolution of collisions and QGP.” `https://particlesandfriends.wordpress.com/2016/10/14/evolution-of-collisions-and-qgp/`. Accessed: 19-06-2018.

[51] D. d'Enterria and B. Betz, "High-pT Hadron Suppression and Jet Quenching," *Lecture Notes in Physics*, vol. 785, pp. 285–339, 11 2009.

[52] K. Aamodt *et al.*, "Suppression of charged particle production at large transverse momentum in central Pb–Pb collisions at $\sqrt{s_{NN}} = 2.76$ Tev," *Physics Letters B*, vol. 696, no. 1, pp. 30–39, 2011.

[53] T. Matsui and H. Satz, "$J/\psi$ Suppression by Quark-Gluon Plasma Formation," *Phys. Lett. B*, vol. 178, pp. 416–422, 1986.

[54] K. A. Olive *et al.*, "Review of Particle Physics," *Chin. Phys.*, vol. C38, p. 33, 2014.

[55] E. Eichten, K. Gottfried, T. Kinoshita, J. Kogut, K. D. Lane, and T. M. Yan, "Spectrum of Charmed Quark-Antiquark Bound States," *Phys. Rev. Lett.*, vol. 34, pp. 369–372, Feb 1975.

[56] A. Adare *et al.*, "$J/\psi$ suppression at forward rapidity in Au + Au collisions at $\sqrt{s_{NN}} = 200$ GeV," *Phys. Rev. C*, vol. 84, p. 054912, Nov 2011.

[57] J. Adam *et al.*, "Differential studies of inclusive $J/\psi$ and $\psi(2s)$ production at forward rapidity in Pb-Pb collisions at $\sqrt{s_{\mathrm{NN}}} = 2.76$ TeV," *Journal of High Energy Physics*, vol. 2016, May 2016.

[58] Zoe Louise Matthews, "Flow." https://www.quantumdiaries.org/2011/11/07/flow/.

[59] A. M. Poskanzer and S. A. Voloshin, "Methods for analyzing anisotropic flow in relativistic nuclear collisions," *Phys. Rev. C*, vol. 58, pp. 1671–1678, 1998.

[60] K. Aamodt *et al.*, "Elliptic Flow of Charged Particles in Pb-Pb Collisions at $\sqrt{s_{NN}} = 2.76$ TeV," *Phys. Rev. Lett.*, vol. 105, p. 252302, Dec 2010.

[61] J. Adam *et al.*, "Direct photon production in Pb–Pb collisions at $\sqrt{s_{NN}} = 2.76$ TeV," *Physics Letters B*, vol. 754, pp. 235–248, 2016.

[62] J. Rafelski and B. Müller, “Strangeness Production in the Quark-Gluon Plasma,” *Physical Review Letters*, vol. 48, no. 16, pp. 1066–1069, 1982.

[63] D. J. Griffiths, *Introduction to elementary particles; 2nd rev. version*, p. 135. Physics textbook, New York, NY: Wiley, 2008.

[64] L. Ahle *et al.*, “Centrality dependence of kaon yields in Si + $A$ and Au+Au collisions at relativistic energies,” *Phys. Rev. C*, vol. 60, p. 044904, Sep 1999.

[65] F. Antinori et al, “Strangeness enhancement at midrapidity in Pb–Pb collisions at 158 A GeV/c: A comparison with VENUS and RQMD models,” *The European physical journal. C, Particles and fields*, vol. 11, no. 1, pp. 79–88, 1999.

[66] D. Evans *et al.*, “Strangeness production in p+W and S+W Interactions at 200 A GeV/c,” *Acta Physica Hungarica New Series Heavy Ion Physics*, vol. 4, pp. 79–89, Dec 1996.

[67] F. Antinori *et al.*, “Energy dependence of hyperon production in nucleus–nucleus collisions at SPS,” *Physics letters. B*, vol. 595, no. 1-4, pp. 68–74, 2004.

[68] F. Antinori *et al.*, “Enhancement of hyperon production at central rapidity in 158 A GeV/c Pb–Pb collisions,” *Journal of Physics. G, Nuclear and Particle Physics*, vol. 32, no. 4, pp. 427–441, 2006.

[69] G. Agakishiev *et al.*, “Strangeness Enhancement in Cu-Cu and Au-Au Collisions at $\sqrt{s_{\rm NN}}$ = 200 GeV,” *Physical Review Letters*, vol. 108, no. 20120217, 2012.

[70] X. Zhang, “STAR results on strangeness production in beam energy scan program,” *Journal of Physics: Conference Series*, vol. 668, no. 1, p. 012033, 2016.

[71] B. B. Abelev *et al.*, “Multi-strange baryon production at mid-rapidity in Pb-Pb collisions at $\sqrt{s_{NN}}$ = 2.76 TeV,” *Phys. Lett.*, vol. B728, pp. 216–227, 2014. [Erratum: Phys. Lett.B734,409(2014)].

[72] B. I. Abelev *et al.*, "Strange particle production in $p + p$ collisions at $\sqrt{s} = 200$ GeV," *Phys. Rev. C*, vol. 75, p. 064901, Jun 2007.

[73] B. Abelev *et al.*, "Multi-strange baryon production in *pp* collisions at $\sqrt{s} = 7$ TeV with ALICE," *Phys. Lett.*, vol. B712, pp. 309–318, 2012.

[74] J. Adam *et al.*, "Multi-strange baryon production in p-Pb collisions at $\sqrt{s_{\mathbf{NN}}} = 5.02$ TeV," *Phys. Lett.*, vol. B758, pp. 389–401, 2016.

[75] B. Abelev *et al.*, "Multiplicity dependence of pion, kaon, proton and lambda production in p–Pb collisions at $\sqrt{s_{\mathrm{NN}}} = 5.02$ TeV," *Physics Letters B*, vol. 728, pp. 25–38, 2014.

[76] J. Adam *et al.*, "Enhanced production of multi-strange hadrons in high-multiplicity proton-proton collisions," *Nature Phys.*, vol. 13, pp. 535–539, 2017.

[77] T. Sjostrand, S. Mrenna, and P. Z. Skands, "A Brief Introduction to PYTHIA 8.1," *Comput. Phys. Commun.*, vol. 178, pp. 852–867, 2008.

[78] T. Pierog, I. Karpenko, J. M. Katzy, E. Yatsenko, and K. Werner, "EPOS LHC: Test of collective hadronization with data measured at the CERN Large Hadron Collider," *Phys. Rev.*, vol. C92, no. 3, p. 034906, 2015.

[79] C. Bierlich and J. R. Christiansen, "Effects of color reconnection on hadron flavor observables," *Phys. Rev.*, vol. D92, no. 9, p. 094010, 2015.

[80] L. Evans and P. Bryant, "LHC Machine," *JINST*, vol. 3, p. S08001, 2008.

[81] "NA62." `https://home.cern/science/experiments/na62`. Accessed: 03-05-2021.

[82] "The Antiproton Decelerator." `https://home.cern/science/accelerators/antiproton-decelerator`. Accessed: 03-05-2021.

[83] E. Mobs, "The CERN accelerator complex - August 2018. Complexe des accélérateurs du CERN - Août 2018." General Photo; Accessed 06/05/21, Aug 2018.

[84] "Linear accelerator 4." `https://home.cern/science/accelerators/linear-accelerator-4`. Accessed: 03-05-2021.

[85] "The Proton Synchrotron." `https://home.cern/science/accelerators/proton-synchrotron`. Accessed: 11-03-2021.

[86] "The Super Proton Synchrotron." `https://home.cern/science/accelerators/super-proton-synchrotron`. Accessed: 11-03-2021.

[87] R. Steerenberg, "LHC report: full house for the LHC," Jul 2017. Accessed: 11-03-2021.

[88] J.-L. Caron, "LHC layout. Schema general du LHC." AC Collection. Legacy of AC. Pictures from 1992 to 2002., Sep 1997.

[89] G. Aad *et al.*, "The ATLAS Experiment at the CERN Large Hadron Collider," *Journal of Instrumentation*, vol. 3, no. 08, p. S08003, 2008.

[90] W. Adam *et al.*, "The CMS experiment at the CERN LHC," *Journal of Instrumentation*, vol. 3, no. 08, p. S08004, 2008.

[91] A. Augusto Alves Jr *et al.*, "The LHCb Detector at the LHC," *Journal of Instrumentation*, vol. 3, no. 08, p. S08005, 2008.

[92] A. Tauro, "ALICE Schematics." General Photo; accessed 16/03/21, May 2017.

[93] R. Sahoo, "Relativistic Kinematics," 2016. Lecture notes for IX SERC School on Experimental High Energy Physics, IIT Madras, India.

[94] *ALICE Inner Tracking System (ITS): Technical Design Report.* Technical design report. ALICE, Geneva: CERN, 1999.

[95] K. Aamodt *et al.*, "The ALICE experiment at the CERN LHC. A Large Ion Collider Experiment," *JINST*, vol. 3, pp. 18–22, 2008.

[96] K. Aamodt *et al.*, "The ALICE experiment at the CERN LHC. A Large Ion Collider Experiment," *JINST*, vol. 3, pp. 22–37, 2008.

[97] K. Aamodt *et al.*, "The ALICE experiment at the CERN LHC. A Large Ion Collider Experiment," *JINST*, vol. 3, pp. 37–46, 2008.

[98] K. Aamodt *et al.*, "The ALICE experiment at the CERN LHC. A Large Ion Collider Experiment," *JINST*, vol. 3, pp. 46–53, 2008.

[99] J. Alme *et al.*, "The ALICE TPC, a large 3-dimensional tracking device with fast read-out for ultra-high multiplicity events," *Nuclear Instruments and Methods in Physics Research Section A: Accelerators, Spectrometers, Detectors and Associated Equipment*, vol. 622, no. 1, pp. 316 – 367, 2010.

[100] P. Sigmund, *Particle Penetration and Radiation Effects: General Aspects and Stopping of Swift Point Charges.* Springer Series in Solid-State Sciences, Springer Berlin Heidelberg, 2006.

[101] B. Abelev *et al.*, "Performance of the ALICE experiment at the CERN LHC," *International Journal of Modern Physics A*, vol. 29, p. 1430044, Sep 2014.

[102] E. Abbas *et al.*, "Performance of the ALICE VZERO system," *Journal of Instrumentation*, vol. 8, p. P10016, Oct 2013.

[103] S. Acharya *et al.*, "Charged-particle pseudorapidity density at mid-rapidity in p-Pb collisions at $\sqrt{s_{\mathrm{NN}}} = 8.16$ TeV," *Eur. Phys. J. C*, vol. 79, p. 307. 23 p, Nov 2018.

[104] M. L. Miller, K. Reygers, S. J. Sanders, and P. Steinberg, "Glauber modeling in high-energy nuclear collisions," *Annual Review of Nuclear and Particle Science*, vol. 57, pp. 205—-243, Nov 2007.

[105] "Reference Multiplicity." Internal communications. last accessed: 25/09/2020.

[106] K. A. Olive *et al.*, “Review of Particle Physics,” *Chin. Phys.*, vol. C38, p. 41, 2014.

[107] K. A. Olive *et al.*, “Review of Particle Physics,” *Chin. Phys.*, vol. C38, p. 84, 2014.

[108] S. Roesler, R. Engel, and J. Ranft, “The Monte Carlo Event Generator DPMJET-III,” *Advanced Monte Carlo for Radiation Physics, Particle Transport Simulation and Applications*, pp. 1033—-1038, 2001.

[109] S. Agostinelli, J. Allison, K. Amako, *et al.*, “Geant4—a simulation toolkit,” *Nuclear Instruments and Methods in Physics Research Section A: Accelerators, Spectrometers, Detectors and Associated Equipment*, vol. 506, no. 3, pp. 250–303, 2003.

[110] E. Willsher, “Hadrochemistry of Particle Production in Small Systems with ALICE at the LHC,” *Springer Proc. Phys.*, vol. 250, pp. 233–237. 5 p, 2020.

[111] E. Willsher, “Multi-strange Particle Production in p-Pb Collisions at $\sqrt{s_{\mathrm{NN}}} = 8.16$ TeV Measured with ALICE at the LHC.” Presentation, International Nuclear Physics Conference, 2019.

[112] K. A. Olive *et al.*, “Review of Particle Physics,” *Chin. Phys.*, vol. C38, p. 87, 2014.

[113] K. A. Olive *et al.*, “Review of Particle Physics,” *Chin. Phys.*, vol. C38, p. 86, 2014.

[114] G. Van Buren, “The $\Sigma^0/\Lambda$ ratio in high energy nuclear collisions,” *J. Phys. G*, vol. 31, pp. S1127–S1130, 2005.

[115] R. Barlow, “Systematic errors: Facts and fictions,” in *Conference on Advanced Statistical Techniques in Particle Physics*, pp. 134–144, 7 2002.

[116] D. S. de Albequerque, “Multi-strange Hadrons in Pb-Pb collisions at the LHC with ALICE.” PhD thesis, Universidade Estadual de Campinas, Aug. 2019.

[117] B. Abelev *et al.*, “Multiplicity dependence of the average transverse momentum in pp, p–Pb, and Pb–Pb collisions at the LHC,” *Physics Letters B*, vol. 727, no. 4, pp. 371–380, 2013.

[118] C. Tsallis, “Possible Generalization of Boltzmann-Gibbs Statistics,” *J Stat Phys*, vol. 52, p. 479, 1988.

[119] E. Schnedermann, J. Sollfrank, and U. Heinz, “Thermal phenomenology of hadrons from 200AGeV S+S collisions,” *Physical Review C*, vol. 48, p. 2462–2475, Nov 1993.

[120] B. Abelev *et al.*, “$K^0_S$ and $\Lambda$ Production in Pb-Pb Collisions at $\sqrt{s_{NN}}$=2.76 TeV,” *Phys. Rev. Lett.*, vol. 111, p. 222301, Nov 2013.

[121] S. Acharya *et al.*, “Multiplicity dependence of (multi-)strange hadron production in proton-proton collisions at $\sqrt{s} = 13$ TeV,” *Eur. Phys. J. C*, vol. 80, no. 2, p. 167, 2020.

[122] S. Bufalino, “Energy and multiplicity dependence of identified particle production in small systems with ALICE at the LHC.” 10th International Workshop on Multiple Partonic Interactions at the LHC, 2018.

# Appendix A

# Cut Study Plots

This chapter contains a complete set of the plots used in this analysis' cut study, a subset of which are shown in section 4.4. These plots were used both for the determination of default cuts, and those values to be used in the systematic uncertainty study.

The plots show signal significance, top, and fraction of signal remaining relative to fully loose cuts, bottom, as a function of cut value. Also displayed are the various values chosen for the different cuts; magenta denotes the value chosen for the default cut, and grey those used in the evaluation of systematics. The plots used for the $\mathrm{K^0_S}$ analysis are shown in figures A.1, A.2 and A.3, and those used for the $\Lambda$ analysis are shown in figures A.4, A.5 and A.6.

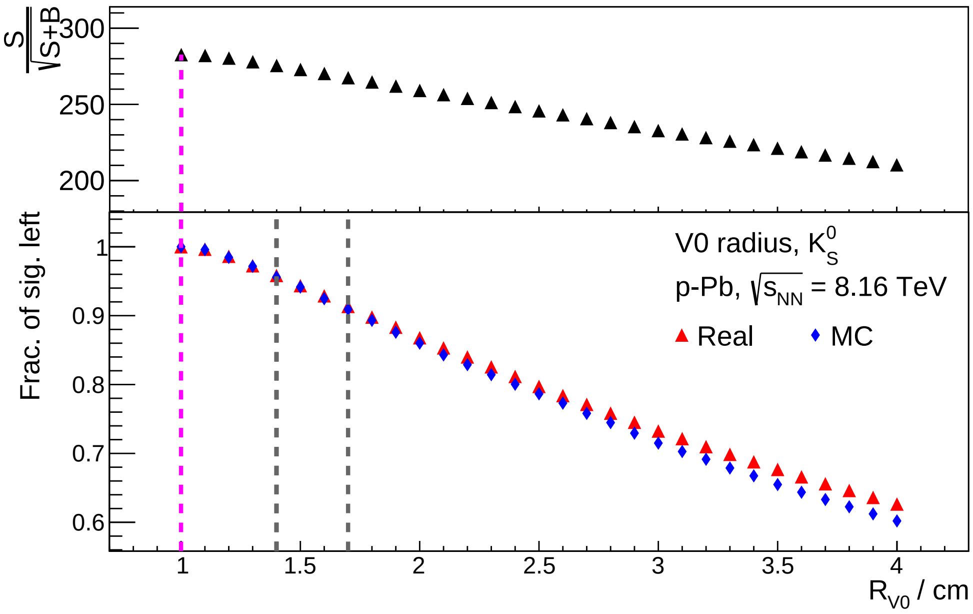

(a) $V^0$ decay radius.

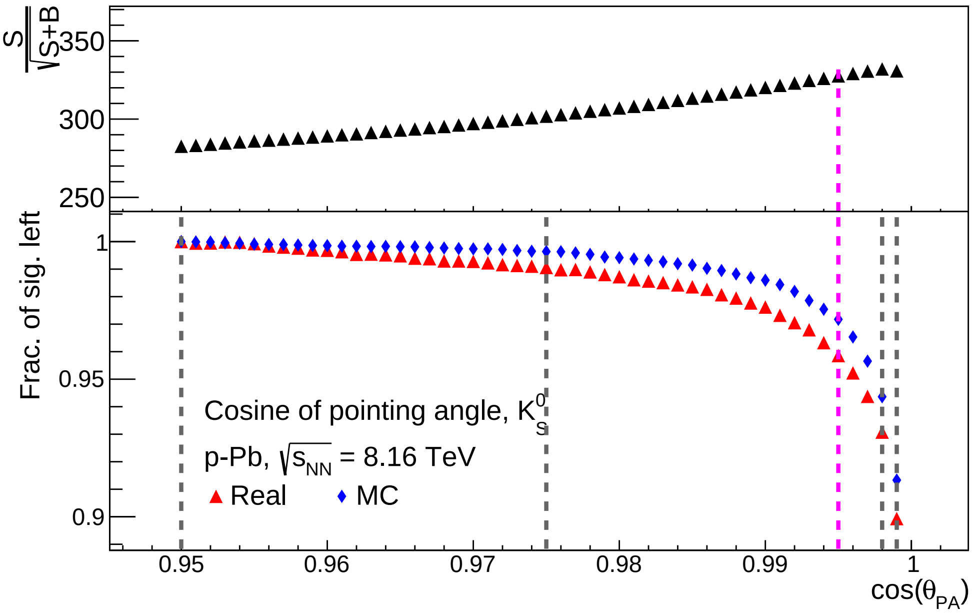

(b) Cosine of pointing angle.

Figure A.1: Signal significance, top, and fraction of signal remaining relative to the loosest cut value available, bottom, for the $K^0_S$ analysis. Red markers indicate real data points, and blue, those from Monte Carlo data.

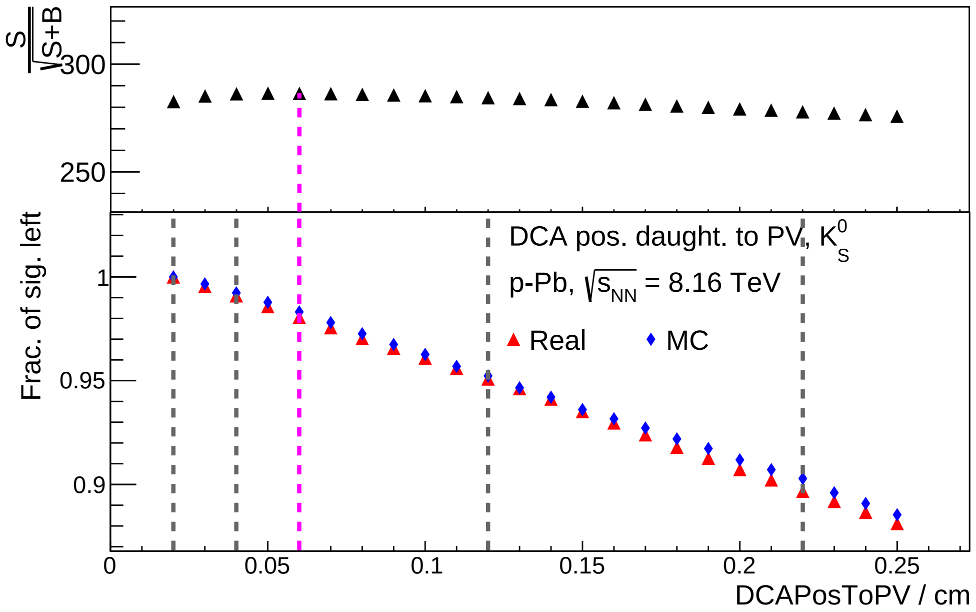

(a) DCA of positive daughter track to primary vertex.

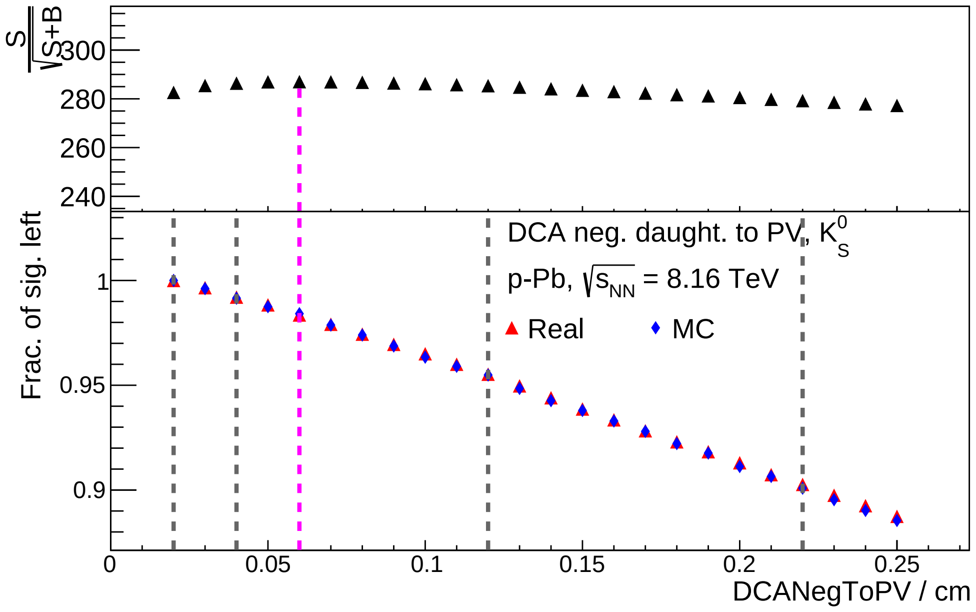

(b) DCA of negative daughter track to primary vertex.

Figure A.2: Signal significance, top, and fraction of signal remaining relative to the loosest cut value available, bottom, for the $K^0_S$ analysis. Red markers indicate real data points, and blue, those from Monte Carlo data.

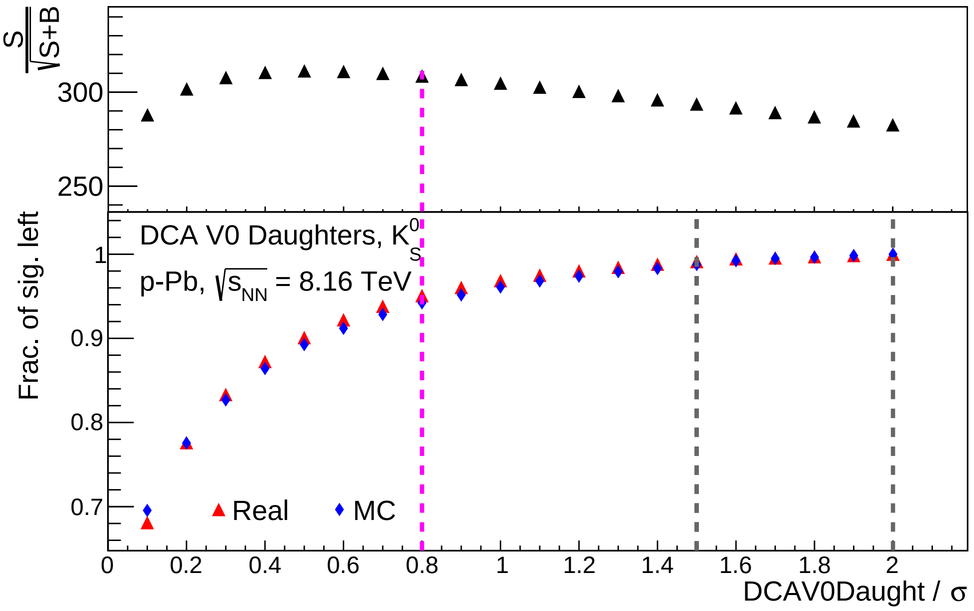

(a) DCA of daughters to each other.

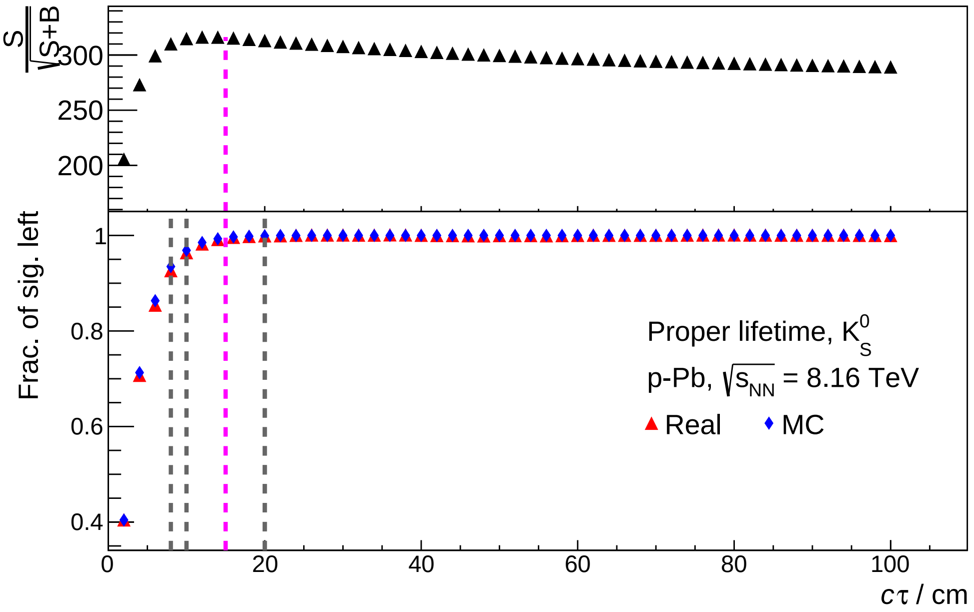

(b) Proper lifetime times the speed of light, $c\tau$.

Figure A.3: Signal significance, top, and fraction of signal remaining relative to the loosest cut value available, bottom, for the $K^0_S$ analysis. Red markers indicate real data points, and blue, those from Monte Carlo data.

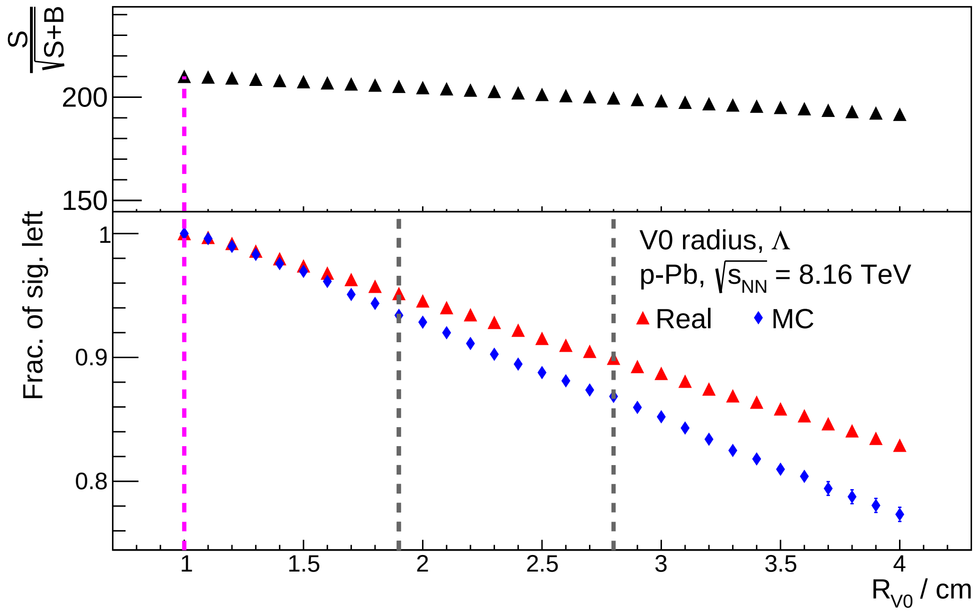

(a) $V^0$ decay radius.

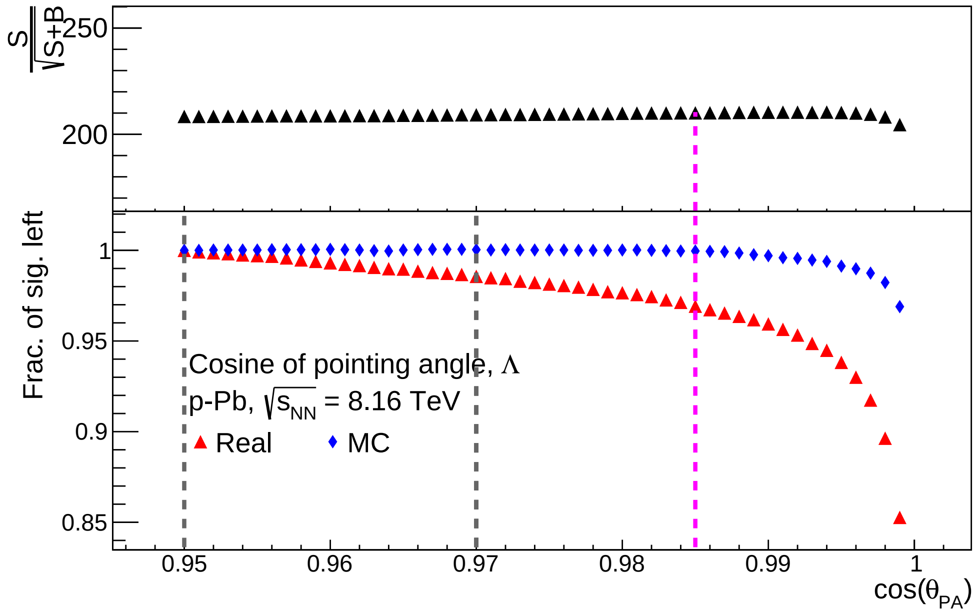

(b) Cosine of pointing angle.

Figure A.4: Signal significance, top, and fraction of signal remaining relative to the loosest cut value available, bottom, for the Λ analysis. Red markers indicate real data points, and blue, those from Monte Carlo data.

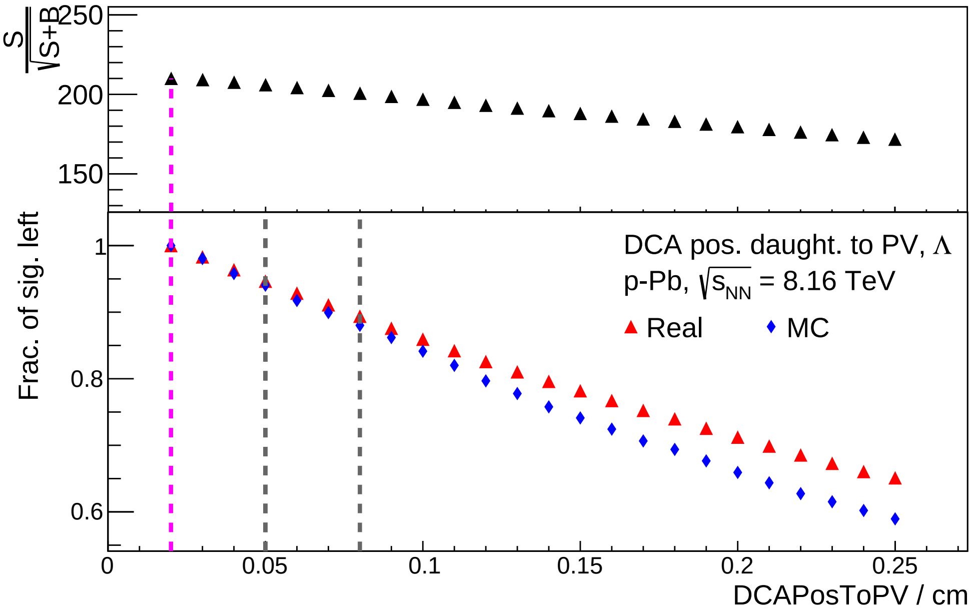

(a) DCA of positive daughter track to primary vertex.

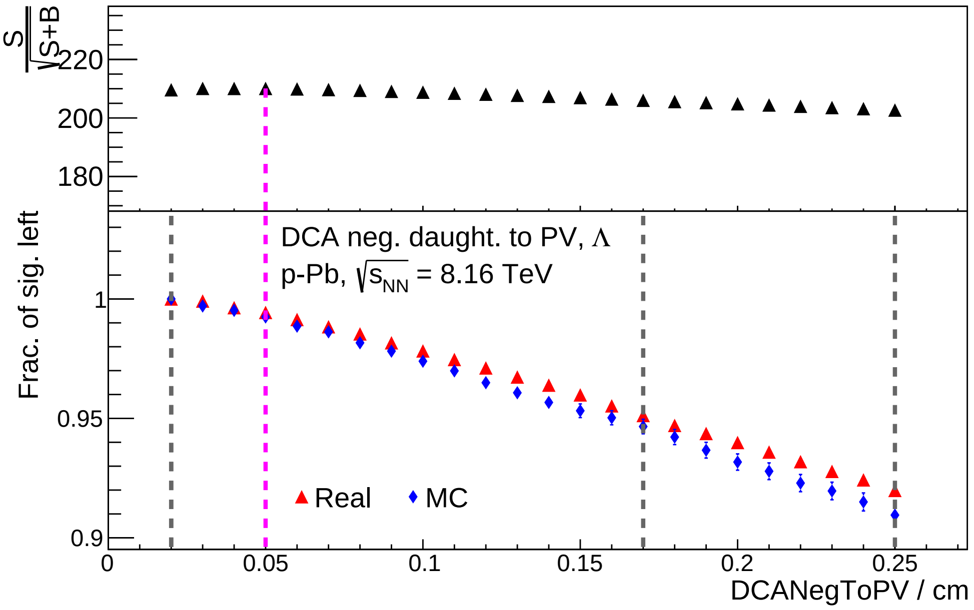

(b) DCA of negative daughter track to primary vertex.

Figure A.5: Signal significance, top, and fraction of signal remaining relative to the loosest cut value available, bottom, for the Λ analysis. Red markers indicate real data points, and blue, those from Monte Carlo data.

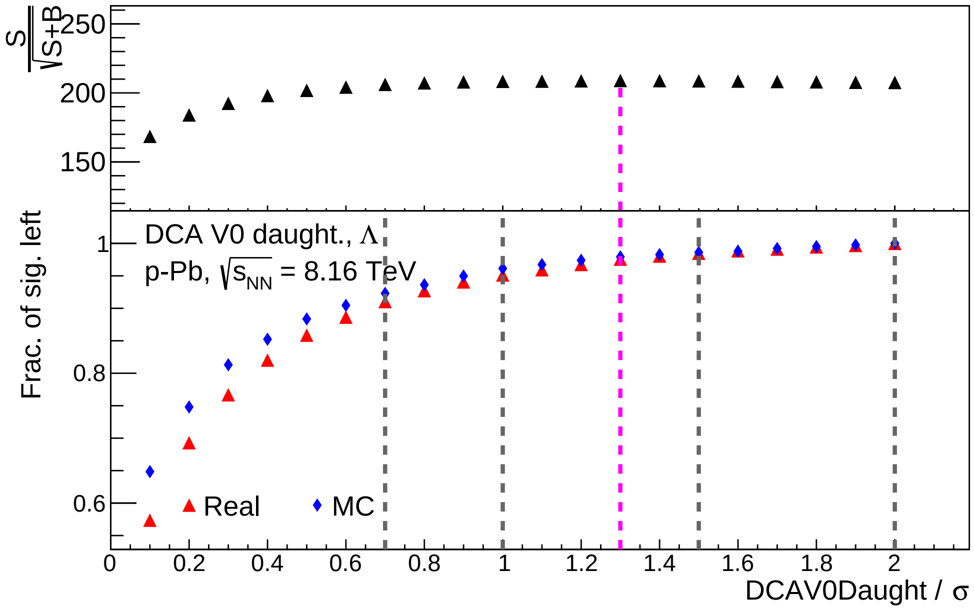

(a) DCA of daughter tracks to each other.

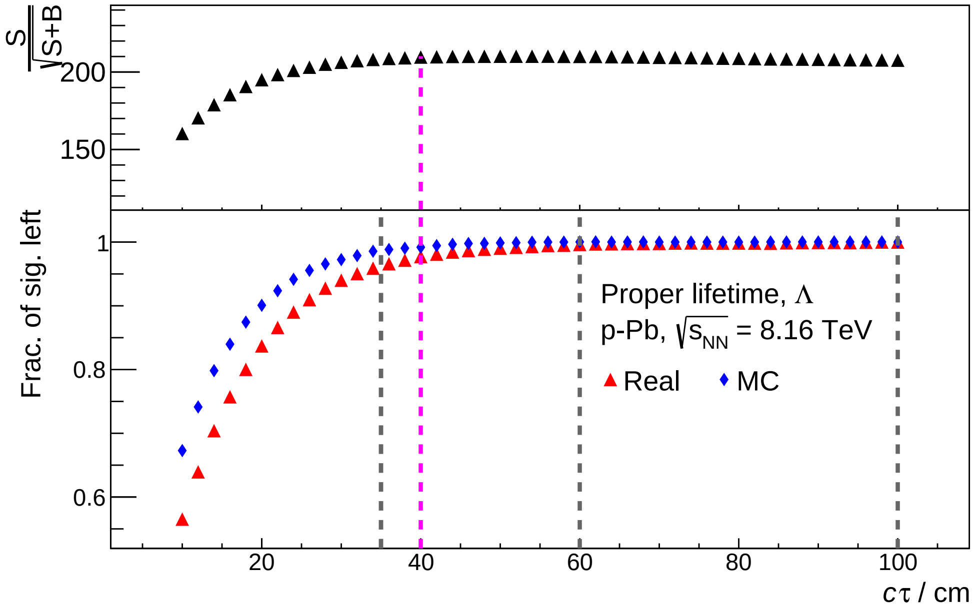

(b) Proper lifetime times the speed of light, $c\tau$.

Figure A.6: Signal significance, top, and fraction of signal remaining relative to the loosest cut value available, bottom, for the $\Lambda$ analysis. Red markers indicate real data points, and blue, those from Monte Carlo data.

# Appendix B

# Self-consistency test plots

Section 4.6 describes a self-consistency test performed on the Monte Carlo data used for the analysis described in this thesis. In particular, figure 4.14 shows a comparison between yields extracted using multiplicity-dependent and multiplicity-independent efficiencies. For the comparison shown in figure 4.14, the same file was used for both candidate selection and efficiency correction. Another result that may be of interest is to perform the comparison again, but using different files to provide the candidates and efficiency correction.

Figures B.1 and B.2 show ratios as a function of final state multiplicity, between the reconstructed yields of $\mathrm{K^0_S}$ candidates to the truth-level yield of the same candidates. The reconstructed yields in figure B.1 are calculated from spectra created using multiplicity-dependent efficiencies, and those in figure B.2 result from the consistent use of multiplicity-integrated efficiencies.

As can be seen the ratios in figure B.1, while consistent with unity within errors, fluctuate much further than in figure B.2. This suggests that the use of multiplicity-integrated efficiencies provides more accurate results than the use of multiplicity-dependent efficiencies, especially in a position where the candidates used to generate the $p_\mathrm{T}$ spectra are not the same as the candidates used to create efficiencies to correct said spectra.

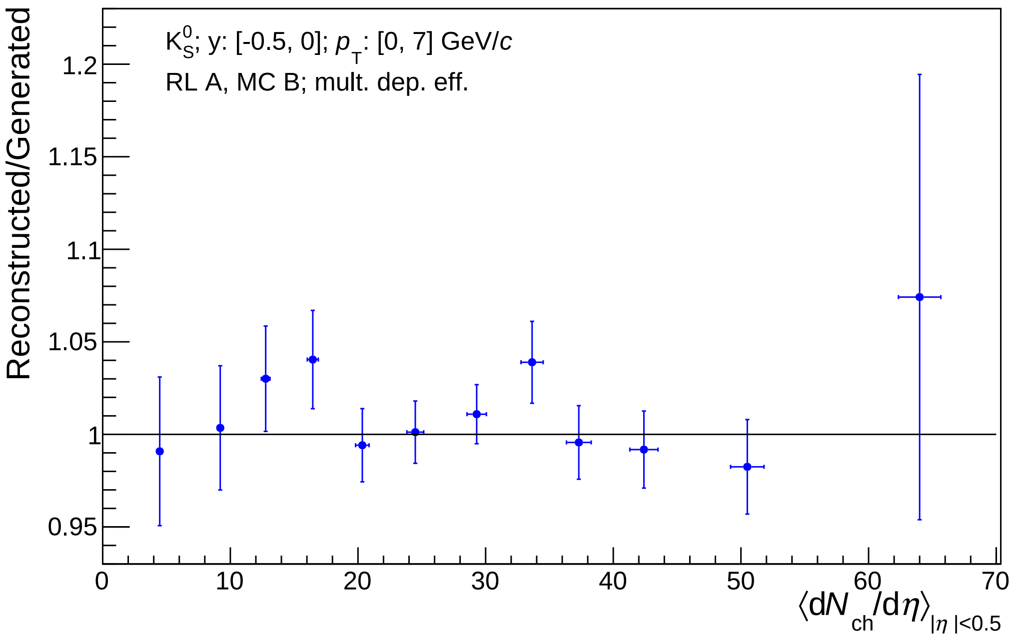

Figure B.1: Ratio between the reconstructed $K^0_S$ yield from MC file A, using multiplicity-dependent efficiencies provided from MC file B, to the truth-level generated yield in file A.

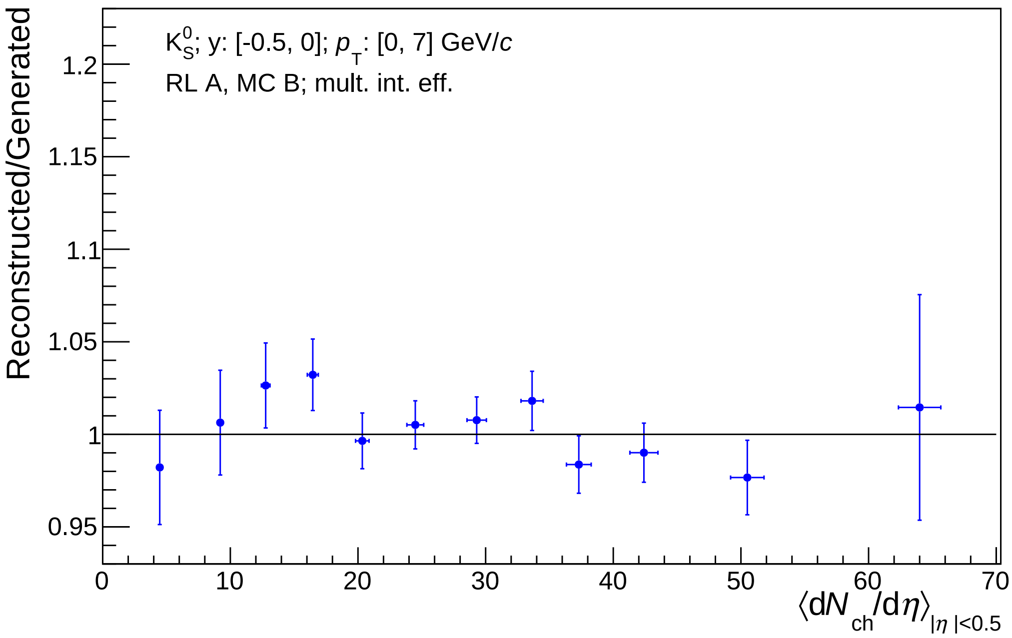

Figure B.2: Ratio between the reconstructed $K^0_S$ yield from MC file A, using multiplicity-integrated efficiencies provided from MC file B, to the truth-level generated yield in file A.

# Appendix C

# Systematic study plots

This chapter contains the plots used for the determination of systematic errors, as described in section 4.7. These show the percentage difference between the default spectra, and those calculated with the different systematic cuts, as a function of $p_T$. The cut values used for this process are given in tables 4.5, for the $\mathrm{K^0_S}$ analysis, and 4.6, for the $\Lambda(\bar{\Lambda})$ analysis. Errors shown are Roger Barlow's sigma [115]; if the maximum deviation between spectra is larger than one sigma, then they go towards the final systematic error.

Figures C.1, C.2, C.3, C.4 and C.5 display plots used in the $\mathrm{K^0_S}$ analysis; figures C.6, C.7, C.8, C.9, C.10 and C.11 show plots used in the $\Lambda$ analysis, and figures C.12, C.13, C.14, C.15 and C.16 show plots from the $\bar{\Lambda}$ analysis.

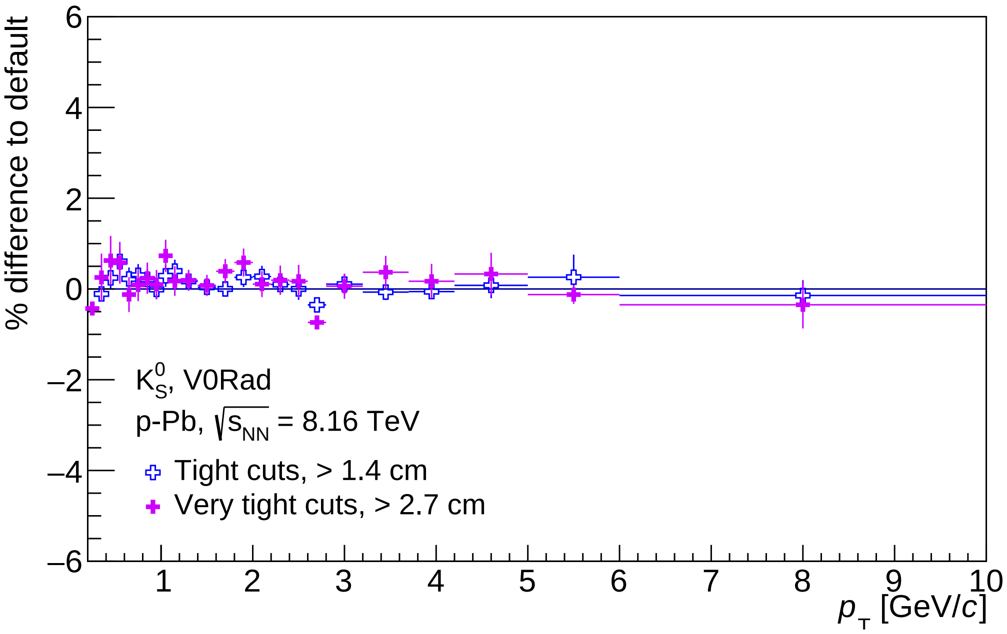

(a) $V^0$ decay radius.

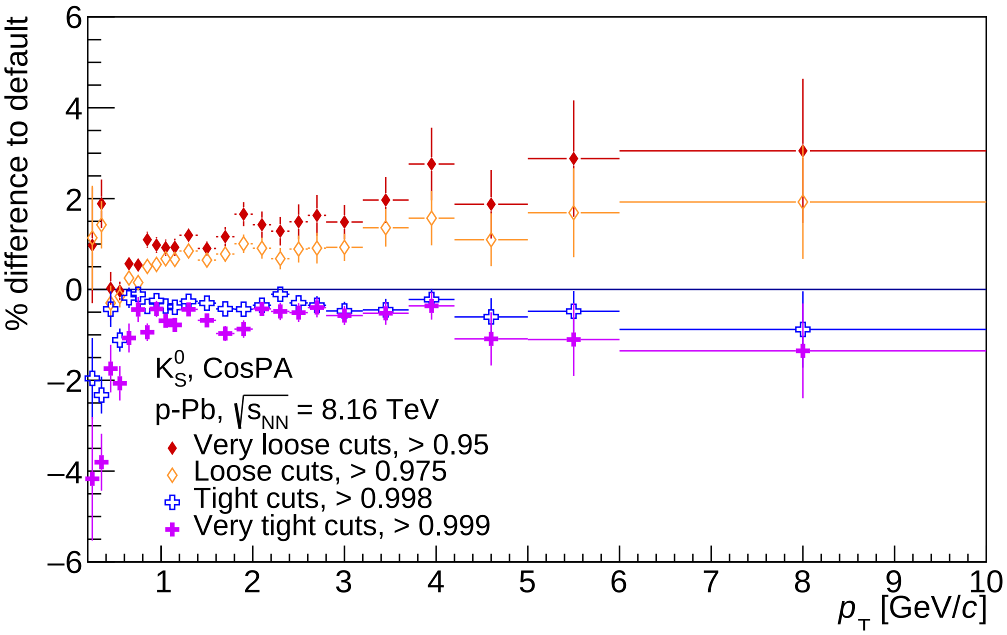

(b) Cosine of pointing angle.

Figure C.1: Ratio of systematic to default spectra as function of $p_T$ due to changes in candidate selection criteria. Shown are plots for the $K^0_S$ analysis.

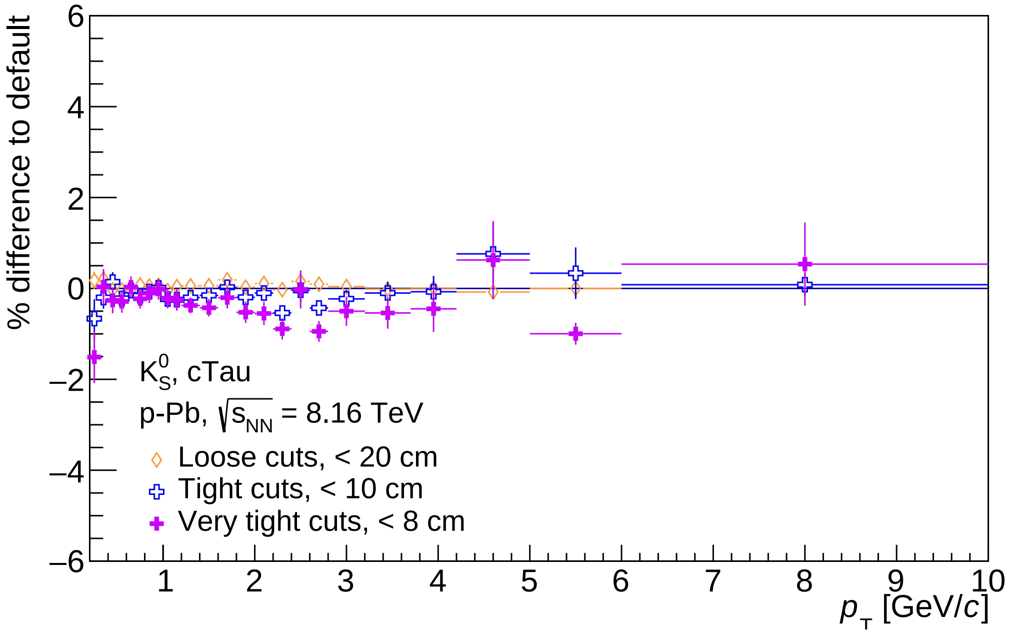

(a) Proper lifetime times the speed of light, $c\tau$.

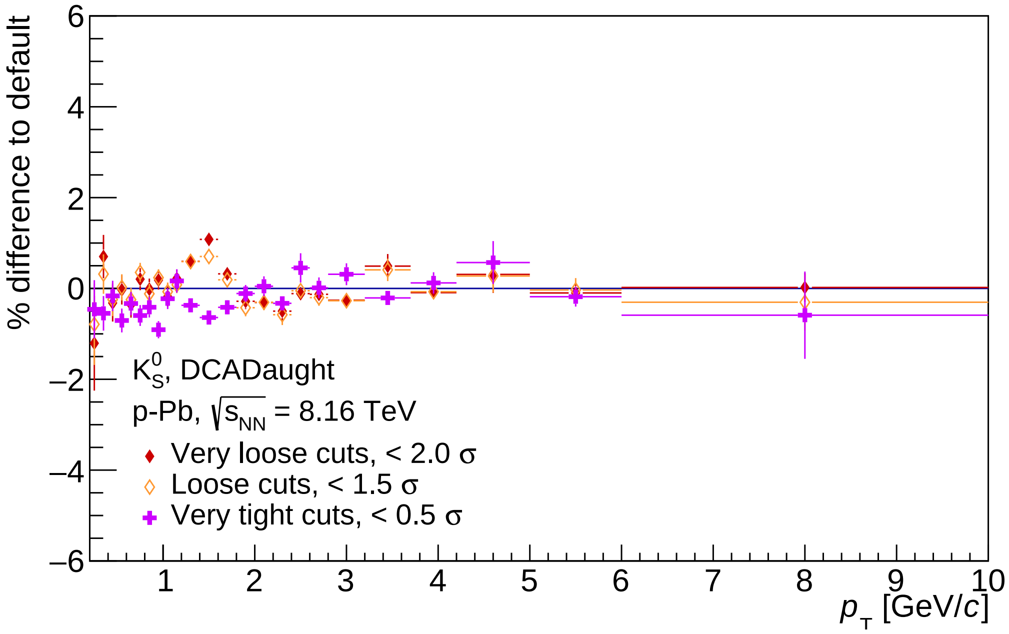

(b) DCA of daughter tracks, to each other.

Figure C.2: Ratio of systematic to default spectra as function of $p_T$ due to changes in candidate selection criteria. Shown are plots for the $K^0_S$ analysis.

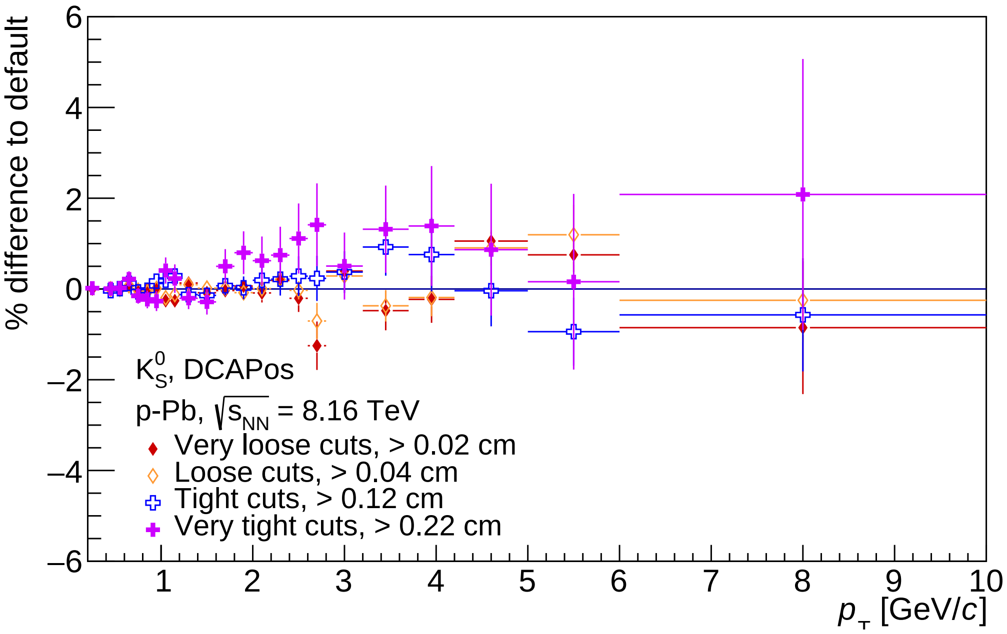

(a) DCA of positive daughter track to primary vertex.

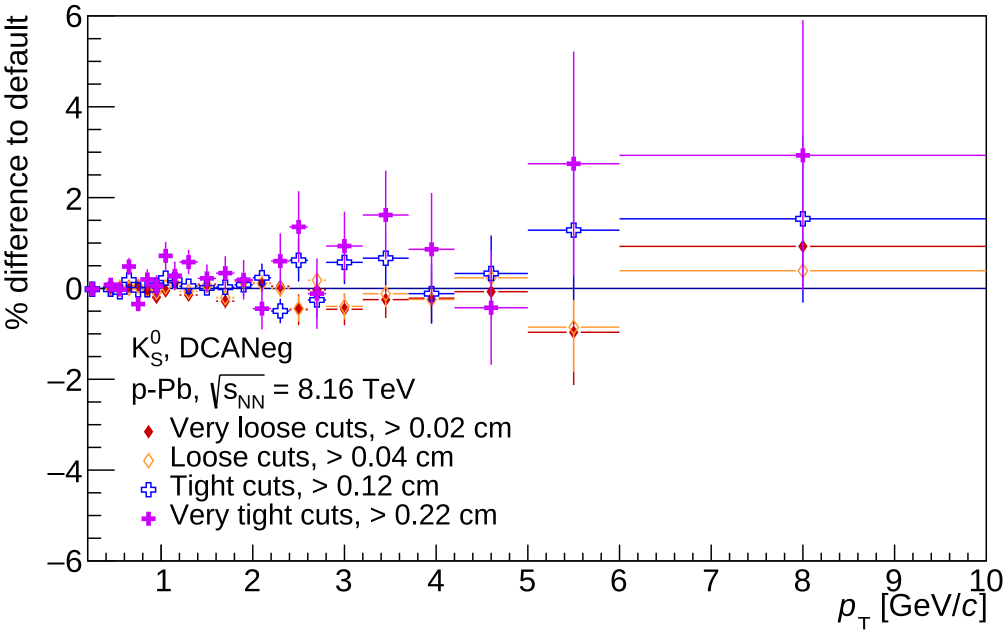

(b) DCA of negative daughter track to primary vertex.

Figure C.3: Ratio of systematic to default spectra as function of $p_T$ due to changes in candidate selection criteria. Shown are plots for the $K^0_S$ analysis.

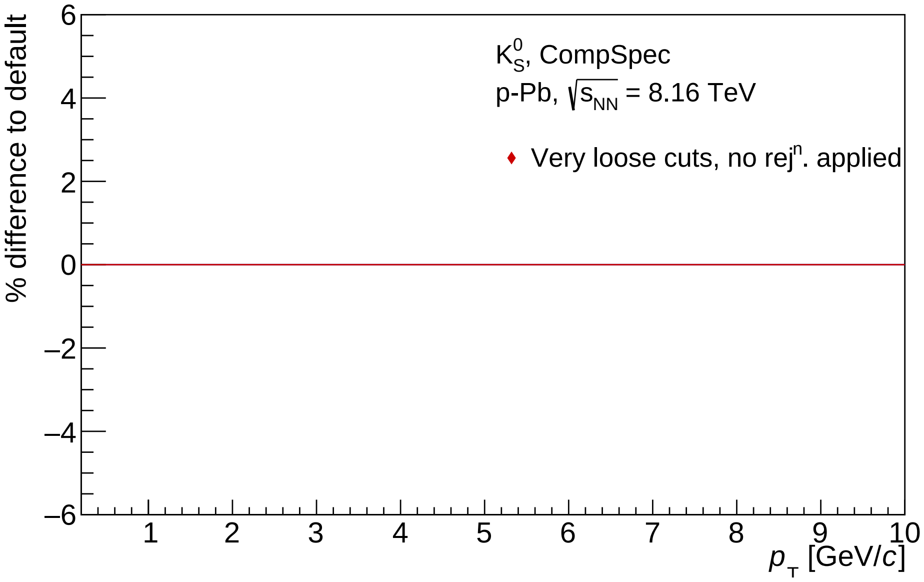

(a) Competing species rejection window. This plot demonstrates that, although a cut was placed on the competing species rejection window, no candidates were removed because of it.

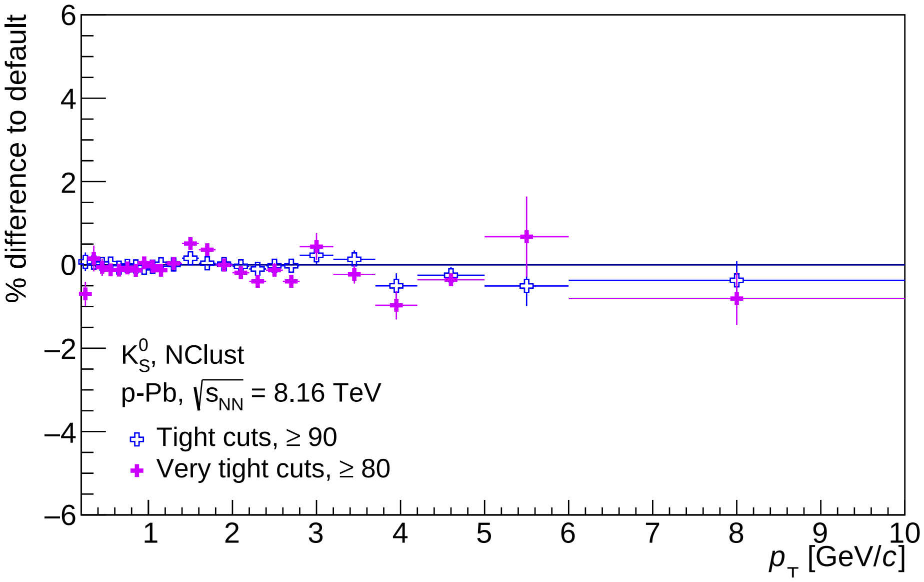

(b) Least number of TPC clusters hit.

Figure C.4: Ratio of systematic to default spectra as function of $p_T$ due to changes in candidate selection criteria. Shown are plots for the $\mathrm{K^0_S}$ analysis.

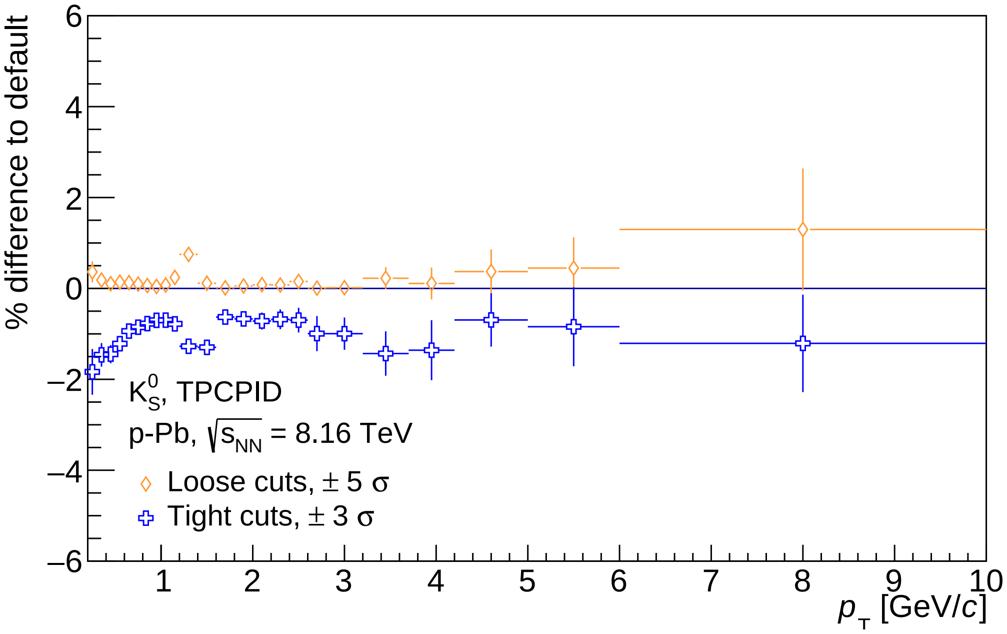

(a) TPC PID information.

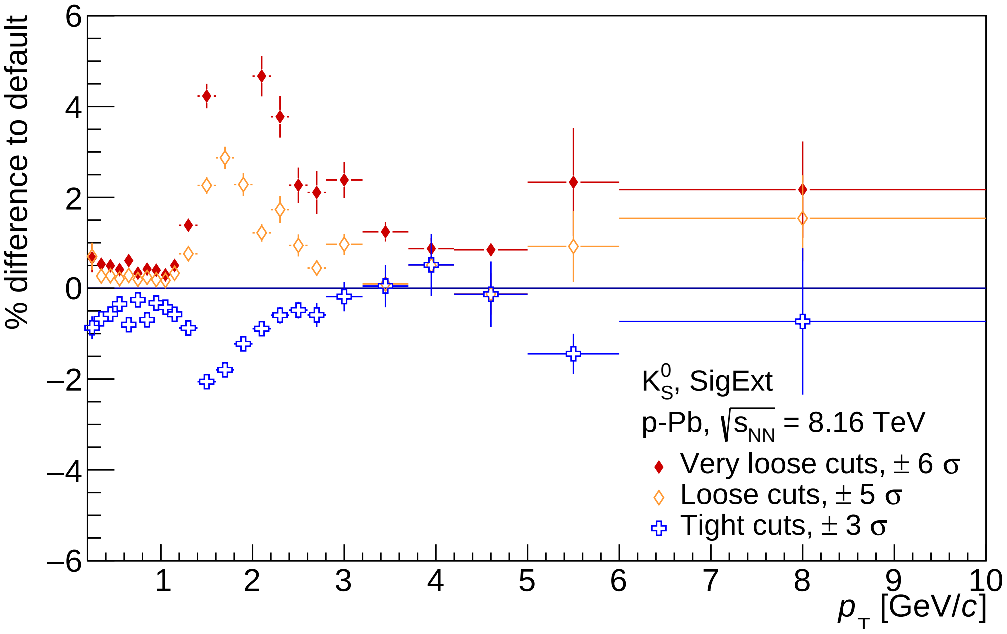

(b) Signal extraction window.

Figure C.5: Ratio of systematic to default spectra as function of $p_T$ due to changes in candidate selection criteria. Shown are plots for the $\mathrm{K}^0_\mathrm{S}$ analysis.

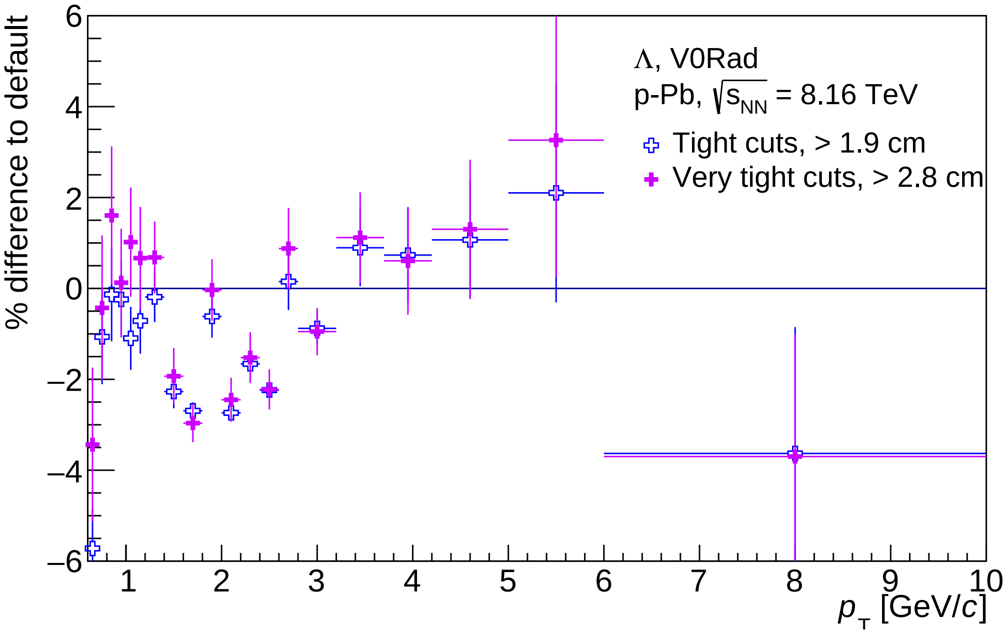

(a) $V^0$ decay radius.

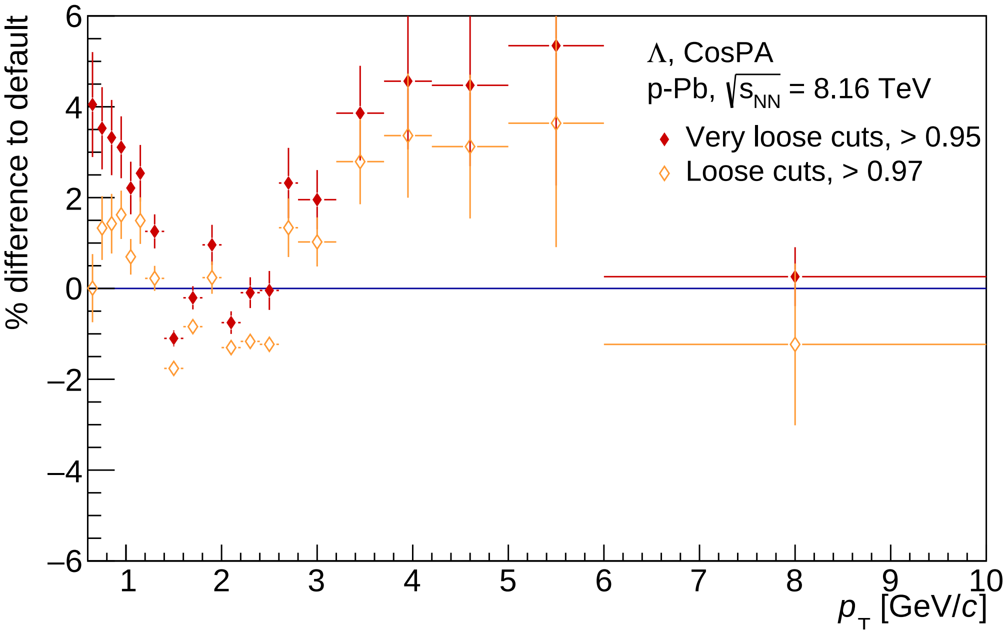

(b) Cosine of pointing angle.

Figure C.6: Ratio of systematic to default spectra as function of $p_T$ due to changes in candidate selection criteria. Shown are plots for the Λ analysis.

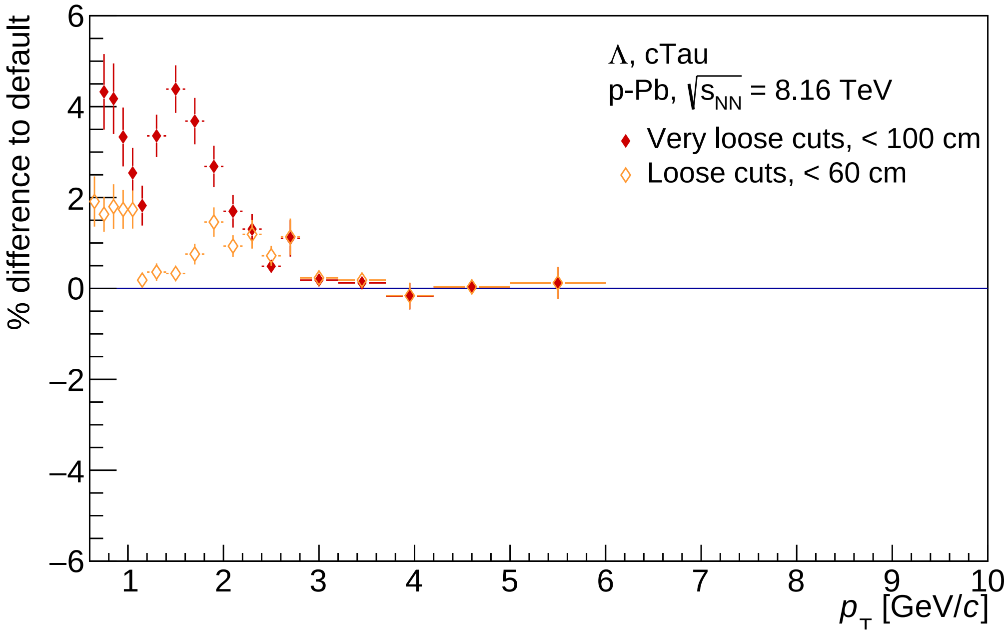

(a) Proper lifetime times the speed of light, $c\tau$.

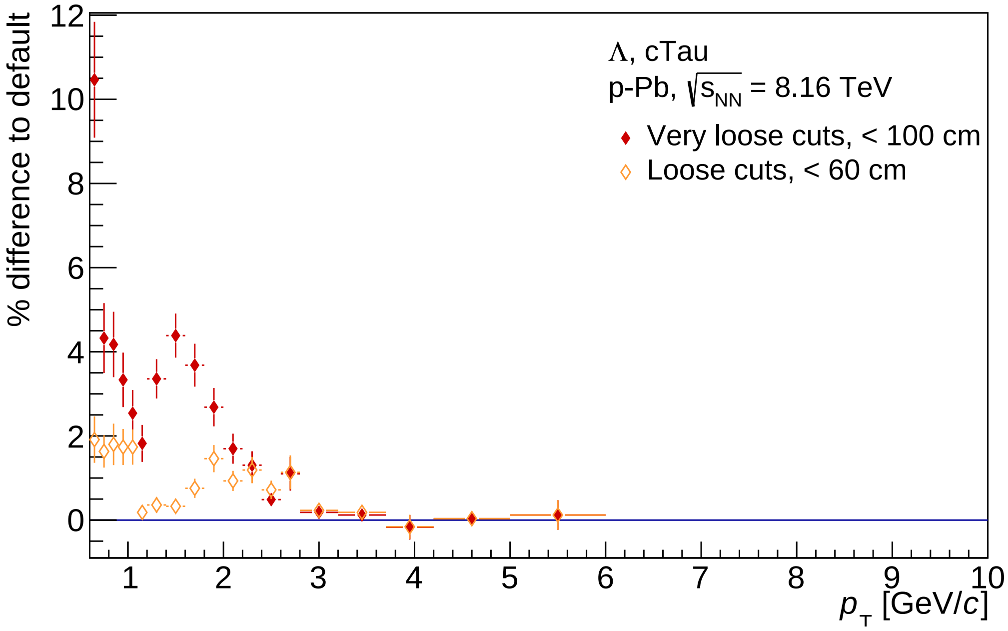

(b) Same as above, with wider y-axis range.

Figure C.7: Ratio of systematic to default spectra as function of $p_T$ due to changes in candidate selection criteria. Shown are plots for the Λ analysis.

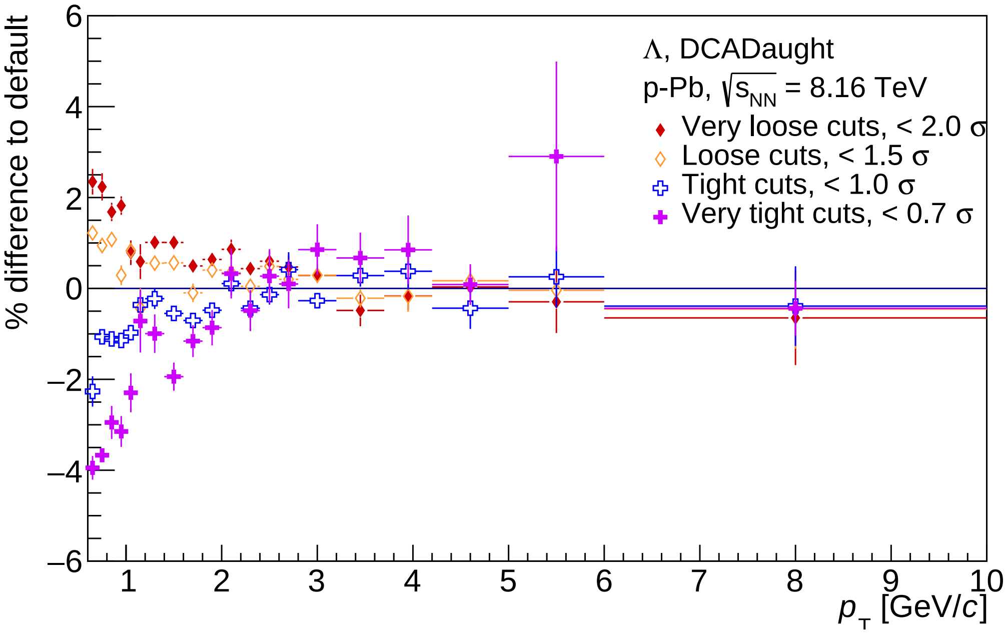

(a) DCA of daughter tracks, to each other.

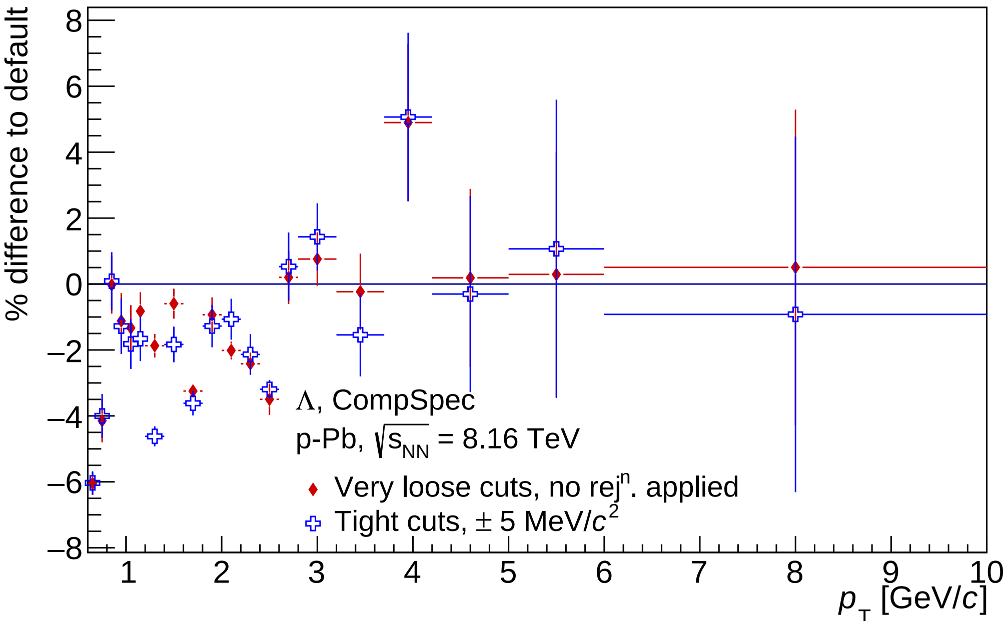

(b) Competing species rejection window.

Figure C.8: Ratio of systematic to default spectra as function of $p_T$ due to changes in candidate selection criteria. Shown are plots for the Λ analysis.

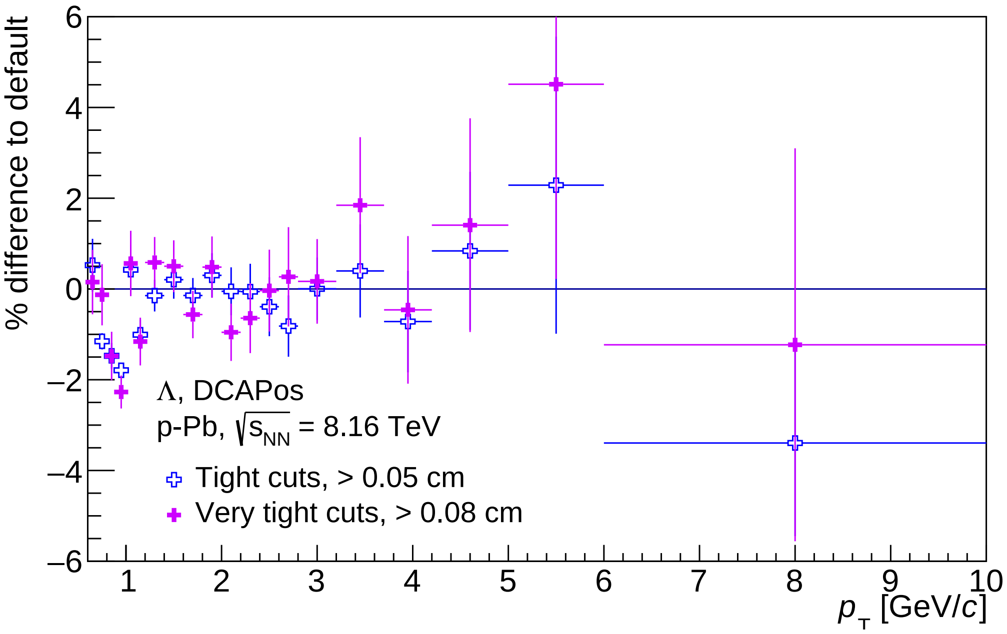

(a) DCA of positive daughter track to primary vertex.

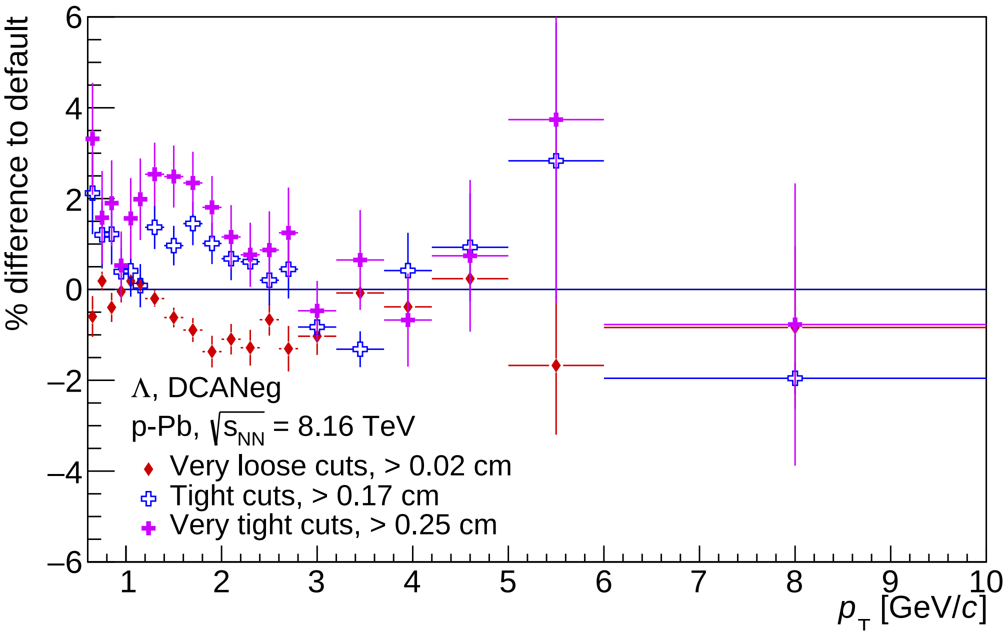

(b) DCA of negative daughter track to primary vertex.

Figure C.9: Ratio of systematic to default spectra as function of $p_T$ due to changes in candidate selection criteria. Shown are plots for the Λ analysis.

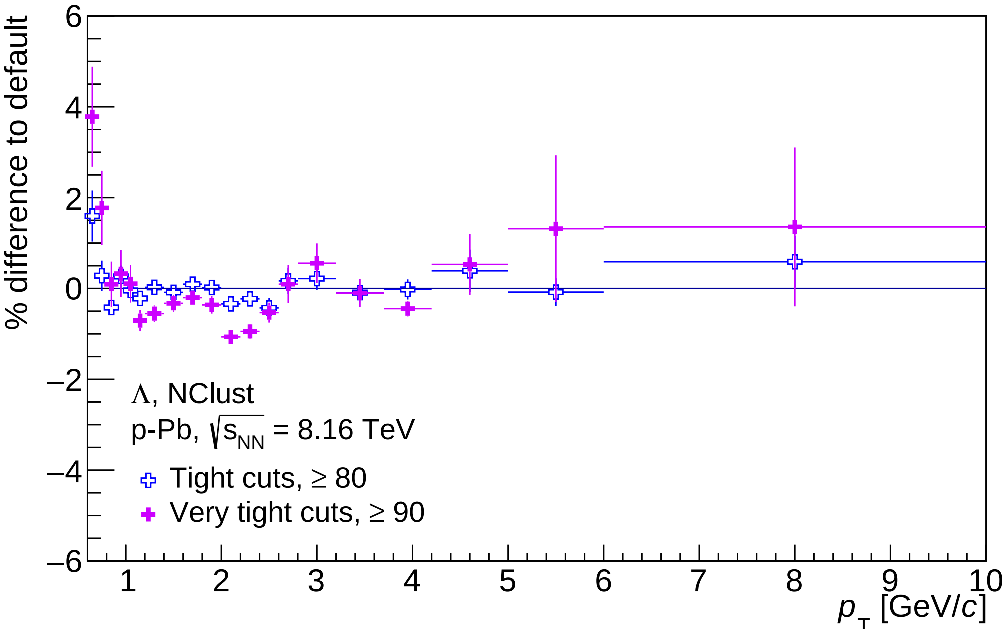

(a) Least number of TPC clusters hit.

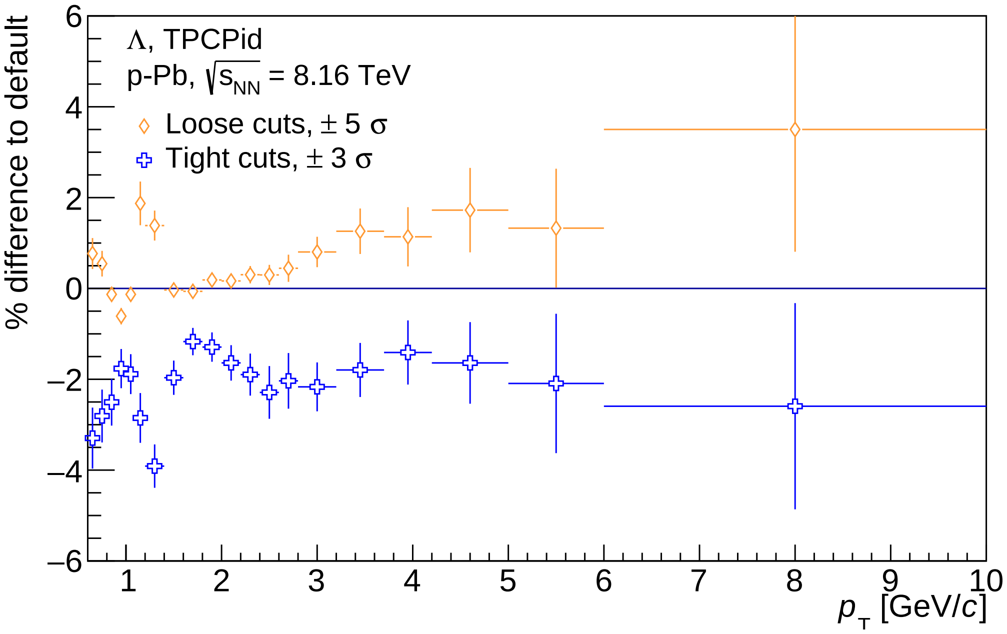

(b) TPC PID information.

Figure C.10: Ratio of systematic to default spectra as function of $p_T$ due to changes in candidate selection criteria. Shown are the plots for the Λ analysis.

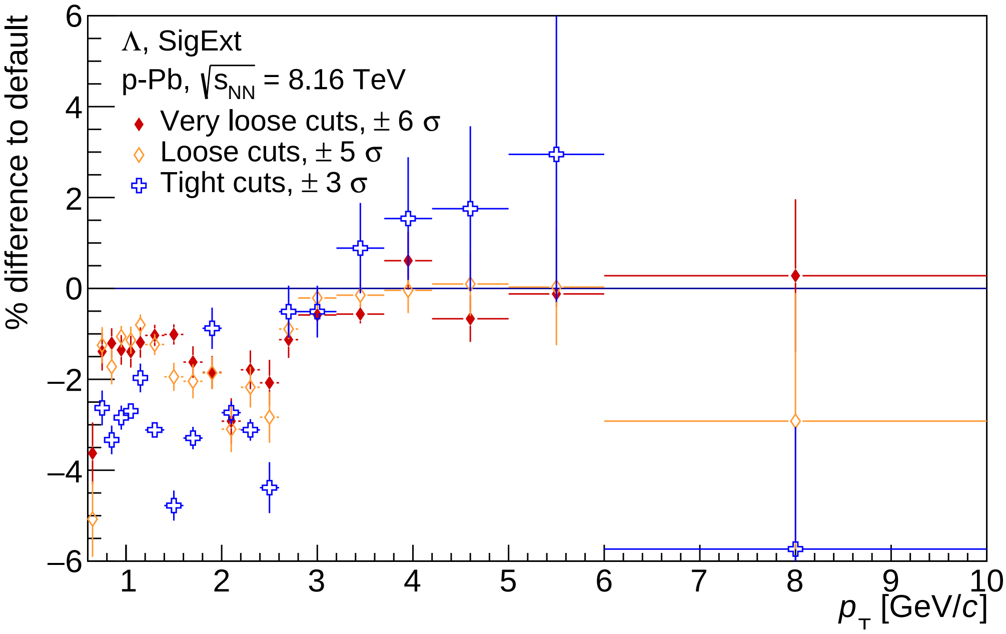

(a) Signal extraction window.

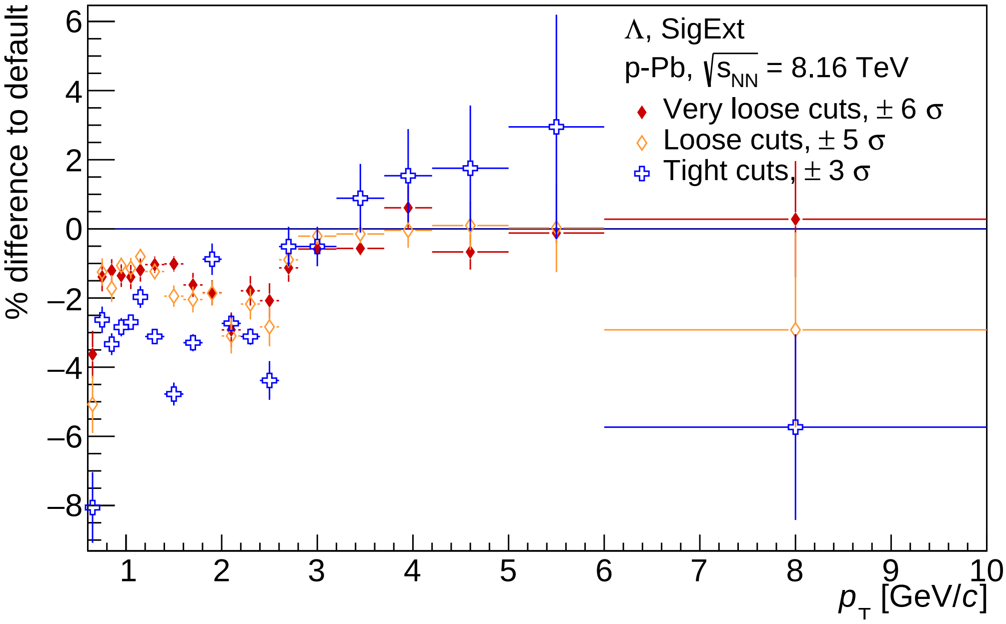

(b) Same as above, with wider y-axis range.

Figure C.11: Ratio of systematic to default spectra as function of $p_T$ due to changes in candidate selection criteria. Shown are plots for the Λ analysis.

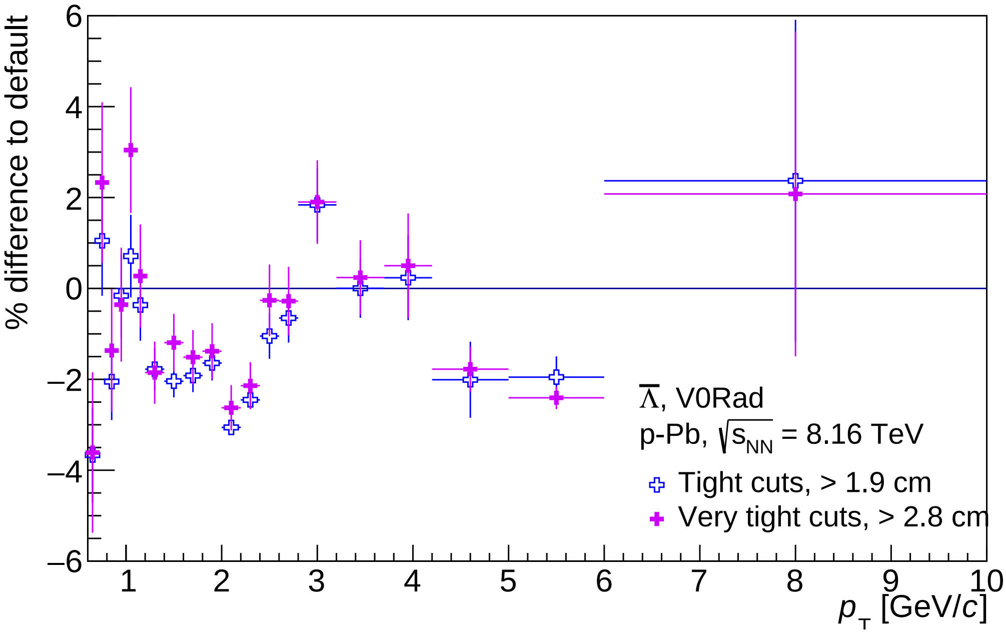

(a) $V^0$ decay radius.

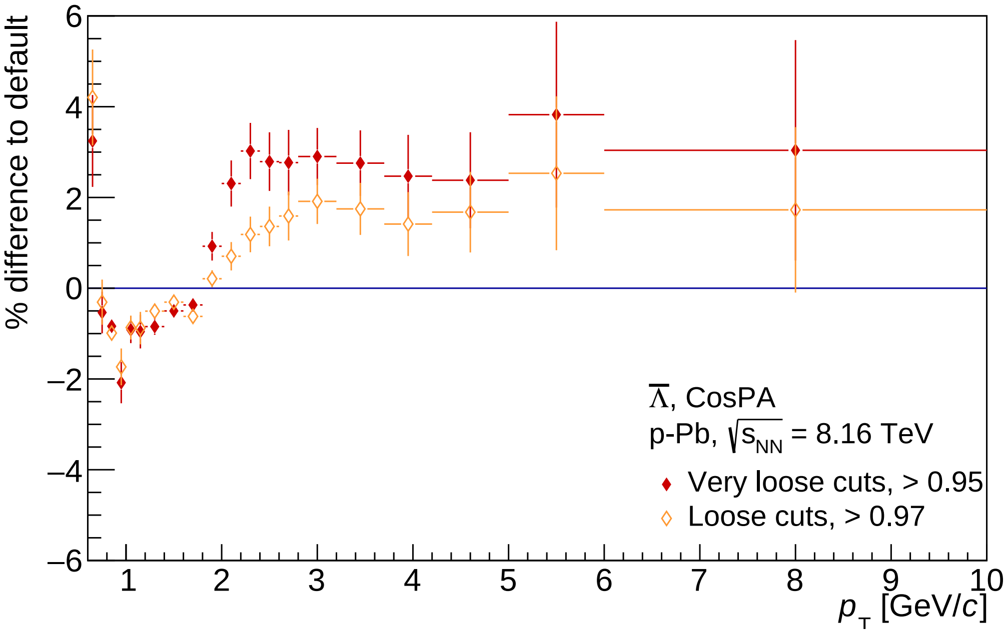

(b) Cosine of pointing angle.

Figure C.12: Ratio of systematic to default spectra as function of $p_T$ due to changes in candidate selection criteria. Shown are plots for the $\bar{\Lambda}$ analysis.

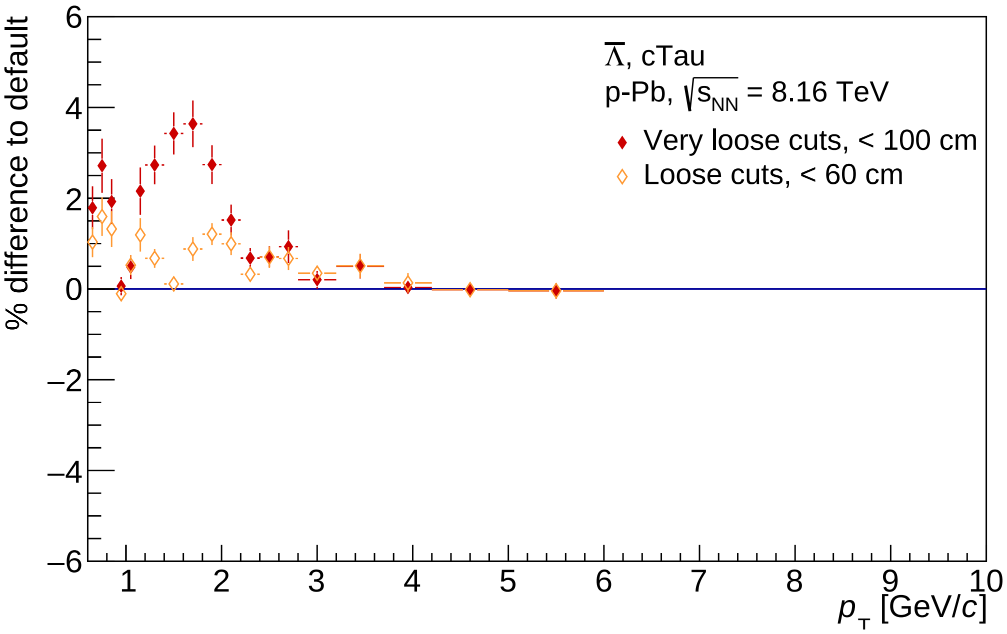

(a) Proper lifetime times the speed of light, $c\tau$.

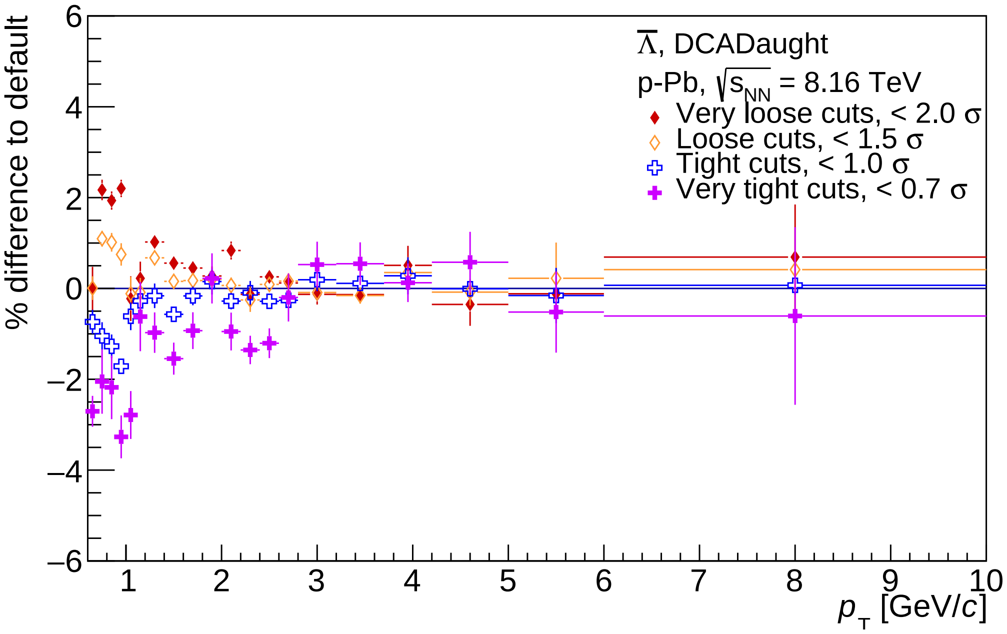

(b) DCA of daughter tracks, to each other.

Figure C.13: Ratio of systematic to default spectra as function of $p_T$ due to changes in candidate selection criteria. Shown are plots for the $\bar{\Lambda}$ analysis.

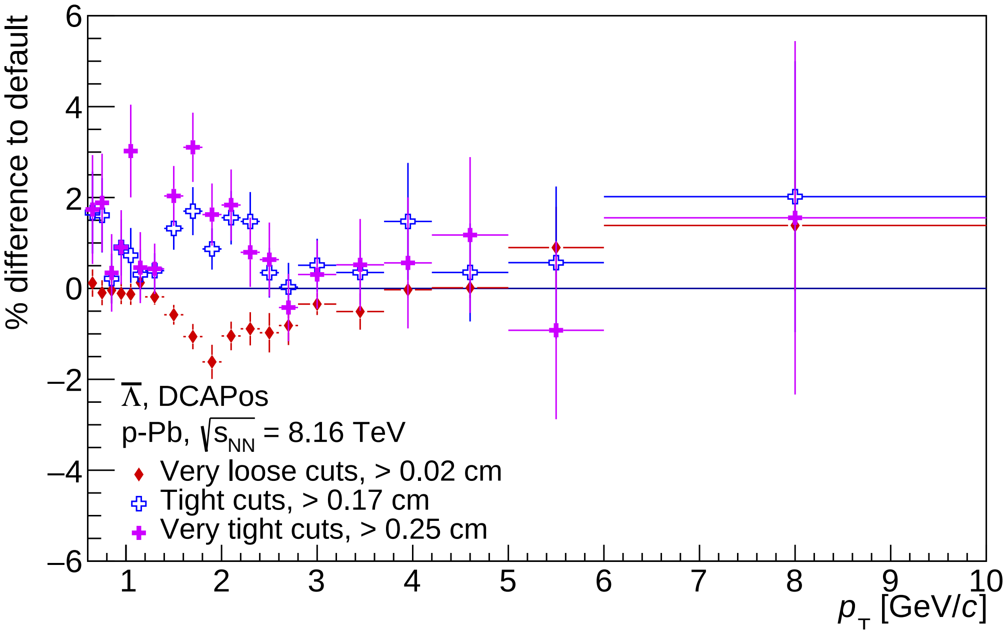

(a) DCA of positive daughter track to primary vertex.

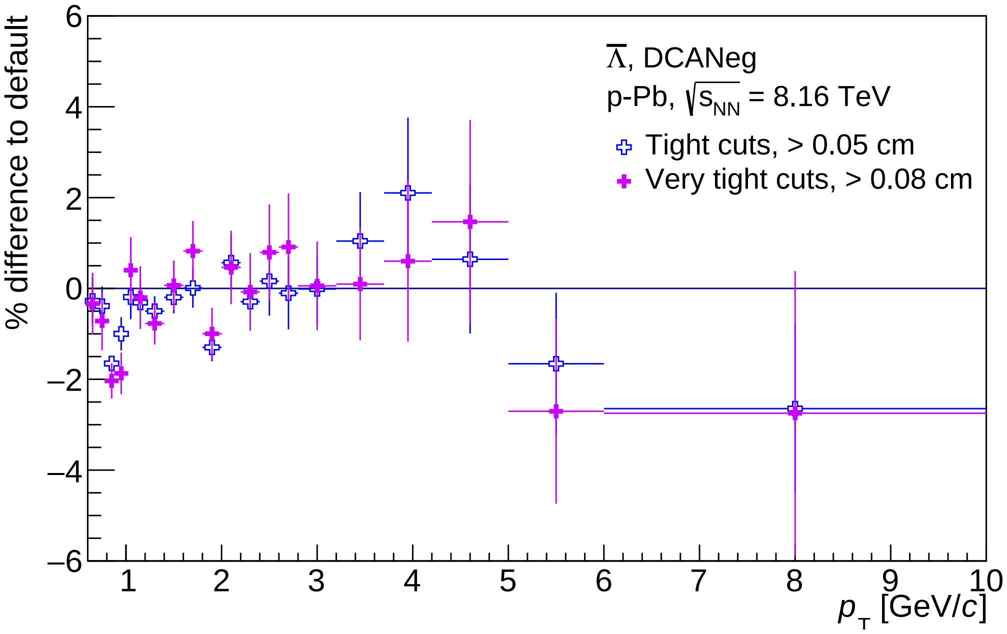

(b) DCA of negative daughter track to primary vertex.

Figure C.14: Ratio of systematic to default spectra as function of $p_T$ due to changes in candidate selection criteria. Shown are plots for the $\bar{\Lambda}$ analysis.

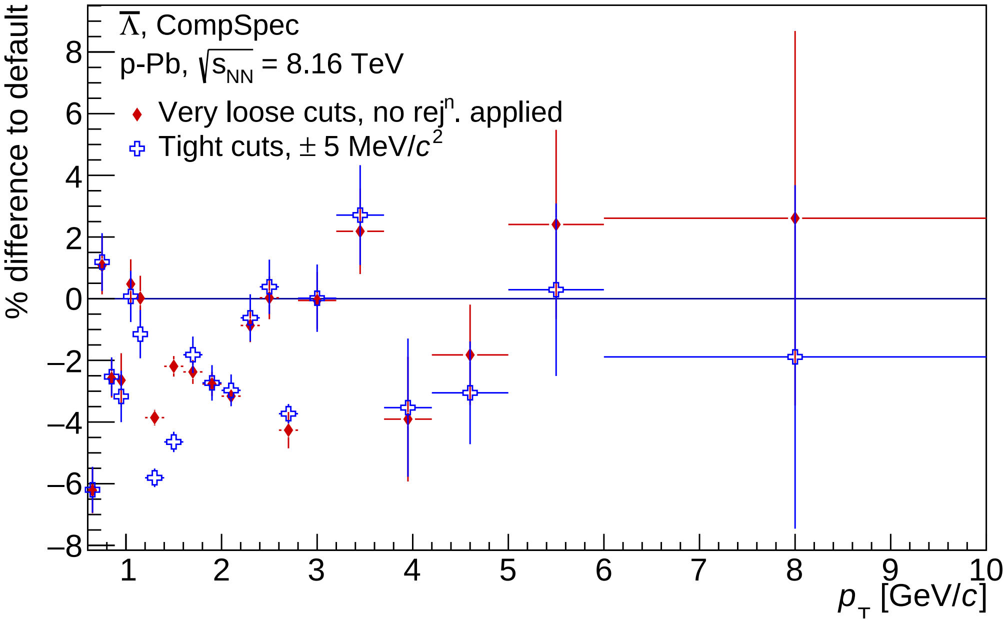

(a) Competing species rejection window.

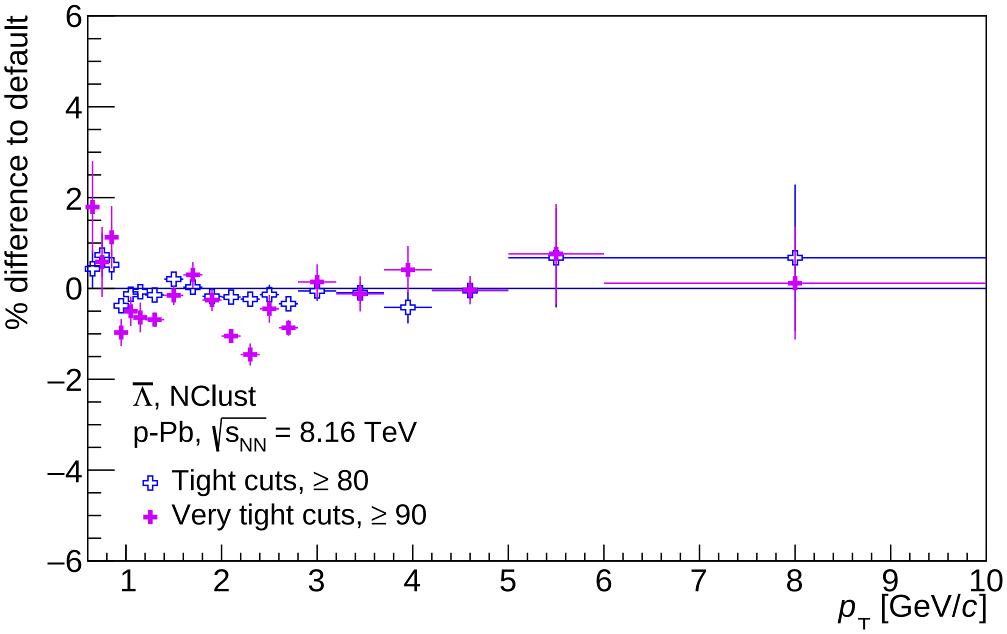

(b) Least number of TPC clusters hit.

Figure C.15: Ratio of systematic to default spectra as function of $p_T$ due to changes in candidate selection criteria. Shown are plots for the $\bar{\Lambda}$ analysis.

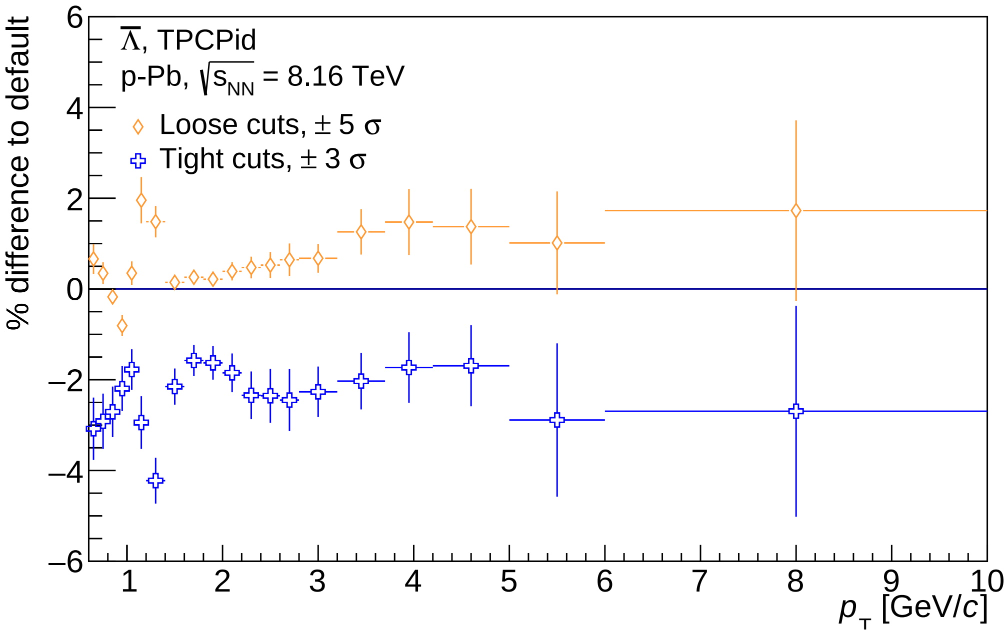

(a) TPC PID information.

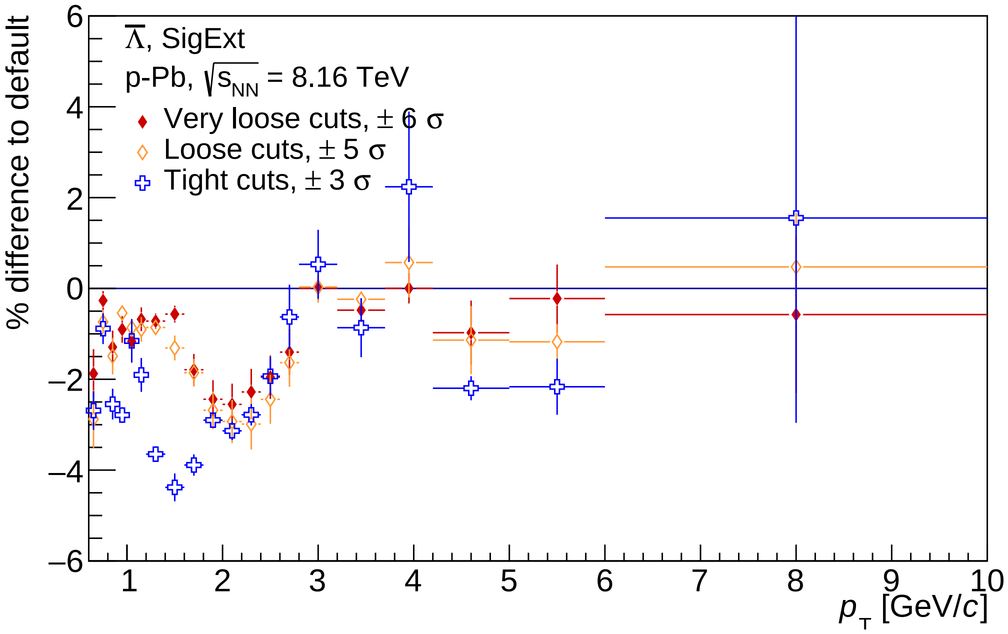

(b) Signal extraction window.

Figure C.16: Ratio of systematic to default spectra as function of $p_T$ due to changes in candidate selection criteria. Shown are plots for the $\bar{\Lambda}$ analysis.

# Appendix D

# Fitting Systematic Plots

The following chapter contains plots displaying the corrected spectra for all multiplicity bins used in this analysis. Also shown are the calculated fits, both using the default Lévy-Tsallis function and alternate functions investigated to evaluate the systematic uncertainty due to the fitting procedure. The method by which this uncertainty was evaluated, as well as a list of all functions used, is contained in section 5.1.1.

Figures D.1 to D.12 show the corrected spectra, calculated fits, and ratio between all fits and real data, for all multiplicity bins in the $\mathrm{K^0_S}$ analysis. The same for the $\Lambda + \bar{\Lambda}$ analysis are shown in plots D.13 to D.24.

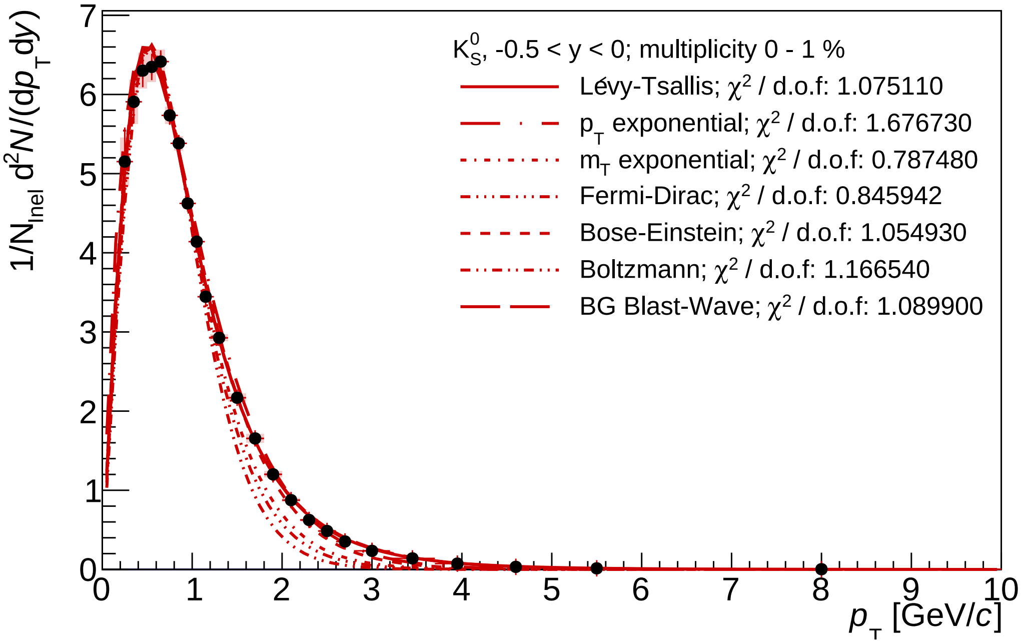

(a) Corrected spectra.

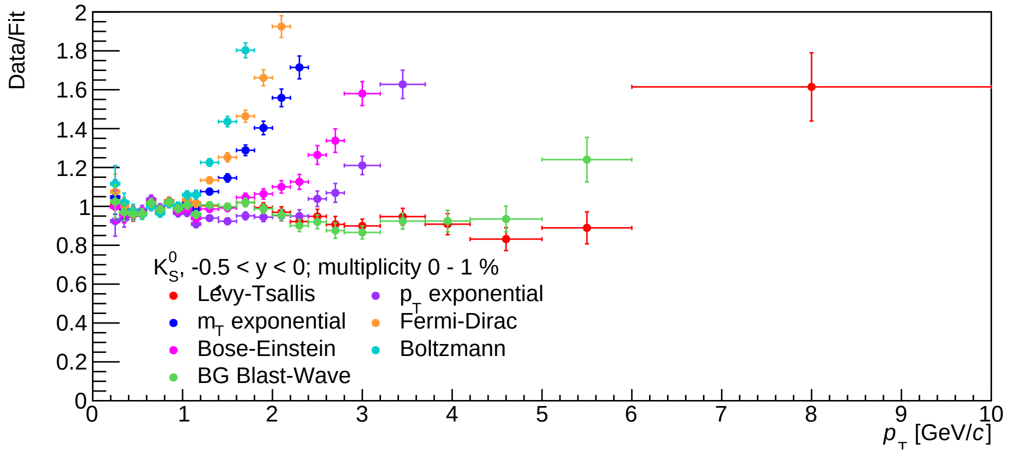

(b) Ratio between fits and data.

Figure D.1: Spectra and calculated fits for the 0-1 % multiplicity bin in the $K_S^0$ analysis. The $\chi^2$ per degree of freedom is shown for each of the functions considered.

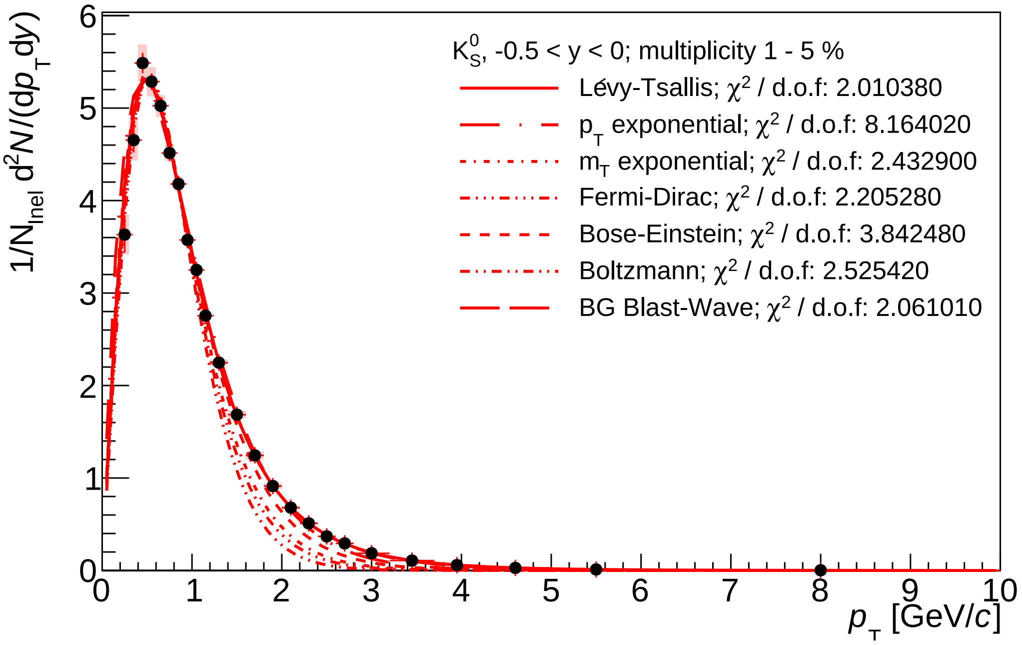

(a) Corrected spectra.

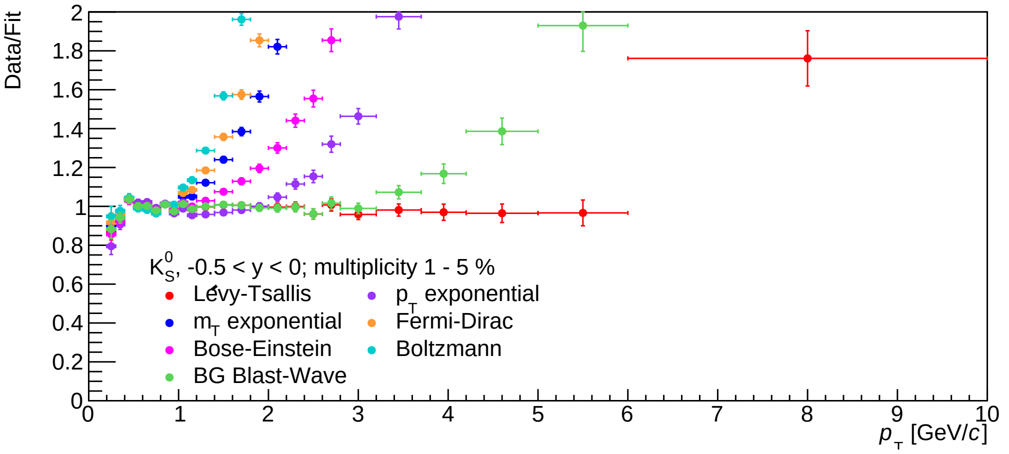

(b) Ratio between fits and data.

Figure D.2: Spectra and calculated fits for the 1-5 % multiplicity bin in the $K^0_S$ analysis. The $\chi^2$ per degree of freedom is shown for each of the functions considered.

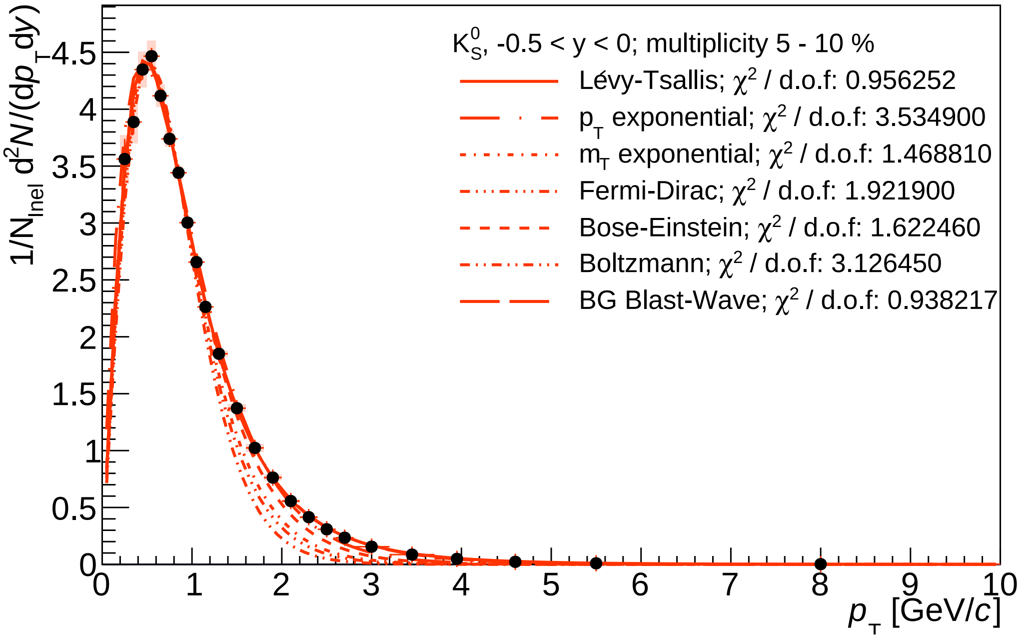

(a) Corrected spectra.

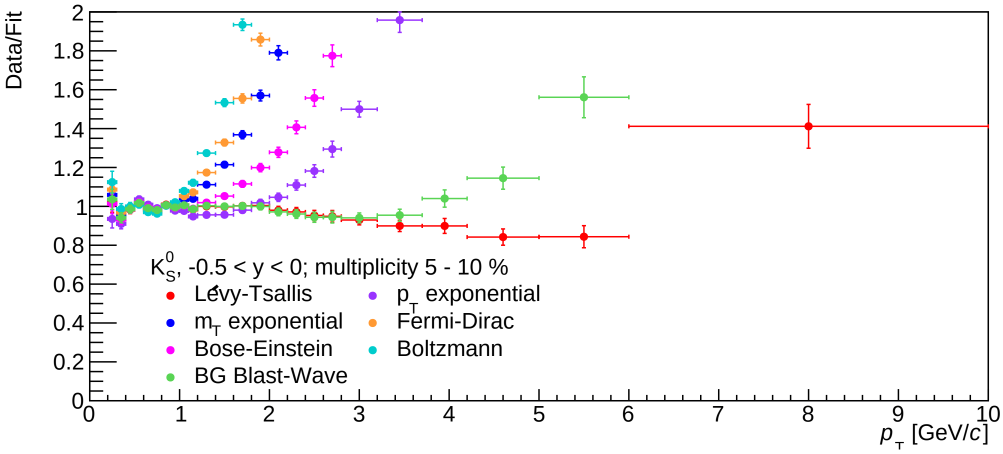

(b) Ratio between fits and data.

Figure D.3: Spectra and calculated fits for the 5-10 % multiplicity bin in the $K^0_S$ analysis. The $\chi^2$ per degree of freedom is shown for each of the functions considered.

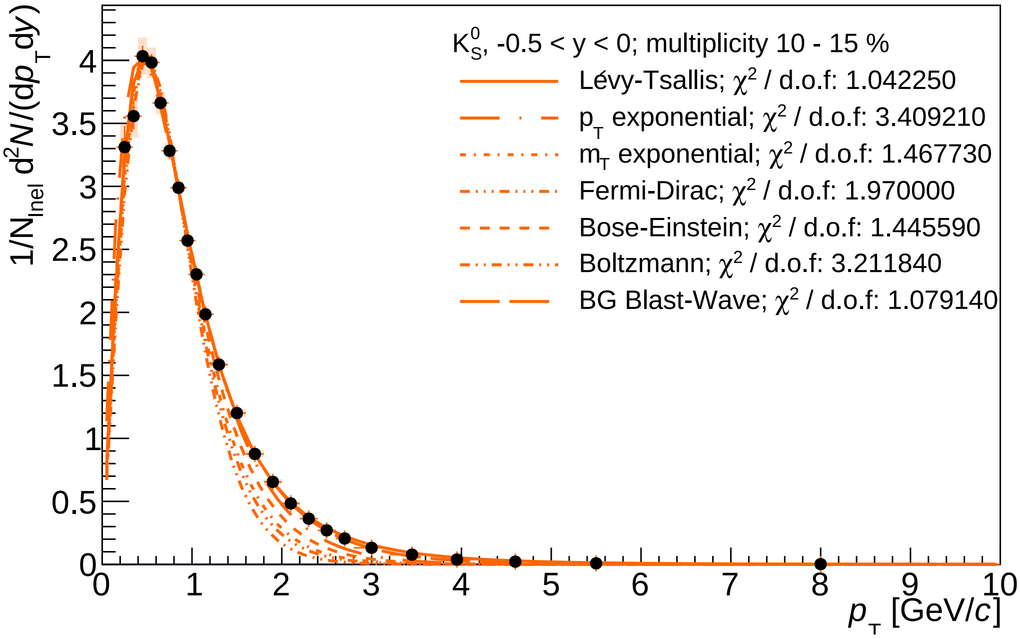

(a) Corrected spectra.

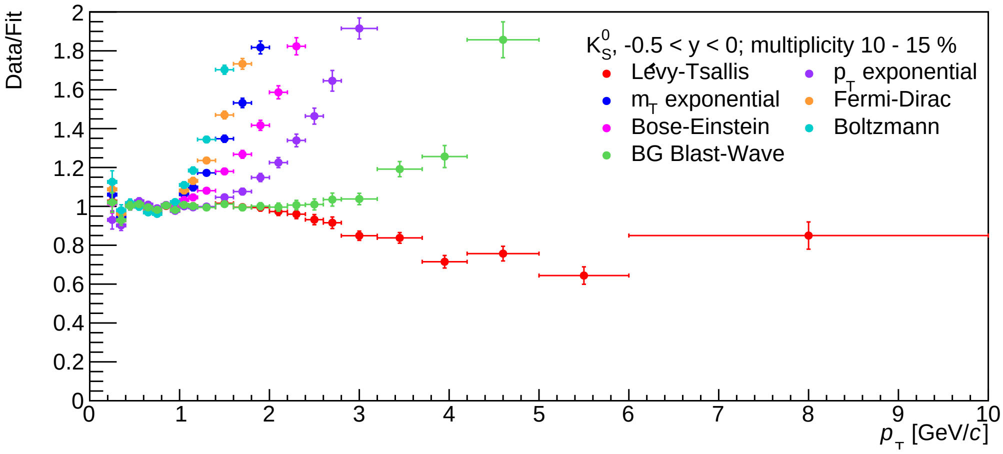

(b) Ratio between fits and data.

Figure D.4: Spectra and calculated fits for the 10-15 % multiplicity bin in the $K^0_S$ analysis. The $\chi^2$ per degree of freedom is shown for each of the functions considered.

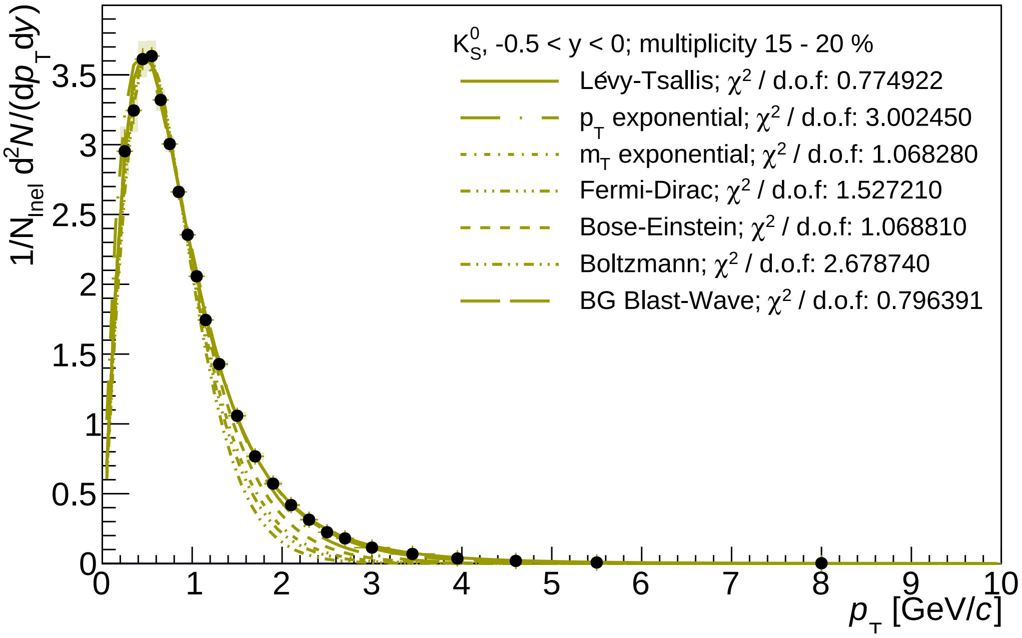

(a) Corrected spectra.

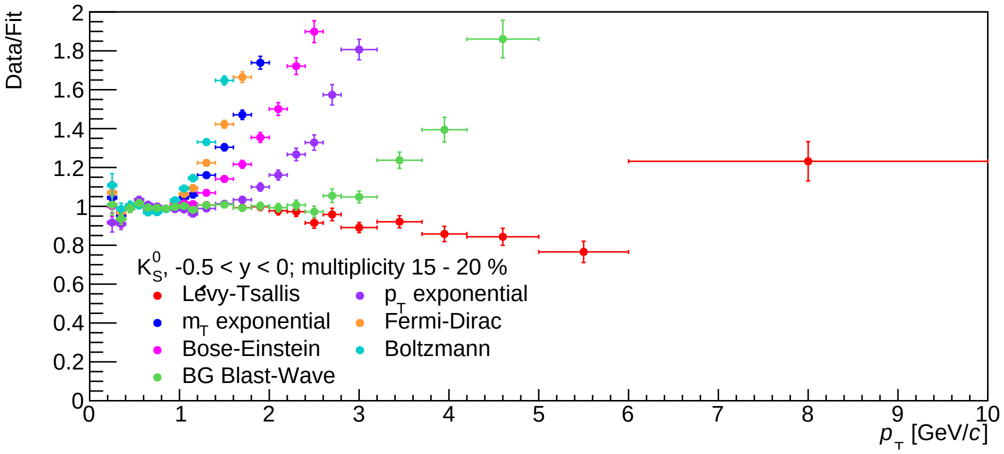

(b) Ratio between fits and data.

Figure D.5: Spectra and calculated fits for the 15-20 % multiplicity bin in the $K^0_S$ analysis. The $\chi^2$ per degree of freedom is shown for each of the functions considered.

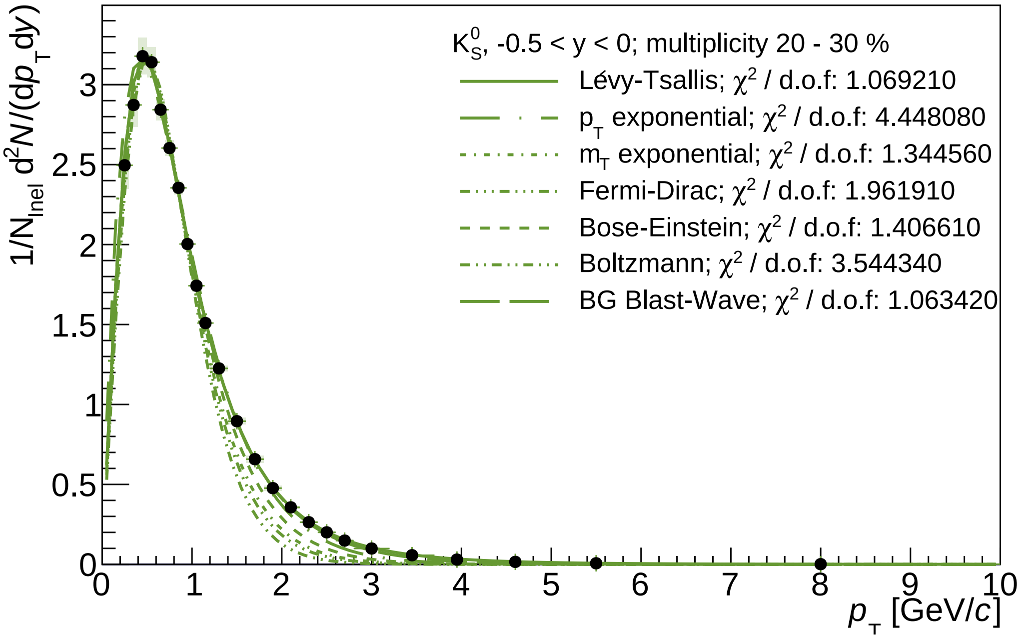

(a) Corrected spectra.

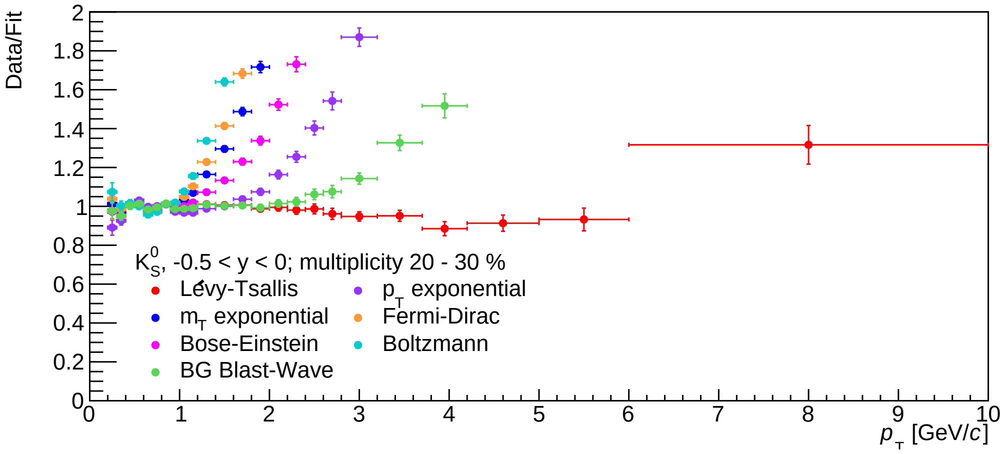

(b) Ratio between fits and data.

Figure D.6: Spectra and calculated fits for the 20-30 % multiplicity bin in the $K^0_S$ analysis. The $\chi^2$ per degree of freedom is shown for each of the functions considered.

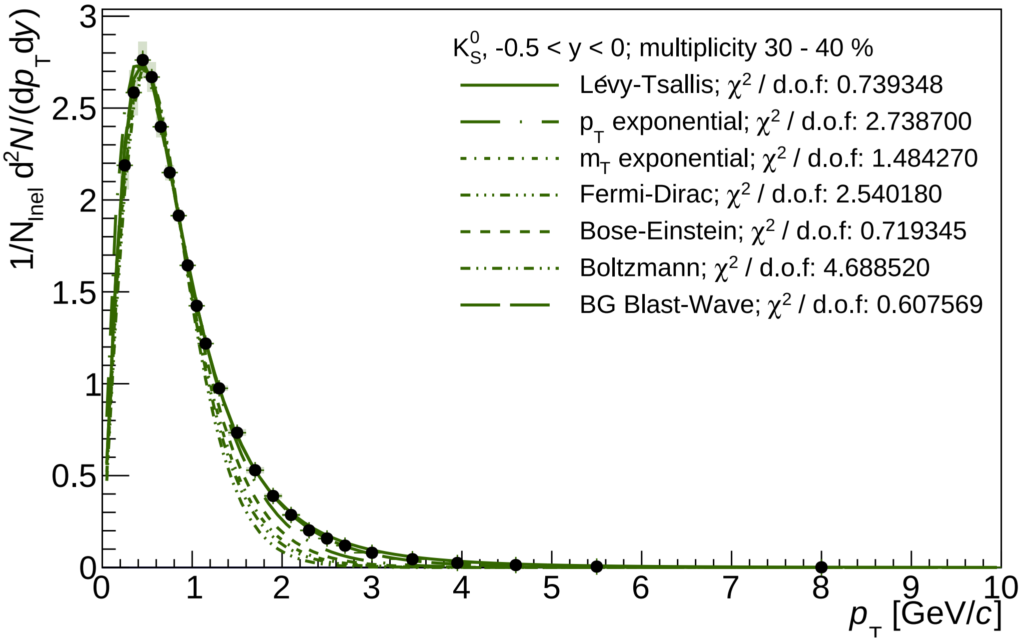

(a) Corrected spectra.

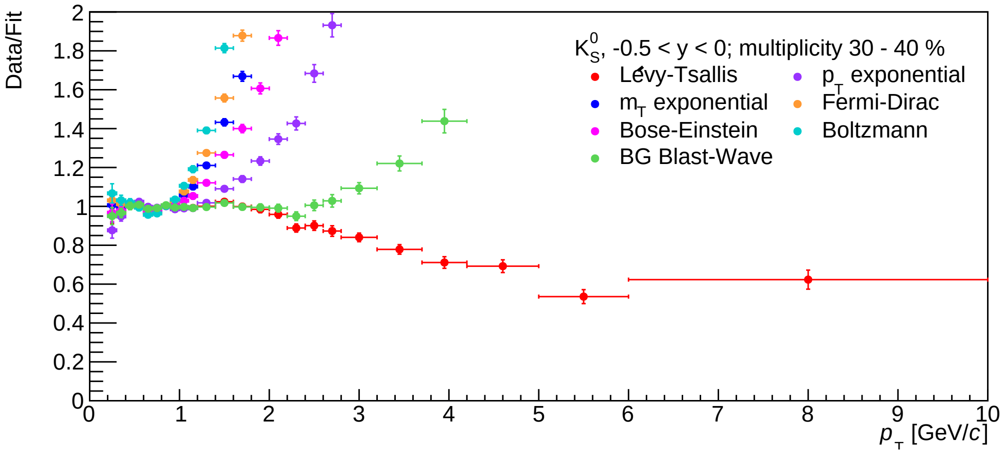

(b) Ratio between fits and data.

Figure D.7: Spectra and calculated fits for the 30-40 % multiplicity bin in the $K^0_S$ analysis. The $\chi^2$ per degree of freedom is shown for each of the functions considered.

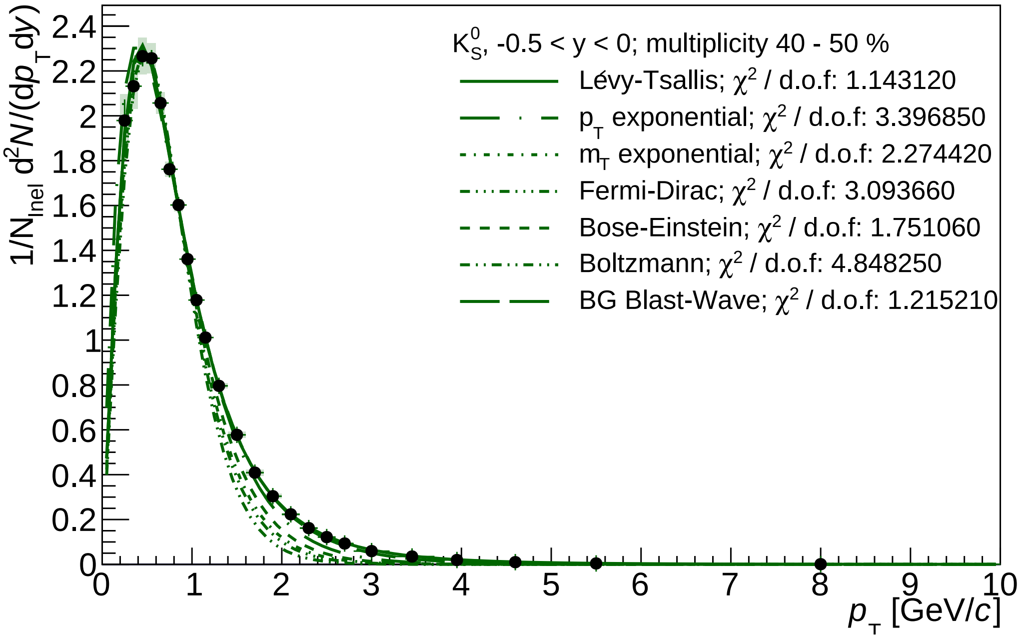

(a) Corrected spectra.

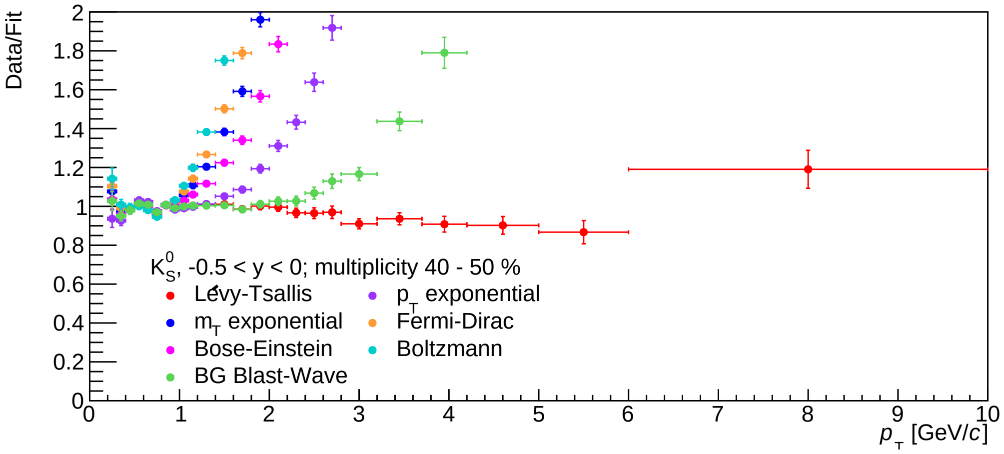

(b) Ratio between fits and data.

Figure D.8: Spectra and calculated fits for the 40-50 % multiplicity bin in the $K^0_S$ analysis. The $\chi^2$ per degree of freedom is shown for each of the functions considered.

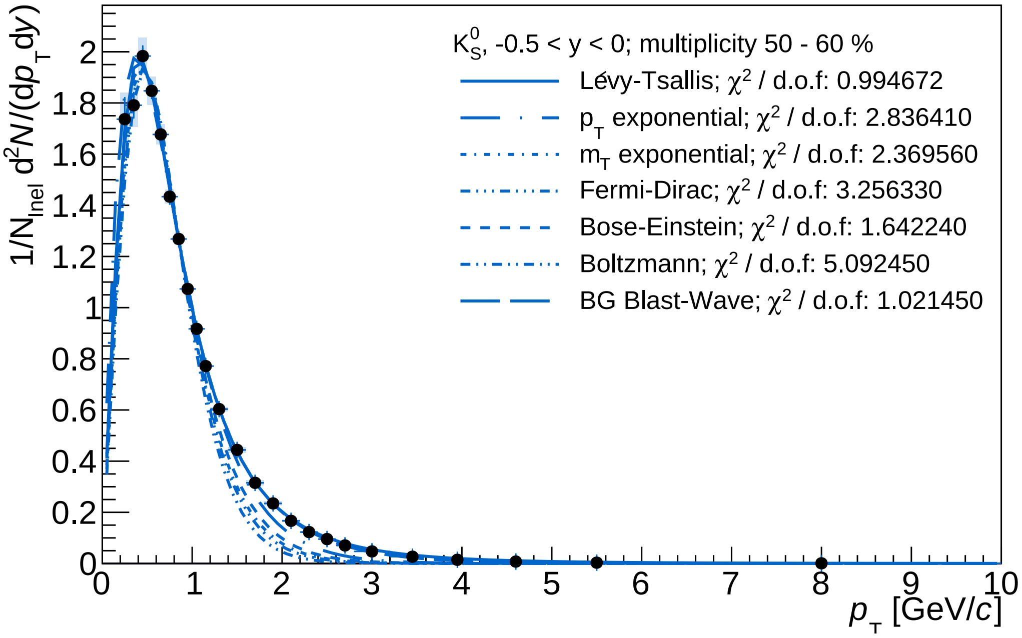

(a) Corrected spectra.

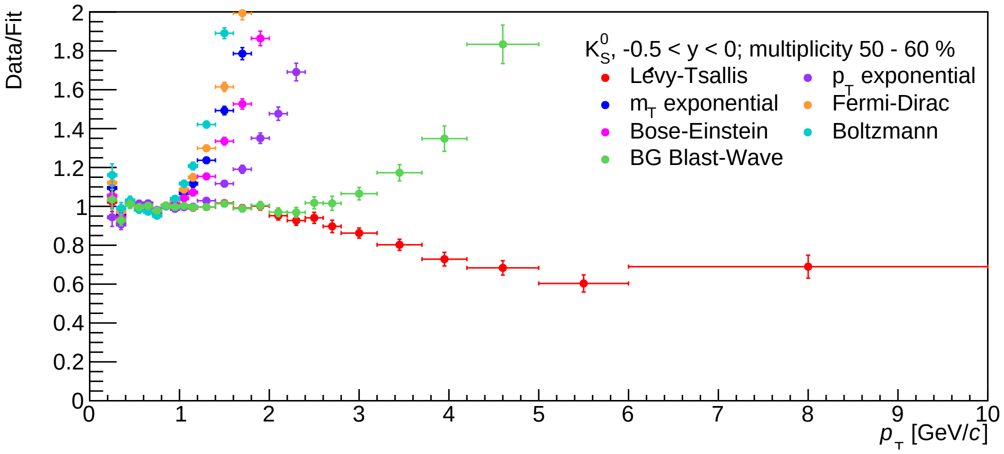

(b) Ratio between fits and data.

Figure D.9: Spectra and calculated fits for the 50-60 % multiplicity bin in the $K^0_S$ analysis. The $\chi^2$ per degree of freedom is shown for each of the functions considered.

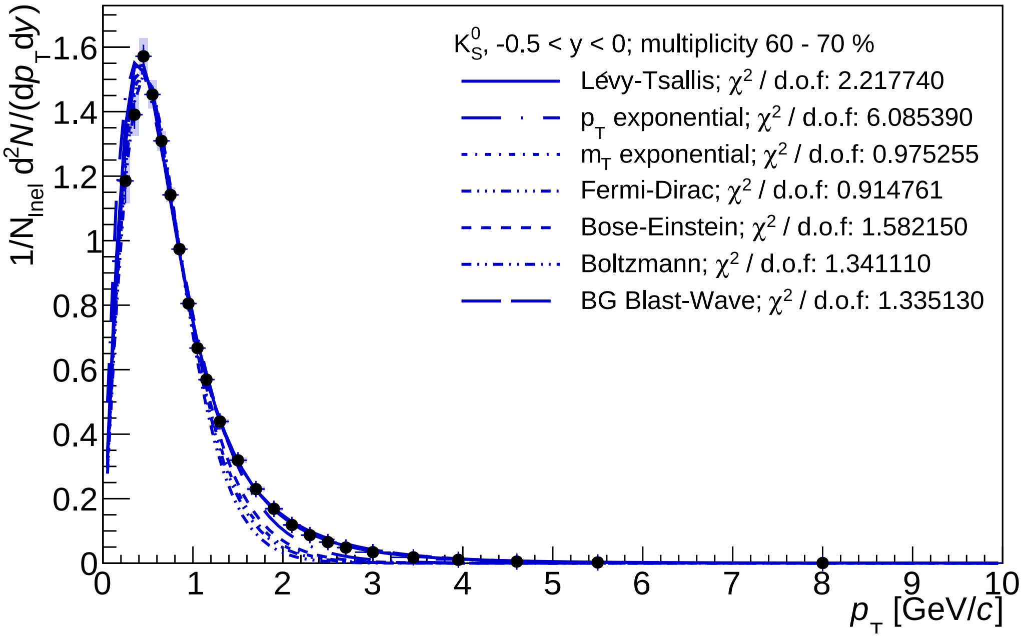

(a) Corrected spectra.

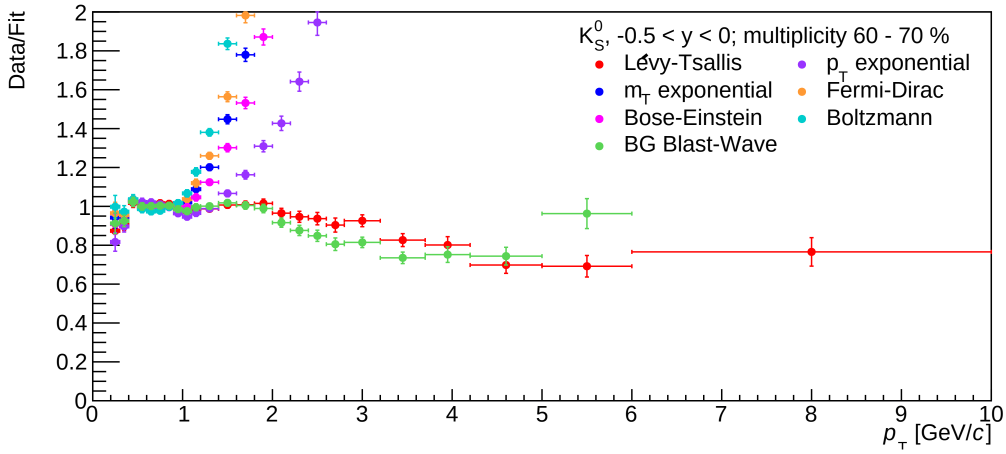

(b) Ratio between fits and data.

Figure D.10: Spectra and calculated fits for the 60-70 % multiplicity bin in the $K^0_S$ analysis. The $\chi^2$ per degree of freedom is shown for each of the functions considered.

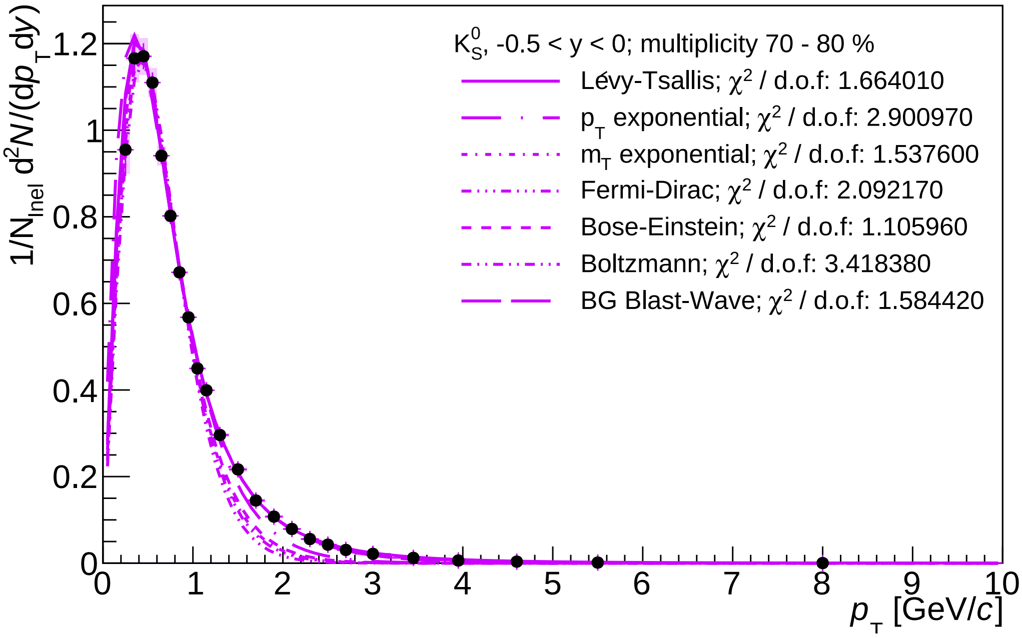

(a) Corrected spectra.

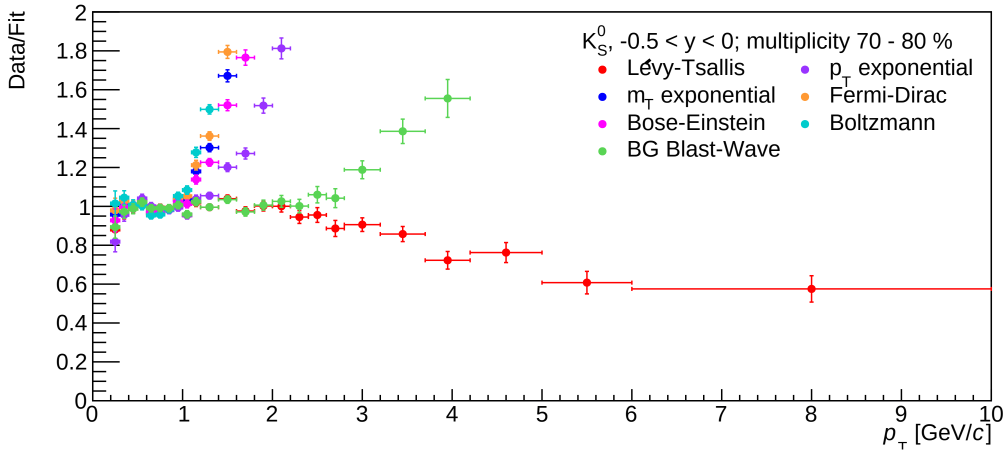

(b) Ratio between fits and data.

Figure D.11: Spectra and calculated fits for the 70-80 % multiplicity bin in the $K^0_S$ analysis. The $\chi^2$ per degree of freedom is shown for each of the functions considered.

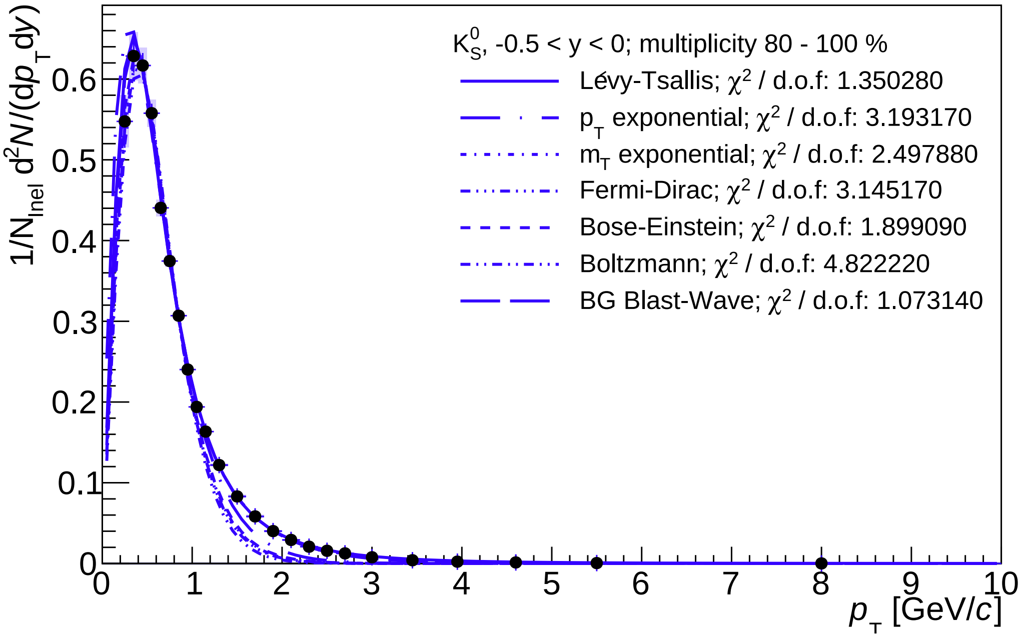

(a) Corrected spectra.

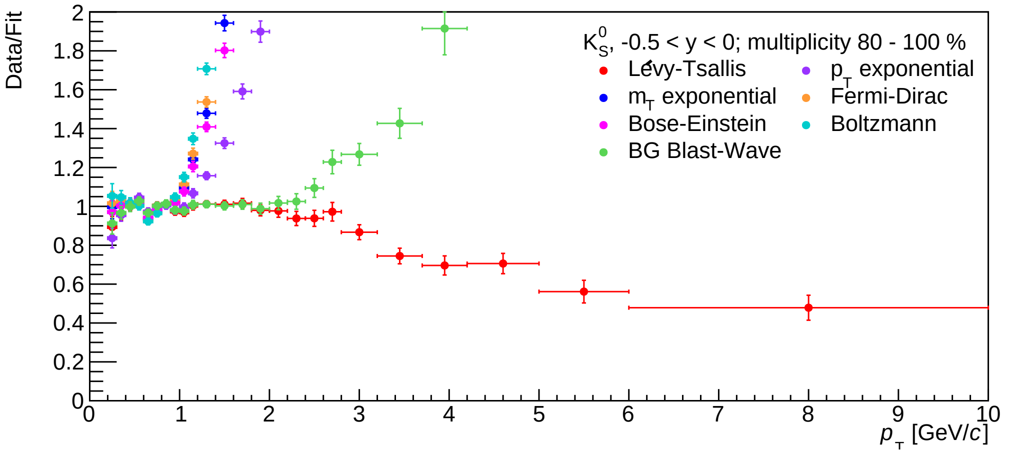

(b) Ratio between fits and data.

Figure D.12: Spectra and calculated fits for the 80-100 % multiplicity bin in the $K^0_S$ analysis. The $\chi^2$ per degree of freedom is shown for each of the functions considered.

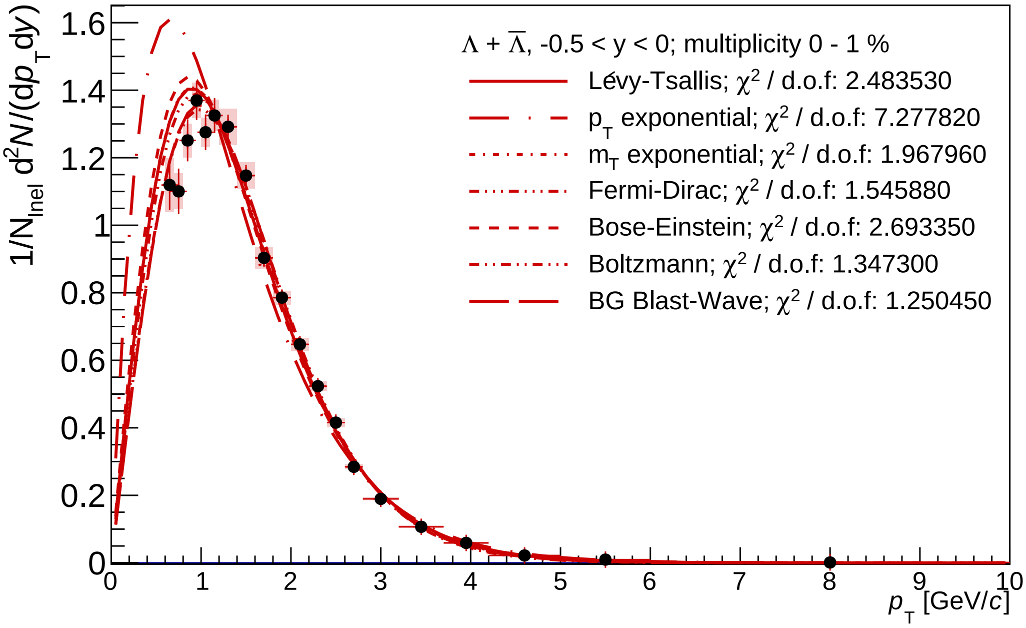

(a) Corrected spectra.

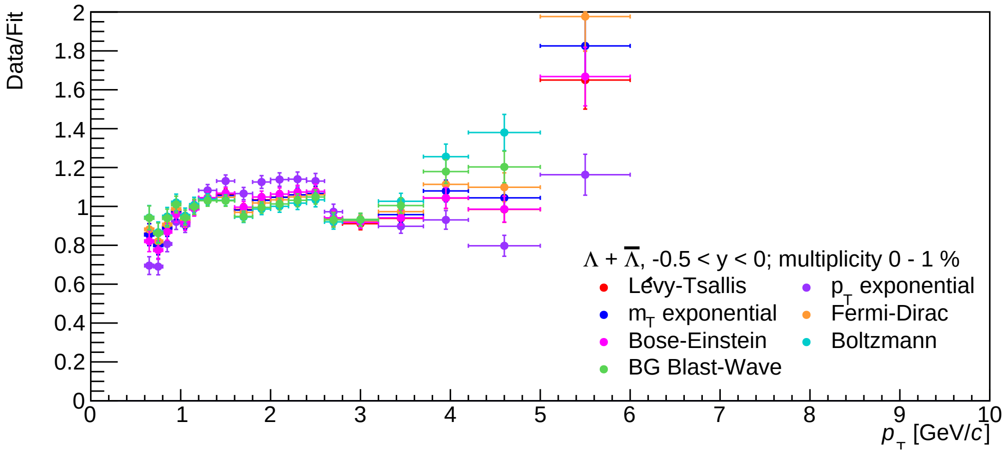

(b) Ratio between fits and data.

Figure D.13: Spectra and calculated fits for the 0-1 % multiplicity bin in the $\Lambda + \bar{\Lambda}$ analysis. The $\chi^2$ per degree of freedom is shown for each of the functions considered.

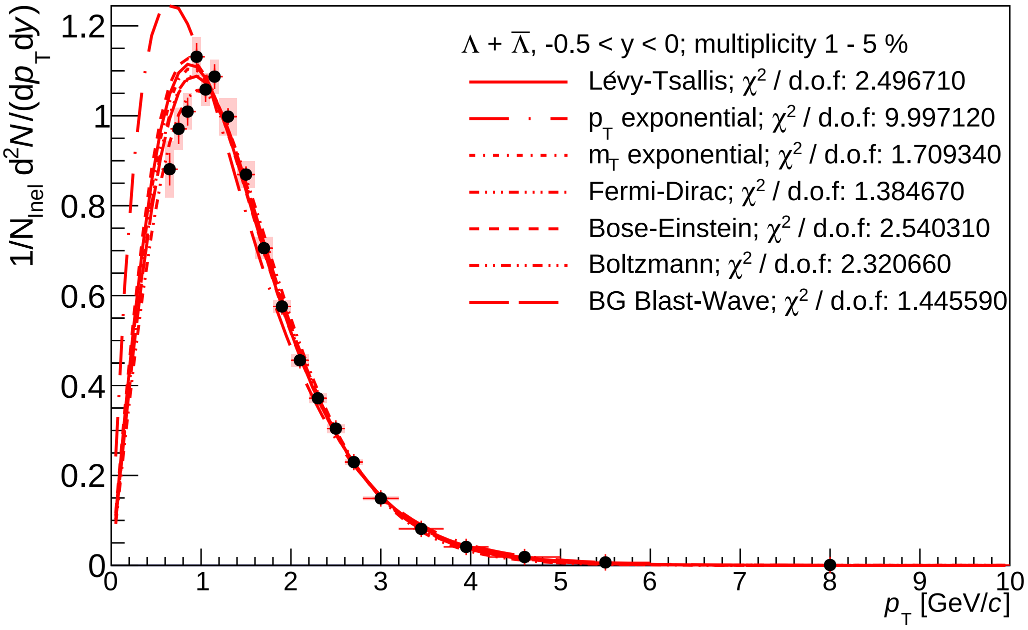

(a) Corrected spectra.

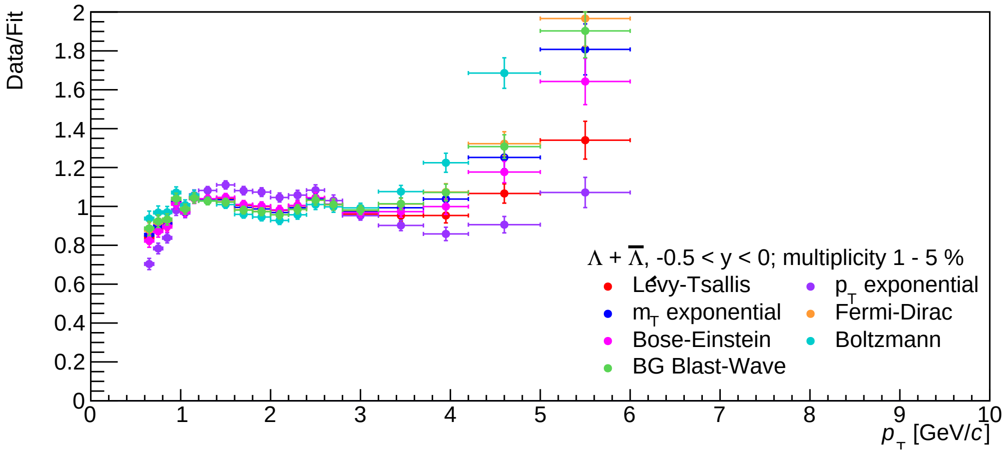

(b) Ratio between fits and data.

Figure D.14: Spectra and calculated fits for the 1-5 % multiplicity bin in the $\Lambda + \bar{\Lambda}$ analysis. The $\chi^2$ per degree of freedom is shown for each of the functions considered.

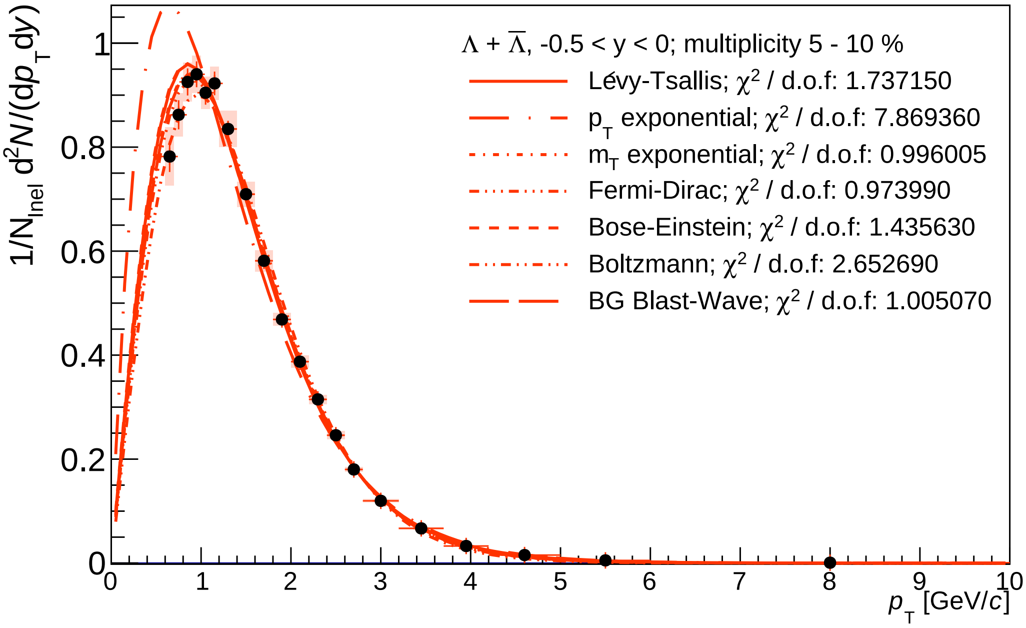

(a) Corrected spectra.

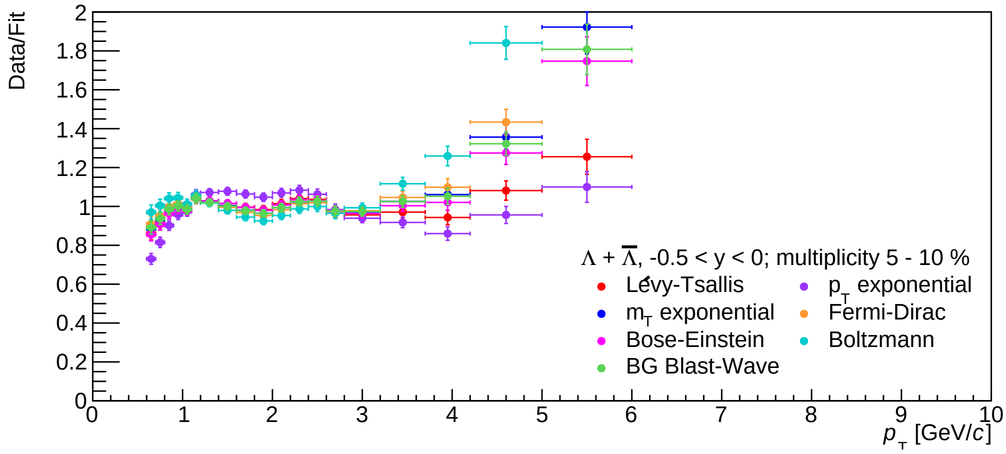

(b) Ratio between fits and data.

Figure D.15: Spectra and calculated fits for the 5-10 % multiplicity bin in the $\Lambda+\bar{\Lambda}$ analysis. The $\chi^2$ per degree of freedom is shown for each of the functions considered.

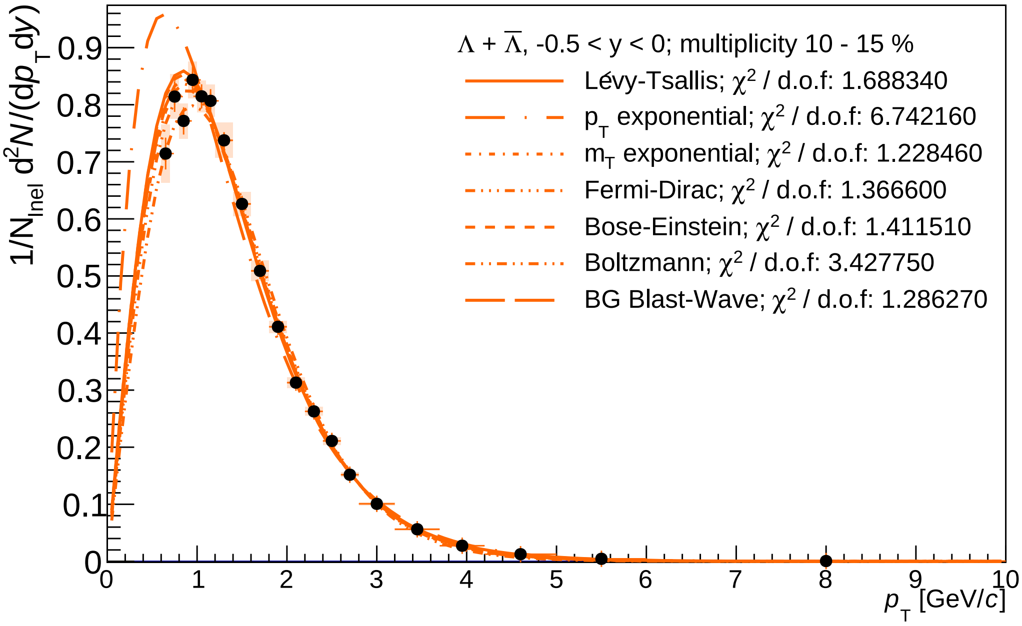

(a) Corrected spectra.

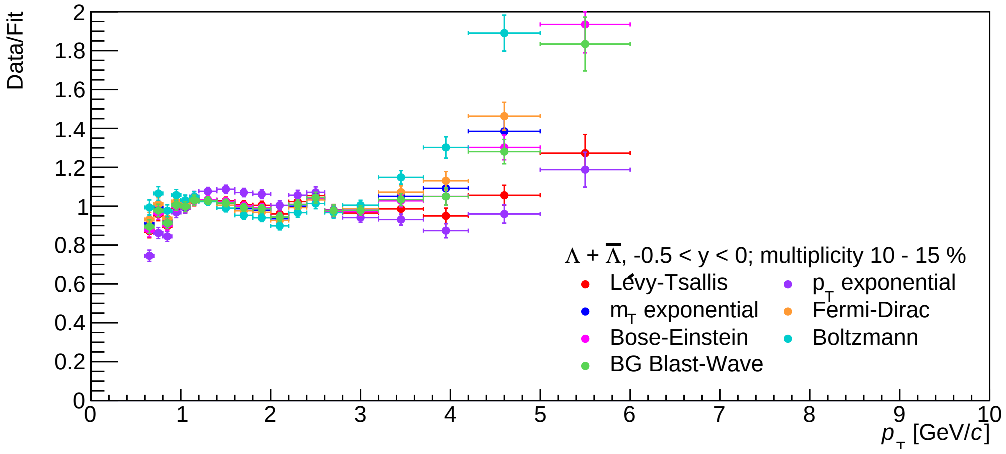

(b) Ratio between fits and data.

Figure D.16: Spectra and calculated fits for the 10-15 % multiplicity bin in the $\Lambda + \bar{\Lambda}$ analysis. The $\chi^2$ per degree of freedom is shown for each of the functions considered.

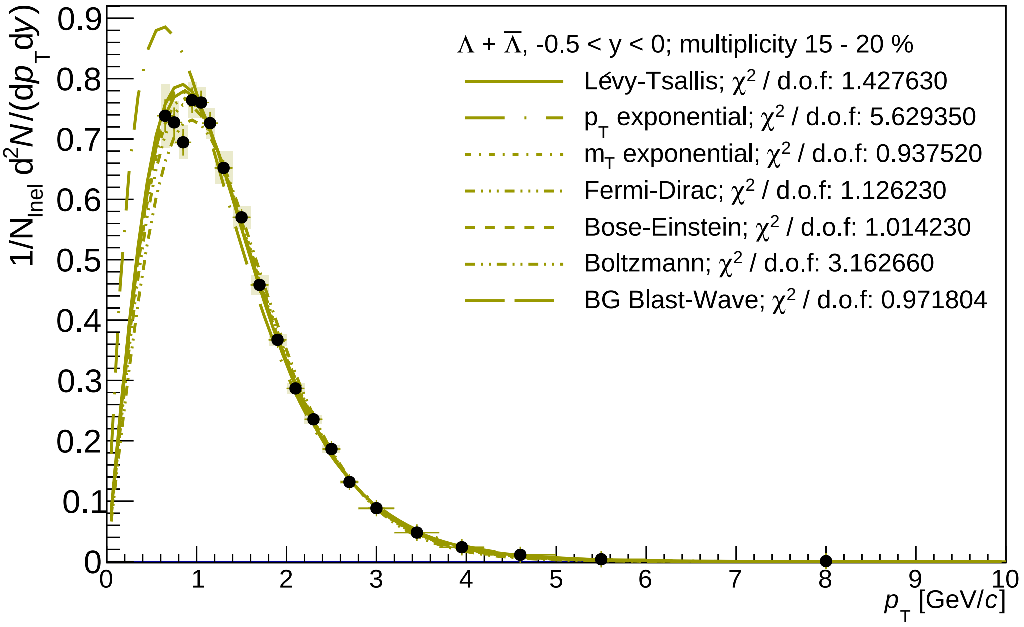

(a) Corrected spectra.

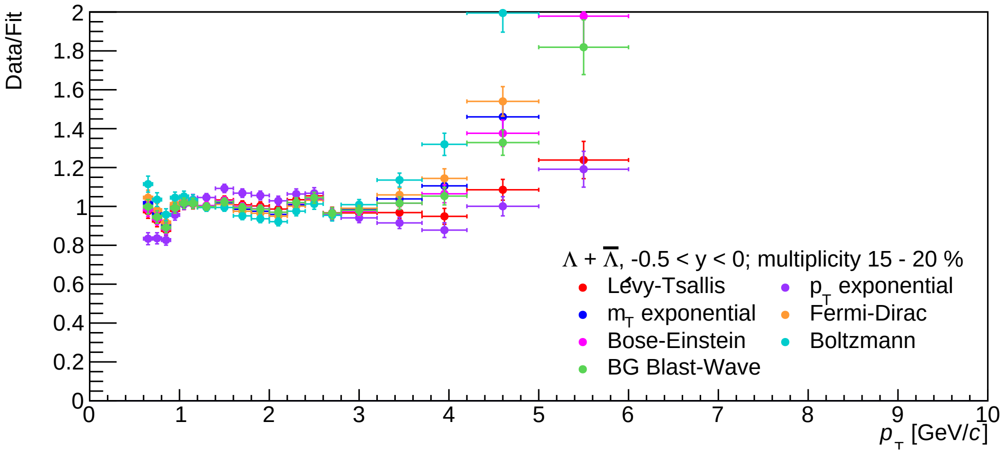

(b) Ratio between fits and data.

Figure D.17: Spectra and calculated fits for the 15-20 % multiplicity bin in the $\Lambda+\bar{\Lambda}$ analysis. The $\chi^2$ per degree of freedom is shown for each of the functions considered.

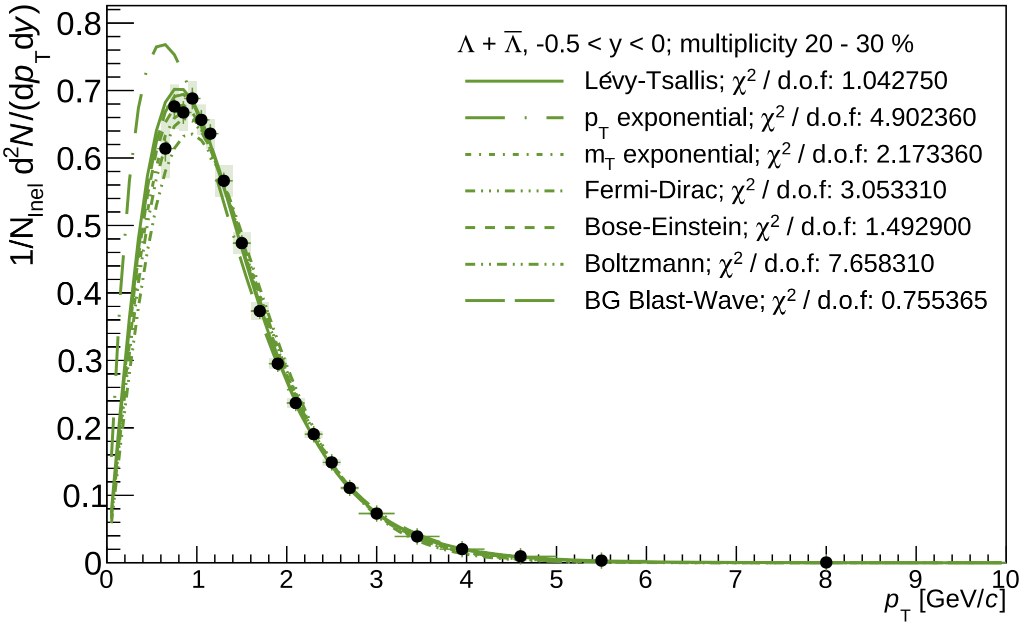

(a) Corrected spectra.

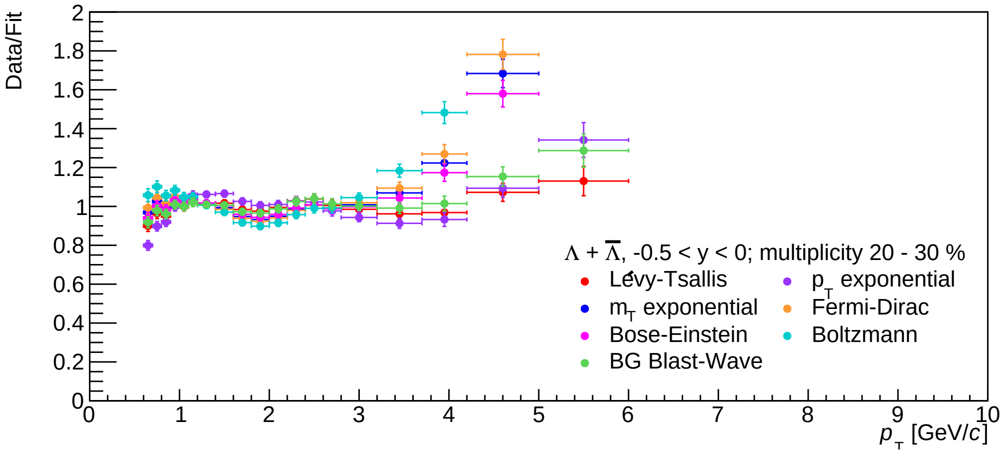

(b) Ratio between fits and data.

Figure D.18: Spectra and calculated fits for the 20-30 % multiplicity bin in the $\Lambda+\bar{\Lambda}$ analysis. The $\chi^2$ per degree of freedom is shown for each of the functions considered.

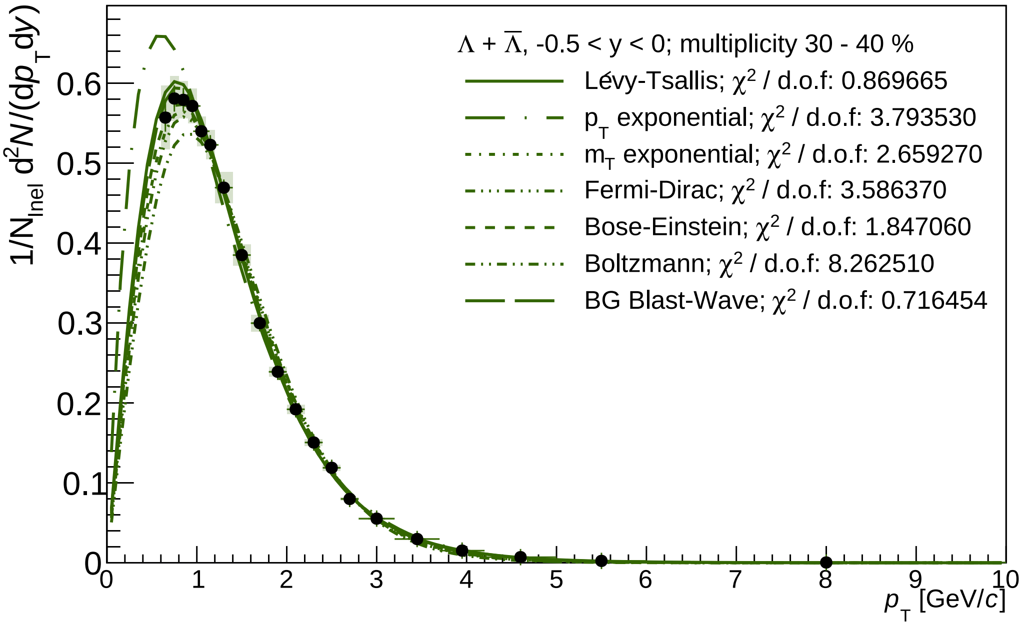

(a) Corrected spectra.

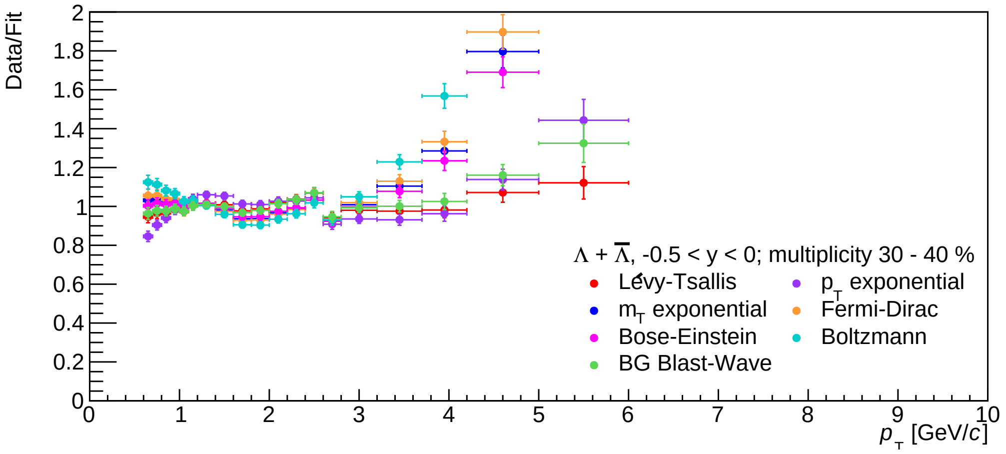

(b) Ratio between fits and data.

Figure D.19: Spectra and calculated fits for the 30-40 % multiplicity bin in the $\Lambda+\bar{\Lambda}$ analysis. The $\chi^2$ per degree of freedom is shown for each of the functions considered.

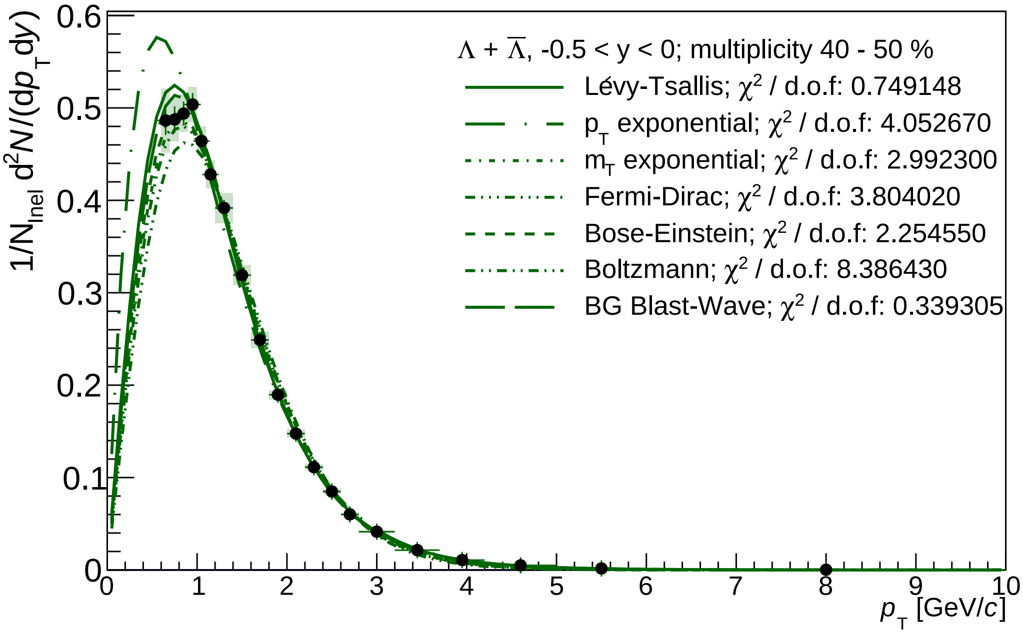

(a) Corrected spectra.

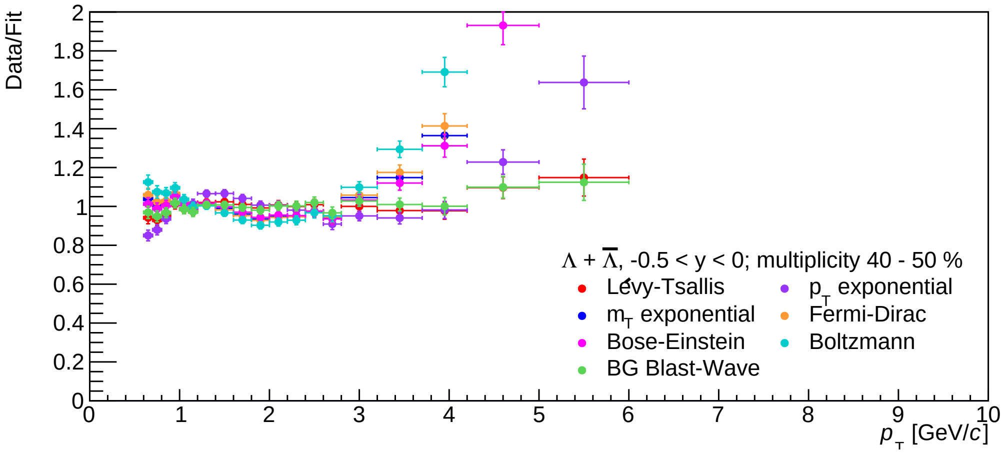

(b) Ratio between fits and data.

Figure D.20: Spectra and calculated fits for the 40-50 % multiplicity bin in the $\Lambda+\bar{\Lambda}$ analysis. The $\chi^2$ per degree of freedom is shown for each of the functions considered.

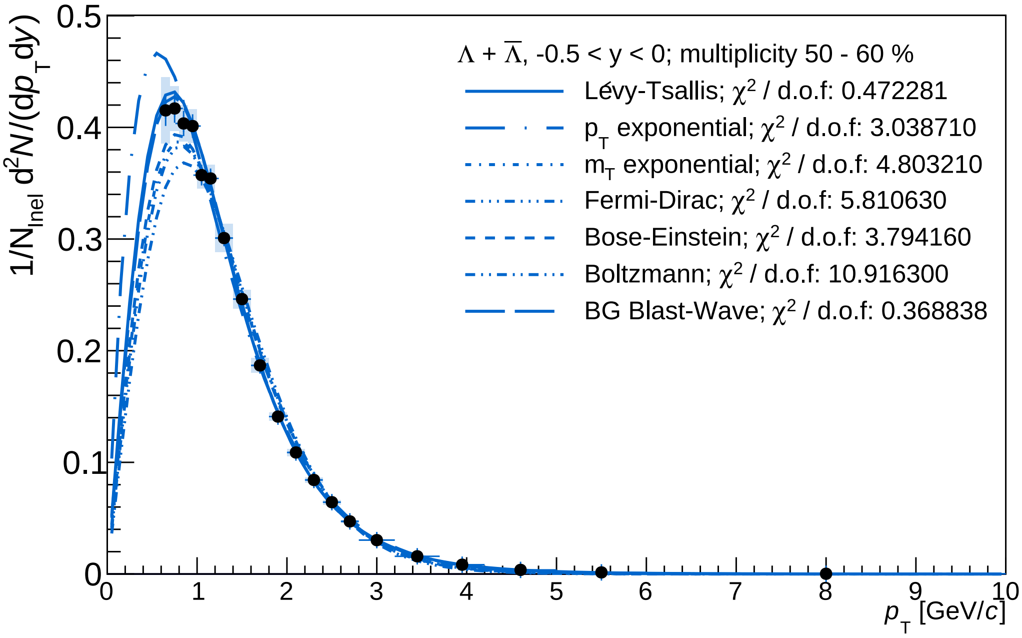

(a) Corrected spectra.

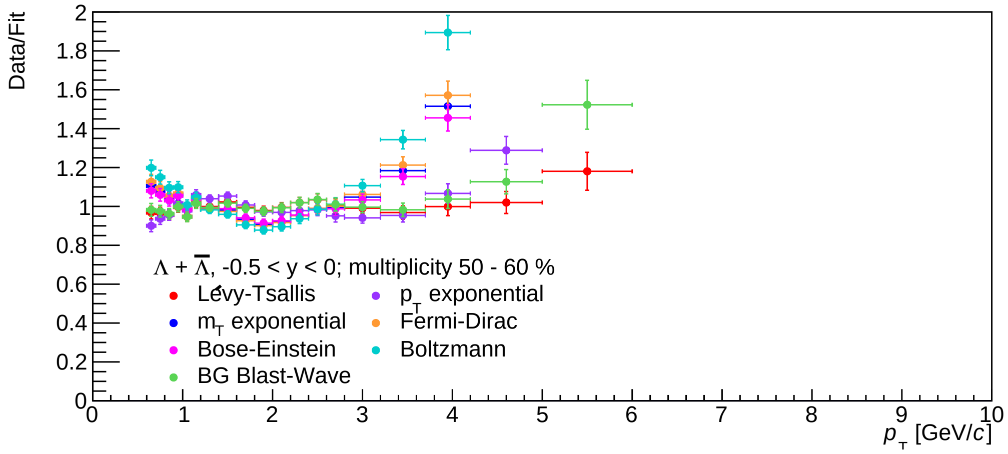

(b) Ratio between fits and data.

Figure D.21: Spectra and calculated fits for the 50-60 % multiplicity bin in the $\Lambda+\bar{\Lambda}$ analysis. The $\chi^2$ per degree of freedom is shown for each of the functions considered.

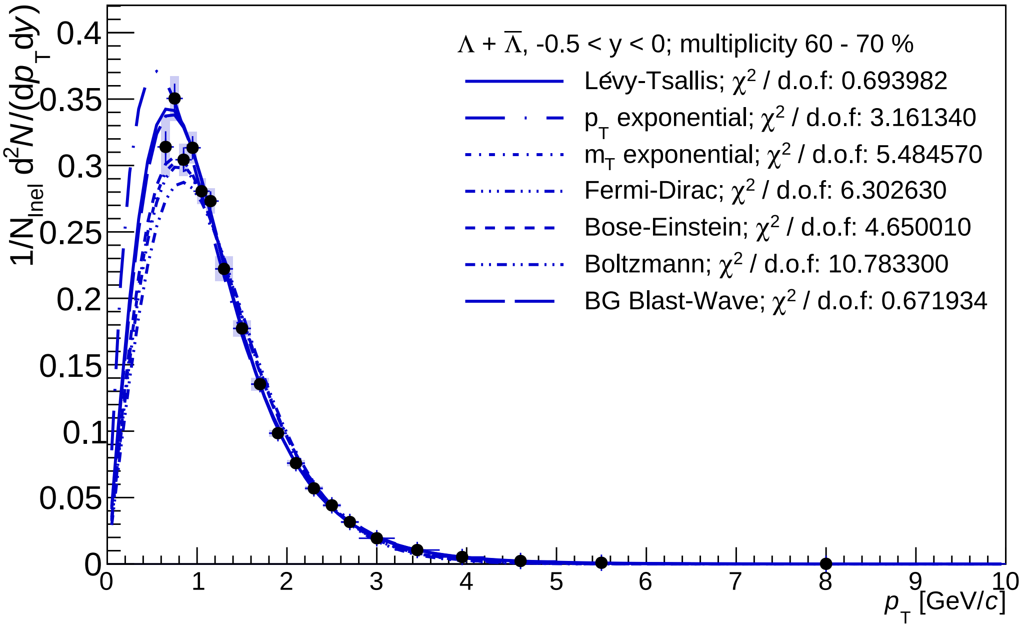

(a) Corrected spectra.

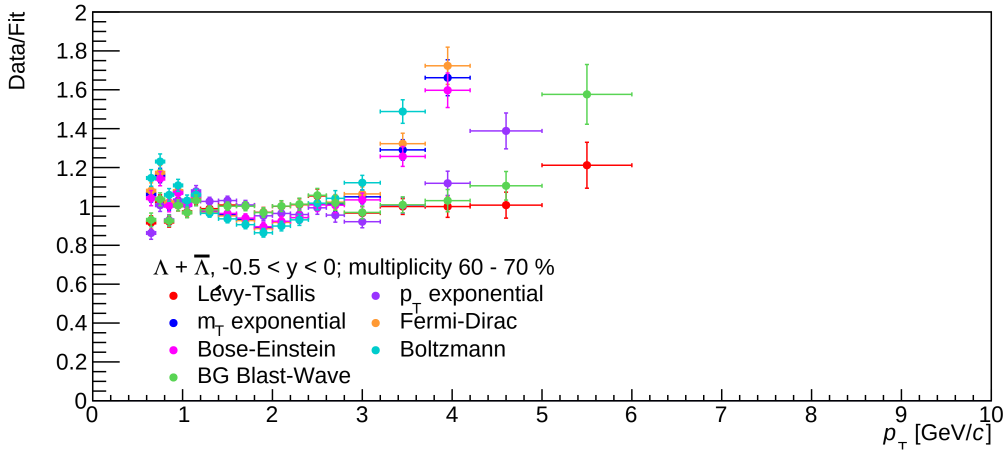

(b) Ratio between fits and data.

Figure D.22: Spectra and calculated fits for the 60-70 % multiplicity bin in the $\Lambda+\bar{\Lambda}$ analysis. The $\chi^2$ per degree of freedom is shown for each of the functions considered.

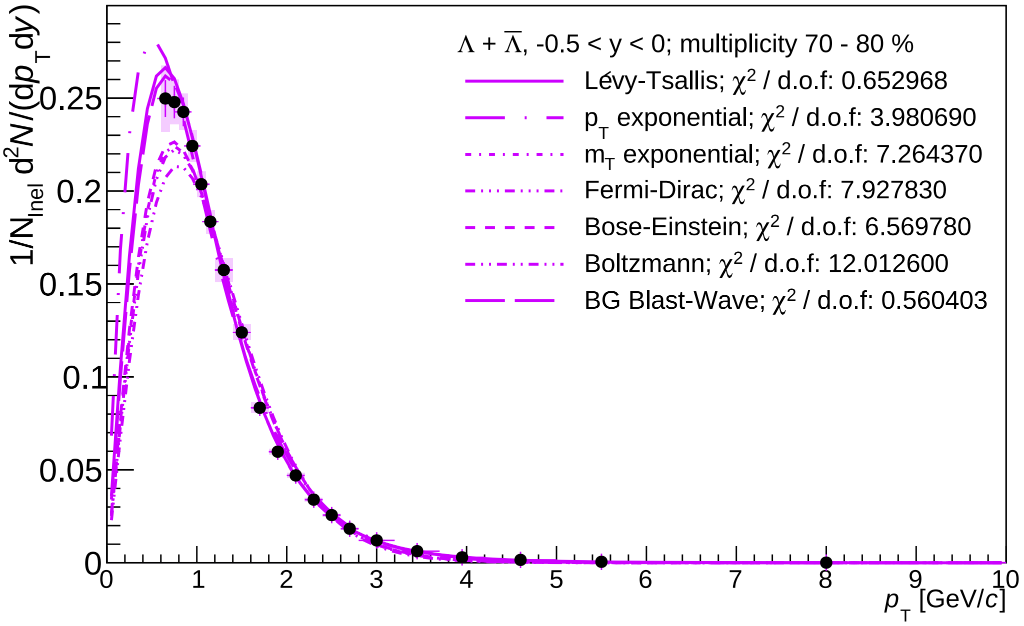

(a) Corrected spectra.

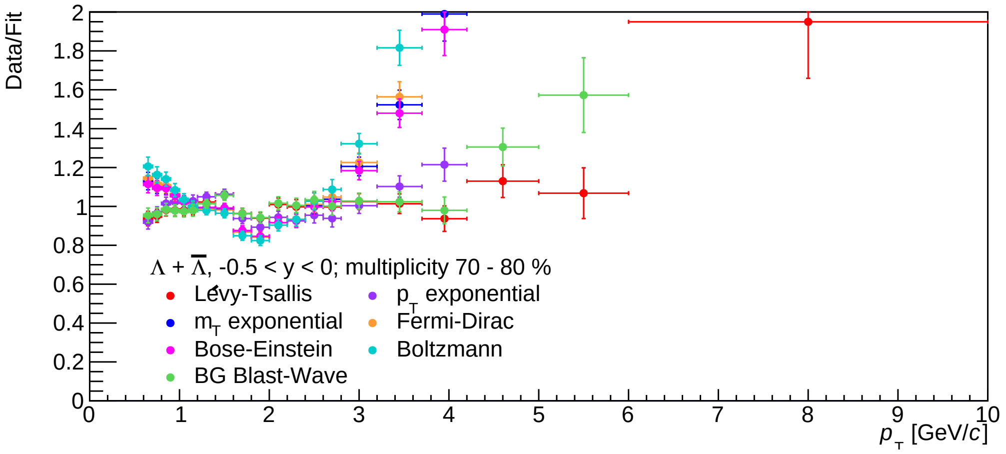

(b) Ratio between fits and data.

Figure D.23: Spectra and calculated fits for the 70-80 % multiplicity bin in the $\Lambda+\bar{\Lambda}$ analysis. The $\chi^2$ per degree of freedom is shown for each of the functions considered.

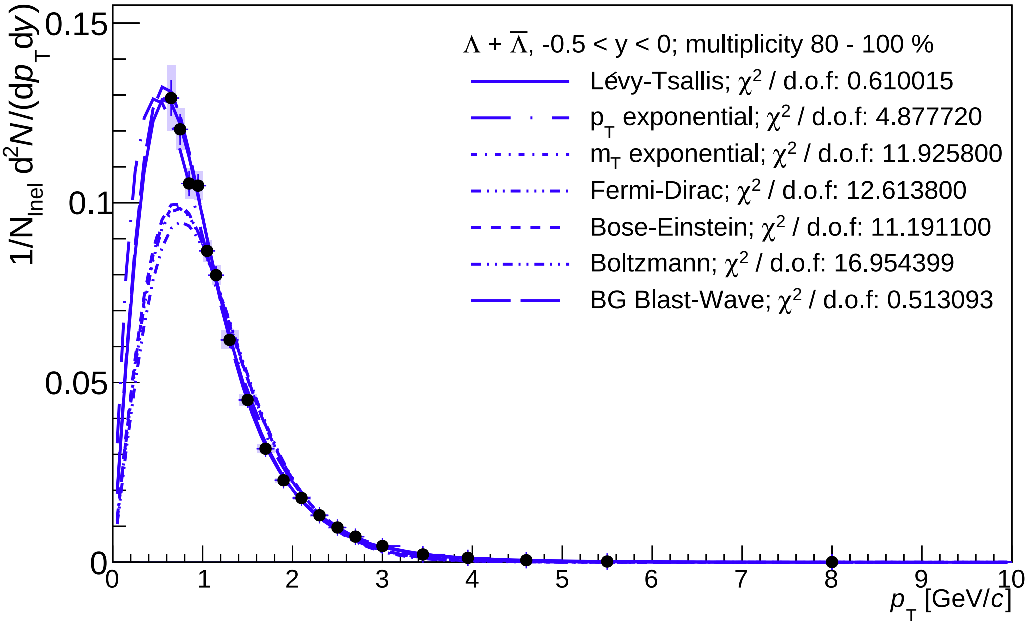

(a) Corrected spectra.

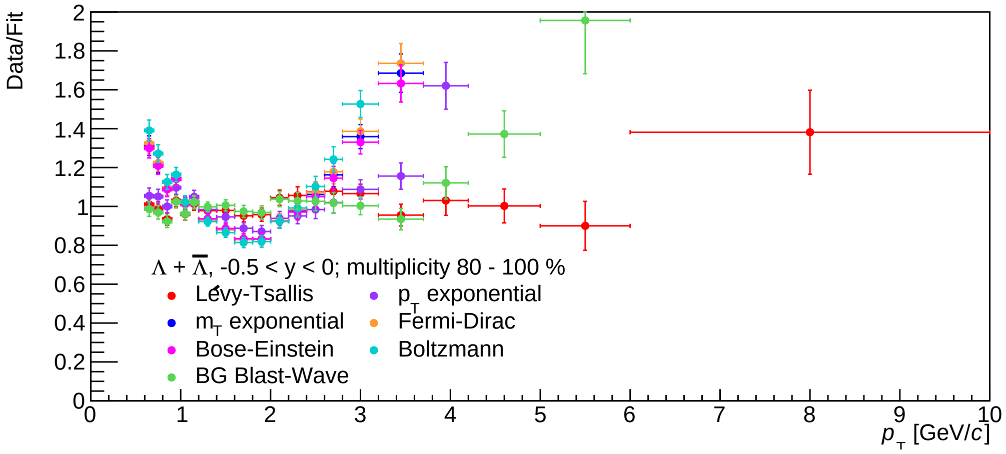

(b) Ratio between fits and data.

Figure D.24: Spectra and calculated fits for the 80-100 % multiplicity bin in the $\Lambda + \bar{\Lambda}$ analysis. The $\chi^2$ per degree of freedom is shown for each of the functions considered.

# Appendix E

# $\Lambda$-to-$K^0_S$ plots

This chapter contains the $\Lambda$-to-$K^0_S$ ratio plots for all multiplicity bins used in this analysis, as described in section 5.3. All plots show both the highest multiplicity results, overlaid with the ratios as calculated for a single other multiplicity bin.

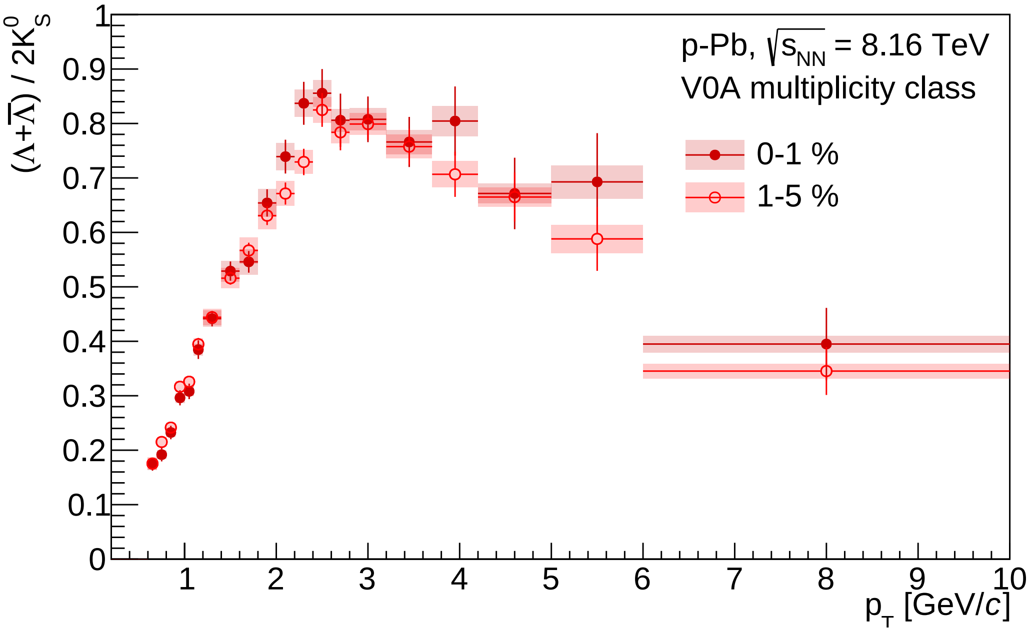

Figure E.1: Ratio of the combined $\Lambda + \bar{\Lambda}$ spectra to two times the $K^0_S$ spectrum, in two multiplicity bins. This plot shows the ratios from the highest multiplicity bin used in this analysis ([0, 1] %), compared to those from the second highest bin ([1, 5] %).

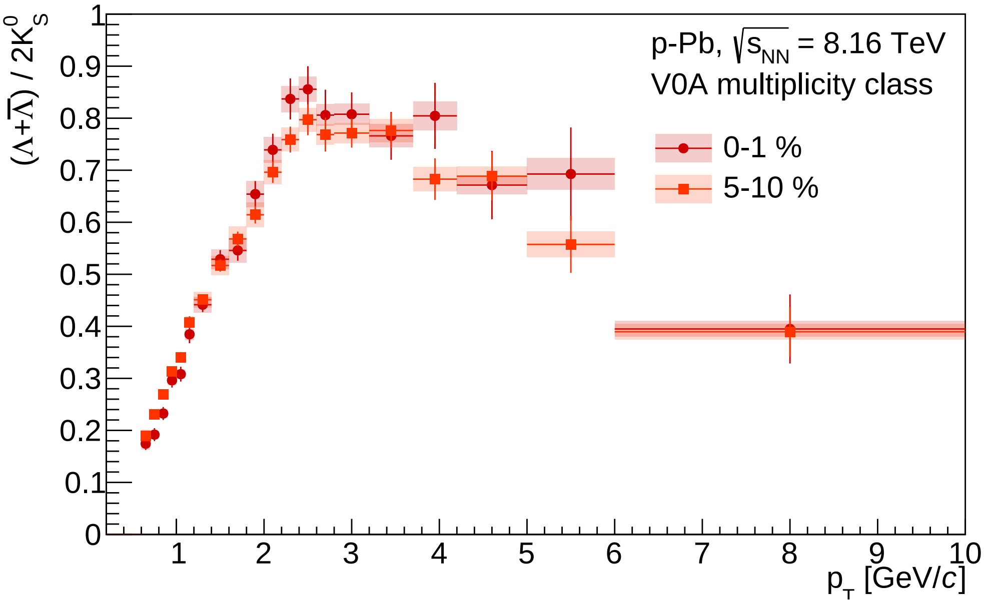

(a) [0, 1] % vs [5, 10] % multiplicity bins.

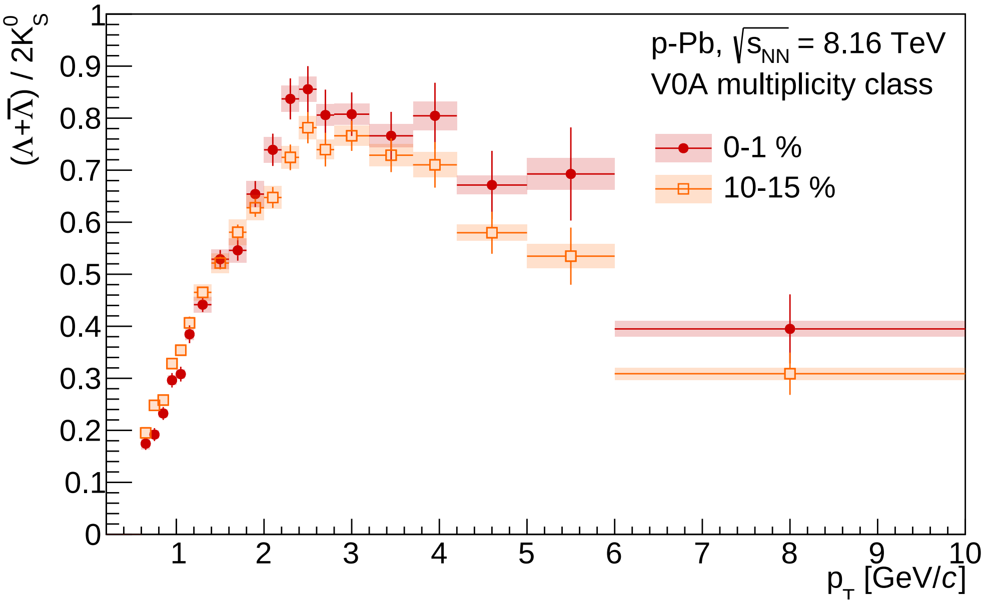

(b) [0, 1] % vs [10, 15] % multiplicity bins.

Figure E.2: Ratio of the combined $\Lambda + \bar{\Lambda}$ spectra to two times the $K^0_S$ spectrum, in two multiplicity bins. Both the highest multiplicity bin ([0, 1] %) and one other bin are shown on each plot.

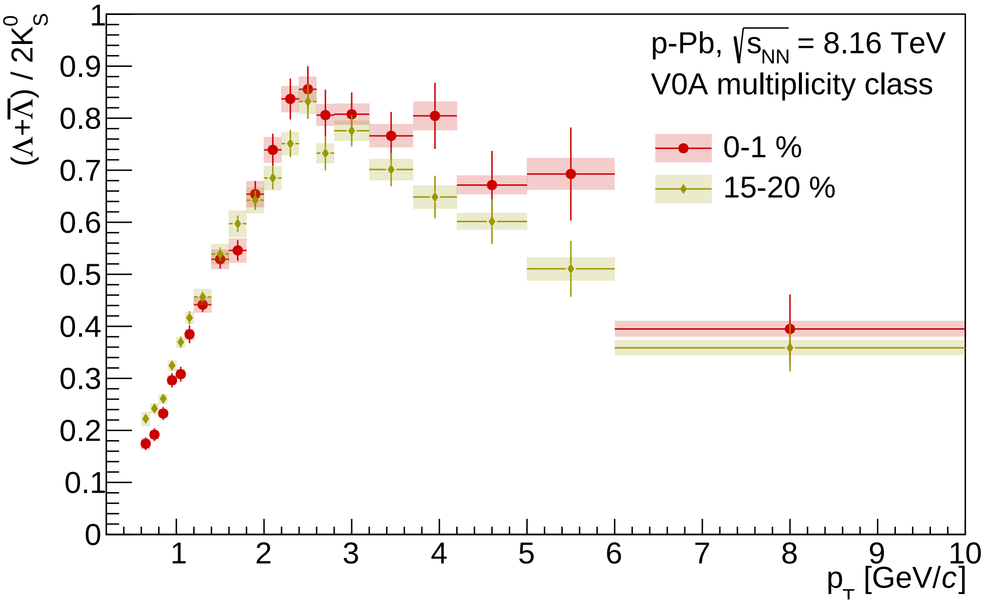

(a) [0, 1] % vs [15, 20] % multiplicity bins.

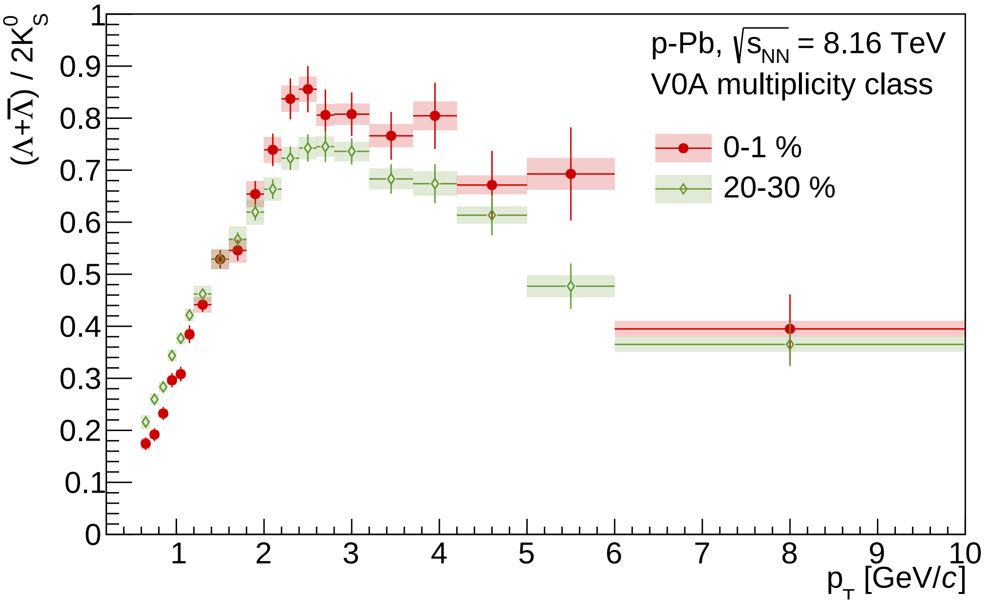

(b) [0, 1] % vs [20, 30] % multiplicity bins.

Figure E.3: Ratio of the combined $\Lambda + \bar{\Lambda}$ spectra to two times the $K^0_S$ spectrum, in two multiplicity bins. Both the highest multiplicity bin ([0, 1] %) and one other bin are shown on each plot.

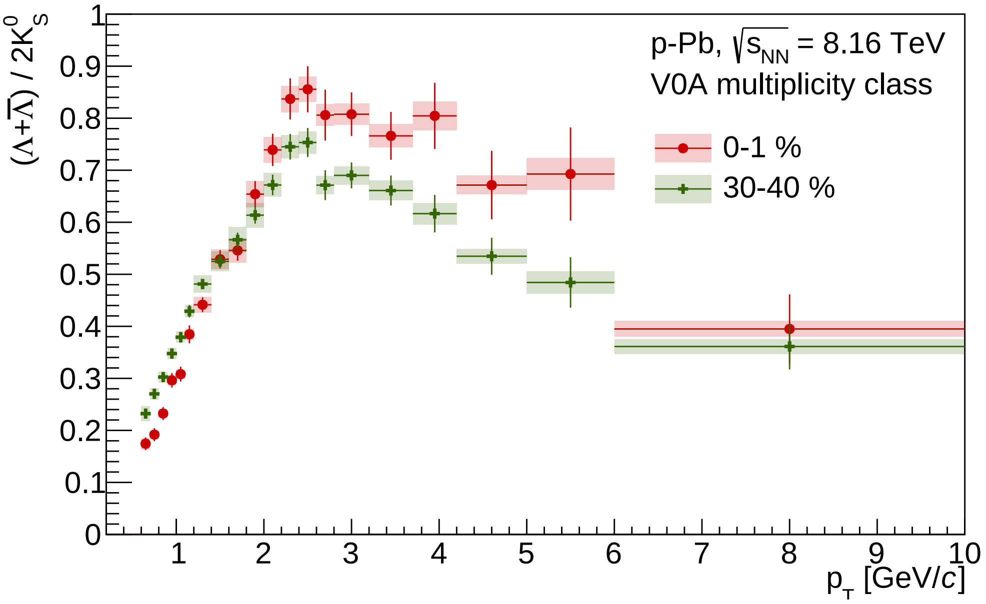

(a) [0, 1] % vs [30, 40] % multiplicity bins.

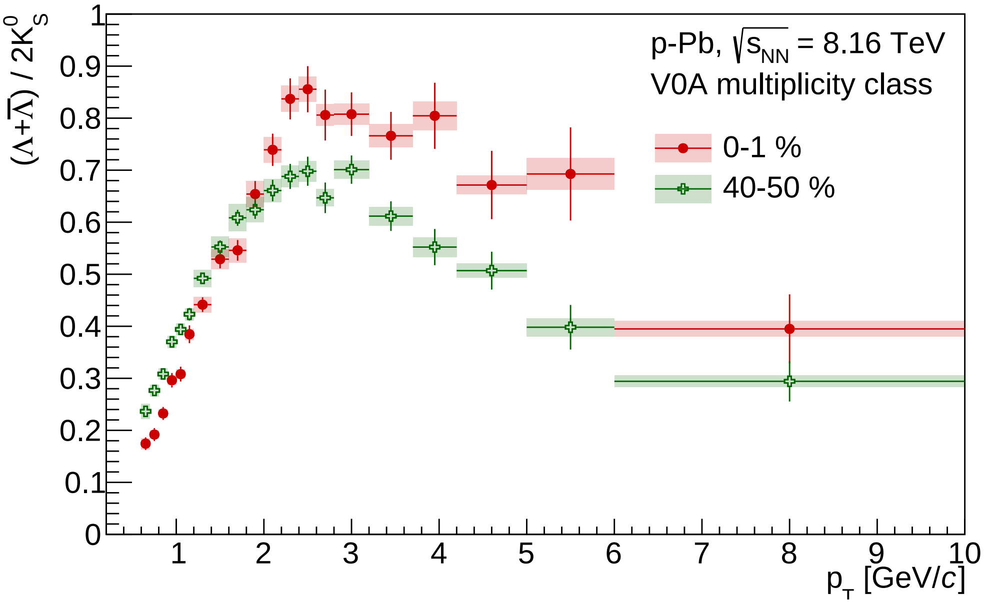

(b) [0, 1] % vs [40, 50] % multiplicity bins.

Figure E.4: Ratio of the combined $\Lambda + \bar{\Lambda}$ spectra to two times the $K^0_S$ spectrum, in two multiplicity bins. Both the highest multiplicity bin ([0, 1] %) and one other bin are shown on each plot.

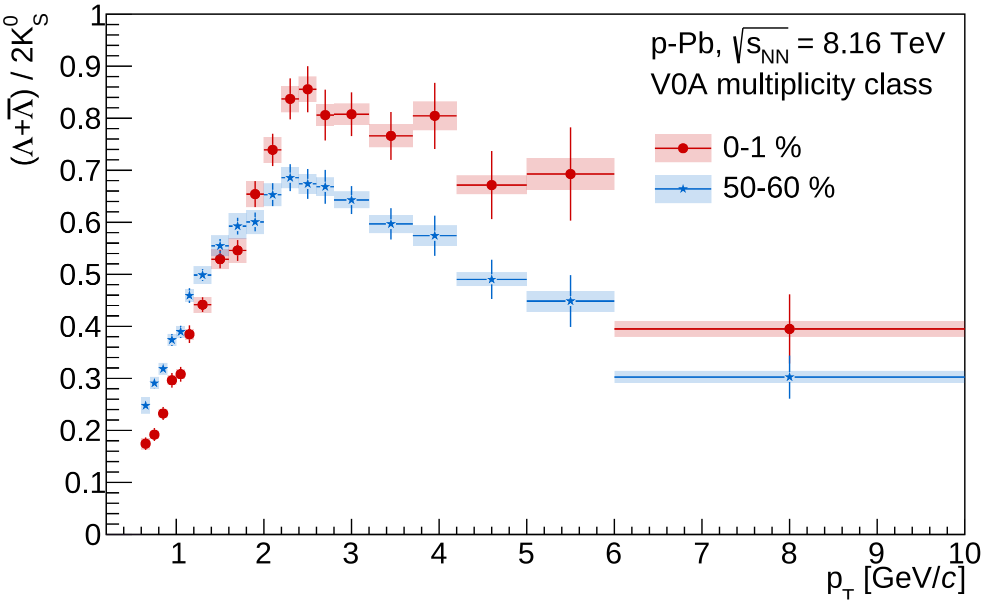

(a) [0, 1] % vs [50, 60] % multiplicity bins.

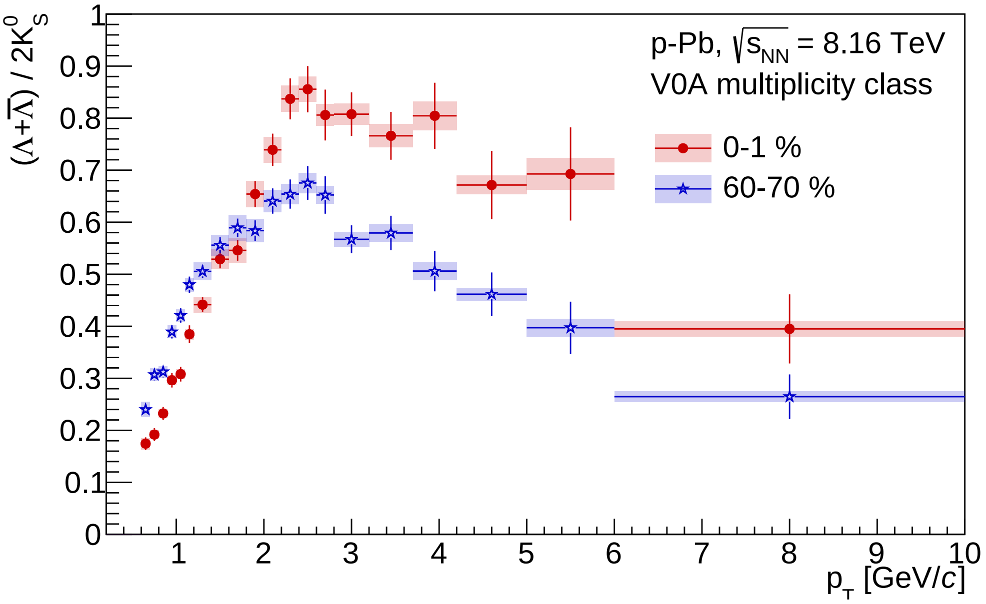

(b) [0, 1] % vs [60, 70] % multiplicity bins.

Figure E.5: Ratio of the combined $\Lambda + \bar{\Lambda}$ spectra to two times the $K^0_S$ spectrum, in two multiplicity bins. Both the highest multiplicity bin ([0, 1] %) and one other bin are shown on each plot.

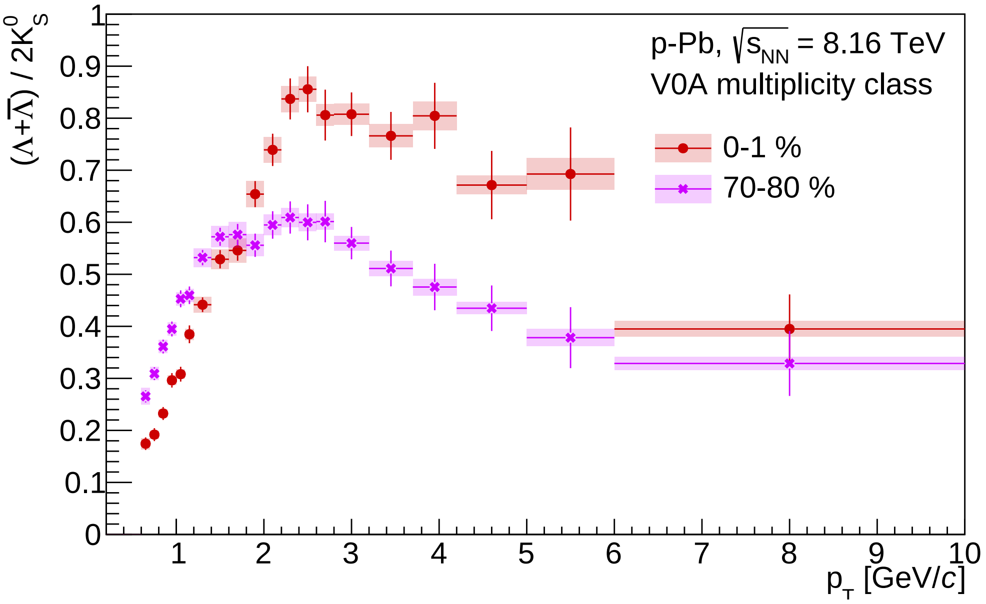

(a) [0, 1] % vs [70, 80] % multiplicity bins.

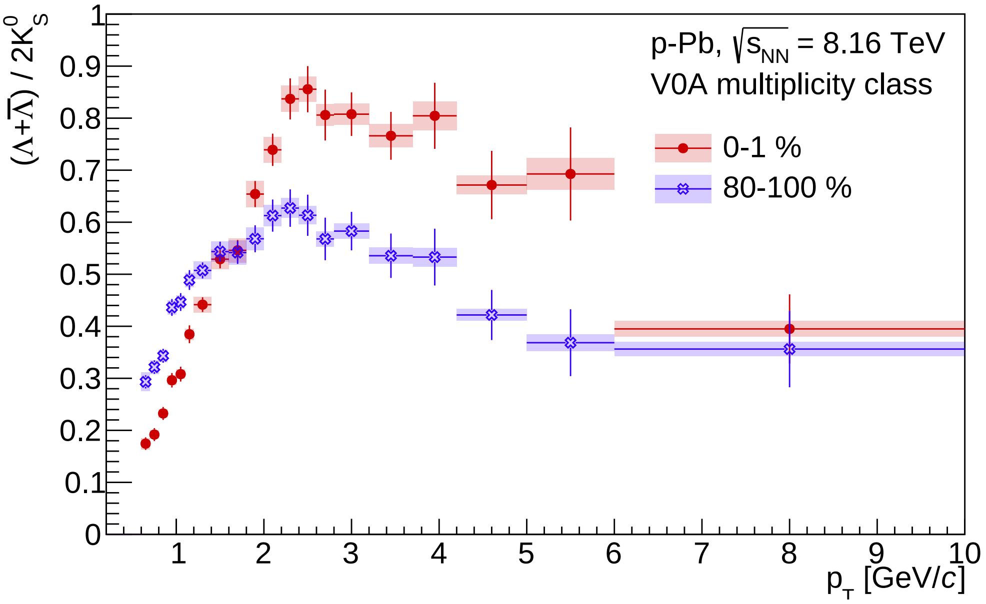

(b) [0, 1] % vs [80, 100] % multiplicity bins.

Figure E.6: Ratio of the combined $\Lambda + \bar{\Lambda}$ spectra to two times the $K^0_S$ spectrum, in two multiplicity bins. Both the highest multiplicity bin ([0, 1] %) and one other bin are shown on each plot.